Title	Split Fermi Surface Properties and Superconductivity in the Non-centrosymmetric Crystal Structure
Author(s)	河井, 友也
Citation	大阪大学, 2008, 博士論文
Version Type	VoR
URL	https://hdl.handle.net/11094/419
rights	
Note	

Doctoral Dissertation

Split Fermi Surface Properties and Superconductivity in the Non-centrosymmetric Crystal Structure

Tomoya Kawai

Department of Physics, Graduate School of Science
Osaka University

February, 2008

Abstract

The electrical and magnetic properties of the non-centrosymmetric rare earth compounds of RTX$_3$ (R: rare earth, T: transition metal and X: Si and Ge) and Ce$_2$TGe$_6$ (T: Pd, Pt) were studied by measuring the electrical resistivity, specific heat, magnetic susceptibility, magnetization and de Haas-van Alphen effect, together with the resistivity measurement under pressure. Two significant experimental results are obtained in RTX$_3$: the antisymmetric spin-orbit interaction and the unique superconducting property, which are based on the non-uniform lattice potential along the non-centrosymmetric tetragonal [001] direction.

As for RTX$_3$, we succeeded in growing single crystals of LaTGe$_3$ (T: Fe, Co, Rh, Ir) and PrCoGe$_3$, and studied the split Fermi surface properties and the magnitude of the antisymmetric spin-orbit interaction $2|\alpha p_\perp|$. The $2|\alpha p_\perp|$ value is found to be changed when LaTGe$_3$ is changed from T = Co, Rh to Ir, but unchanged in LaIrX$_3$ from X = Si to Ge. It is noticed that this $2|\alpha p_\perp|$ value is large in LaIrSi$_3$ and LaIrGe$_3$: $2|\alpha p_\perp| = 460$ K in LaCoGe$_3$, 510 K in LaRhGe$_3$, 1090 K in LaIrGe$_3$ and 1100 K in LaIrSi$_3$ for the main outer orbits named α of bands 69 and 70 electron Fermi surfaces, for example. This is mainly due to the large effective atomic number of Ir and a large distribution of the radial wave function of Ir-5d electrons close to the nuclear center, compared with those of Co and Rh. In the case of a paramagnet PrCoGe$_3$ and LaFeGe$_3$ with the relatively large cyclotron effective mass, the corresponding $2|\alpha p_\perp|$ value is found to become small: $2|\alpha p_\perp| = 280$ K in PrCoGe$_3$ and 460 K in LaCoGe$_3$ for main orbits α, and 130 K for main orbits in LaFeGe$_3$. It is experimentally confirmed that the antisymmetric spin-orbit interaction becomes small in magnitude with increasing the cyclotron mass, being inversely proportional to the cyclotron mass.

We investigated the magnetic susceptibility for CeTSi$_3$ and CeTGe$_3$ single crystals. The susceptibility for $H // [100]$, χ_a, is found to be larger than that for $H // [001]$, χ_c, except for CeCoGe$_3$. This characteristic feature was clarified from the analyses of the crystalline electric field. The Néel temperature and the electronic specific heat coefficient were plotted as a function of volume in the crystal structure for CeTSi$_3$ and CeTGe$_3$. This relation roughly corresponds to the Doniach phase diagram indicating the competition between the RKKY interaction and the Kondo effect. We thus studied the effect of pressure on the electronic states in antiferromagnets CeTGe$_3$ (T: Co, Rh, Ir) by measuring the resistivity under pressure. No noticeable change of the Néel temperature was observed up to 8 GPa in CeRhGe$_3$ and CeIrGe$_3$, which are far from the magnetic quantum critical point. On the other hand, the Néel temperature in CeCoGe$_3$ was strongly decreased as a function of pressure, and pressure-induced superconductivity was observed in the pressure region from 5.4 GPa to about 7.5 GPa in CeCoGe$_3$. The slope of upper critical field H_c2 at 6.5 GPa for $H // [001]$ is found to be extremely large: $-\mathrm{d}H_\mathrm{c2}/\mathrm{d}T = 200$ kOe/K at the superconducting transition temperature $T_\mathrm{sc} = 0.69$ K, and the upper critical field indicates an upturn feature with decreasing temperature. $H_\mathrm{c2}(0)$ is roughly estimated to be about 200 kOe. This might be an experimental evidence of the spin-triplet superconductivity in the non-centrosymmetric crystal structure.

Contents

1 Introduction

The f-electrons of cerium and uranium compounds exhibit a variety of characteristic features including spin and charge orderings, spin and valence fluctuations, heavy fermions and anisotropic superconductivity. In these compounds, the Ruderman-Kittel-Kasuya and Yosida (RKKY) interaction[1–3] and the Kondo effect[4] compete with each other. The RKKY interaction enhances the long-range magnetic order, where the f-electrons with magnetic moments are treated as localized electrons, and the indirect f-f interaction is mediated by the spin polarization of the conduction electrons. On the other hand, the Kondo effect quenches the magnetic moments of the localized f-electrons by the spin polarization of the conduction electrons, producing a spin singlet state, which leads to a heavy fermion state with an extremely large effective mass at low temperatures. The competition between the RKKY interaction and the Kondo effect was discussed by Doniach as a function of $|J_{cf}|D(\varepsilon_{\mathrm{F}})$,[5,6] where J_{cf} is the magnetic exchange interaction and $D(\varepsilon_{\mathrm{F}})$ is the density of states of conduction electrons at the Fermi energy.

Experimentally $|J_{cf}|D(\varepsilon_{\mathrm{F}})$ is replaced by pressure. The electronic states are changed by pressure from the magnetically ordered state to the paramagnetic state. The magnetic ordering temperature T_{mag} becomes zero in some cases at critical pressure P_{c}: $T_{\mathrm{mag}} \to 0$ at $P \to P_{\mathrm{c}}$. Characteristic features such as the non-Fermi liquid nature, the heavy fermion state or anisotropic superconductivity are observed around this critical pressure.[7,8]

The most important observation for heavy fermion superconductors such as $\mathrm{CeCu_2Si_2}$,[9] $\mathrm{UPd_2Al_3}$[10] and $\mathrm{UPt_3}$[11] is that superconductivity is realized in the magnetically ordered state and/or in the magnetic fluctuating state. The corresponding physical quantities such as the specific heat and the spin-lattice relaxation rate do not follow the exponential dependence of $e^{-\Delta/k_{\mathrm{B}}T}$ in the superconducting state, which is expected from the Bardeen-Cooper-Schrieffer (BCS) theory,[12] but obey a power law of T^n. Here Δ is the superconducting energy gap and n is an integer. This means that the superconducting gap possesses line and/or point nodes. These results are based on the fact that conduction electrons with 10 - 100 m_0 (m_0: rest mass of an electron) are of an f-electron character, which originates from the strong Coulomb repulsion between the f-electrons. These conduction electrons condense into Cooper pairs. The symmetry of the superconducting condensate is determined from the NMR technique to be of a p-wave spin triplet state or a d-wave spin singlet state.

Very recently, a new aspect of superconductivity appeared, namely superconductivity in the non-centrosymmetric crystal structure. It was reported that the spin-triplet superconductivity might be realized in $\mathrm{CePt_3Si}$ with the non-centrosymmetric tetragonal structure.[13,14] Pressure-induced superconductivity was also observed for a ferromagnet UIr,[15–17] and antiferromagnets $\mathrm{CeRhSi_3}$,[18–20] $\mathrm{CeIrSi_3}$[8,21,22] and $\mathrm{CeCoGe_3}$[23] with the non-centrosymmetric crystal structure. These compounds are the non-centrosymmetric heavy fermion compounds. In addition to these heavy fermion f-electron systems, the spin-triplet nature was also reported in a non-magnetic compound $\mathrm{Li_2Pt_3B}$,[24] whereas the usual BCS superconductivity is realized in the similar non-magnetic compound $\mathrm{Li_2Pd_3B}$.[25,26]

The existence of inversion symmetry in the crystal structure is believed to be a favorable factor for the formation of Cooper pairs, especially for the spin-triplet configuration because one conduction electron with a momentum $\boldsymbol{p}$ and an up-spin state and the other conduction electron with a momentum $-\boldsymbol{p}$ and an up-spin state belong to two different Fermi surfaces, separated by 10 - 1000 K in energy. This occurs via the antisymmetric spin-orbit interaction, which is based on the non-uniform lattice potential in the non-centrosymmetric crystal structure. It is needed to clarify the nature and the magnitude of the antisymmetric spin-orbit interaction in the non-centrosymmetric crystal structure.

In the present thesis, we studied experimentally the antisymmetric spin-orbit interaction via the de Haas-van Alphen experiment for high-quality single crystals of non-centrosymmetric compounds RTX_3(R: rare earth, T: transition metal, and X: Ge and Si). This is fundamentally important to consider superconductivity without inversion center in the crystal structure. Electrical and magnetic properties of $CeTX_3$ were also clarified experimentally, together with pressure-induced superconductivity in an antiferromagnet $CeCoGe_3$.

In Chaps. 2 and 3, we will give a review including fundamental background of the present study and the relevant previous study of RTX_3(R: rare earth, T: transition metal, and X: Ge and Si) and another non-centrosymmetric compounds Ce_2TGe_6(T: transition metal). In Chap. 4, we will present the motivation of the present study. Next, we will introduce the single crystal growth and the experimental methods including de Haas-van Alphen(dHvA) effect and high pressure measurement in Chap. 5. In Chap. 6, we show the experimental results, with analyses and discussion. Finally, the present study is summarized and concluded in Chap. 7.

2 Review of Relevant Physics in f-Electron Systems

2.1 CEF effect and the RKKY interaction

The $4f$ electrons in the Ce atom are pushed deeply into the interior of the closed $5s$ and $5p$ shells because of the strong centrifugal potential $\ell(\ell+1)/r^2$, where $\ell = 3$ holds for the f electrons. This is a reason why the $4f$ electrons possess an atomic-like character in the crystal.[27] On the other hand, the tail of their wave function spreads to the outside of the closed $5s$ and $5p$ shells, which is highly influenced by the potential energy, the relativistic effect and the distance between the Ce atoms. This results in the hybridization of the $4f$ electrons with the conduction electrons. These cause various phenomena such as magnetic ordering, quadrupolar ordering, valence fluctuations, Kondo lattice, heavy fermions, Kondo insulators and unconventional superconductivity.
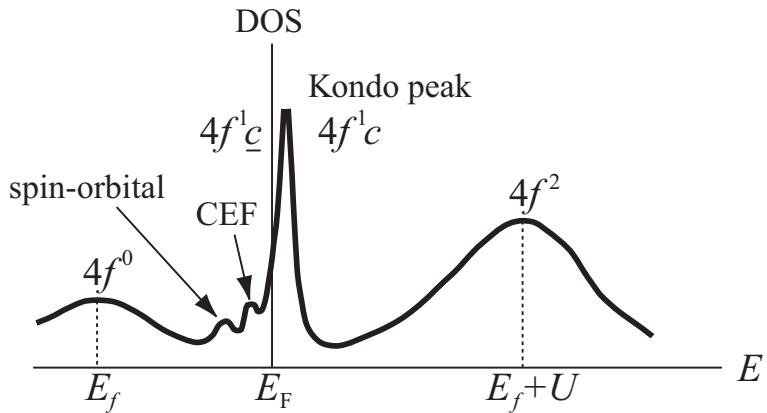

Fig. 2.1 Density of states (DOS) of the $4f$ electron in the Ce compound (Ce^{3+}), cited from ref. 28.

The Coulomb repulsive force of the $4f$ electron at the same atomic site, U, is so strong, e.g., $U \simeq 5$ eV in the Ce compounds (see Fig. 2.1), that occupancy of the same site by two $4f$ electrons is usually prohibited. In the Ce compounds, the tail of the $4f$ partial density of states extends to the Fermi level even at room temperature, and thus the $4f$ level approaches the Fermi level in energy and the $4f$ electron hybridizes strongly with the conduction electrons. This $4f$-hybridization coupling constant is denoted by V_{cf}. When U is strong and V_{cf} is ignored, the freedom of the charge in the $4f$ electron is suppressed, while the freedom of the spin is retained, representing the $4f$-localized state. Naturally, the degree of localization depends on the level of the $4f$ electron, E_f, where larger E_f helps to increase the localization.

In the localized $4f$-electronic scheme, the $4f$ ground multiplets, which obey the Fund rule in the LS-multiplets, split into the J-multiplets ($J = 7/2$ and $J = 5/2$ in Ce^{3+}) by
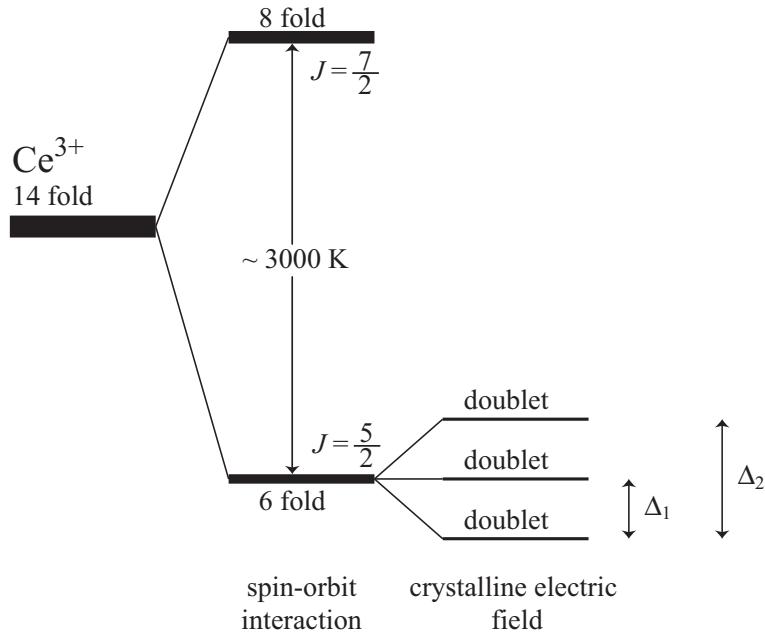
Fig. 2.2 Level scheme of the $4f$ electron in Ce^{3+}.

the spin-orbit interaction. Moreover, the J-multiplets split into the $4f$ levels based on the crystalline electric field (CEF), as shown in Fig. 2.2.

The electronic state of the point rare earth electron is influenced from the electric field of the surrounding negative ions. It is called the crystalline electric field (CEF) effect. The electrostatic potetial can be expressed as follows:

$$\phi(\boldsymbol{r}) = \sum_i \frac{q_i}{|\boldsymbol{r} - \boldsymbol{R}_i|}, \tag{2.1}$$

where $\boldsymbol{r}$ is the position vector of the $4f$ electron in Ce^{3+}, q_i is the charge of the six-coordinated negative ion and $\boldsymbol{R}_i$ is the position vector of the corresponding ion.

For example, we consider the next case: the negative ion with the charge q is located at $(a, 0, 0)$, $(-a, 0, 0)$, $(0, a, 0)$, $(0, -a, 0)$, $(0, 0, a)$ and $(0, 0, -a)$, as shown in Fig. 2.3. We express eq. (2.1) by the Taylor expansion, and get the following equation:

$$
\begin{aligned}
\phi(x, y, z) \; \simeq \; & \frac{6q}{a} + D_4 \left\{ \left(x^4 + y^4 + z^4\right) - \frac{3}{5}r^4 \right\} \\
& + D_6 \left\{ \left(x^6 + y^6 + z^6\right) + \frac{15}{4} \left(x^2 y^4 + x^2 z^4 + y^2 x^4 + y^2 z^4 + z^2 x^4 \right. \right. \\
& \left. \left. + \; z^2 y^4\right) - \frac{15}{14} r^6 \right\},
\end{aligned}
\tag{2.2}
$$

where $D_4 = 35q/4a^5$ and $D_6 = -21q/2a^7$.
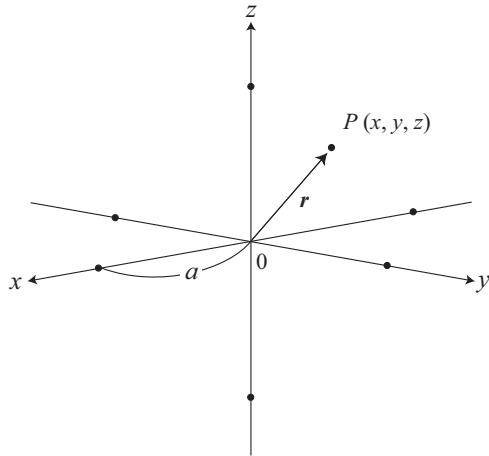
Fig. 2.3 Six-coordinated negative ions and the $4f$ electron at the point P.

Considering the charge distribution of the f electron, $\rho(r)$, the static potential energy is expressed as follows:

$$\int \rho(r)\phi(r)d^3r, \tag{2.3}$$

where $\phi(r)$ can be expanded by the multiplet term of the coordination x, y, z and eq. (2.3) is expressed by the multiplet term of the coordination which is equivalent to the multiplet of the angular momentum operator based on the Wigner-Eckart's theorem in quantum mechanics. For example,

$$\begin{aligned}
\int (3z^2 - r^2)\rho(r)d^3r &= \alpha_J \left\langle r^2 \right\rangle \left\{ 3J_z^2 - J(J+1) \right\} \\
&= \alpha_J \left\langle r^2 \right\rangle O_2^0. \tag{2.4}
\end{aligned}$$

We can represent the following CEF Hamiltonian corresponding to eqs. (2.2) and (2.3) by the Wigner-Eckart's theorem as follows:

$$\mathcal{H}_{\mathrm{CEF}} = B_4^0 \left(O_4^0 + 5O_4^4 \right) + B_6^0 \left(O_6^0 - 21O_6^4 \right). \tag{2.5}$$

Here we ignored the first term of eq. (2.2), because it have no coordination. $\mathcal{H}_{\mathrm{CEF}}$ is called the crystalline electric field Hamiltonian and the operator O_n^m: O_4^0, O_4^4, O_6^0, O_6^4 and so on, called Stevens operators. These operators are expressed by the matrix representation by Hutchings.[29, 30]

Next, we consider the case which Ce^{3+} is influenced by the cubic crystalline electric field: $L = 3$, $S = 1/2$, $J = 5/2$ and $M = \frac{5}{2}, \frac{3}{2}, \frac{1}{2}, -\frac{1}{2}, -\frac{3}{2}, -\frac{5}{2}$. Therefore, the multiplet with the $J = 5/2$ case (sixfold degenerate of $2J + 1 = 6$) splits by the CEF effect. For $J = 5/2$, $O_6^0 = O_6^4 = 0$, and O_4^0 and O_4^4 can be expressed as follows:

$$O_4^0 = 35J_z^4 - 30J(J+1)J_z^2 + 25J_z^2 - 6J(J+1) + 3J^2(J+1)^2 \tag{2.6}$$

$$O_4^4 = \frac{1}{2}(J_+^4 + J_-^4) \tag{2.7}$$

where $J_\pm = J_x \pm iJ_y$. The operator O_n^m can be expressed by (6×6)-matrix. Therefore, the CEF Hamiltonian of the cubic Ce^{3+} is expressed as follows:

$$
\mathcal{H}_{\mathrm{CEF}} =
\begin{array}{c}
\\
\langle\frac{5}{2}| \\
\langle\frac{3}{2}| \\
\langle\frac{1}{2}| \\
\langle-\frac{1}{2}| \\
\langle-\frac{3}{2}| \\
\langle-\frac{5}{2}|
\end{array}
\begin{array}{cccccc}
|\frac{5}{2}\rangle & |\frac{3}{2}\rangle & |\frac{1}{2}\rangle & |-\frac{1}{2}\rangle & |-\frac{3}{2}\rangle & |-\frac{5}{2}\rangle
\end{array}
\left(
\begin{array}{cccccc}
60B_4^0 & 0 & 0 & 0 & 60\sqrt{5}B_4^0 & 0 \\
0 & -180B_4^0 & 0 & 0 & 0 & 60\sqrt{5}B_4^0 \\
0 & 0 & 120B_4^0 & 0 & 0 & 0 \\
0 & 0 & 0 & 120B_4^0 & 0 & 0 \\
60\sqrt{5}B_4^0 & 0 & 0 & 0 & -180B_4^0 & 0 \\
0 & 60\sqrt{5}B_4^0 & 0 & 0 & 0 & 60B_4^0
\end{array}
\right) \tag{2.8}
$$

Next we represent the energy level state $|i\rangle$ and its energy scheme E_i as follows:

$$\mathcal{H}_{\mathrm{CEF}}|i\rangle = E_i|i\rangle. \tag{2.9}$$

Following wave functions and energies are obtained:

$$
\left.
\begin{array}{rcl}
|\Gamma_7^\alpha\rangle &=& \frac{1}{\sqrt{6}}|\frac{5}{2}\rangle - \sqrt{\frac{5}{6}}|-\frac{3}{2}\rangle \\
|\Gamma_7^\beta\rangle &=& \frac{1}{\sqrt{6}}|-\frac{5}{2}\rangle - \sqrt{\frac{5}{6}}|\frac{3}{2}\rangle
\end{array}
\right\}
\quad E_{\Gamma_7} = -240B_4^0 \tag{2.10}
$$

$$
\left.
\begin{array}{rcl}
|\Gamma_8^\nu\rangle &=& \sqrt{\frac{5}{6}}|\frac{5}{2}\rangle + \frac{1}{\sqrt{6}}|-\frac{3}{2}\rangle \\
|\Gamma_8^\kappa\rangle &=& \sqrt{\frac{5}{6}}|-\frac{5}{2}\rangle + \frac{1}{\sqrt{6}}|\frac{3}{2}\rangle \\
|\Gamma_8^\lambda\rangle &=& |\frac{1}{2}\rangle \\
|\Gamma_8^\mu\rangle &=& |-\frac{1}{2}\rangle
\end{array}
\right\}
\quad E_{\Gamma_8} = 120B_4^0 \tag{2.11}
$$

The energy state $-240B_4^0$ is named Γ_7 and the energy state $120B_4^0$ is Γ_8. We show in Fig. 2.4 the space charge distribution of Γ_7 and Γ_8 states. The quartet Γ_8 wave function expands along the x, y, z directions. On the other hand, the doublet Γ_7 expands along the $\langle 111 \rangle$ direction so as to avoid these axes. If the negative ions approach to the cerium ion along the principal axes, the Coulomb energy of the $4f$ electron is preferable to the Γ_7 ground state, compared with the Γ_8 ground state, indicating that the Γ_8 state becomes an excited state.

In general, the CEF Hamiltonian can be expressed as follows:

$$\mathcal{H}_{\mathrm{CEF}} = \sum_{n,m} B_n^m O_n^m. \tag{2.12}$$
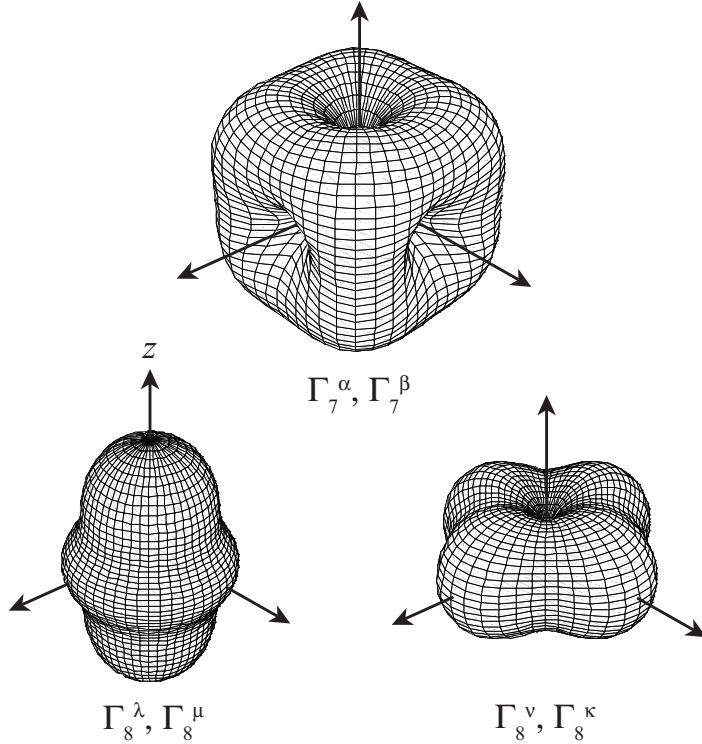
Fig. 2.4 Space charge distribution of Γ_7 and Γ_8 states.

If the number of the f electron is odd, namely, J has the half-integer for Ce^{3+} Nd^{3+} Sm^{3+} Dy^{3+} Er^{3+} and Yb^{3+}, the $4f$ energy level always possesses the doublet. This is called Kramers theorem, and this doublet is called the Kramers doublet. Kramers degeneration is based on the time reversal symmetry and the doublet ground state always holds even if the crystal structure is changed into the low symmetry. Namely, its magnetic properties are different whether the number of the f electron is odd or even. When the magnetic field is applied to the system, all the degenerated $4f$ states, including the Kramers doublet, split into singlets.

We can obtain the mangetic moment of the f electron by measuring the magnetic susceptibility or magnetization under magnetic field H, considering the Zeeman energy term, as follows:

$$\mathcal{H} = \mathcal{H}_{\mathrm{CEF}} - g_J \mu_{\mathrm{B}} H J_z \qquad (\boldsymbol{H}/\!/z), \qquad (2.13)$$

where $|i\rangle$ is the state of the $4f$ energy level i, E_i is the eigenvalue and μ_i is the magnetic moment of the energy level. The energy level is influenced by the other energy levels. We represent this energy state as $|\tilde{i}\rangle$ and $E_i(H)$. Namely, we calculate the energy state under magnetic field $|\tilde{i}\rangle$ and $E_i(H)$ by diagonalizing the matrix of the Hamiltonian eq. (2.8). We calculate the magnetization and the magnetic susceptibility by $|\tilde{i}\rangle$ and $E_i(H)$. Here,

the Helmholtz free energy F can be expressed by the partial function Z as follows:

$$F = -k_{\mathrm{B}}T \ln Z, \tag{2.14}$$

$$Z = \sum_i e^{-\frac{E_i(H)}{k_{\mathrm{B}}T}}. \tag{2.15}$$

The magnetization M is expressed as the differential of F by magnetic field:

$$
\begin{aligned}
M &= -\frac{\partial F}{\partial H} \\
&= \frac{\displaystyle\sum_i \mu_{z_i} e^{-E_i(H)/k_{\mathrm{B}}T}}{\displaystyle\sum_i e^{-E_i(H)/k_{\mathrm{B}}T}} \\
&\equiv \langle \mu_{z_i} \rangle,
\end{aligned}
\tag{2.16}
$$

where μ_{z_i} is the magnetic moment of the state $|\tilde{i}\rangle$.

$$
\begin{aligned}
\mu_{z_i} &= -\frac{\partial E_i(H)}{\partial H} \\
&= g_J \mu_{\mathrm{B}} \langle \tilde{i}|J_z|\tilde{i}\rangle.
\end{aligned}
\tag{2.17}
$$

Namely, the magnetization M correspond to the average $\langle \mu_{z_i} \rangle$ of the magnetic moment μ_{z_i}.

The magnetic susceptibility χ is the differential of magnetization $\partial M/\partial H (H \to 0)$:

$$\chi = \frac{1}{k_{\mathrm{B}}T}\left(\left\langle \left(\frac{\partial E_i(H)}{\partial H}\right)^2\right\rangle - \left\langle \frac{\partial E_i(H)}{\partial H}\right\rangle^2\right) - \left\langle \frac{\partial^2 E_i(H)}{\partial H^2}\right\rangle. \tag{2.18}$$

In case of the calculation of the magnetic susceptibility, we can treat the Zeeman energy $-g_J \mu_{\mathrm{B}} H J_z$ as the perturbation. The energy $E_i(H)$ by the second perturbation can be expressed as follows:

$$E_i(H) = E_i - g_J \mu_{\mathrm{B}} H \langle i|J_z|i\rangle + (g_J \mu_{\mathrm{B}})^2 H^2 \sum_{j(\neq i)} \frac{|\langle j|J_z|i\rangle|^2}{E_j - E_i}. \tag{2.19}$$

By using eq (2.19), eq. (2.18) is obtained as

$$\chi = \frac{(g_J \mu_{\mathrm{B}})^2 \displaystyle\sum_i e^{-E_i/k_{\mathrm{B}}T}\left(|\langle i|J_z|i\rangle|^2 + 2k_{\mathrm{B}}T \displaystyle\sum_{j(\neq i)} \frac{|\langle j|J_z|i\rangle|^2}{E_j - E_i}\right)}{k_{\mathrm{B}}T \displaystyle\sum_i e^{-E_i/k_{\mathrm{B}}T}}. \tag{2.20a}$$

Eq. (2.20a) is the general expression of the magnetic susceptibility under consideration of CEF, but another expression is often used:

$$\chi = \frac{(g_J\mu_B)^2}{\sum_i e^{-E_i/k_BT}} \left(\frac{\sum_i |\langle i|J_z|i\rangle|^2 e^{-E_i/k_BT}}{k_BT} + \sum_i \sum_{j(\neq i)} |\langle j|J_z|i\rangle|^2 \frac{e^{-E_i/k_BT} - e^{-E_j/k_BT}}{E_j - E_i} \right).$$

(2.20b)

The first term is the Curie term which can be determined from the diagonal terms of the matrix J_z, and the second term is related to the non-diagonal terms. Namely, it is the Van-Vleck term, which is related to the transition between the states. It is known from eq. (2.20) that the magnetic susceptibility can be determined from the state of the f electron without magnetic field.

Next, we calculate J_z for the cubic Ce^{3+}. The J_z matrix can be expressed as follows:

$$J_z = \begin{array}{c} \\ \langle\Gamma_7^\alpha| \\ \langle\Gamma_7^\beta| \\ \langle\Gamma_8^\nu| \\ \langle\Gamma_8^\kappa| \\ \langle\Gamma_8^\lambda| \\ \langle\Gamma_8^\mu| \end{array} \begin{pmatrix} |\Gamma_7^\alpha\rangle & \left|\Gamma_7^\beta\right\rangle & |\Gamma_8^\nu\rangle & |\Gamma_8^\kappa\rangle & |\Gamma_8^\lambda\rangle & |\Gamma_8^\mu\rangle \\ -\frac{5}{6} & 0 & \frac{2\sqrt{5}}{3} & 0 & 0 & 0 \\ 0 & \frac{5}{6} & 0 & -\frac{2\sqrt{5}}{3} & 0 & 0 \\ \frac{2\sqrt{5}}{3} & 0 & \frac{11}{6} & 0 & 0 & 0 \\ 0 & -\frac{2\sqrt{5}}{3} & 0 & -\frac{11}{6} & 0 & 0 \\ 0 & 0 & 0 & 0 & \frac{1}{2} & 0 \\ 0 & 0 & 0 & 0 & 0 & -\frac{1}{2} \end{pmatrix}.$$

(2.21)

We obtain the magnetic moment as $-5/7\,\mu_B$ for $|\Gamma_7^\alpha\rangle$ and $+5/7\,\mu_B$ for $|\Gamma_7^\beta\rangle$ from $g_J = 6/7$. The summation over the two degenerated states of the Γ_7 state is zero. The magnetic moments for $|\Gamma_8^\nu\rangle$ $|\Gamma_8^\kappa\rangle$, $|\Gamma_8^\lambda\rangle$ and $|\Gamma_8^\mu\rangle$ are $11/7\,\mu_B$, $-11/7\,\mu_B$, $3/7\,\mu_B$ and $-3/7\,\mu_B$, respectively. Eq. (2.20b) can be expressed as follows (Γ_7 is the ground state, Γ_8 is the excited state and $E_{\Gamma_8} - E_{\Gamma_7} = \Delta$):

$$\chi_z = \frac{(g_J\mu_B)^2}{1 + 2e^{-\Delta/k_BT}} \left\{ \frac{\frac{25}{36} + \frac{65}{18}e^{-\Delta/k_BT}}{k_BT} + \frac{40\left(1 - e^{-\Delta/k_BT}\right)}{9\Delta} \right\}.$$

(2.22)

Figure 2.5(a) and (b) show the temperature dependence of the inverse magnetic susceptibility and magnetization, respectively, on the basis of eqs. (2.16), (2.20) and (2.21), for three cases: no CEF, Γ_7 ground state and Γ_8 ground state with the splitting energy $\Delta = 200\,K$ between Γ_7 and Γ_8. If there is no CEF, $\Delta \to 0$ and $\chi_z = \frac{35}{4}\left(g_J\mu_B\right)^2/3k_BT$. The case of $\Delta \to 0$ is equivalent to the expression $k_BT \gg \Delta$ and to the Curie law which ignores CEF. When Γ_7 is the ground state, the magnetization approaches the magnetic

moment of $0.7 \sim 0.8\,\mu_B$. On the other hand, when Γ_8 is the ground state, the magnetization becomes $1.7 \sim 1.8\,\mu_B$. If the Zeeman energy due to the magnetic field is larger than the CEF splitting energy, the magnetization becomes the saturated magnetic moment $g_J J$.

The $4f$-localized situation is applied to most of the lanthanide compounds in which Ruderman-Kittel-Kasuya-Yosida (RKKY) interaction plays a predominant role in magnetism.[1–3] The mutual magnetic interaction between the $4f$ electrons occupying different atomic sites cannot be of a direct type such as $3d$ metal magnetism, but should be indirect one, which occurs only through the conduction electrons.

In the RKKY interaction, a localized spin $\boldsymbol{S}_i$ of the $4f$ electron interacts with a conduction electron with spin $\boldsymbol{s}$, which leads to a spin polarization of the conduction electron. This polarization interacts with another neighboring spin $\boldsymbol{S}_j$ and therefore creates an indirect interaction between the spins $\boldsymbol{S}_i$ and $\boldsymbol{S}_j$. This indirect interaction extends to the far distance and damps with a sinusoidal $2k_F$ oscillation (named the Friedel oscillation), where k_F is half of the caliper dimension of the Fermi surface. When the number of $4f$ electrons increases in such a way that the lanthanide element changes from Ce to Gd or reversely from Yb to Gd in the compound, the magnetic moment becomes larger and the RKKY interaction stronger, leading to the magnetic order. The ordering temperature roughly follows the de Gennes relation, $(g_J - 1)^2 J(J + 1)$. Here g_J is the Landé g-factor and J is the total angular momentum.

2.2   Kondo effect and heavy fermions

Contrary to what happens at a large U, higher V_{cf} tends to enhance the hybridization of the $4f$ electron with conduction electrons, thus accelerating the delocalization of the $4f$ electron. The delocalization of the $4f$ electron tends to make the $4f$ band wide. When
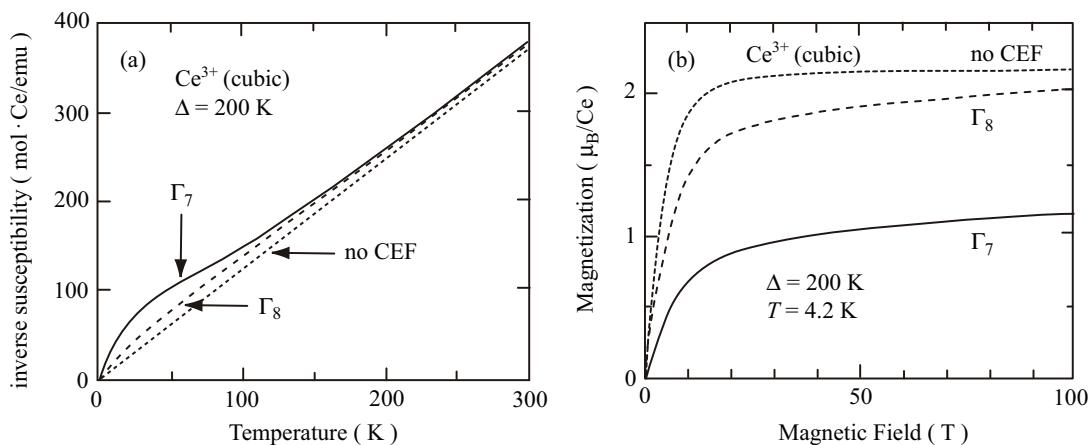

Fig. 2.5 (a) Inverse magnetic susceptibility and (b) magnetization for $\Delta = 200\,\mathrm{K}$ in cubic Ce^{3+}.

$E_f > V_{cf}$, the $4f$ electron is still better localized and the Kondo regime is expected in the Ce compounds.

The study of Kondo effect began when a low-temperature resistivity minimum was found for non-magnetic metals with ppm-order magnetic impurities. Kondo showed theoretically that the logarithmic resistivity increase at low temperatures as a result of the spin-flip scattering of the conduction electrons by the localized magnetic moments of impurities.[4] In the $3d$-based dilute alloys, the magnetic impurity Kondo effects can be observed only in the case of very low concentration $3d$ magnetic impurities. This is because the degeneracy of the localized spins is very important for the Kondo effect. When the concentration of $3d$ magnetic impurities is increased, the $3d$ elements would come near each other and thus the overlapping or interaction between $3d$ shells would occur, which would lift the degeneracy of the impurity spin and suppress the Kondo spin-flip process.

Since the observation of the $\rho(T) \sim \ln T$ dependence in $CeAl_3$ by Buschow *et al.*[31], many rare earth compounds, in particular, Ce compounds were found to show the anomalous behavior similar to the impurity Kondo effect. In these compounds, the $4f$ ions have very high concentration and can even form the crystalline lattice with the anions and thus it cannot be considered as the impurities. From the appearance of a Kondo-like behavior, this phenomenon is called the dense Kondo effect.
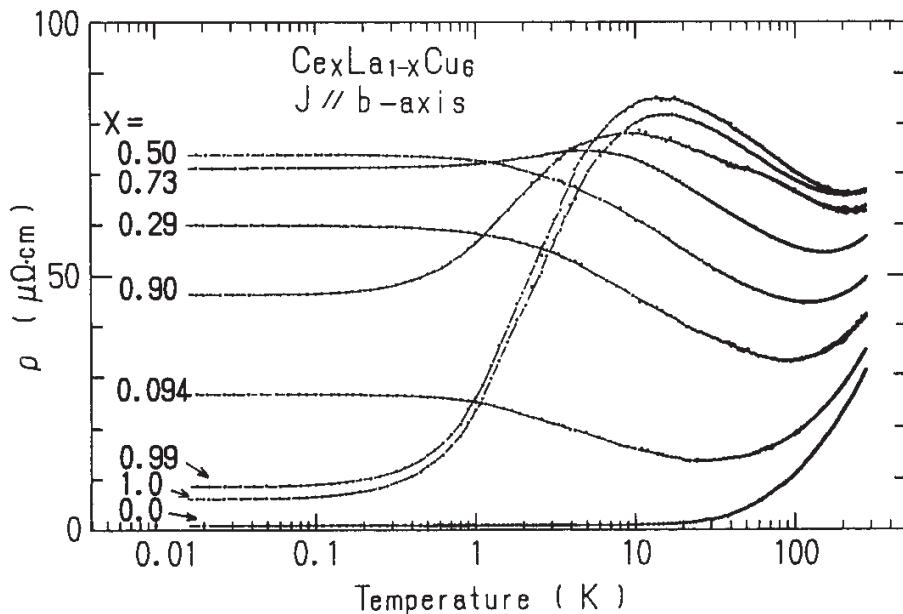

Fig. 2.6 Temperature dependence of the electrical resistivity in $Ce_xLa_{1-x}Cu_6$.[32]

The property of the dense Kondo effect at high temperatures is the same as that of the dilute Kondo system, but at low temperatures it is quite different in behavior. For instance, we show the temperature dependence of the electrical resistivity in $Ce_xLa_{1-x}Cu_6$[32] in Fig. 2.6. This resistivity increases logarithmically with decreasing the

temperature for all range of concentration. The Kondo effect occurs independently at each Ce site, because the slope of the logarithmically curve is almost proportional to the concentration of Ce. In $CeCu_6$ ($x = 1$), the behavior is, however, very different from the dilute Kondo impurity system. The resistivity increases with decreasing the temperature, forms a maximum around $15\,K$ and decreases rapidly at lower temperatures, following the Fermi liquid nature of $\rho = \rho_0 + AT^2$. This behavior is in contrast to the dilute system ($x = 0.094$) characterized by a resistivity minimum.

The many-body Kondo bound state is now understood as follows: For the simplest case of no orbital degeneracy, the localized spin $S(\uparrow)$ is coupled antiferromagnetically with the conduction electrons $s(\downarrow)$. Consequently the singlet state $\{S(\uparrow){\cdot}s(\downarrow){\pm}S(\downarrow){\cdot}s(\uparrow)\}$ is formed with the binding energy $k_B T_K$. Here the Kondo temperature T_K is the single energy scale. In other words, disappearance of the localized moment is thought to be due to the formation of a spin-compensating cloud of the conduction electrons around the impurity moment.

The Kondo temperature in the Ce compounds is large compared with the magnetic ordering temperature based on the RKKY interaction. For example, the Ce ion is trivalent ($J = \frac{5}{2}$) and the $4f$ energy level splits into the three doublets by the crystalline electric field, namely possessing the splitting energy of Δ_1 and Δ_2, as shown in Fig. 2.2.

The Kondo temperature is given as follows [33]:

$$T_K^h = D \exp\left\{-\frac{1}{3|J_{cf}|D(E_F)}\right\} \qquad \text{when } T > \Delta_1, \Delta_2, \tag{2.23}$$

and

$$T_K = \frac{D^2}{\Delta_1 \Delta_2} D \exp\left\{-\frac{1}{|J_{cf}|D(E_F)}\right\} \quad \text{when } T < \Delta_1, \Delta_2. \tag{2.24}$$

Here D, $|J_{cf}|$ and $D(E_F)$ are the band width, exchange energy and the density of states at the Fermi energy E_F, respectively. If we assume $T_K \simeq 5\,K$ for $D = 10^4\,K$, $\Delta_1 = 100\,K$ and $\Delta_2 = 200\,K$, the value of $T_K^h \simeq 50\,K$ is obtained, which is compared with the $S = \frac{1}{2}$-Kondo temperature of $10^{-3}\,K$ defined as $T_K^0 = D \exp\{-1/|J_{cf}|D(E_F)\}$. These large values of the Kondo temperature shown in eqs. (2.23) and (2.24) are due to the orbital degeneracy of the $4f$ levels. Therefore, even at low temperatures the Kondo temperature is not T_K^0 but T_K shown in eq. (2.24).

On the other hand, the magnetic ordering temperature is about $5\,K$ in the Ce compounds, which can be simply estimated from the de Gennes relation of $(g_J - 1)^2 J(J + 1)$ under the consideration of the Curie temperature of about $300\,K$ in Gd. Therefore, it depends on the compound whether magnetic ordering occurs at low temperatures or not.

The ground state properties of the dense Kondo system are interesting in magnetism, which are highly different from the dilute Kondo system. In the cerium intermetallic compounds such as $CeCu_6$, cerium ions are periodically aligned whose ground state cannot be a scattering state but becomes a coherent Kondo-lattice state.

The effective mass of the conduction electron in the Kondo lattice of $CeCu_6$ is extremely large, compared with the one of the free electron. It is reflected in the electronic specific heat coefficient γ and magnetic susceptibility $\chi(0)$, which can be expressed as

$$\gamma = \frac{2\pi^2 {k_B}^2}{3} D(E_F) \tag{2.25a}$$

$$= \frac{{k_B}^2 k_F}{3\hbar^2} m_c^* \qquad \text{(free electron model)}, \tag{2.25b}$$

and

$$\chi(0) = 2{\mu_B}^2 D(E_F) \tag{2.26a}$$

$$= {\mu_B}^2 \frac{k_F}{\pi^2 \hbar^2} m_c^* \quad \text{(free electron model)}. \tag{2.26b}$$

where k_F is Fermi wave number. These parameters are proportional to the effective mass.

The electrical resistivity ρ decreases steeply with decreasing the temperature, following a Fermi liquid behavior as $\rho \sim AT^2$ with a large value of the coefficient A [33]. The $\sqrt{A}$ value is proportional to the effective mass of the carrier m_c^* and thus inversely proportional to the Kondo temperature. Correspondingly, the electronic specific heat coefficient γ roughly follows the simple relation $\gamma \sim 10^4/T_K$ (mJ/K^2·mol) because the Kramers doublet of the $4f$ levels is changed into the γ value in the Ce compounds:

$$R \ln 2 = \int_0^{T_K} \frac{C}{T} dT, \tag{2.27}$$

$$C = \gamma T, \tag{2.28}$$

thus

$$\gamma = \frac{R \ln 2}{T_K} = \frac{5.8 \times 10^3}{T_K} \text{ (mJ/K}^2\text{·mol)}. \tag{2.29}$$

It reaches $1600 \, \text{mJ/K}^2$·mol for $CeCu_6$ [34] because of a small Kondo temperature of 4-5 K. The conduction electrons possess large effective masses and thus move slowly in the crystal. Actually in $CeRu_2Si_2$, an extremely heavy electron of $120 \, m_0$ was detected from the de Haas-van Alphen (dHvA) effect measurements [35,36].

Therefore, the Kondo-lattice system is called a heavy fermion or heavy electron system. It is noticed that the Ce Kondo-lattice compound with magnetic ordering also possesses the large γ value even if the RKKY interaction overcomes the Kondo effect at low temperatures. For example, the γ value of CeB_6 is $260 \, \text{mJ/K}^2$·mol [37], which is roughly one hundred times as large as that of LaB_6, $2.6 \, \text{mJ/K}^2$·mol [38]. This means that the Kondo effect at high temperatures influences the electronic state, although the $4f$ electron is localized and orders antiferromagnetically.

A significant correlation factor is thought to be the ratio of the measured magnetic susceptibility $\chi(0)$ to the observed γ value:

$$R_{\mathrm{W}} \equiv \left(\frac{\pi^2 k_{\mathrm{B}}^2}{\gamma}\right) \left\{\frac{\chi(0)}{\mu_{\mathrm{B}}^2 g_J^2 J(J+1)}\right\}. \tag{2.30}$$

This ratio R_{W} is called Wilson-Sommerfeld ratio. Stewart [39] evaluated R_{W} for the heavy fermion system, as shown in Fig. 2.7. He suggested that in the f electron system R_{W} is not 1 but roughly 2. Kadowaki and Woods stressed the importance of a universal relationship between A and γ, as shown in Fig. 2.8.[40, 41] They noted that the ration A/γ has a common value of 1.0×10^{-5} $\mu\Omega$·cm·K^2·mol^2/mJ^2. In Fig. 2.8, another line shown by a broken line is presented.[40, 41]
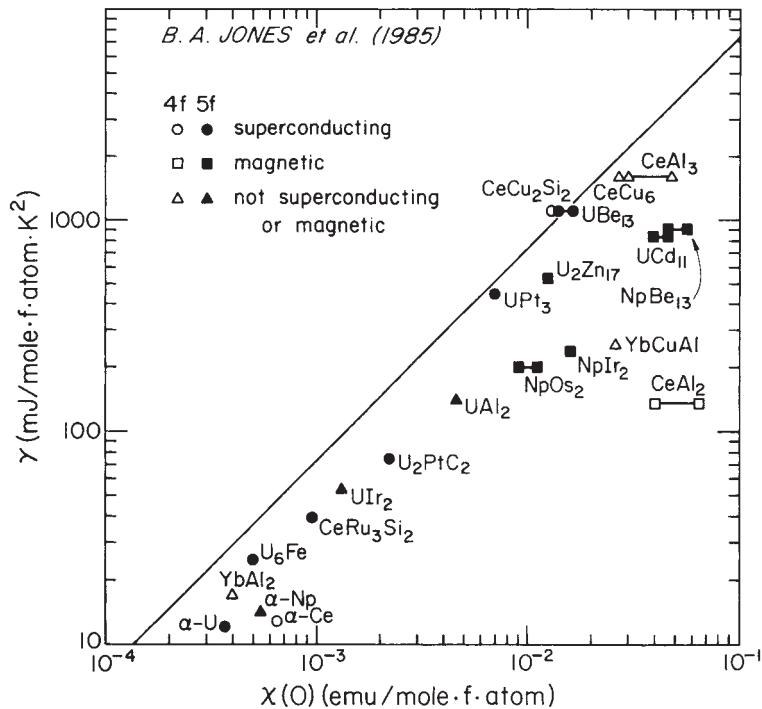

Fig. 2.7 The specific heat coefficient versus the susceptibility for some heavy fermion systems. The values are extrapolated to zero by a variety of methods. Any free, non-interacting fermion gas would lie on the straight line.[42]
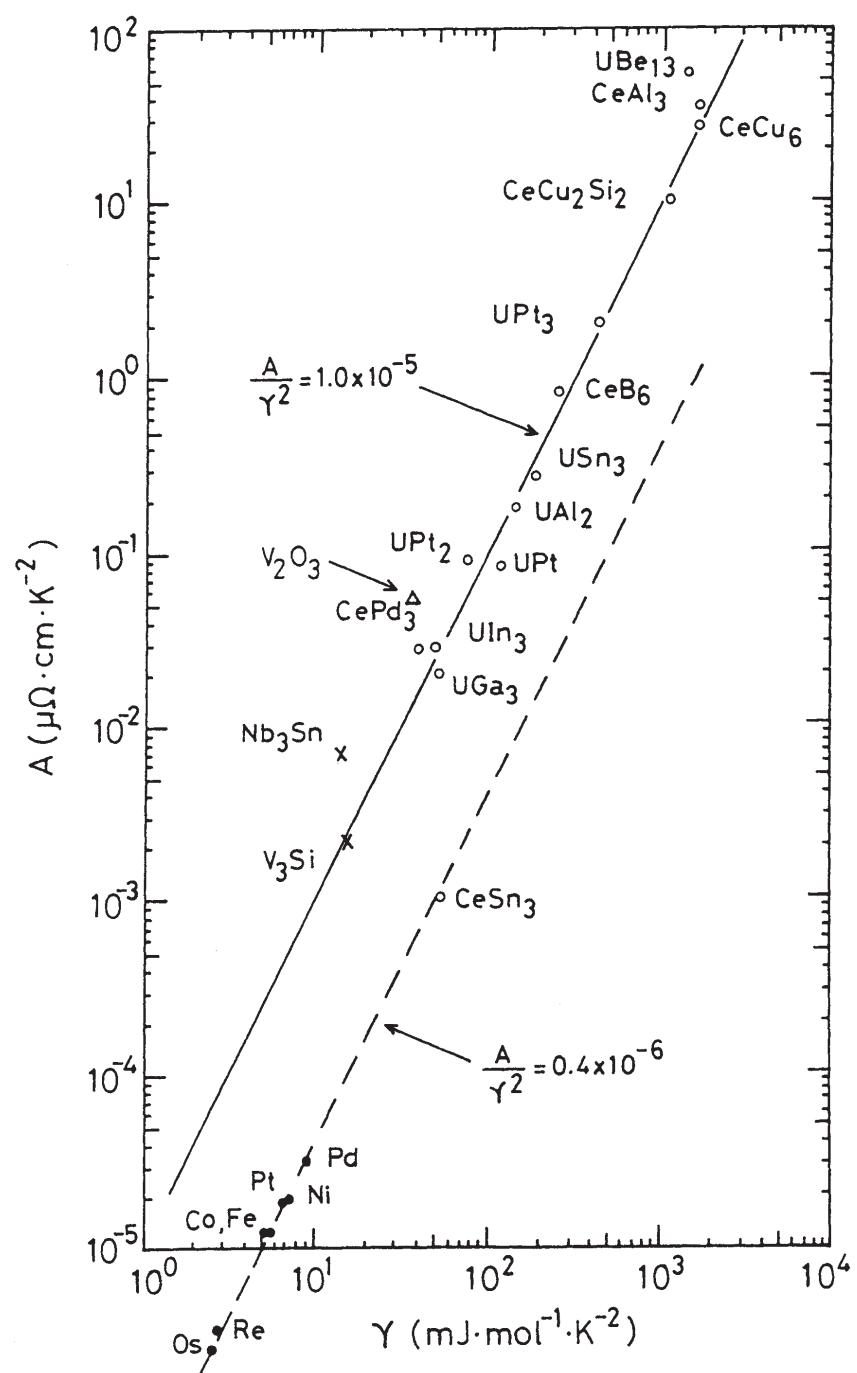
Fig. 2.8 A vs γ in the logarithmic scale.[40]

2.3 Competition between the RKKY interaction and the Kondo effect

The electronic state in the cerium compound can be qualitatively understood by the competition between the Kondo screening and the tendency towards magnetic ordering via RKKY-type indirect exchange mechanism. The Kondo temperature T_K depends exponentially on $|J_\mathrm{cf}|$ as follows:

$$T_\mathrm{K} \propto e^{-\frac{1}{D(\epsilon_\mathrm{F})|J_\mathrm{cf}|}}, \tag{2.31}$$

The magnitude of an indirect RKKY interaction can be characterized by the ordering temperature T_RKKY as follows:

$$T_\mathrm{RKKY} \propto |J_\mathrm{cf}|^2 D(E_\mathrm{F}), \tag{2.32}$$

where

$$J_\mathrm{cf} \simeq \frac{V_\mathrm{cf}^2}{E_\mathrm{F} - E_\mathrm{f}}. \tag{2.33}$$

Actually the magnitude of this interaction is also dominated by the de Gennes factor, and eq. (2.32) is given by the product with $(g_J - 1)^2 J(J + 1)$. This leads to the phase diagram for a Kondo lattice, originally derived by Doniach[6] and emphasized by Brandt and Moshchalkov[43]. Figure 2.9 is well known as the Doniach phase diagram. If $|J_\mathrm{cf}|D(E_\mathrm{F})$ is small, the compound becomes an antiferromagnet with a large magnetic moment, while with increasing $|J_\mathrm{cf}|D(E_\mathrm{F})$, both the magnetic moment and the ordering temperature tend to zero. The critical point where T_N becomes zero is called a **quantum critical point** (QCP). Above the quantum critical point, Kondo-lattice paramagnetism is realized and consequently the f-atom valency becomes unstable, leading to the heavy fermion system. Here, the heavy fermion system is based on the Landau's Fermi liquid, where the interacting electron system or the heavy electron system is related to the non-interacting one by the scaling law without a phase transition. The characteristic features are $\rho = \rho_0 + AT^2$, $C/T = \gamma$ and $\chi = \chi(0)$ at low temperatures: $\sqrt{A} \sim \gamma \sim \chi(0)$.

Nearby the quantum critical point, the cerium compounds with an extraordinary wide variety of possible ground states are found. These include Kondo-lattice compounds with magnetic ordering ($CeIn_3$, $CeAl_2$, CeB_6), small-moment antiferromagnets ($CePd_2Si_2$, $CeAl_3$), an anisotropic superconductor ($CeCu_2Si_2$), no-ordered Kondo-lattice compounds or the heavy fermion compounds ($CeCu_6$, $CeRu_2Si_2$) and valence fluctuation compounds ($CeNi$, $CeRh_2$, $CeRu_2$, $CeSn_3$). Significant differences are small between the heavy fermion compounds ($CeCu_6$, $CeRu_2Si_2$) and ($CeNi$, $CeRh_2$, $CeRu_2$, $CeSn_3$), mainly depending on the magnitude of the Kondo temperature.
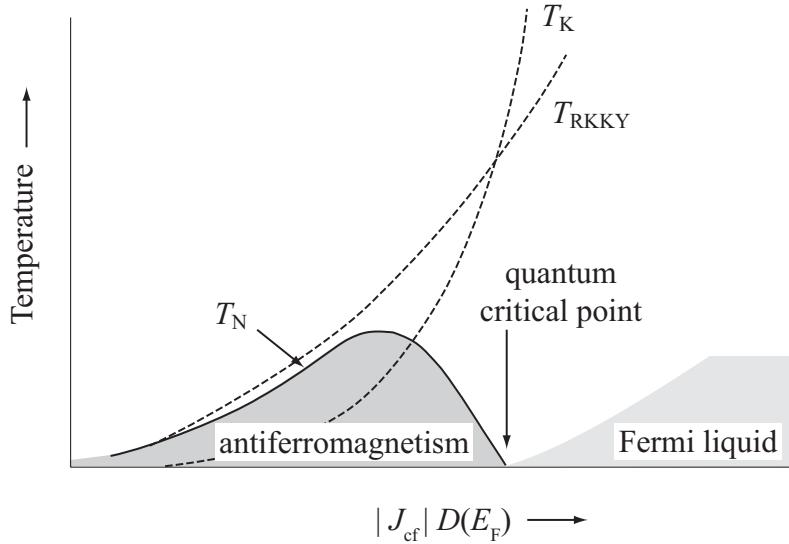
Fig. 2.9 Doniach phase diagram.[43]

We note the non-magnetic cerium compounds at low temperatures. In $CeCu_6$ and $CeRu_2Si_2$ with a small Kondo temperature, there exist no magnetic ordering but exist antiferromagnetic correlations between the Ce sites[44], showing the metamagnetic transition in the magnetic field: $H_c = 2\,T$ in $CeCu_6$[45] and $8\,T$ in $CeRu_2Si_2$.[46] The results of dHvA experiments[36,47,48] and the band calculations[49] in $CeRu_2Si_2$ show that $4f$ electrons are itinerant. Namely, the $4f$ electrons in the cerium compounds such as $CeSn_3$ with a large Kondo temperature, which belong to the valence-fluctuation regime, are also itinerant in the ground state and contribute directly to the formation of the Fermi surface.[50,51]

Furthermore, we pay attention to the non-magnetic Ce compounds to clarify the magnitude of Kondo temperature reflected in the magnetic susceptibility. Figure 2.10 shows the temperature dependence of the magnetic susceptibility in some cerium compounds without magnetic ordering: $CeCu_6$ ($T_K \simeq 5\,K$), $CeRu_2Si_2$ ($20\,K$), $CeNi$ ($150\,K$) and $CeSn_3$ ($200\,K$). The magnetic susceptibility in these compounds follows the Curie-Weiss law at higher temperatures, possessing the magnetic moment near Ce^{3+} of $2.54\,\mu_B$, while it becomes approximately temperature-independent with decreasing the temperature, namely showing a broad maximum and then forming enhanced Pauli paramagnetism. The temperature $T_{\chi max}$ indicating the peak of the susceptibility almost corresponds to the characteristic temperature T_K. The valence of Ce atoms seems to be changed from Ce^{3+} into Ce^{4+} (non-magnetic state) with decreasing the temperature.

Experimentally, pressure corresponds to $|J_{cf}|D(\epsilon_F)$. For example, the Néel temperature T_N in an antiferromagnet decreases with increasing pressure, and becomes zero: $T_N \to 0$ for $P \to P_c$. The electronic state can be tuned by pressure. Namely, the antiferromagnet is changed into the non-magnetic compound. Around the quantum critical point, the heavy fermion state is realized as mentioned above, together with the non-Fermi
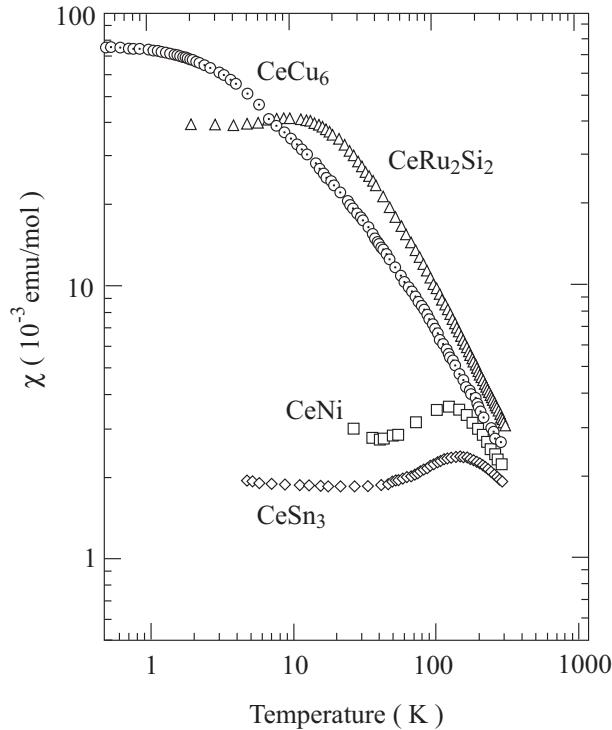
Fig. 2.10 Temperature dependence of the magnetic susceptibility for typical Ce compounds.

liquid nature and appearance of superconductivity.

The non-Fermi liquid behavior around the quantum critical point is one of the recent topics in the f electron system. In the non-Fermi liquid system the following relations are characterized:

$$\rho \;\sim\; T^n \quad \text{with } n < 2, \tag{2.34}$$
$$C/T \;\sim\; -\log T. \tag{2.35}$$

The typical non-Fermi liquid nature and appearance of superconductivity were observed in $CeCu_2Ge_2$ under pressure.[52] $CeCu_2Ge_2$ is an antiferromagnet with $T_N = 4\,K$, but superconductivity is realized under pressure as in a heavy fermion superconductor $CeCu_2Si_2$. Figure 2.11 shows the low-temperature resistivity of $CeCu_2Ge_2$ for $9.7{<}P{<}18.6\,GPa$. At $15.6\,GPa$, the electrical resistivity decreases linearly with decreasing temperature: $\rho \sim T^n\,(n=1)$, and becomes zero below the superconducting transition temperature $T_{sc} = 1.8\,K$.

Finally we note how the electronic state changes as a function of the distance between neighboring two f electrons. Figure 2.12 shows the relation of the electronic specific heat coefficient γ vs the lattice constant in UX_3.[53] The uranium compounds UX_3 with the cubic $AuCu_3$-type crystal structure, where X is a group IVB (X: Si, Ge, Sn and Pb) element of the periodic table, show various magnetic properties: Pauli paramagnetism
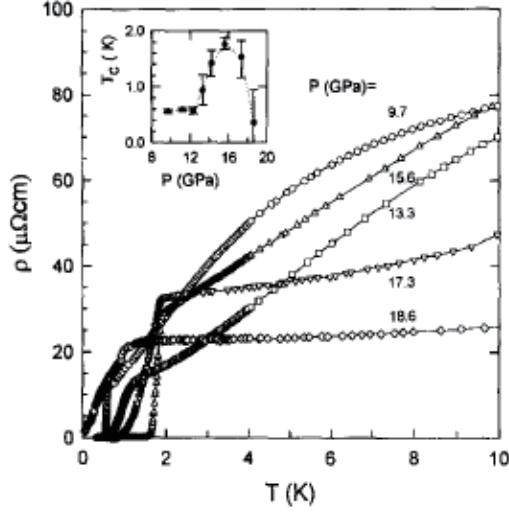
**Fig. 2.11** Low-temperature resistivity under various pressure in $CeCu_2Ge_2$.[52]
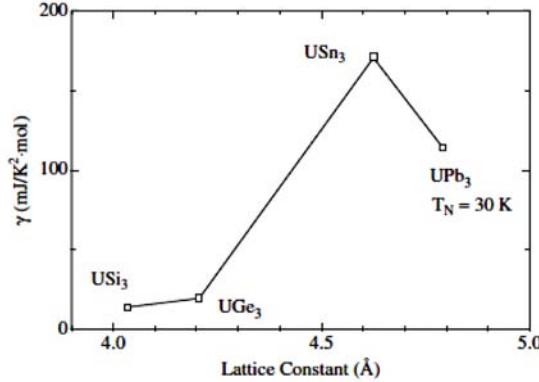
Fig. 2.12 γ vs the lattice constant in UX_3.[53]

in USi_3 and UGe_3, spin fluctuation in USn_3, and antiferromagnetism in UPb_3. The variety in the magnetic properties is closely related to the lattice constant or the distance between the U atoms, d_{U-U}. This is reflected in the electronic specific heat coefficient γ, which varies from $14\,mJ/K^2{\cdot}mol$ in USi_3 to $170\,mJ/K^2{\cdot}mol$ in USn_3, as shown in Fig. 2.12. When the antiferromagnetic order occurs at $T_N = 30\,K$ in UPb_3, the γ value is reduced to $110\,mJ/K^2{\cdot}mol$. The γ value in the UX_3 (IVB) series thus depends on the lattice constant, d_{U-U}. We can be deduced from Fig. 2.12 that as d_{U-U} becomes shorter, the wave function of $5f$ electrons is overlapped, enhancing Pauli itinerancy, while with increasing d_{U-U}, forming a heavy fermion state, as shown in USn_3, and finally the $5f$-electronic state exhibits magnetic ordering. A change of the elements from Pb to Si corresponds to an application of pressure.

2.4 Fermi surface properties

Fermi surface studies are very important to know the ground-state properties of the rare earth compounds.[27] As mentioned in Sec. 2.2, the ground state of the Ce compounds is mainly determined by the competition between the RKKY interaction and the Kondo effect (see Fig. 2.9). When T_{RKKY} overcomes T_{K}, the ground state is the magnetic ordered one and $4f$ electron is regarded as localized. On the other hand, when the Kondo effect is dominant, the ground state is the non-magnetic one and the $4f$ electrons become itinerant.

In the $4f$-localized system, the Fermi surface is similar to that of corresponding La compound, but the presence of $4f$ electrons alters the Fermi surface through the $4f$-electron contribution to the crystal potential and through the introduction of new Brillouin zone boundaries and magnetic energy gaps which occur when $4f$-electron moments order. The latter effect may be approximated by a band-folding procedure where the paramagnetic Fermi surface is folded into a smaller Brillouin zone based on the magnetic unit cell, because the magnetic unit cell is larger than the chemical one. If the magnetic energy gaps associated with the magnetic structure are small enough, conduction electrons undergoing cyclotron motion in the presence of magnetic field can tunnel through these gaps and circulate the orbit on the paramagnetic Fermi surface. If this magnetic breakthrough (breakdown) effect occurs, the paramagnetic Fermi surface might be observed in the de Haas-van Alphen (dHvA) effect even in the presence of magnetic order.

For Kondo-lattice compounds with magnetic ordering, the Kondo effect is expected to have minor influence on the topology of the Fermi surface, representing that the Fermi surfaces of the Ce compounds are roughly similar to those of the corresponding La compounds, but are altered by the magnetic Brillouin zone boundaries mentioned above. Nevertheless, the effective masses of the conduction carriers are extremely large compared with those of La compounds, as noted in the case of CeB_6. In this system a small amount of $4f$ electron most likely contributes to make a sharp density of states at the Fermi energy. Thus, the energy band becomes flat around the Fermi energy, which brings about the large mass.

In some cerium compounds such as $CeCu_6$, $CeRu_2Si_2$, $CeNi$ and $CeSn_3$, the magnetic susceptibility follows the Curie-Weiss law with a moment of Ce^{3+}, $2.54\,\mu_{\mathrm{B}}/Ce$, has a maximum at a characteristic temperature $T_{\chi\mathrm{max}}$, and becomes constant at lower temperatures (see Fig. 2.10). This characteristic temperature $T_{\chi\mathrm{max}}$ corresponds to the Kondo temperature T_{K} as mentioned in Sec. 2.2. A characteristic peak in the susceptibility is a crossover from the localized $4f$ electron to the itinerant one. The Fermi surface is thus highly different from that of the corresponding La compound. The cyclotron mass is also extremely large, reflecting a large γ-value of $\gamma \simeq 10^4/T_{\mathrm{K}}$ (mJ/K^2·mol).

The cerium compounds are thus classified as either the localized electron system or the itinerant electron system.

2.5 Superconductivity

The microscopic theory of superconductivity, which was provided by Bardeen, Cooper and Schrieffer in 1957,[12] is based on an idea that when an attractive interaction between fermions is present, the stable ground state is no longer the degenerated Fermi gas but becomes a coherent state in which the electrons are combined into pairs of spin-singlet with zero total momentum (Cooper pairs). A conduction electron attracts the positive ion and distorts the lattice by moving in the lattice, and then the distortion attracts another conduction electron. Namely, the interaction between two electrons mediated by the phonon form the Cooper pair of the electrons. Since an excited energy of BCS type superconductor has an isotropic superconducting gap Δ, namely the superconducting energy gap is opened over the entire of the Fermi surface, the temperature dependence of physical quantities obey the exponential law theoretically.

It is difficult to express superconductivity for the compounds which have heavy quasi-particles located adjacent to the quantum critical point by the attraction mediated the phonon because of strongly Coulomb repulsion. It have been found the heavy fermion superconductor located adjacent to the quantum critical point. This superconductor does not obey the exponential law of the temperature but obey the power law. We explain the present unconventional (anisotropic) superconductivity in the next section.

1) Anisotropic superconductivity

Heavy fermion superconductors are, however, well known to show the power law in physical properties such as the electronic specific heat C_e and the nuclear spin-lattice relaxation rate $1/T_1$, not indicating an exponential dependence predicted by BCS theory. This indicates the existence of an anisotropic gap, namely existence of a node in the energy gap. When we compare the phonon-mediated attractive interaction based on the BCS theory to the strong repulsive interaction among the f electrons, it is theoretically difficult for the former interaction to overcome the latter one. To avoid a large overlap of the wave functions of the paired particles, the heavy electron system would rather choose an anisotropic channel, like a p-wave spin triplet or a d-wave spin singlet state, to form Cooper pairs.

Figure 2.13 shows a schematic view of the superconducting parameter with the s-, d- and p-wave pairing. The order parameter $\Psi(\boldsymbol{r})$ with the even parity (s- and d-wave) is symmetric with respect to $\boldsymbol{r}$, where one electron with the up-spin state of the Cooper pair is simply considered to be localized at the center of $\Psi(\boldsymbol{r})$, $\boldsymbol{r} = 0$, and the other electron with the down-spin state is localized at $\boldsymbol{r}$. The width of $\Psi(\boldsymbol{r})$ with respect to $\boldsymbol{r}$ is called the coherence length ξ. For example, UPd_2Al_3 is consider to be a d-wave superconductor from the NMR Knight shift experiment,[10] which corresponds to the case (b) in Fig. 2.13. On the other hand, $\Psi(\boldsymbol{r})$ with odd parity (p-wave) is not symmetric with respect to $\boldsymbol{r}$, where the parallel spin state is shown in Fig. 2.13(c). From the NMR Knight shift experiment, UPt_3 is considered to possess odd parity in symmetry.[11]

For an anisotropic state, there are three kinds of gap structures, as shown in Fig. 2.14.

(a) *s*-wave   (b) *d*-wave   (c) *p*-wave
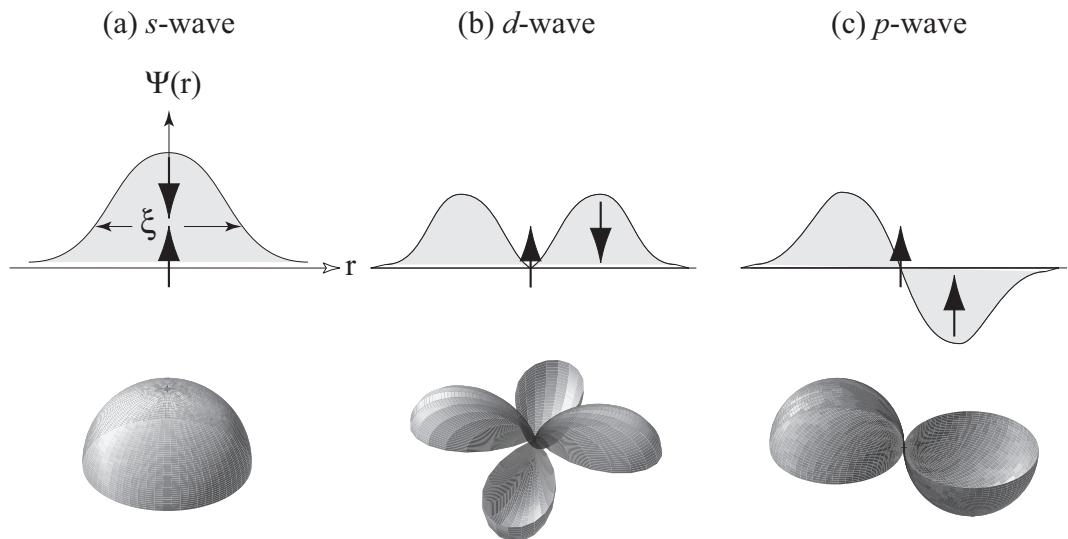
Fig. 2.13 Schematic view of the superconducting parameter with the *s*-, *d*- and *p*-wave pairing.

(a) normal state   (b) BCS type

(c) polar type   (d) axial type
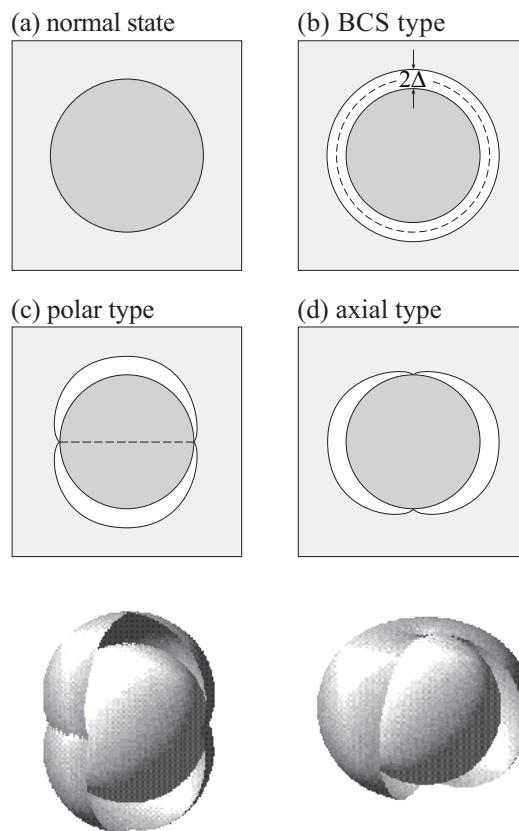
Fig. 2.14 Schematic picture of the gap structures: (a) normal state, (b) BCS-type superconductor, which has an isotropic gap, (c) polar type and (d) axial type.

First one indicates the superconducting gap, which is the same as the *s*-wave and is isotropic. This is called the Balian-Werthamer (BW) state. Second one shows a line node in the equator on the Fermi surface. This structure is called the polar type, as shown in Fig. 2.14(c). Third one has a point node in the pole on the Fermi surface. This condition has the Anderson-Brinkman-Morel (ABM) state. This is called the axial type, as shown in Fig. 2.14(d).

2) Pressure-induced superconductivity

The study of unconventional superconductivity is still active in condensed matter physics, ever since the discovery of the first heavy fermion superconductor, $CeCu_2Si_2$.[9] Recently, some Ce-based heavy fermion compounds were found to exhibit superconducting under pressure, as shown in Fig. 2.15 for $CeIn_3$.[54] In these compounds, superconductivity appears around the quantum critical point. The similar pressure-induced superconductivity was also reported for the other Ce-based compounds such as $CeCu_2Ge_2$[55] and $CeRh_2Si_2$.[56,57] In these compounds, the attractive force between quasiparticles are possible to be magnetically mediated, not to be phonon-mediated.

$CeCu_2Si_2$ is a superconductor with $T_{sc} = 0.7\,K$ at ambient pressure. When pressure is applied, T_{sc} initially remains close to its ambient pressure value but shows a sudden increase of $T_{sc} = 2\,K$ at about $3\,GPa$.[58] This strange superconducting phase was also
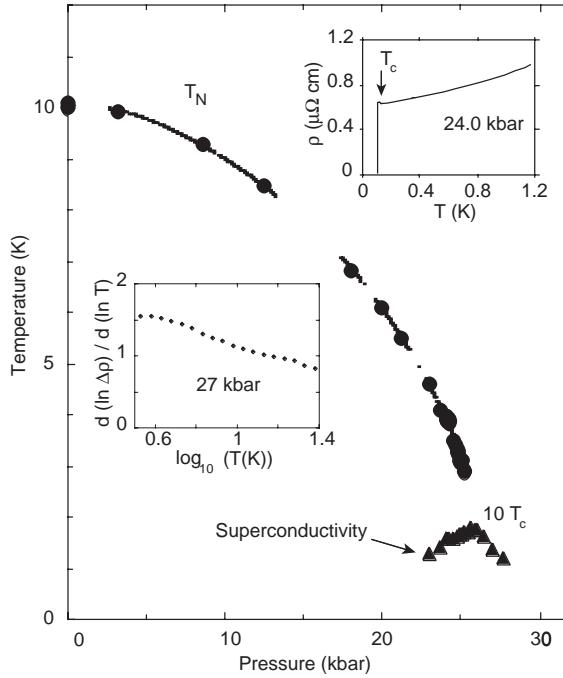

Fig. 2.15 Pressure phase diagram in $CeIn_3$. Superconductivity is observed below T_{sc} in a narrow window where the Néel temperature T_N tends to zero.[54]
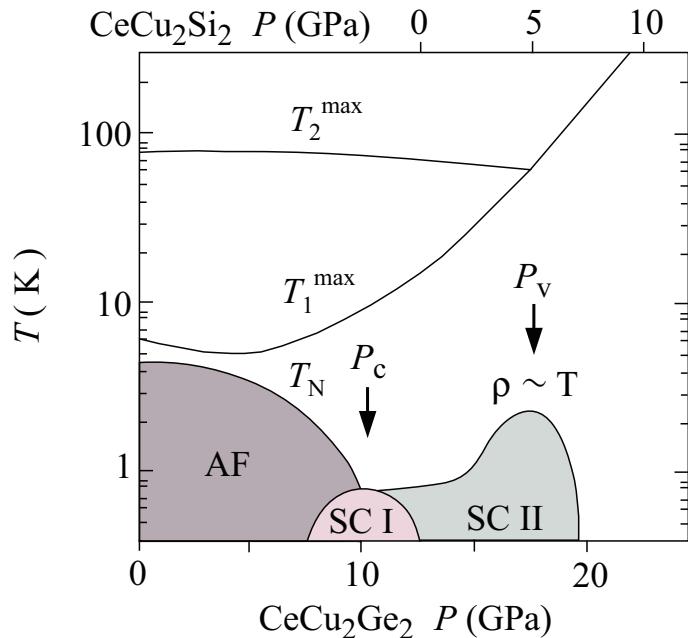
Fig. 2.16 Schematic temperature-pressure phase diagram of $CeCu_2(Si/Ge)_2$.[59] Super-conductivity is observed in a wide window.

observed in a pressure-induced superconductor $CeCu_2Ge_2$.[55] According to the report by Holmes *et al.*,[59] these anomalies can be linked with an abrupt change of the Ce valence, and suggested a second quantum critical point at a pressure P_v, where critical valence fluctuations provide the superconducting pairing mechanism, which is compared with superconducting pair mechanism based on spin fluctuations at ambient pressure in $CeCu_2Si_2$ or at $10\,GPa$ in $CeCu_2Ge_2$, as shown in Fig. 2.16. Figure 2.16 shows the temperature-pressure phase diagram for $CeCu_2(Si/Ge)_2$ showing the two critical pressures P_c and P_v.

3) Superconductivity in the non-centrosymmetric crystal structure

Recently, it has been reported that $CePt_3Si$ is the first heavy-fermion superconductor lacking a center of inversion symmetry in the tetragonal structure, where the upper critical field $H_{c2} = 4.5\,T$ exceeds the Pauli paramagnetic limiting field $H_p = 1.4\,T$,[13] and the spin relaxation rate of ^{195}Pt-NMR indicated a clear peak structure just below the superconducting transition temperature $T_{sc} = 0.75\,K$.[60] Subsequently, Akazawa *et al.* found pressure-induced superconductivity in a ferromagnet UIr with the monoclinic structure,[15,16] which also lacks inversion symmetry in the crystal structure. In addition, Kimura *et al.* reported pressure-induced superconductivity in an antiferromagnet $CeRhSi_3$, which crystallizes in the tetragonal crystal structure without inversion symmetry.[18–20] Moreover, similar superconducting properties are observed in

CeIrSi$_3$[8, 21, 22)] and CeCoGe$_3$.[23)]

The experimental technique of NQR/NMR has proved to be a useful tool to determine the symmetry of the superconducting condensate. For example, UPt$_3$ was shown to be the first case of odd-parity (p- or f-wave type) superconductivity,[11)] while even-parity (d-wave type) superconductivity is realized in UPd$_2$Al$_3$.[10)] For the study of these superconductors, it was assumed that the crystal structure has an inversion center, which makes it possible to consider separately the even (spin-singlet) and odd (spin-triplet) components of the superconducting order parameter. When inversion symmetry is absent in the crystal structure, such classification for superconductivity is no longer possible. The order parameter contains not only a spin-singlet part, but also an admixture of a spin-triplet state.[61)]

In this section, the characteristic features of superconductivity which is realized in a non-centrosymmetric crystal, are explained on the basis of the recently reported theoretical studies. When the crystal structure lacks inversion symmetry, the Fermi surface splits into two Fermi surfaces due to the Rashba-type antisymmetric spin-orbit interaction.[62)]

Here, the effect of spin-splitting of the Fermi surface via the antisymmetric spin-orbit interaction is discussed from the viewpoint of the conduction electrons in the non-centrosymmetric tetragonal crystal structure. The spin-orbit interaction for the conduction electrons can be calculated by considering the following effective single-band Hamiltonian with the Rashba-type spin-orbit interaction:[62)]

$$\mathcal{H} = \frac{\boldsymbol{p}^2}{2m^*} + \alpha(\boldsymbol{p} \times \boldsymbol{n}) \cdot \boldsymbol{\sigma} \tag{2.36}$$

α denotes the strength of the spin-orbit coupling, $\boldsymbol{p}$ is a momentum of conduction electrons, $\boldsymbol{n}$ is a unit vector taken to be parallel to the z-axis or the c-axis (the [001] direction), $\boldsymbol{\sigma}$ is the Pauli matrices, and the m^* is the effective mass. The term $\alpha(\boldsymbol{p} \times \boldsymbol{n}) \cdot \boldsymbol{\sigma}$ is explained as follows. The non-uniform lattice potential $V(\boldsymbol{r})$ in the tetragonal crystal structure induces the electric field $(-\nabla V(\boldsymbol{r}))$ along the [001] direction. The effective magnetic field, which approximately corresponds to $\boldsymbol{p} \times \nabla V$, namely $\alpha(\boldsymbol{p} \times \boldsymbol{n})$ in eq. (2.36) is brought about for moving conduction electrons with the momentum $\boldsymbol{p}$ in this electric field. The term $\alpha(\boldsymbol{p} \times \boldsymbol{n}) \cdot \boldsymbol{\sigma}$ is regarded as a Zeeman energy arising from the magnetic interaction between this effective magnetic field and spins of the conduction electrons.

By diagonalizing this Hamiltonian, the following two energies, which correspond to two separated energy bands, are obtained:

$$\epsilon_{p\pm} = \frac{p^2}{2m^*} \mp \alpha p_\perp, \tag{2.37}$$

where $p_\perp = \sqrt{p_x^2 + p_y^2}$ is the component of the moment $\boldsymbol{p}$ normal to $\boldsymbol{n}$. A simple example of the Fermi surface splitting due to the Rashba-type spin-orbit interaction with ∇V parallel to the z-axis is shown in Fig. 2.17. Note that in Fig. 2.17 the spin quantization axis is chosen along $\boldsymbol{p} \times \nabla V$. The degenerate spherical Fermi surface splits into two sheets, namely up-spin and down-spin bands, except for high-symmetry line $\boldsymbol{p} // z$, as shown in Fig. 2.17(a). One of the two separated Fermi surfaces has a smaller volume and

the other has a larger volume than the spherical Fermi surface, as shown in Fig. 2.17(b). Arrows indicate spins on the Fermi surfaces for the up-spin and down-spin bands. An important point is that a conduction electron with a momentum $\boldsymbol{p}$ and an up-spin state and another conduction electron with a momentum $-\boldsymbol{p}$ and an up-spin state belong to two different Fermi surfaces, which are separated by $2|\alpha p_\perp|$. A simple p-wave pairing is thus prohibited because $|\alpha p_\perp|$ is about 10 - 1000 K, shown later experimentally, which is much larger than the superconducting energy gap of a few Kelvin. On one of the spin-orbit split Fermi surfaces, namely the $(+)$-band in Fig. 2.17, the Cooper pair between electrons with momentum p, spin $\uparrow$ and momentum $-p$, spin $\downarrow$ is formed. This state, denoted as $|p, \uparrow\rangle| - p, \downarrow\rangle$, is *not* a spin singlet state, because the counterpart of this state $|p', \downarrow\rangle| - p', \uparrow\rangle$ is formed on another Fermi surface and thus the superposition between these two states is not possible.[63] Actually, the pairing state $|p, \uparrow\rangle{-}p, \downarrow\rangle$ and $|p, \downarrow\rangle{-}p, \uparrow\rangle$ are the admixture of spin singlet and triplet states as easily verified by

$$|\boldsymbol{p}, \uparrow\rangle| - \boldsymbol{p}, \downarrow\rangle = \frac{1}{2}(|\boldsymbol{p}, \uparrow\rangle| - \boldsymbol{p}, \downarrow\rangle - |\boldsymbol{p}, \downarrow\rangle| - \boldsymbol{p}, \uparrow\rangle) \quad \text{(singlet)}$$
$$+ \frac{1}{2}(|\boldsymbol{p}, \uparrow\rangle| - \boldsymbol{p}, \downarrow\rangle + |\boldsymbol{p}, \downarrow\rangle| - \boldsymbol{p}, \uparrow\rangle) \quad \text{(triplet)}$$

$$|\boldsymbol{p}', \downarrow\rangle| - \boldsymbol{p}', \uparrow\rangle = \frac{1}{2}(|\boldsymbol{p}, \uparrow\rangle| - \boldsymbol{p}, \downarrow\rangle - |\boldsymbol{p}, \downarrow\rangle| - \boldsymbol{p}, \uparrow\rangle). \quad \text{(singlet)}$$
$$+ \frac{1}{2}(|\boldsymbol{p}, \uparrow\rangle| - \boldsymbol{p}, \downarrow\rangle + |\boldsymbol{p}, \downarrow\rangle| - \boldsymbol{p}, \uparrow\rangle) \quad \text{(triplet)}$$
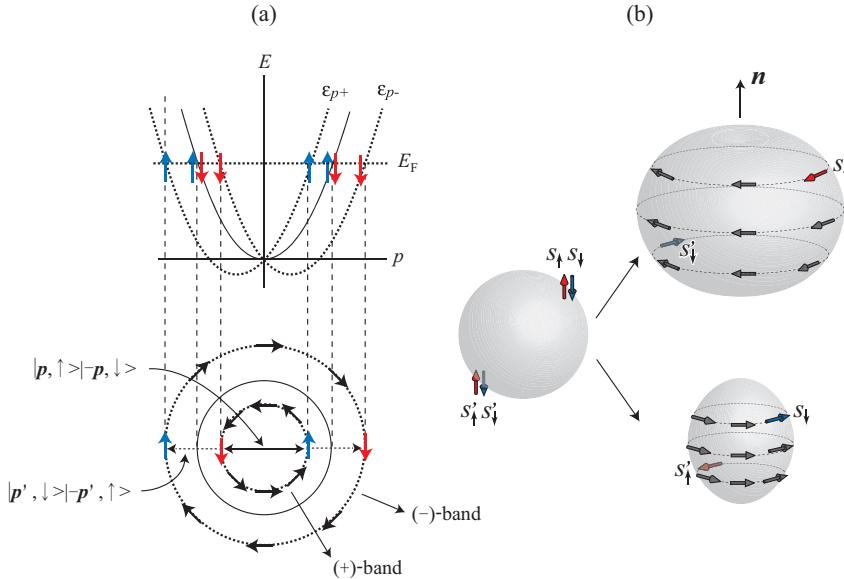

Fig. 2.17 Two separated (a) energy bands and (b) Fermi surfaces in the non-centrosymmetric crystal structure.

The first and second terms of the right-hand side express a spin singlet state and a spin triplet state, respectively, with the in-plane spin projection S_{inplane} equal to 0. Since we take the spin quantization axis parallel to the xy-plane, this triplet state corresponds to the $S_z = \pm 1$ state for the spin quantization axis along the z-direction. This means that the $\boldsymbol{d}$-vector of the triplet component is parallel to the plane. The above explanation is also applicable to general cases with more complicated form of ∇V. This unique superconducting state exhibits various interesting electromagnetic properties as extensively argued by many authors.[61,63–74] Frigeri *et al.* also proposed the possible existence of spin-triplet pairing state in the non-centrosymmetric crystal, where the inversion symmetry breaking in the presence of a spin-orbit interaction was introduced on the basis of the Rashba model.[74] It was clarified that, in contrast to a common belief, the spin-triplet pairing state is not entirely excluded in such systems. The favorable pairing state for the triplet state is of the p-wave type. The $\boldsymbol{d}$ vector, which is characteristic of the spin-triplet superconductivity, is parallel to $\boldsymbol{p}_\perp$: $\boldsymbol{d}(\boldsymbol{k}) = \Delta(\hat{\boldsymbol{x}}k_y - \hat{\boldsymbol{y}}k_x)$, and the order parameter becomes a mixture of spin-singlet and spin-triplet components.

Next we show a theoretically suggested superconducting gap for the non-centrosymmetric superconductor with the Rashba-type spin-orbit coupling. Here we consider a two-component order parameter with spin-singlet and spin-triplet components as follows:

$$\Delta(\boldsymbol{k}) = \{\Psi(\boldsymbol{k})\sigma_0 + \boldsymbol{d}(\boldsymbol{k}) \cdot \boldsymbol{\sigma}\} \cdot i\sigma_y, \tag{2.38}$$

where $\Psi(\boldsymbol{k})$ is the spin-singlet component, $\boldsymbol{d}(\boldsymbol{k}) = \Delta(-k_x, k_y, 0)$ is the d-vector which characterizes a spin-triplet component, $\boldsymbol{\sigma}$ is the Pauli matrices and σ_0 is the unit matrix. The theoretical calculation by Hayashi *et al.*[71] has shown that the superconducting energy gap is different on the separated two Fermi surfaces and is expresses by

$$\Delta(\theta) = |\Psi \pm \Delta\sin\theta|. \tag{2.39}$$

Figure 2.18 shows schematic structures of the superconducting energy gap on the separated Fermi surfaces. Here, the superconducting energy gap on the S_+-Fermi surface has the shape of s-wave (the equivalent gap) + p-wave (the axial type) and is nodeless. On the other hand, line nodes appear in the superconducting energy gap on the S_--Fermi surface, leading to the low-temperature power law behavior of $1/T_1$[60] and the specific heat divided by temperature C/T in CePt$_3$Si.[75]

Next we discuss the effect of the magnetic field on the superconducting state. Principally, there are two mechanism, by which a magnetic field interacts with the electrons in the superconducting state. Both mechanisms are pair breaking and lead to the destruction of the superconducting state at a critical field. These mechanisms are as follows.

1) Orbital pair breaking

This is due to an interaction of the field with the orbital motion of the electrons and described by the term $(e/m)(\boldsymbol{p} \cdot \boldsymbol{A})$, where $\boldsymbol{A}$ is the vector potential. This term corresponds to the Lorentz force.
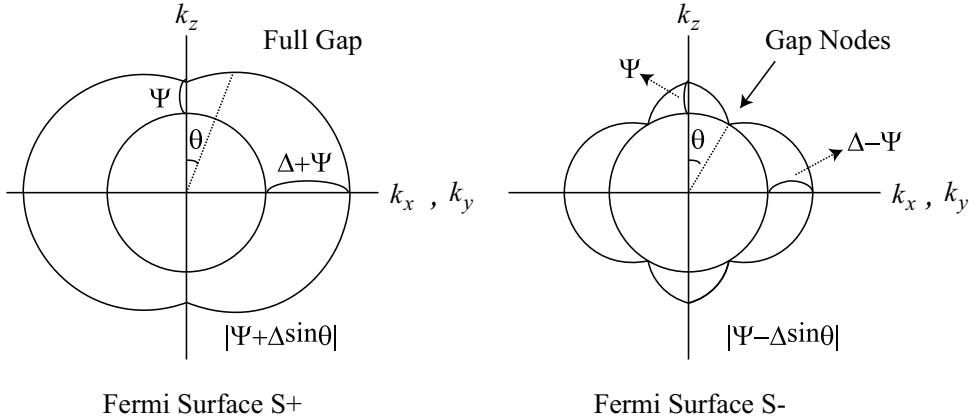
Fig. 2.18 Gap structures on the Fermi surface, cited from refs. 71.

2) Pauli limiting

This comes from an interaction with the spins of electrons and is described by $g_J\mu_B\boldsymbol{S} \cdot \boldsymbol{H}$.

Orbital pair breaking takes place in all superconducting states, both conventional and non-conventional ones. For small magnetic fields, this is the only important pair breaking mechanism due to the external field. Therefore, it determines the initial slope of H_{c2} at T_{sc}. The critical field determined only by orbital pair breaking is defined as orbital critical field H_{c2}^*, in the absence of any other pair breaking effect. The upper critical field at $T = 0\,\mathrm{K}$ varies between $H_{c2}^* = -0.693\,(\mathrm{d}H_{c2}^*/\mathrm{d}T)\cdot T_{sc}$ for a conventional superconductor in the dirty limit and $H_{c2}^* = -0.850\,(\mathrm{d}H_{c2}^*/\mathrm{d}T)\cdot T_{sc}$ for a polar triplet state. Because of the similarity of the upper critical fields, one can hardly make any statements about the order parameter for a superconductor just based on an analysis of H_{c2}^*. The discussion of the critical field is, therefore, concentrated on the second pair breaking mechanism, Pauli limiting.

The influence of the magnetic field on the spins of the electrons in the superconducting states has first been reported by Clogston[76] and by Chandrasekhar.[77] The physical reason for this mechanism is that, in a coventional superconductor, the Cooper pairs have a total spin $S = 0$. Therefore, the spin susceptibility $\chi_s = 0$ (s-wave state). For this reason, the normal state becomes energetically more favourable for the system when the magnetic energy $\frac{1}{2}\chi_n H^2$ of the normal state reaches the condensation energy $\frac{H_c^2}{8\pi}$ of the superconductor. In a BCS superconductor, this gives rise to an upper limit of $H_{c2}(0)$. This field is called Pauli limiting field and expressed as $H_p = 1.857 \times 10^4\,T_{sc}$ (Oe). Pauli limiting occurs also in all other superconducting states, in which χ_s is reduced compared with the susceptibility of the normal state χ_n. When the spin susceptibility of the superconducting state χ_s has a substantial value compared with χ_n, the superconducting condensation energy can be expressed by

$$\frac{1}{2}(\chi_n - \chi_s)H_p^2 = \frac{1}{8\pi}H_c^2. \tag{2.40}$$

By using the equations $\chi_n = 2\mu_B^2 D(\epsilon_F)$ and the relation of BCS theory: $\frac{H_c^2}{8\pi} = \frac{1}{2}D(\epsilon_F)\Delta_0^2$, the Pauli limiting field will be expresses as:

$$H_p = \frac{\Delta_0}{\sqrt{2}\sqrt{1 - \chi_s^s(T)/\chi_n^s}\mu_B}. \tag{2.41}$$

In conventional superconductors $(s = 0$ and $\ell = 0)$, as in all the non-conventional singlet superconductors $(s = 0, \ell = 0, 2, 4, \cdots)$, the spin susceptibility in the superconducting state $\chi_s = 0$. Therefore, the Pauli limiting is maximum. On the other hand, in some simple triplet state $(s = 1, \ell = 1, 3, \cdots)$, the z-component of the Cooper pair spins can only be $s_z = \pm 1$. As long as the spin part of the order parameter can rotate freely with respect to orbital part, $\chi_s = \chi_n$ for these equal spin pairing state. In this case, the Pauli limiting does not occur. The order parameter of the equal spin pairing states has an intrinsic anisotropy. An intermediate case between the singlet and the equal spin pairing states has been taken by the Balian-Werthamer (BW) state.[78] It exhibits $\chi_s = \frac{2}{3}\chi_n$ and therefore, shows reduced Pauli limiting.

Next we discuss the spin susceptibility in the noncentrosymmetric superconductor with antisymmetric spin-orbit interaction. Frigeri *et al.* proposed that the Van Vleck term of spin susceptibility χ_s^s in the system without inversion symmetry has a finite value by the strong spin-orbit interaction.[79] Namely, the paramagnetic effect decreases in the spin singlet state.

The spin susceptibility for the singlet s-wave gap function is shown in Fig. 2.19.[79] The left panel shows the temperature dependence of the spin susceptibility for the field along the c-axis $(\chi_{//} = \chi_c)$. The middle panel shows the spin susceptibility for the field in the ab-plane $(\chi_\perp = \chi_a = \chi_c)$ as a function of the temperature for three different values of the spin-orbit coupling α. The susceptibility increases with the spin-orbit coupling strength. When α becomes very large, the resulting susceptibility looks very similar to that obtained for the triplet p-wave gap function, as shown in the right panel of Fig. 2.19. For the spin-triplet phase, we chose the pairing state $\boldsymbol{d}(\boldsymbol{k}) = \Delta(\hat{\boldsymbol{x}}k_y - \hat{\boldsymbol{y}}k_x)$. Therefore, for the superconducting state in the non-centrosymmetric crystal structure, the similar properties of the spin susceptibilities make it difficult to distinguish between a spin-triplet and spin-singlet order parameter through NMR measurements in the strong spin-orbit coupling limit.
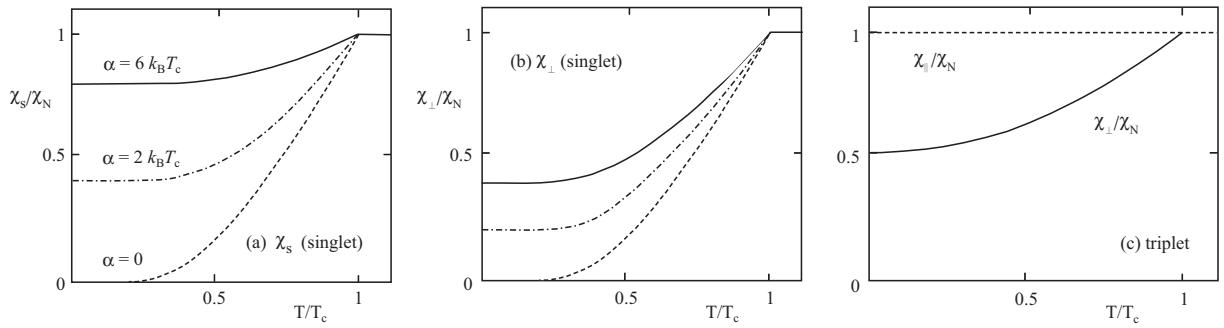
Fig. 2.19 (a), (b) Spin susceptibility in the case of singlet s-wave gap function for $\boldsymbol{g_k} \propto (-k_y, k_x, 0)$ (CePt$_3$Si). The spin susceptibility in the ab-plane $\chi_\perp$ and along the c-axis $\chi_{//}$ as a function of T for three different values of the antisymmetric spin-orbit coupling α. The susceptibility in the superconducting state ($T/T_c < 1$) increases with the spin-orbit coupling strength. The susceptibility is more strongly suppressed in the ab-plane than along the c-axis. At $T = 0$ we have $\chi_\perp^s = \chi_{\parallel}^s/2$ and (c) Spin susceptibility for a spin-triplet p-wave gap function $\boldsymbol{d}(\boldsymbol{k}) \,//\, \boldsymbol{g_k} \propto (-k_y, k_x, 0)$ (CePt$_3$Si). The susceptibility is in this case independent of the spin-orbit coupling α. In the superconducting state, the susceptibility in the ab-plane coincides with that of the normal state.[79]

3 Relevant Previous Study

3.1 RTX$_3$(R: rare earth, T: transition metal, X: Si, Ge)

3.1.1 Crystal structure of RTX$_3$

In the present study, the electrical and magnetic properties were investigated experimentally by using single crystals of RTX$_3$ intermetallic compounds, where R is the rare earth, T is the transition metal and X is Si and Ge. RTX$_3$ compounds often crystallize in the tetragonal BaNiSn$_3$-type crystal structure, which is related with ThCr$_2$Si$_2$-type well-known typical heavy-fermion system.[80,81] Figure 3.1 shows (a)BaNiSn$_3$-, (b)ThCr$_2$Si$_2$- and (c)CaBe$_2$Ge$_2$-type crystal structures. The latter two crystal structure possess inversion center, while in the BaNiSn$_3$-type RTX$_3$ compound, the R atoms occupy corners and the body center of the tetragonal structure, but the T and X atoms lack inversion symmetry in the crystal. The lack of inversion center in the crystal bring about the non-uniform lattice potential $V(\boldsymbol{r})$ along c-axis whereas the non-uniform lattice potential perpendicular to c-axis $(a - b$ plane$)$ is canceled out due to the four-hold symmetry along c-axis $C_{4\nu}$ in the tetragonal structure. This is characteristic in the RTX$_3$ compound with the BaNiSn$_3$-type crystal structure.

CeTX$_3$ with the BaNiSn$_3$-type crystal structure is known to possess 11 compounds, namely CeCoSi$_3$, CeRuSi$_3$, CeRhSi$_3$, CePdSi$_3$, CeOsSi$_3$, CeIrSi$_3$, CePtSi$_3$, CeFeGe$_3$, CeCoGe$_3$, CeRhGe$_3$ and CeIrGe$_3$,[82–91] while CeNiGe$_3$ and CeRuGe$_3$ crystallize in SmNiGe$_3$-, ScNiGe$_3$-type crystal structures,[92,93] respectively. The physical properties of LaTX$_3$ and CeTX$_3$(T: transition metal, X: Si and Ge) have been studied on the polycrystalline sample.[88,94–96] Among these studies, Muro *et al.* studied systematically the polycrystalline CeTX$_3$ (T: Rh and Ir, X: Si and Ge) compounds from the viewpoint of the Kondo effect.[97–99] We show in Table 3.I the physical properties of CeTX$_3$.


(a) BaNiSn$_3$ (b) ThCr$_2$Si$_2$ (c) CaBe$_2$Ge$_2$
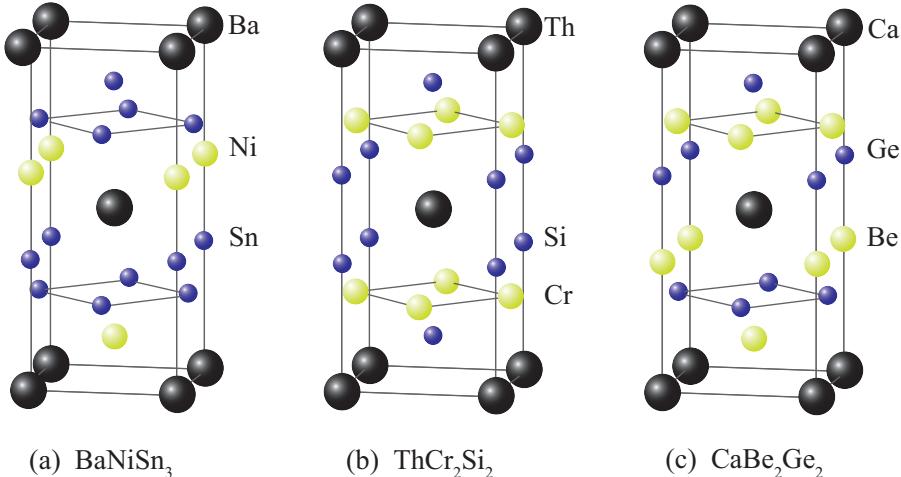
Fig. 3.1 (a) BaNiSn$_3$-, (b) ThCr$_2$Si$_2$- and (c) CaBe$_2$Ge$_2$-type crystal structure.

Table 3.I Volume of the unit cell, magnetic ground state, electronic specific heat coefficient γ, Néel temperature T_N, Weiss temperature Θ_p and effective magnetic moment μ_eff of CeTX$_3$ and corresponding references are shown. The abbreviations P and AF denote paramagnetic and antiferromagnetic ground states, respectively. The abbreviations IV and HF denote intermediate-valence and heavy-fermion states, respectively, where we consider the compounds with $\gamma > 100\,\mathrm{mJ/K^2 \cdot mol}$ to be the heavy-fermion ones.

Compounds		V (Å^3)	Magnetism	γ (mJ/mol·K^2)	T_N (K)	Θ_p (K)	μ_eff (μ_B)	reference
CeCoSi$_3$		163.6	P(IV)	37	—	-840	2.80	96
CeRuSi$_3$		175.7	P(IV)		—			89, 94
CeRhSi$_3$	$\begin{cases} a \\ c \end{cases}$	174.8	AF(HF)	110	1.8	$\begin{cases} \text{-112} \\ \text{-160} \end{cases}$	$\begin{cases} 2.65 \\ 2.65 \end{cases}$	100, 101
CePdSi$_3$		180.6	AF	57	3/5.2	-26	2.56	88, 99
CeOsSi$_3$			P(IV)					94
CeIrSi$_3$	$\begin{cases} a \\ c \end{cases}$	177.1	AF(HF)	105	5.0	$\begin{cases} \text{-186} \\ \text{-109} \end{cases}$	$\begin{cases} 2.57 \\ 2.64 \end{cases}$	21, 22
CePtSi$_3$		175.5	AF		11			90, 102
CeFeGe$_3$		186.8	P(HF)	150	—	-92	2.55	95
CeCoGe$_3$	$\begin{cases} a \\ c \end{cases}$	183.4	AF	32	21/12/8	$\begin{cases} \text{-71} \\ \text{-29} \end{cases}$	$\begin{cases} 2.23 \\ 2.16 \end{cases}$	103
CeRhGe$_3$		193.6	AF	40	14.6/10/0.55	-28	2.53	97
CeIrGe$_3$		193.5	AF	80	8.7/4.7/0.7	-21	2.39	97

3.1.2 CeRhSi$_3$

Single crystals of an antiferromagnet CeRhSi$_3$ were grown for the first time in RTX$_3$ by the Czochralski method, with the residual resistivity $\rho_0 = 0.7$ and $0.8\,\mu\Omega\cdot$cm, and the residual resistivity ratio RRR $(= \rho_{RT}/\rho_0$; ρ_{RT} denotes resistivity at room temperature) RRR $= 64$ and 150 for the current along [100] and [001], respectively, indicating a high-quality sample.[100] The magnetic susceptibility follows the Curie-Weiss law with Ce^{3+} ($\mu_{eff} = 2.65\,\mu_B$/Ce for $H \,//\, [100]$ and [001]),[100,101] as shown in Fig. 3.2. The magnetic susceptibility is characteristic. The susceptibility for $H \,//\, [100]$ is larger than that for $H \,//\, [001]$ in magnitude. As shown in Table 3.I, CeRhSi$_3$ orders antiferromagnetically below $T_N = 1.8$ K. CeRhSi$_3$ is a heavy fermion antiferromagnet because the electronic specific heat coefficient γ is large, $110\,$mJ/K$^2\cdot$mol.[101]
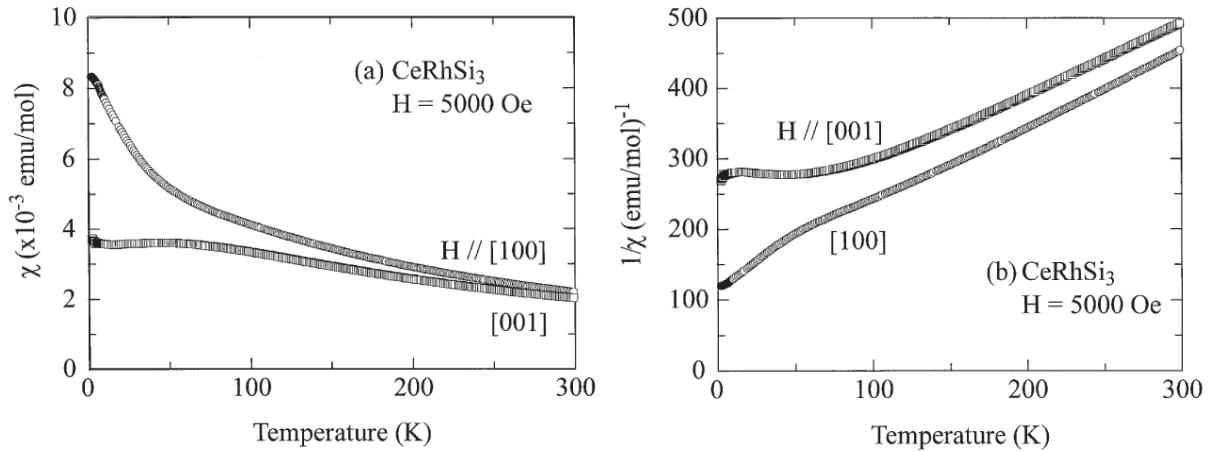
Fig. 3.2 Temperature dependence of (a) the magnetic susceptibility and (b) the inverse magnetic susceptibility in CeRhSi$_3$.[100,101]

The dHvA experiment was done for CeRhSi$_3$, together with a non-4f reference compound LaRhSi$_3$, as shown in Fig. 3.3.[100] Branches α and β_i correspond to the main Fermi surfaces with the cyclotron effective mass of $15\,m_0$ for branch β_2 for $H\,//\,[100]$.
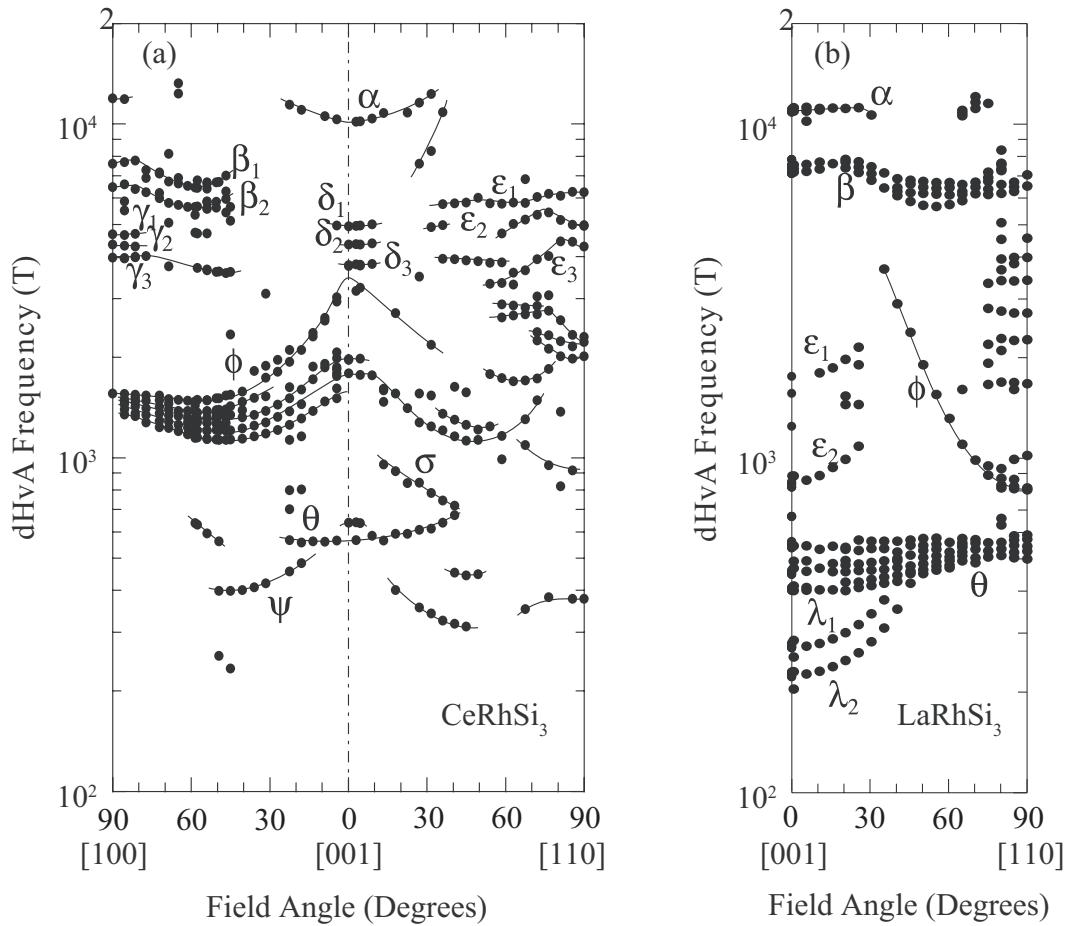
Fig. 3.3 Angular dependence of the dHvA frequency (a) in CeRhSi$_3$ and (b) its reference compound LaRhSi$_3$.[20, 100]

Superconductivity was discovered under pressure.[18] The corresponding pressure phase diagram is shown in Fig. 3.4.[20] With increasing pressure, the Néel temperature $T_N = 1.6$ K in the present sample increases, has a maximum around 8 K, and then decreases monotonically. Superconductivity is observed in a wide pressure range from a low pressure of 2 kbar(0.2 GPa) to about 30 kbar(3 GPa), or over 3 GPa. A maximum of the superconducting transition temperature is $T_{sc} = 1.1$ K at 2.6 GPa. Characteristic is the upper critical field H_{c2}, as shown in Figs. 3.5(a) and 3.5(b). When the magnetic field is directed along the a-axis ([100] direction) at 2.6 GPa, the upper critical field is slightly suppressed with decreasing temperature. On the other hand, the upper critical field for $H // c$-axis ([001] direction) possesses an upturn feature with decreasing temperature.[19] The upturn feature is often observed in strong-coupling superconductors such as UBe$_{13}$ in f-electron systems.[104] The upper critical field at 0 K, H_{c2}, is roughly estimated to 300 kOe, indicating an extremely large value of $H_{c2}(0)$. This might be an experimental evidence for spin-triplet superconductivity which is realized only for $H // [001]$ (c-axis).
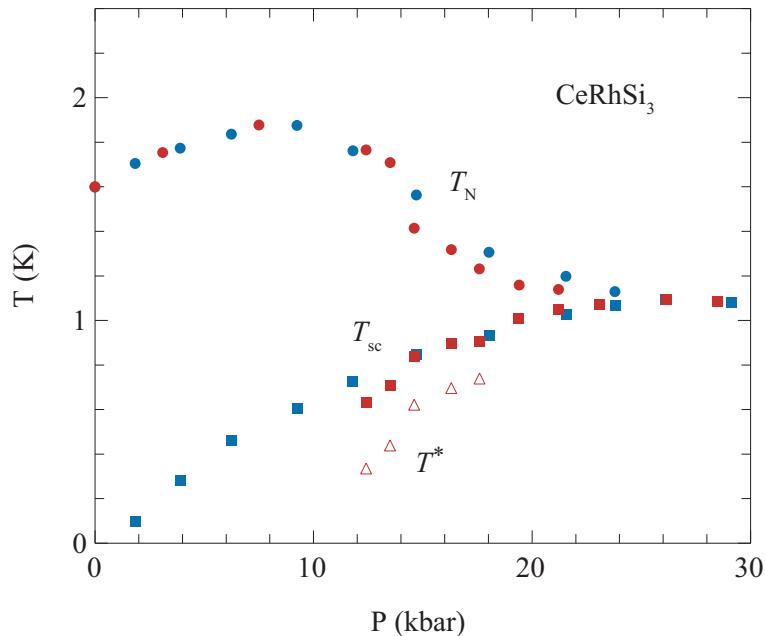
Fig. 3.4 Temperature-pressure (T-P) phase diagram of CeRhSi$_3$ based on the resistivity measurements.[20]
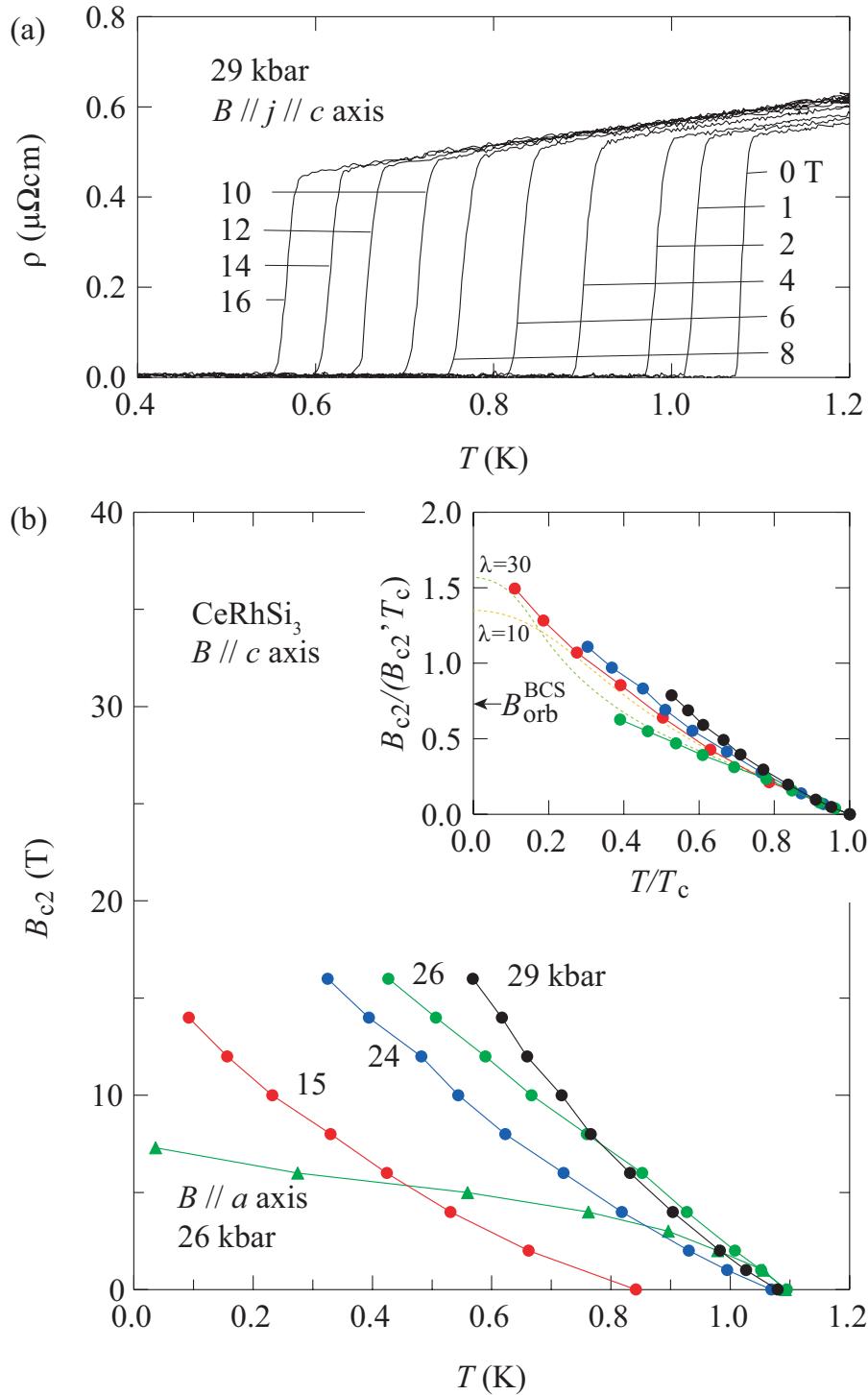
Fig. 3.5 (a) Resistivity curves for $B // c$ from 0 to 16 T at 29 kbar.[19] (b) $B_{c2} - T$ phase diagrams for $B // c$ at $P = 15$, 24, 26, and 29 kbar. Inset: $B_{c2}(T)$ curves for the $B // c$ normalized by the initial slope. The arrow indicates the orbital limit $B_{orb}^{BCS} = 0.73\, B'_{c2}T_c$. The dashed curves are theoretical predictions based on the strong-coupling model using the coupling strength parameter $\lambda = 10$ and 30.[105]

3.1.3 CeCoGe₃

Single crystals of CeCoGe₃ were grown by the Bi-flux method. The residual resistivity and residual resistivity ratio are $\rho_0 = 0.97\,\mu\Omega\cdot$cm and RRR = 124 for current $J\,//\,[100]$ and $2.90\,\mu\Omega\cdot$cm and 94 for current $J\,//\,[001]$, indicating a high-quality sample. The low-temperature magnetic susceptibility from 5 to 30 K and the inverse magnetic susceptibility for the magnetic field along [100] and [001] are shown in Figs. 3.6(a) and 3.6(b), respectively. It is noted that the susceptibility for $H\,//\,[001]$ is larger than that for $H\,//\,[100]$. Below the Néel temperature $T_{N1} = 21$ K, CeCoGe₃ becomes an antiferromagnet, and the [001] direction is an easy-axis in magnetization. The susceptibility is highly anisotropic in this temperature range. In fact, the magnetization for $H\,//\,[001]$ at
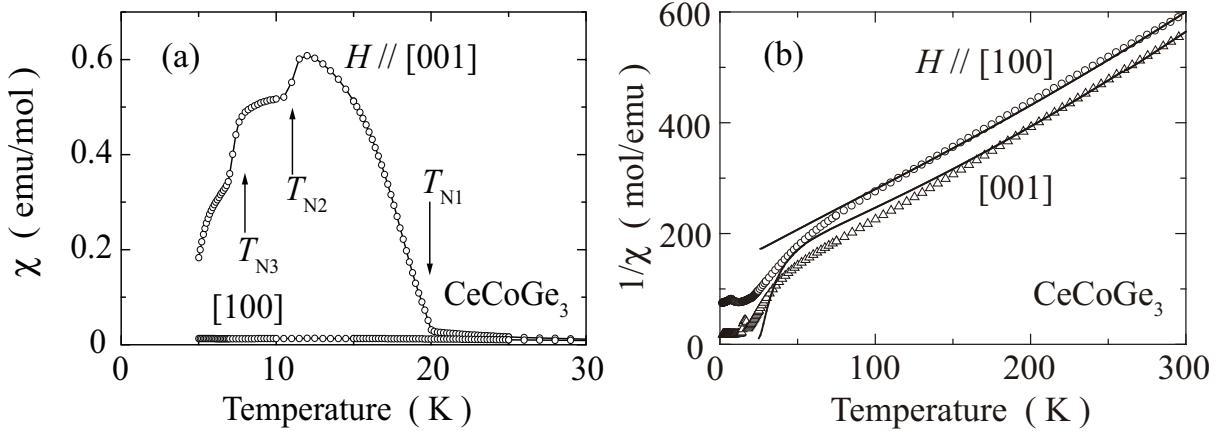
Fig. 3.6 (a) Low-temperature susceptibility and (b) the inverse magnetic susceptibility of CeCoGe₃ for $H\,//\,[001]$ and [100]. The arrows indicate the magnetic transitions. Solid lines are the results of the CEF calculation.[103]
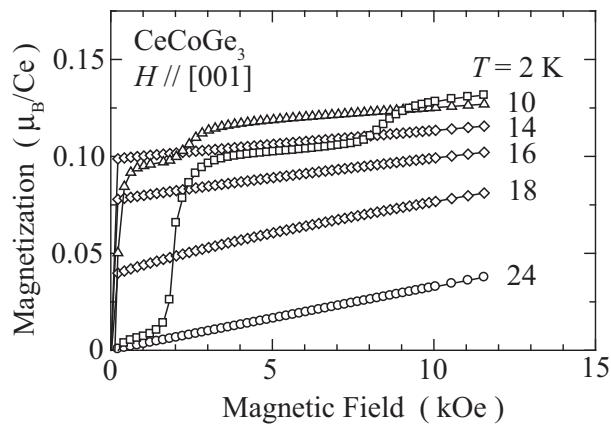
Fig. 3.7 Low-field magnetization curves for $H\,//\,[001]$ at selected temperatures.[103]

Table 3.II CEF parameters, energy level schemes and the corresponding wave functions for CeCoGe$_3$.[103]

CEF parameters					
B_2^0 (K)	B_4^0 (K)	B_4^4 (K)	λ_1 (emu/mol)$^{-1}$	λ_2 (emu/mol)$^{-1}$	χ_0 (emu/mol)
3	-1	0	$\lambda_1^{x,y}=0$	$\lambda_2^{x,y}=-125$	$\chi_0^{x,y}=-3.5\times10^{-4}$
			$\lambda_1^z=450$	$\lambda_2^z=-60$	$\chi_0^z=-4.3\times10^{-4}$
energy levels and wave functions						
E(K)	$\vert-5/2\rangle$	$\vert-3/2\rangle$	$\vert-1/2\rangle$	$\vert+1/2\rangle$	$\vert+3/2\rangle$	$\vert+5/2\rangle$
318	0	0	0	0	1	0
318	0	1	0	0	0	0
114	1	0	0	0	0	0
114	0	0	0	0	0	1
0	0	0	1	0	0	0
0	0	0	0	1	0	0

2 K shows metamagnetic transitions at $H = 1.9$ and 8.4 kOe, as shown by open squares in Fig. 3.7. At 24 K, the magnetization increases linearly as a function of magnetic field. The magnetic susceptibility follows the Curie-Weiss law at temperatures larger than 150 K, as shown in Fig. 3.6(b). The solid lines in Fig. 3.6(b) are the results of the CEF calculations, where the constant magnetic susceptibility χ_0 is subtracted from the experimental data. The CEF parameters are represented in Table 3.II.

The typical isothermal magnetization curves for $H \mathbin{//} [100]$ and $[001]$ at 2 K are shown in Fig. 3.8(a). A three-step metamagnetic transition is observed for $H \mathbin{//} [001]$: $H_{c1} = 1.9$ kOe, $H_{c2} = 8.4$ kOe and $H_{c3} = 30$ kOe. It was also confirmed from the pulsed high-field magnetization measurement that there is no metamagnetic transition above $H_{c3} = 30$ kOe, as shown in Fig. 3.8(b). For $H \mathbin{//} [100]$, the magnetization increases linearly up to 70 kOe and the magnetization at 70 kOe is found to be $0.15\,\mu_{\rm B}$/Ce, indicating highly anisotropic magnetizations.

As shown in Fig. 3.8(a), at 2 K, the metamagnetic transition with three steps is found at $H_{c1} = 1.9$ kOe, $H_{c2} = 8.4$ kOe and $H_{c3} = 30$ kOe. The third metamagnetic transition H_{c3} increases from a field $H_{c3} = 30$ kOe at 2 K to $H_{c3} = 41$ kOe at 16 K and then decreases to lower fields for temperatures above 16 K and finally disappears at 22 K, as shown in Fig. 3.8(c), where the magnetization at higher temperatures increases linearly as a function of magnetic field, indicating the paramagnetic state. A magnetic phase diagram was thus constructed, as shown in Fig. 3.9. The characteristic feature of the phase diagram is that the metamagnetic transition with three steps is observed below 8 K and then reduced into two steps above 8 K. The two-step metamagnetic transition is observed in a very narrow temperature range from $T_{\rm N3} = 8$ K to $T_{\rm N2} = 12$ K. The one-step metamagnetic transition is thus observed in the temperature range from $T_{\rm N2} = 12$ K to $T_{\rm N1} = 21$ K, although in this temperature range, CeCoGe$_3$ possesses a ferromagnetic spontaneous magnetic moment at low fields, as shown in Fig. 3.7.
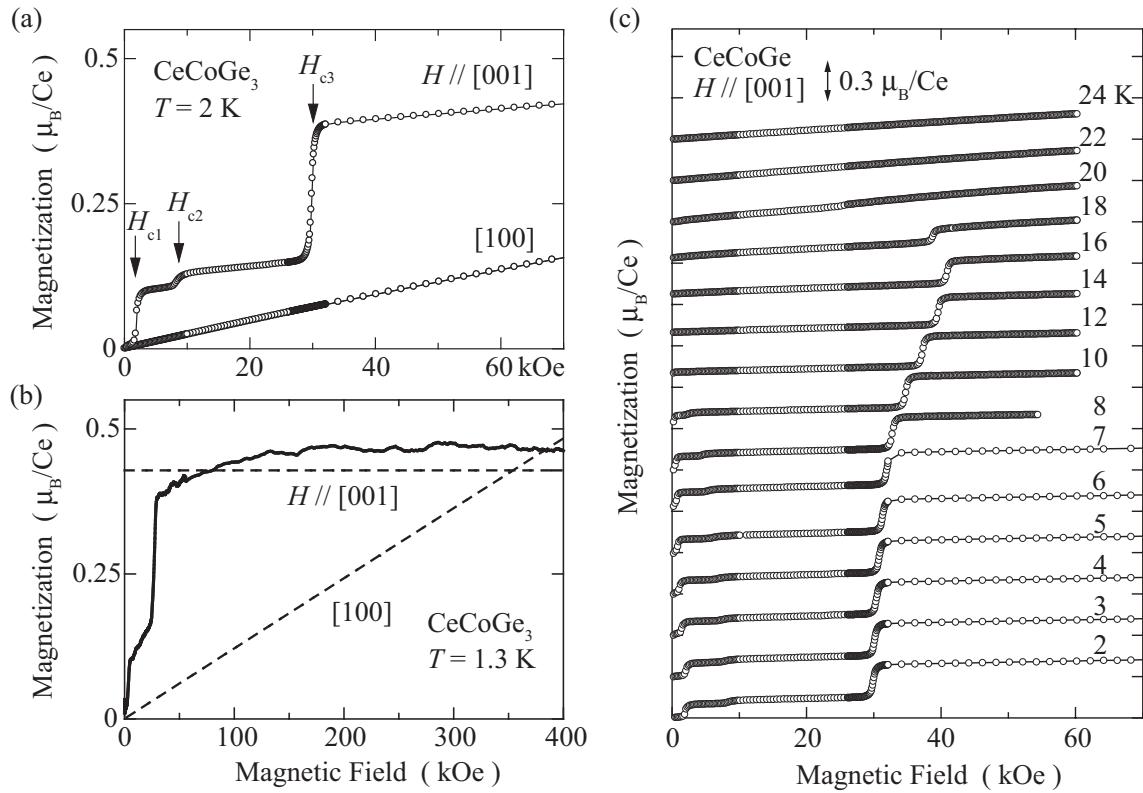
Fig. 3.8 (a) Magnetization at 2 K, measured by the SQUID magnetometer, (b) pulsed-field magnetization at 1.3 K and (c) isothermal magnetization $H // [001]$ at various temperature in CeCoGe₃. Dashed lines in (b) are the results of CEF calculations.[103)]
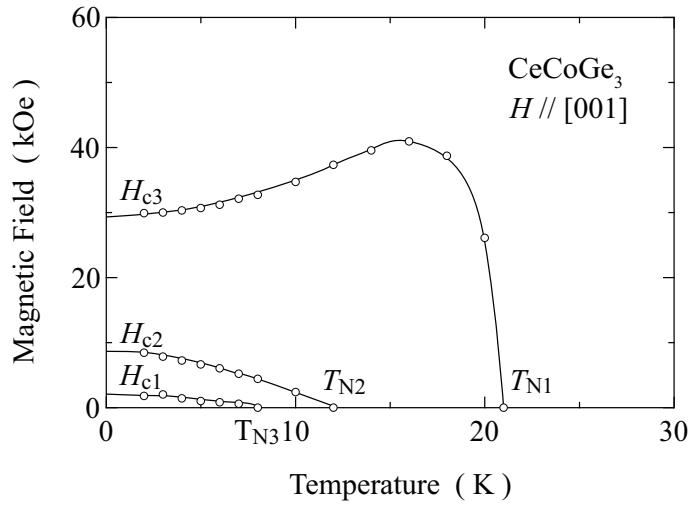

Fig. 3.9 Magnetic phase diagram of CeCoGe₃ for the field along [001].[103)]

The dHvA experiment was carried out for CeCoGe$_3$ and its non-4f reference com-
pound LaCoGe$_3$.[106] The angular dependence of the dHvA frequency in CeCoGe$_3$ and
LaCoGe$_3$ is shown in Figs. 3.10(a) and 3.10(b), respectively. Figure 3.10(c) corresponds
to the theoretical one based on the full potential APW (FLAPW) energy band structure
calculation. The corresponding energy band structure, density of states and Fermi sur-
faces are shown in Figs. 3.11(a), 3.11(b) and 3.11(c), respectively. Here, the 4f level
of La is shifted upward by 0.2 Ry in the band calculation. From these results of band
calculations, the dHvA branches of LaCoGe$_3$ are identified as follows:
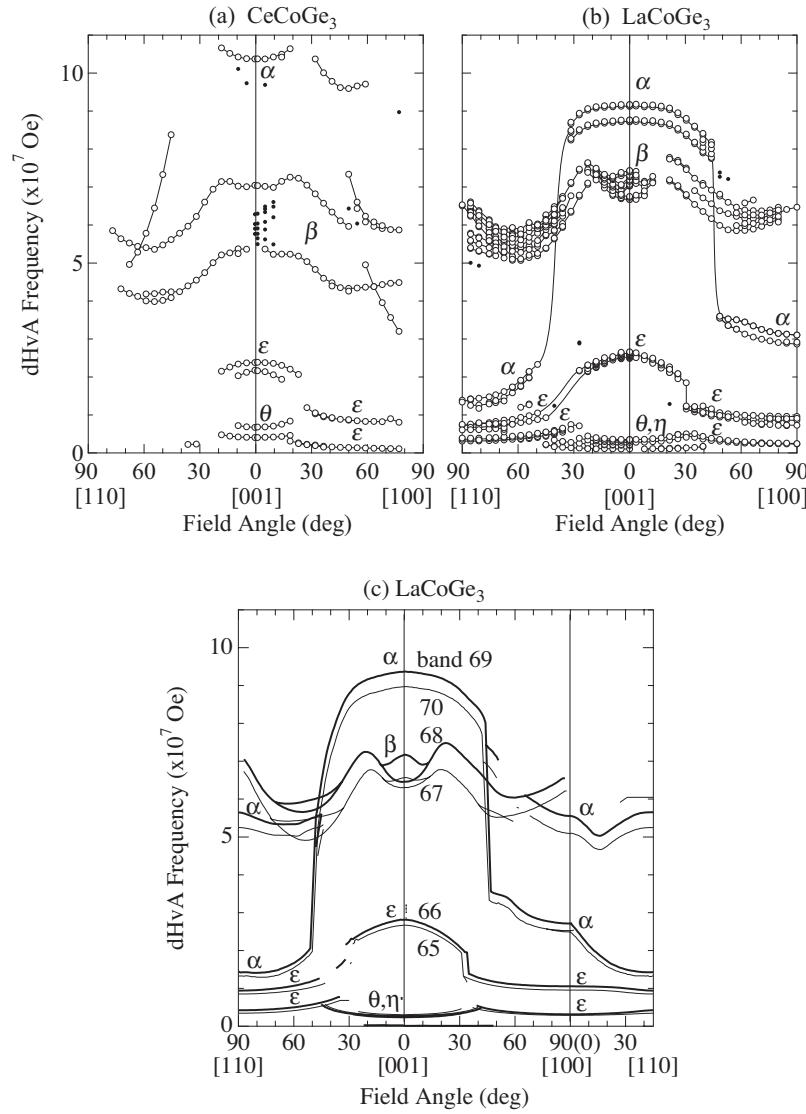
Fig. 3.10 Angular dependence of dHvA frequency in (a) CeCoGe$_3$, (b) LaCoGe$_3$, and
(c) LaCoGe$_3$, obtained by the energy band calculations.[106]

1) Branch α and η are the outer and inner orbits of bands 69- and 70-electron Fermi surfaces, respectively.

2) Branch β is due to the bands 67- and 68-hole Fermi surfaces.

3) Branches ε and θ are due to the outer and inner orbits of band 65- and 66-hole Fermi surfaces, respectively.

There exist three different Fermi surfaces. Each Fermi surface is found to consist of two different Fermi surfaces in volume but similar in topology. This is due to the small magnitude of antisymmetric spin-orbit interaction in LaCoGe₃, for example, $2|\alpha p_\perp| = 460\,\mathrm{K}$ for branch α.

The dHvA branches in CeCoGe₃, which were observed in the field-induced ferromagnetic state (or the paramagnetic state), are similar to those in LaCoGe₃, but the splitting of two similar dHvA branches is large compared with that in LaCoGe₃. This is due to an enhancement of the ferromagnetic exchange interaction in CeCoGe₃. The main dHvA branch of CeCoGe₃ is found to possess the relatively large cyclotron mass $m_c^* \simeq 10\,m_0$, which is compared with $1\,m_0$ in LaCoGe₃.
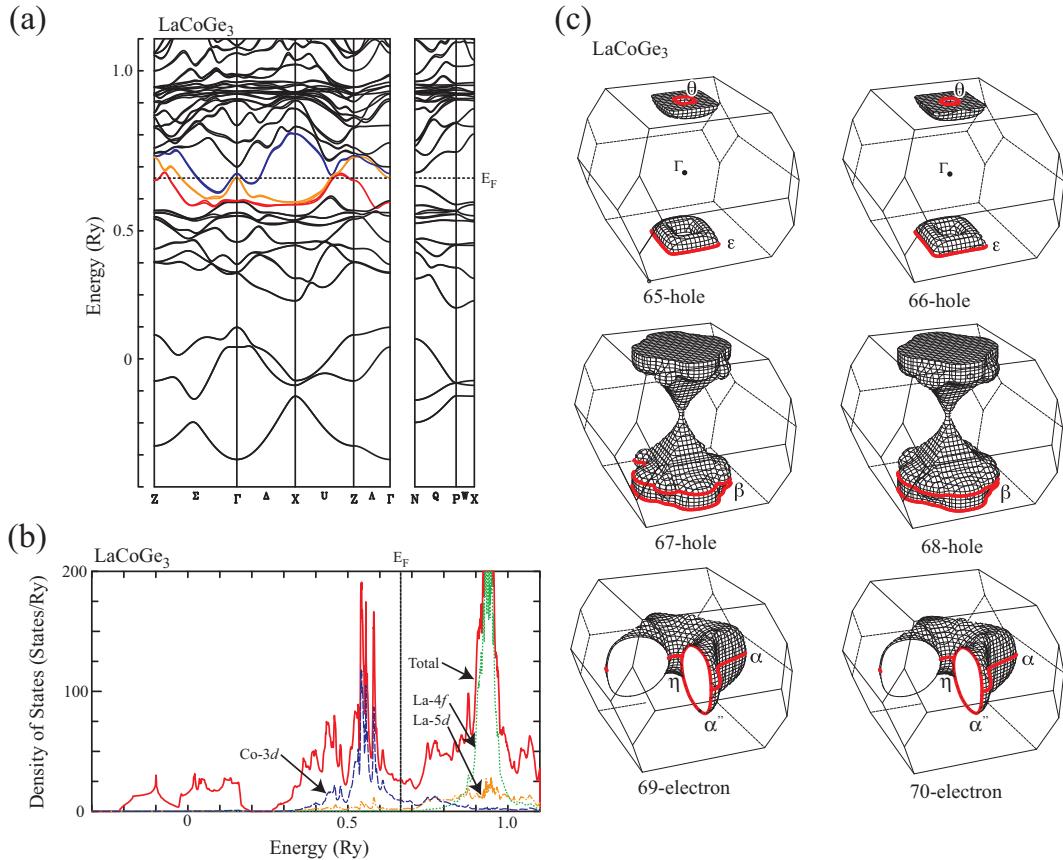
Fig. 3.11 (a) FLAPW energy band structure along the symmetry lines. (b) Calculated total (solid line) and partial (dashed line: Co-3d, dotted line: La-4f, dot-dash line: La-5d) densities of states. (c) Theoretical Fermi surfaces in LaCoGe₃. The Fermi level is denoted by E_{F}.[106]

The pressure experiment was done for a polycrystal sample of CeCoGe$_3$ by using the Bridgeman anvil cell up to 5.6 GPa.[23] Figure 3.12 shows the temperature dependence of the electrical resistivity under several pressures. The resistivity drop due to superconductivity appears below about 4.5 GPa, and the resistivity zero is obtained above 5 GPa. The pressure phase diagram is shown in Fig. 3.13. The Néel temperature most likely becomes zero above $P_c \simeq 5.5$ GPa. Here, the onset of the resistivity drop is defined as the superconducting transition temperature T_{sc} in this experiment, whereas the temperature showing zero resistivity is defined as T_{sc} in the present thesis study, presented in Chap. 6.2.

At 5.6 GPa, the resistivity measurement was done under several magnetic fields, as shown in Fig. 3.14. The resistivity zero is broken by applying magnetic fields of 0.1 T or 1 kOe, although the onset of superconductivity is stable up to 4.5 T.

The polycrystal sample was used instead of the high-quality single crystal because the dHvA signal was observed in the single crystal sample. This was mainly due to the sample grown by the Bi-flux method. Bi was included in subgrain boundaries of the single crystal CeCoGe$_3$, which produces superconductivity of Bi at 4 - 9 K at pressure higher than 2 GPa. In the present experiment, we used almost the same single crystal sample grown by the Bi-flux method, but inclusions of Bi were subtracted completely by adjusting the thickness of the single crystal sample.
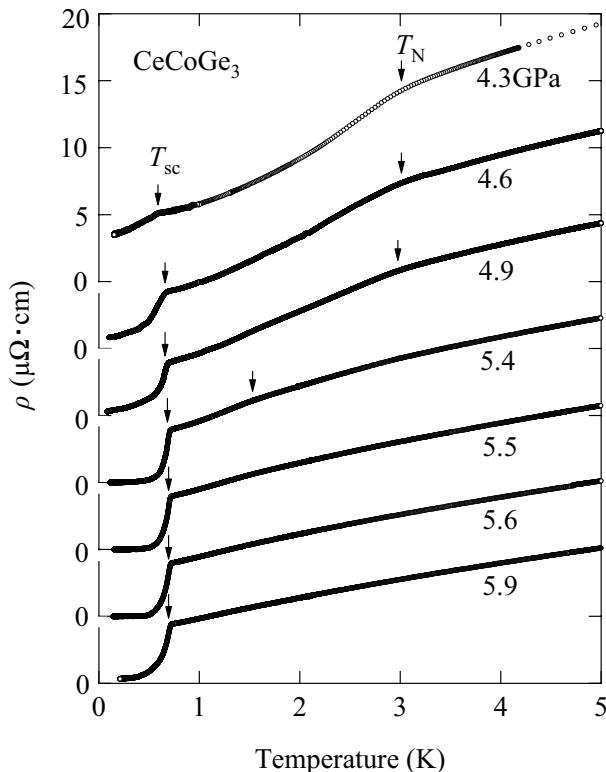
Fig. 3.12 Temperature dependence of the electrical resistivity under several pressures in a polycrystalline CeCoGe$_3$.[23]
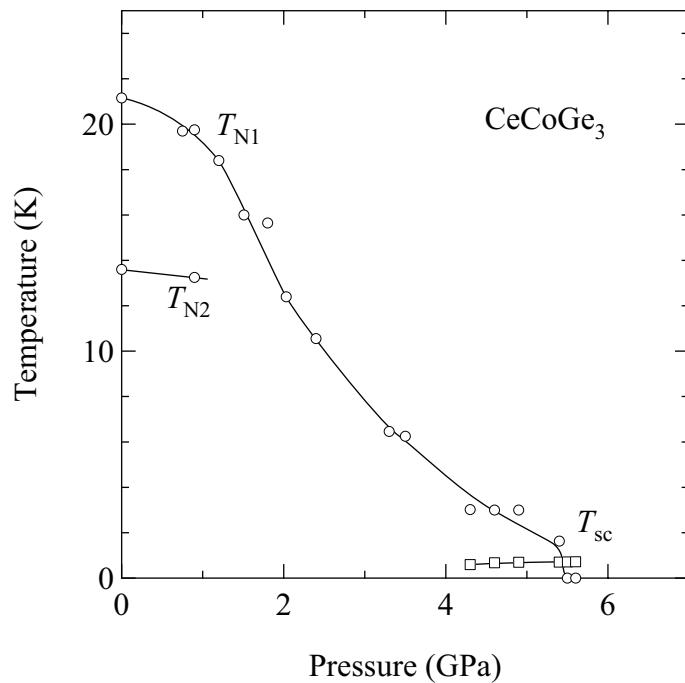
**Fig. 3.13** Pressure phase diagram in a polycrystalline $CeCoGe_3$.[23)]
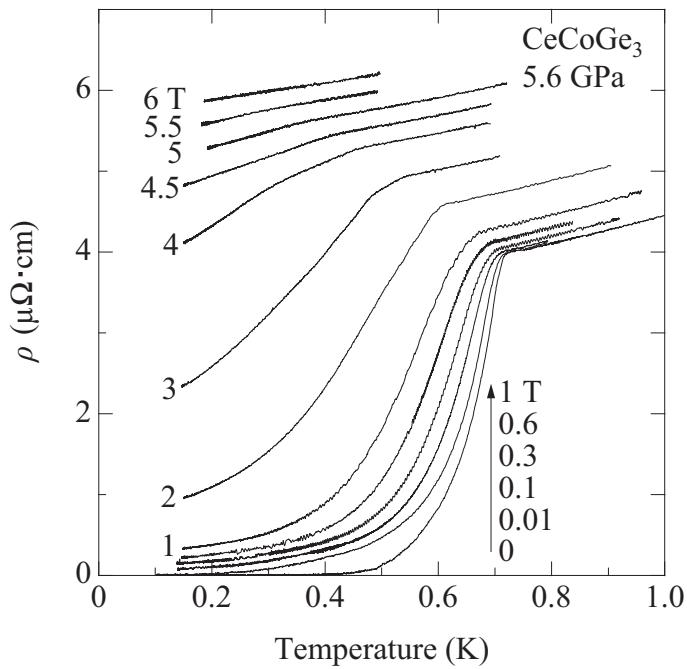
Fig. 3.14 Temperature dependence of the electrical resistivity under several magnetic fields in a polycrystalline $CeCoGe_3$.[23)]

3.1.4   CeIrSi$_3$

Single crystals of CeIrSi$_3$ and its non-4f reference compound LaIrSi$_3$ were grown by the Czochralski method.[21, 22)] The residual resistivity ρ_0 and the residual resistivity ratio RRR are $\rho_0 = 0.40\,\mu\Omega$·cm and RRR = 100 for current $J\,//\,[110]$, and $\rho_0 = 0.48\,\mu\Omega$·cm and RRR = 110 for $J\,//\,[001]$, respectively, indicating a high-quality sample. The magnetic susceptibility is very similar to that of CeRhSi$_3$, as shown in Fig. 3.15. Solid lines in Fig. 3.15 are the result of the CEF calculations. The CEF parameters are summarized in Table 3.III
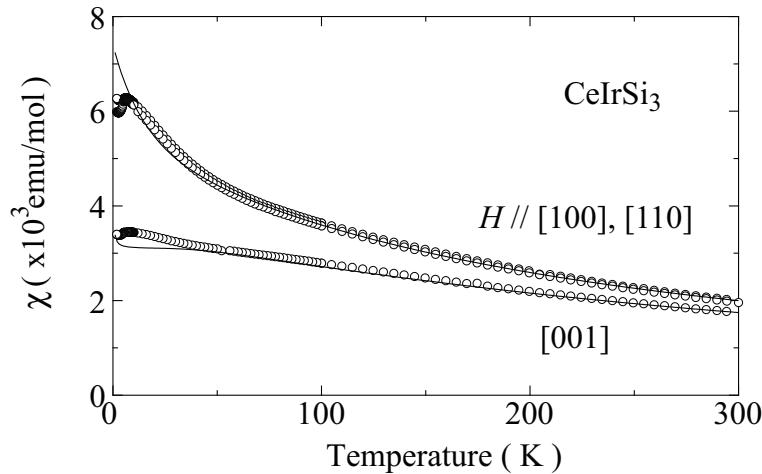
Fig. 3.15 Temperature dependence of the magnetic susceptibility χ for $H\,//\,[100]$, [110], and [001] in CeIrSi$_3$. The solid lines are the CEF curves.[22)]

Table 3.III   CEF parameters B_m^l, the molecular exchange constant λ, energy levels E and the corresponding wave functions in CeIrSi$_3$.[22)]

CEF parameters				
B_2^0 (K)	B_4^0 (K)	B_4^4 (K)	λ_x (mol/emu)	λ_z (mol/emu)
8.35	0.1	8.3	-135	-91
χ_{0x} (mol/emu)	χ_{0z} (mol/emu)			
-4.0×10^{-5}	-1.3×10^{-4}			

Energy levels and wave functions						
E (K)	$|+5/2\rangle$	$|+3/2\rangle$	$|+1/2\rangle$	$|-1/2\rangle$	$|-3/2\rangle$	$|-5/2\rangle$
462	0.796	0	0	0	0.605	0
462	0	0.605	0	0	0	0.796
149	0	0	1	0	0	0
149	0	0	0	1	0	0
0	-0.605	0	0	0	0.796	0
0	0	0.796	0	0	0	-0.605

The angular dependence of the dHvA frequency in LaIrSi$_3$ and the theoretical one is shown in Figs. 3.16(a) and 3.16(b), respectively. The detected branches are approximately the same as those in LaCoGe$_3$. The corresponding Fermi surfaces in LaIrSi$_3$ are shown in Fig. 3.17.
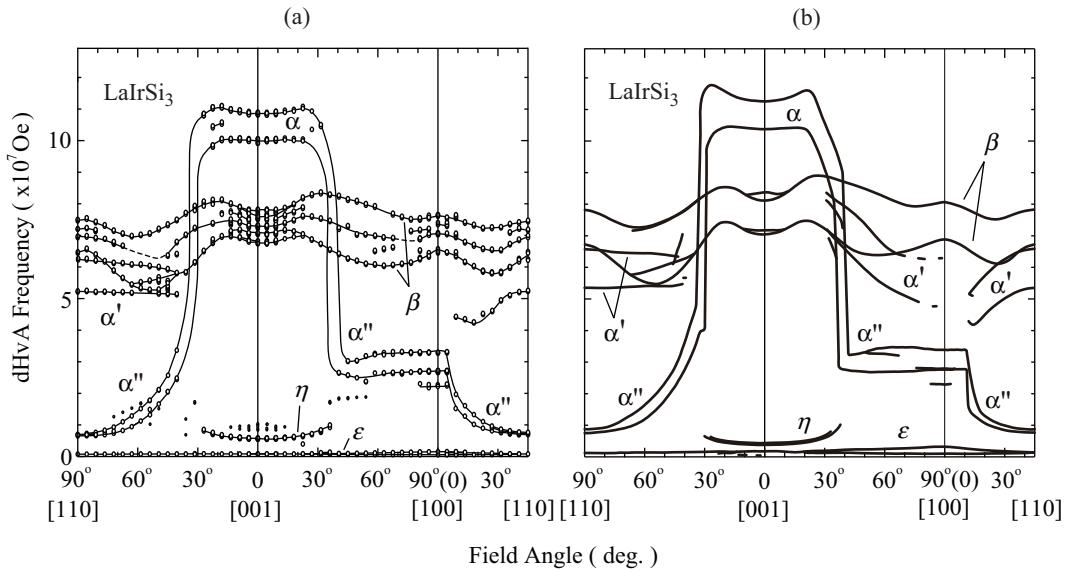

**Fig. 3.16** (a) Angular dependence of dHvA frequency in LaIrSi$_3$, and (b) the theoretical one.[22]
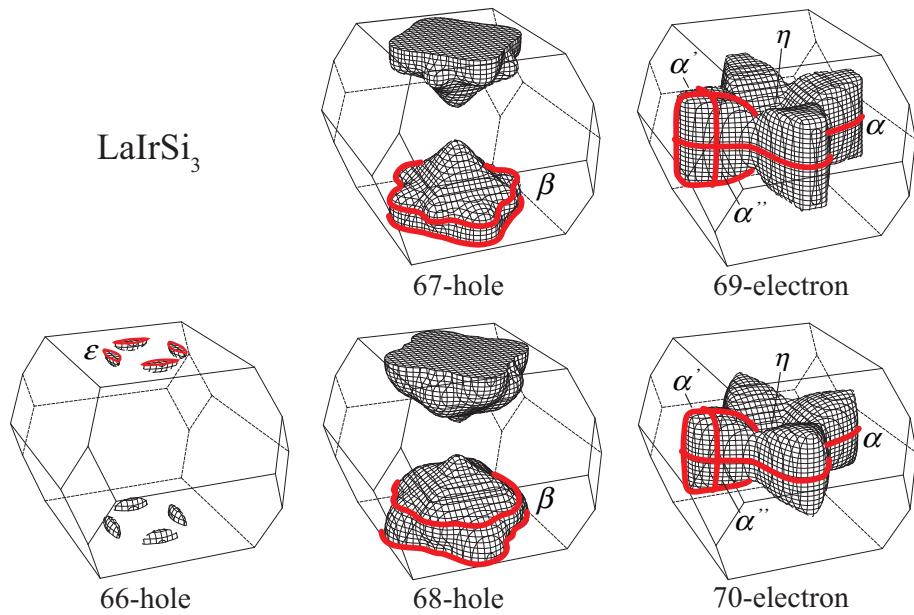
Fig. 3.17 Theoretical Fermi surfaces of LaIrSi$_3$.[22]

The effect of pressure on the electronic state was investigated for an antiferromagnet CeIrSi$_3$. As shown in Fig. 3.18, Néel temperature $T_N = 5$ K at ambient pressure decreases monotonically, and superconductivity appears above 1.9 GPa, possessing the maximum of the superconducting transition temperature $T_{sc} = 1.6$ K at 2.6 GPa. Characteristic is also the upper critical field, as shown in Fig. 3.19. The upper critical field indicates the upturn feature with decreasing temperature. The $H_{c2}(0)$ value is estimated to be 350 - 450 kOe. This is due to the strong-coupling superconducting nature of CeIrSi$_3$, as noted in CeRhSi$_3$. This was experimentally confirmed from the ac-specific heat measurement for CeIrSi$_3$.[107]

Figure 3.20 shows the temperature dependence of the ac-specific heat at several pressures. At 1.31 GPa, the antiferromagnetic ordering is observed at $T_N = 4.5$ K, but at 2.19 GPa, the antiferromagnetism with $T_N = 1.7$ K coexists with superconductivity with $T_{sc} = 1.4$ K. Only superconductivity is observed above the critical pressure $P_c = 2.25$ GPa. It is noted that the specific heat indicates a huge jump at the superconducting transition above P_c. The jump of the ac-specific heat $\Delta C_{ac}/C_{ac}(T_{sc})$ at 2.58 GPa is 5.75 at $T_{sc} = 1.6$ K, which is extremely large compared with the BCS value of $\Delta C/\gamma T_{sc} = 1.43$. This value is the largest in all the superconductors. An antiferromagnet CeIrSi$_3$ is thus changed into a strong-coupling superconductor. The γ value at 2.58 GPa is roughly estimated as $\gamma = 100 \pm 20$ mJ/K^2·mol, which is approximately the same as $\gamma = 120$ mJ/K^2·mol at ambient pressure.
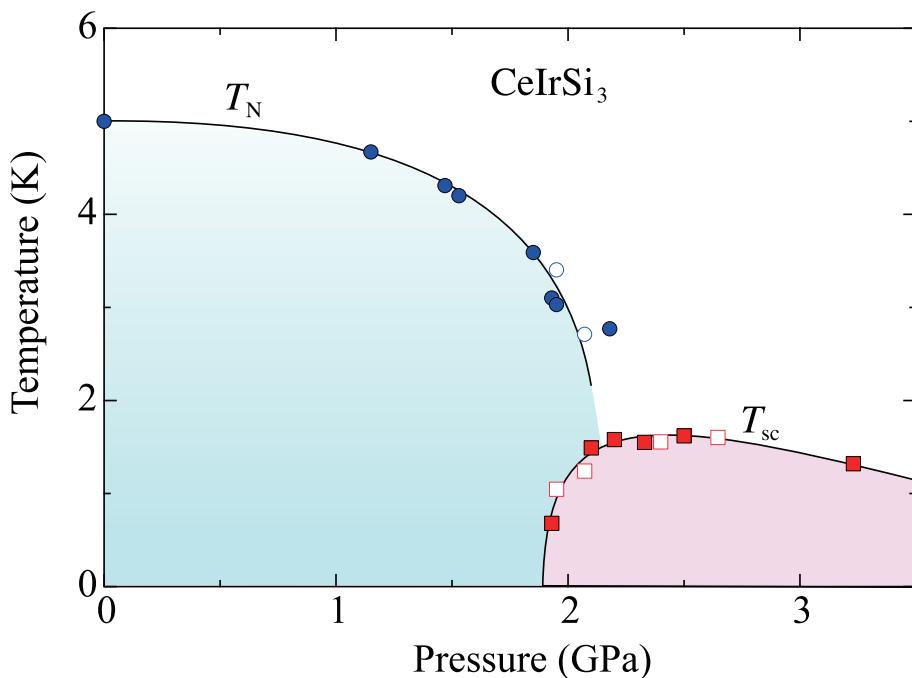

**Fig. 3.18** Pressure phase diagram in CeIrSi$_3$.[22]
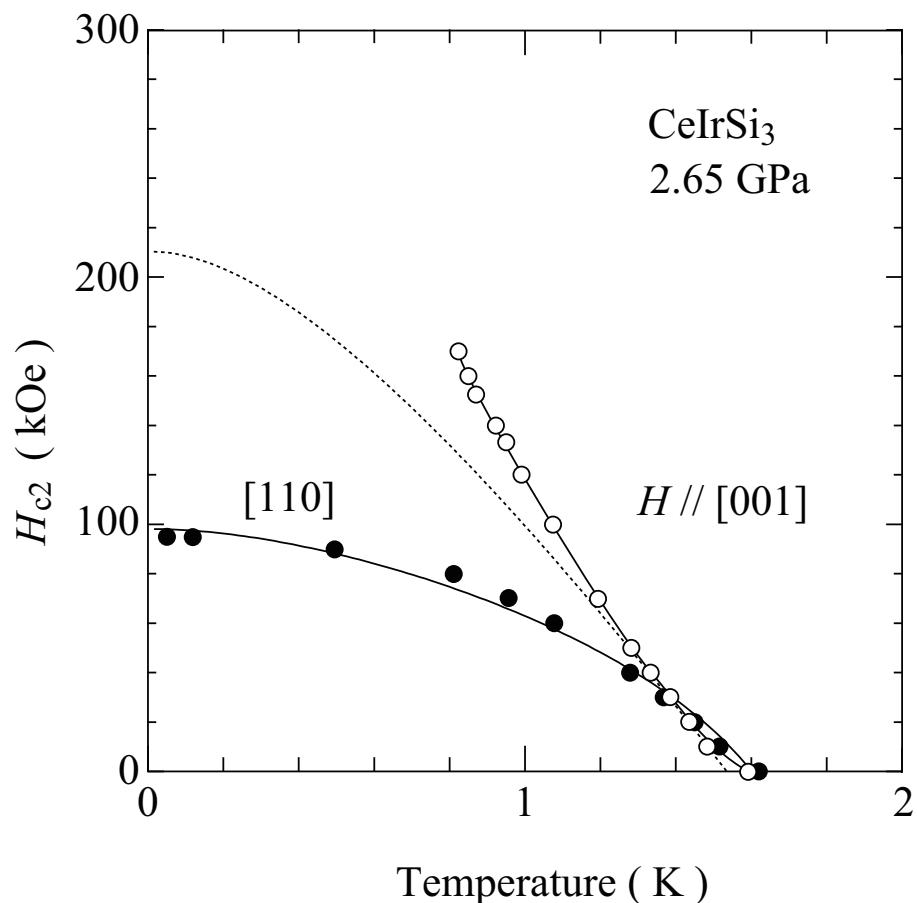
Fig. 3.19 Temperature dependence of the upper critical field in CeIrSi$_3$ at 2.65 GPa. The dotted line is a visual guide based on the WHH theory for $H /\!/ [001]$.[22)]
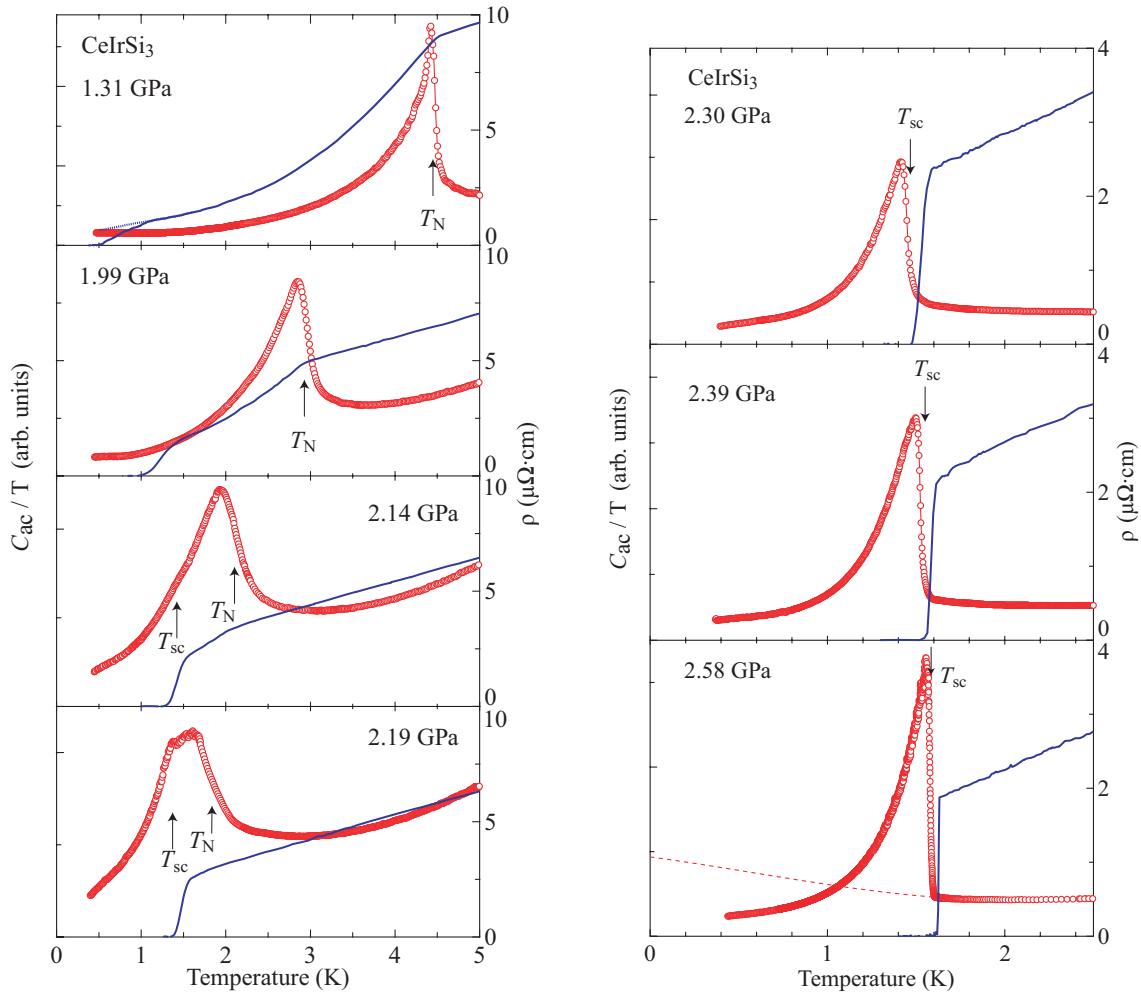
Fig. 3.20 Temperature dependences of the ac heat capacity C_{ac} (circles, left side) and electrical resistivity ρ (lines, right side) at 1.31, 1.99, 2.14, 2.19, 2.30, 2.39, and 2.58 GPa in CeIrSi$_3$. The dotted line indicates the entropy balance below T_{sc} at 2.58 GPa.[107]

3.2 Ce$_2$TGe$_6$(T: Pd, Cu)

3.2.1 Crystal structure and the magnetic properties of Ce$_2$TGe$_6$(T: transition metal)

Ternary compounds Ce$_2$TGe$_6$, where T is a transition metal belonging to group 10 and 11 in the periodic table, namely Ni, Pd, Pt, Cu, Ag and Au, were reported to be crystallized in the Ce$_2$CuGe$_6$-type non-centrosymmetric orthorhombic crystal structure with space group $Amm2$ (#38),[108–114] as shown in Fig. 3.21. The characteristic crystallographic feature of Ce$_2$TGe$_6$ (T: transition metal) is that the lattice constant is elongated along the c-axis, almost 5 times longer than those of the a- and b-axes, and the Ce-atoms in the crystal structure possess two crystallographically inequivalent sites, named Ce1 and Ce2. The physical properties of Ce$_2$TGe$_6$(T: transition metal) were studied on the polycrystalline samples.[92, 112, 113, 115–119] The magnetic properties in Ce$_2$TGe$_6$ are summarized in Table 3.IV
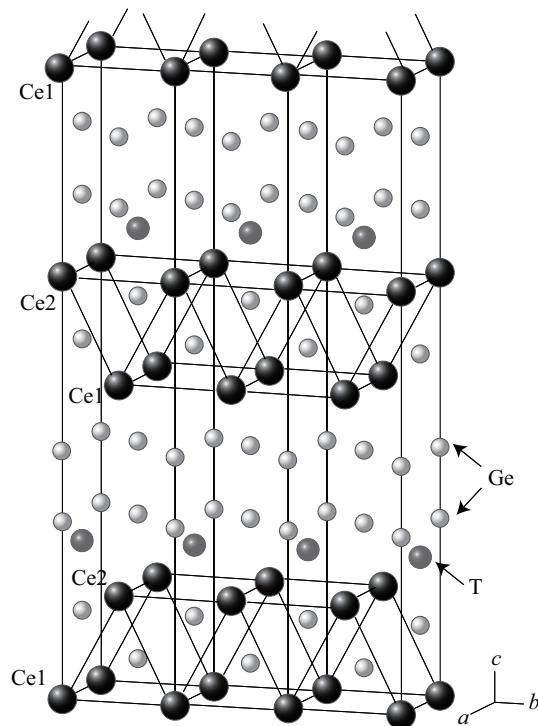
Fig. 3.21 Crystal structure of Ce$_2$TGe$_6$ (T: transition metal) with 3 unit cells along b-axis.

Table 3.IV Volume of the unit cell, magnetic ground state, electronic specific heat co-efficient γ, Néel temperature T_N, Weiss temperature Θ_p and effective magnetic moment μ_{eff} of CeTX$_3$ and corresponding references are shown. The abbreviations P and AF denote paramagnetic and antiferromagnetic ground states, respectively. The abbreviations IV and HF denote intermediate-valence and heavy-fermion states, respectively, where we consider the compounds with $\gamma > 100$mJ/K^2·mol to be the heavy-fermion ones.

Compounds	V (Å^3)	Magnetism	γ (mJ/mol·K^2·Ce)	T_N (K)	Θ_p (K)	μ_{eff} (μ_B)	reference
Ce$_2$NiGe$_6$	368.0	AF	—	10.4/6.8	—	2.45	113, 114
Ce$_2$CuGe$_6$	370.1	AF	12.2	15	-6.7	2.48	109, 112, 118
Ce$_2$PdGe$_6$	374.9	AF	14	11.5	-16.1	2.52	116, 117
Ce$_2$AgGe$_6$	387.0	—	—	—	—	—	109
Ce$_2$PtGe$_6$	374.0	AF	—	9.0	-7.0	2.43	116
Ce$_2$AuGe$_6$	384.0	—	—	—	—	—	109

3.2.2   Ce$_2$PdGe$_6$

The magnetic properties of polycrystalline Ce$_2$PdGe$_6$ were studied by Fan *et al.*[117] and Strydom *et al.*[116]. Strydom *et al.* reported that the temperature dependence of the magnetic susceptibility indicates an antiferromagnetic ordering around 11.4 K. The magnetization at $T = 1.9$ K was very small up to a field of 10 kOe. With increasing the magnetic field, they observed a metamagnetic transition just above 10 kOe, with a saturation moment of 0.9 μ_B/Ce, as shown in Figs. 3.22(a) and 3.22(b), respectively. Fan *et al.* also mentioned that the T^3-dependence of the magnetic contribution to the heat capacity below the Néel temperature T_N is ascribed to the spin-wave, as shown in Fig. 3.23. They also determined the electronic specific heat coefficient γ of 28 mJ/mol·K^2 and Θ_D of 270 K, and the magnetic entropy is 90% of $2R\ln2$ at the Néel temperature, suggesting a doublet ground state.

(a)　　　　　　　　　　　　　　　　　(b)
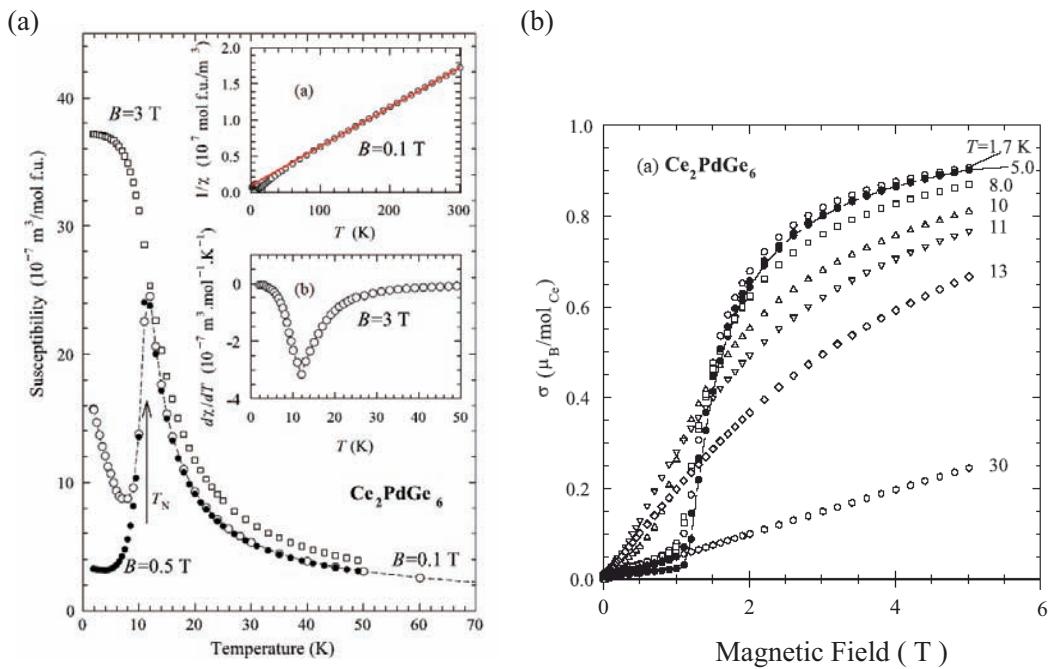
**Fig. 3.22** (a)Temperature dependence of the magnetic susceptibility and (b) the magnetization curve at 4.2 K in polycrystalline Ce$_2$PdGe$_6$.[116]
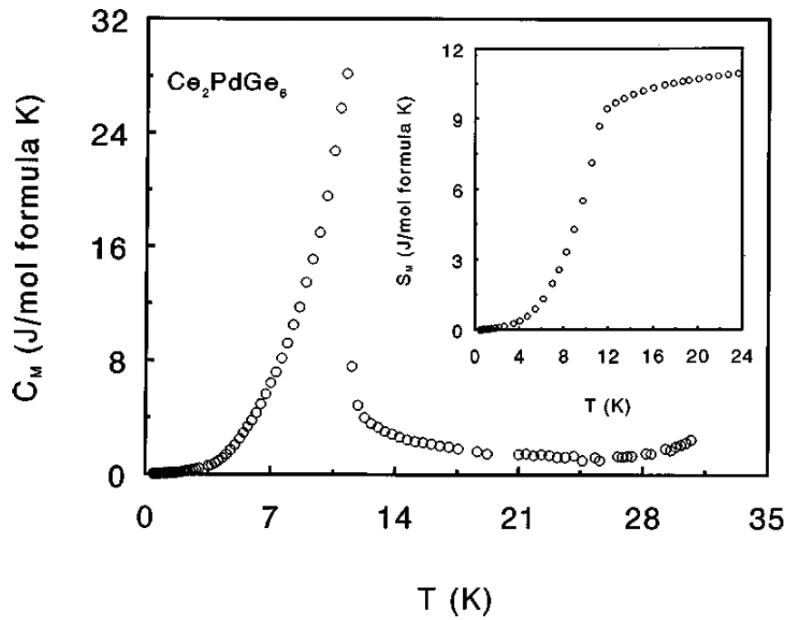


Fig. 3.23 (a)Temperature dependence of the specific heat in polycrystalline Ce$_2$PdGe$_6$.[117]

3.2.3 Ce_2CuGe_6

The magnetic properties of polycrystalline Ce_2CuGe_6 were studied by Yamamoto *et al.*[112], Konyk *et al.*[115] and Tseng *et al.*[118]. They reported that the temperature dependence of the magnetic susceptibility indicates a ferrimagnetic ordering around 14.7 K and the residual magnetization in magnetization curve at 4.2 K is $7.8 \times 10^{-4} \mu_B$/f.u., as shown in Figs. 3.24(a) and 3.24(c), respectively. A linear Curie-Weiss law with an effective magnetic moment of $2.66 \, \mu_B$/Ce and the paramagnetic Curie temperature of -2 K is found in the temperature range between 70 - 300 K, as shown in Fig. 3.24(b).

Tseng *et al.* mentioned that in Ce_2CuGe_6 the $4f$ electrons are localized and the T^3-dependence of the magnetic contribution to the heat capacity below the Néel temperature $T_N = 14.7$ K is ascribed to the spin-wave for an antiferromagnetic material, as shown in Fig. 3.25(b). They also determined the electronic specific heat coefficient γ and Θ_D to
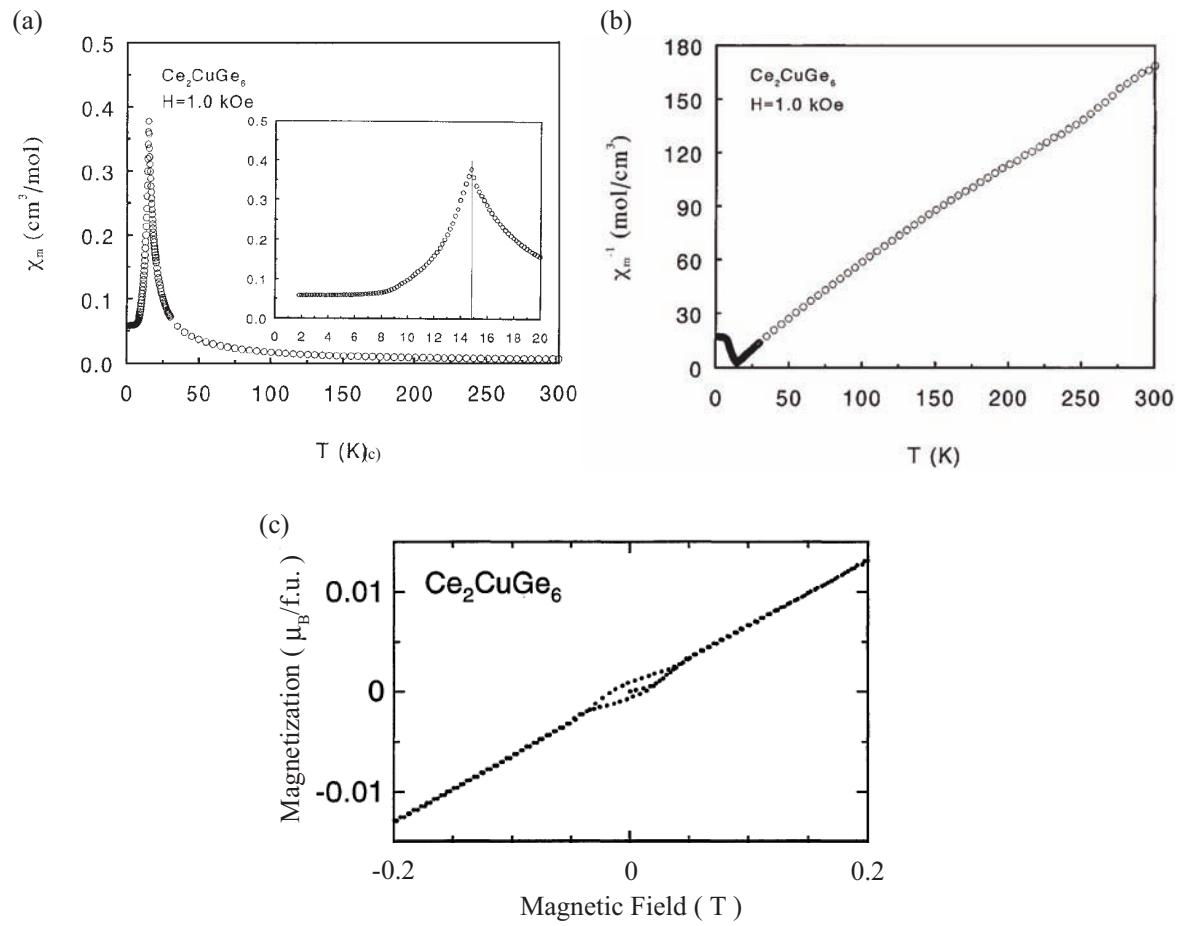

Fig. 3.24 (a) Temperature dependence of the magnetic susceptibility and (b) the inverse magnetic susceptibility[118], and (c) the magnetization curve at 4.2 K[112] in polycrystalline Ce_2CuGe_6.

be 12.2 mJ/mol·K^2 and 280 K, respectively, and the magnetic entropy is almost $2R\ln2$ at Néel temperature, indicating a doublet ground state.
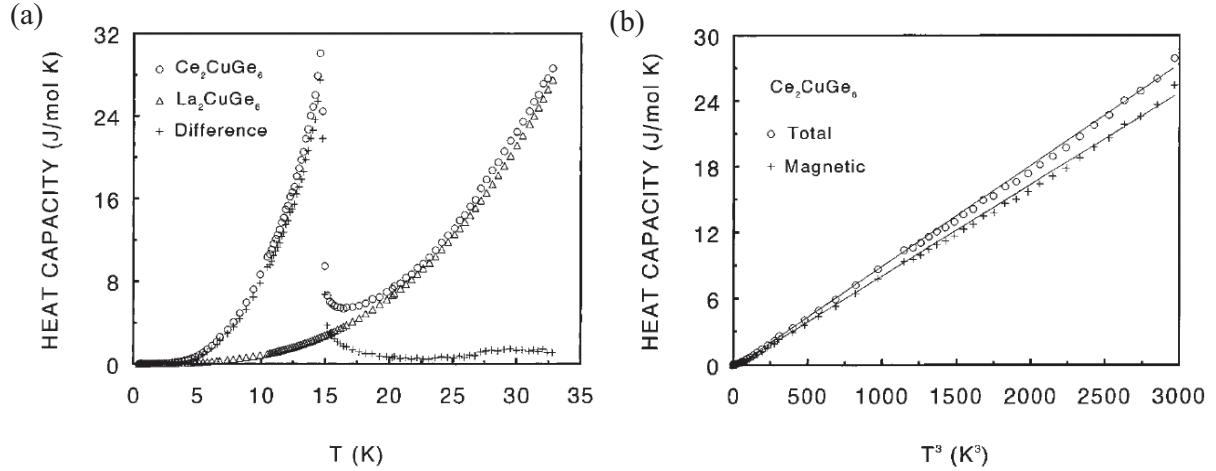
**Fig. 3.25** (a)Temperature dependence and (b)T^3-dependence of the heat capacity in polycrystalline Ce$_2$CuGe$_6$.[118]

4 Motivation of the Present Study

Heavy-fermion superconductivity is found to coexist with antiferromagnetism as well as ferromagnetism. Furthermore, it is widely recognized that pressure P is a useful tuning parameter to find superconductivity in magnetically ordered f-electron compounds [8,120]. With increasing pressure, the magnetic ordering temperature T_{mag} becomes zero at the critical pressure P_c in some compounds: $T_{mag} \rightarrow 0$ for $P \rightarrow P_c$. Namely, the antiferromagnetic state in the cerium compound, for example, is changed into the paramagnetic state at pressures higher than P_c. The heavy fermion state is formed around P_c as a result of the competition between the RKKY interaction and the Kondo effect. Heavy-fermion superconductivity is often observed in this pressure region.

Recently superconductivity in the non-centrosymmetric crystal structure has been reported in CePt$_3$Si[13,14] with the tetragonal structure ($P4mm$), UIr[15–17] with the monoclinic structure ($P2_1$), CeRhSi$_3$[18–20], CeIrSi$_3$[8,21,22] and CeCoGe$_3$[23] with the tetragonal BaNiSn$_3$-type structure ($I4mm$). The existence of inversion symmetry in the crystal structure is believed to be a favorable factor for the formation of Cooper pairs, especially for the spin-triplet configuration because in the non-centrosymmetric crystal structure, one conduction electron with a momentum $\boldsymbol{p}$ and an up-spin state and the other conduction electron with a momentum $-\boldsymbol{p}$ and an up-spin state belong to two different Fermi surfaces, separated by 10 - 1000 K in energy. Here, two Fermi surfaces are very similar to each other in topology but are different in the volume of the Fermi surface. This splitting of the Fermi surface occurs via the antisymmetric spin-orbit interaction $\alpha(\boldsymbol{p}\times\boldsymbol{n})\cdot\boldsymbol{\sigma}$, where α denotes the strength of the spin-orbit coupling, $\boldsymbol{n}$ is a unit vector taken to be the [001] direction (c-axis) in CePt$_3$Si, CeRhSi$_3$, CeIrSi$_3$ and CeCoGe$_3$, for example, and $\boldsymbol{\sigma}$ is the Pauli matrix[62,74]. Namely, the non-uniform lattice potential $V(\boldsymbol{r})$ in the tetragonal structure, such as in CePt$_3$Si, CeRhSi$_3$, CeIrSi$_3$ and CeCoGe$_3$, induces an electric field ($-\nabla V(\boldsymbol{r})$) along the [001] direction (c-axis). The effective magnetic field, which approximately corresponds to $\boldsymbol{p}\times\nabla V(\boldsymbol{r})$, namely $\alpha(\boldsymbol{p}\times\boldsymbol{n})$, is brought about for the conduction electron with the momentum $\boldsymbol{p}$ in this electric field. The antisymmetric spin-orbit interaction $\alpha(\boldsymbol{p}\times\boldsymbol{n})\cdot\boldsymbol{\sigma}$ is regarded as the Zeeman energy arising from the magnetic interaction between this effective magnetic field and the spin of the conduction electron under zero magnetic field. The energy band is thus split into two different bands.[62,69,121]

If inversion symmetry exists or the antisymmetric spin-orbit interaction is neglected, a pair of bands is degenerated, and then the pair of Fermi surfaces becomes the same. Under magnetic fields, these degenerated Fermi surfaces in the crystal with inversion symmetry split into two bands, depending on the up- and down-spin states, which means breaking of the time reversal symmetry. This is well known as Zeeman splitting. The split Fermi surfaces, however, correspond to the same dHvA frequency in the dHvA experiment, because the observed dHvA frequency corresponds to the extremal cross-sectional area S_F of the Fermi surface extrapolated to zero field, as shown in Fig. 4.1(a). If the inversion symmetry is absent, the pair of Fermi surfaces possesses two different Fermi surfaces and corresponds to two different dHvA signals, as shown in Fig. 4.1(b), which is similar to
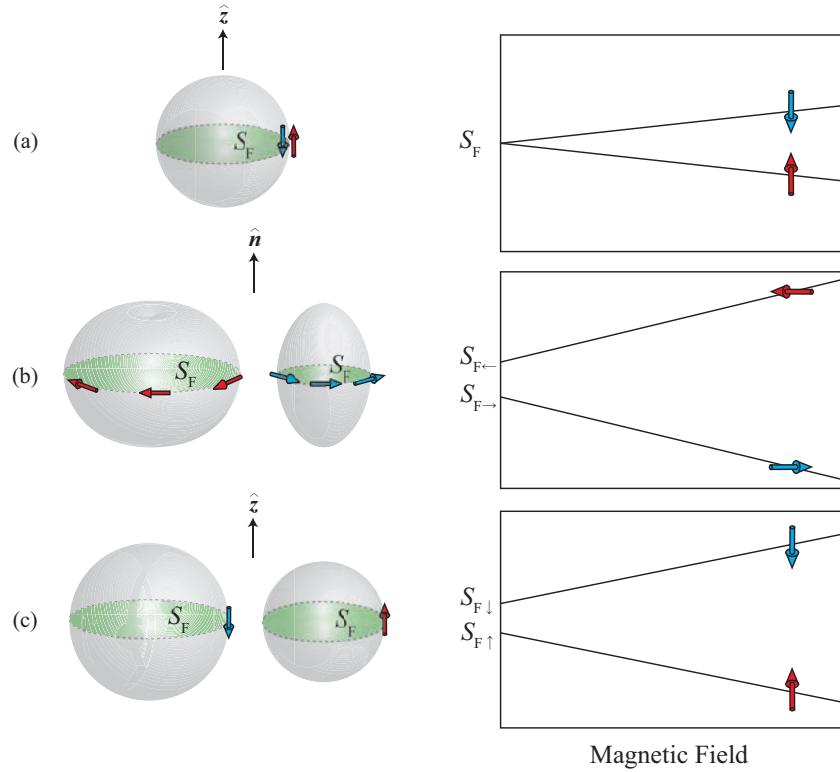
Fig. 4.1 Fermi surface and the corresponding field dependence of the dHvA frequency in (a) the usual degenerated non-magnetic metal, (b) the non-magnetic metal without inversion symmetry in the crystal structure, and (c) the $4f$-localized ferromagnet.

that in the $4f$-localized ferromagnet, as shown in Fig. 4.1(c).

There exist so many compounds without inversion symmetry in the crystal structure. It is, however, difficult to grow high-quality single crystals for detecting the de Haas-van Alphen (dHvA) signal. A few dHvA experiments were previously done for the non-centrosymmetric compounds. We briefly introduce the split Fermi surfaces based on the antisymmetric spin-orbit interaction. The first dHvA experiment was done for a valence fluctuation compound Yb_4Sb_3 with the anti-Th_3P_4 type crystal structure, as shown in Fig. 4.2(a).[122] Five nearly spherical Fermi surfaces were detected in the dHvA experiment, as shown in Fig. 4.2(b), with relatively large cyclotron masses ranging from 1.8 to $10.5m_0$.[122] The next dHvA experiment was also carried out for the similar compounds of ferromagnets U_3As_4 and U_3P_4, with $m_c^* = 7\text{-}70\,m_0$,[123] and a ferromagnet UIr mentioned above.[124] It is, however, not easy to estimate the antisymmetric spin-orbit interaction for these compounds.

A relation of crystal structures between LaPtAs and CePtAs is interesting. LaPtAs crystallizes in the LiGaGe-type hexagonal structure ($P6_3mc$) without inversion symmetry along the c-axis, while CePtAs crystallizes in the YPtAs-type hexagonal structure ($P6_3/mmc$) with inversion symmetry, as shown in Fig. 4.3. Namely, the crystal
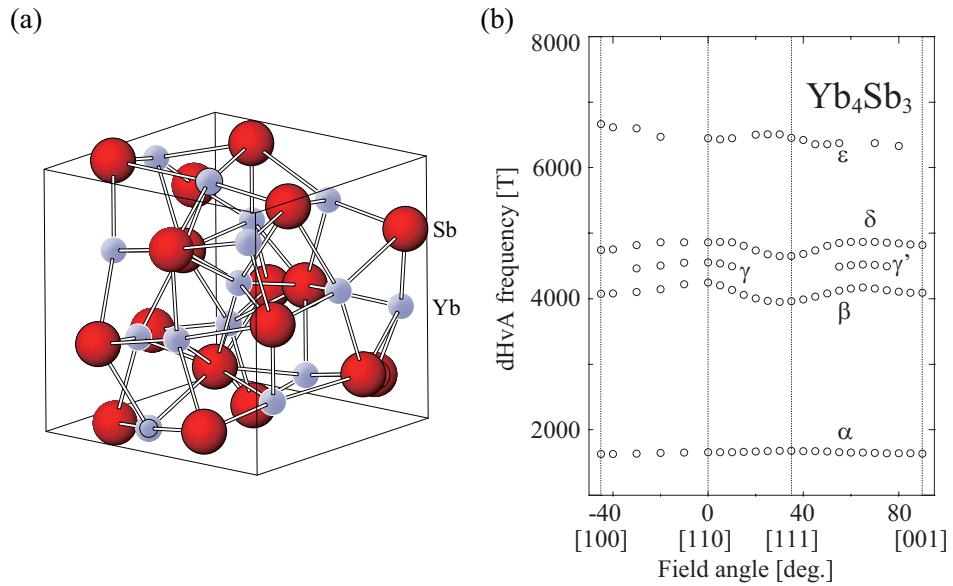
Fig. 4.2 (a) anti-Th_3P_4-type crystal structure and (b) the angular dependence of the dHvA frequency in Yb_4Sb_3.[122]
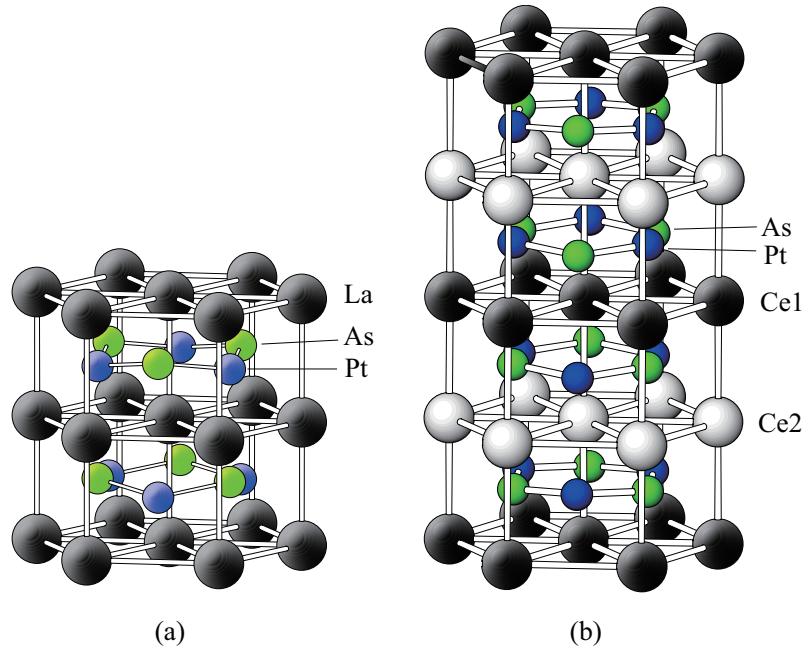

Fig. 4.3 Crystal structures in (a)LaPtAs and (b)CePtAs.

structure of CePtAs is the double hexagonal structure, where the LiGaGe-type hexagonal structure is symmetrically inverted along the c-axis. Unfortunately the dHvA experiment was not carried out for LaPtAs, although several cylindrical Fermi surfaces were obtained in the dHvA experiment for antiferromagnets CePtAs and CePtP.[125]

Furthermore, the dHvA experiments were also carried out for LaRhSi$_3$ and CeRhSi$_3$,[20] as mentioned in Chap. 3. The antisymmetric spin-orbit interaction was not determined experimentally. Recently, the Fermi surface properties of LaPt$_3$Si, CePt$_3$Si, LaCoGe$_3$, CeCoGe$_3$ and LaIrSi$_3$ were clarified from the dHvA experiments and energy band calculations.[22,75,106,126] The antisymmetric spin-orbit interaction was obtained to be $2|\alpha p_\perp| = 2400\,\mathrm{K}$ in LaPt$_3$Si[126] and $460\,\mathrm{K}$ in LaCoGe$_3$[106] and $1100\,\mathrm{K}$ in LaIrSi$_3$ for the main Fermi surface.[22]

In the present study, we have grown the single crystals LaFeGe$_3$, LaRhGe$_3$, LaIrGe$_3$ and PrCoGe$_3$ by the Bi-flux method, which have no inversion center in the crystal structure, and compared their characteristic features of split Fermi surfaces with the previous results of LaCoGe$_3$ and LaIrSi$_3$. It is our purpose to clarify a change of the Fermi surfaces and the magnitude of the antisymmetric spin-orbit interaction $2|\alpha\boldsymbol{p}_\perp|$ for a systematic change of the potentials when the transition metal T in LaTGe$_3$ is changed from T = Co, Rh to Ir and T = Fe to Co, and LaIrX$_3$ is changed from X = Si to Ge. It expected that the nuclear potential is highly different in T = Co, Rh and Ir and X = Si and Ge. Especially, the atomic number of Ir is large compared with those Co and Rh because the rare earth elements are inserted in the periodic table. A paramagnet PrCoGe$_3$ is also investigated to clarify the $2|\alpha\boldsymbol{p}_\perp|$ value when the cyclotron mass in PrCoGe$_3$ is nearly twice as large as that of LaCoGe$_3$. We considered that the present systematic study is important to consider superconductivity in the non-centrosymmetric crystal structure in the f-electron systems as well as the other compounds such as non-magnetic compounds Li$_2$Pt$_3$B and Li$_2$Pd$_3$B.

The purpose in the present study is also to clarify the superconducting property in the non-centrosymmetric crystal structure. Frigeri $et\,al.$ studied the possible existence of the spin-triplet pairing in the non-centrosymmetric compounds such as CePt$_3$Si with the tetragonal structure.[74,79] The favorable pairing state for the spin-triplet state is of the p-wave type: $\boldsymbol{d}(\boldsymbol{k}) = \Delta(k_y\boldsymbol{x} - k_x\boldsymbol{y})$, and the order parameter becomes a mixture of spin-singlet and spin-triplet components. The corresponding spin susceptibility becomes a non-zero residual susceptibility at $0\,\mathrm{K}$: the spin susceptibility for the magnetic field along the [001] direction, $\chi(H\,//\,[001])$ is unchanged below the superconducting transition temperature T_sc, revealing the spin-triplet superconductivity with $\boldsymbol{H} \perp \boldsymbol{d}$, and $\chi(H \perp [001])$ becomes $\chi(H\,//\,[001])/2$ at $0\,\mathrm{K}$, revealing an effect of the mixture of spin-singlet and spin-triplet components. The gap structure was given by considering a two-component order parameter with spin-singlet and spin-triplet components. Line nodes can appear on one of the two Fermi surfaces, while the other Fermi surface possesses a full gap. Many characteristic properties are experimentally observed in CePt$_3$Si,[13,14] UIr,[15,17] CeRhSi$_3$,[18–20] CeIrSi$_3$[21,22] and CeCoGe$_3$[23] in the f-electron systems.

Among them, an antiferromagnet CeIrSi$_3$ with the non-centrosymmetric tetragonal structure indicates the characteristic pressure-induced superconductivity,[21,22] as de-

scribed in Chap. 3. Superconductivity is observed in the wide pressure region from about 2 GPa to 4 GPa, and the critical pressure P_c, where the Néel temperature $T_N = 5$ K at ambient pressure becomes zero, is $P_c \simeq 2.25$ GPa. The maximum of the superconducting transition temperature T_{sc} is $T_{sc} \simeq 1.6$ K around 2.5 GPa. The upper critical field H_{c2} for the magnetic field $H \mathbin{/\mkern-5mu/} [110]$ is slightly suppressed by the paramagnetic effect with decreasing temperature and reaches $H_{c2}(0) = 95$ kOe at $P = 2.6$ GPa, indicating the spin-singlet character. On the other hand, no such paramagnetic suppression is realized for $H \mathbin{/\mkern-5mu/} [001]$ and indicates an upturn increase of H_{c2} with decreasing temperature. The upper critical field at 0 K is most likely $H_{c2}(0) = 350$ - 450 kOe in the recent experiment under high magnetic fields up to 280 kOe at $P = 2.6$ GPa. The present result H_{c2} for $H \mathbin{/\mkern-5mu/} [001]$ might become an experimental evidence for the spin-triplet superconductivity in the non-centrosymmetric crystal structure. The similar superconductivity is observed in CeRhSi$_3$.[18–20]

The present experimental efforts were mainly contributed to an observation of superconductivity in another CeTX$_3$. Ternary rare earth compounds CeTX$_3$(T: transition metal, X: Si, Ge) including CeRhSi$_3$, CeIrSi$_3$ and CeCoGe$_3$ mentioned above crystallize in the unique tetragonal BaNiSn$_3$-type crystal structure.[82–91] The electrical and magnetic properties of CeTX$_3$ were mainly studied by using polycrystal samples,[88, 94–99] except CeRhSi$_3$,[18–20, 100] CeIrSi$_3$[21, 22] and CeCoGe$_3$.[103, 106] We grew the other CeTX$_3$ single crystals to investigate the electrical and magnetic properties. In the present study, we clarified the electrical and magnetic properties of CeTX$_3$ single crystals and carried out the pressure experiments to find superconductivity by measuring the electrical resistivity under pressure.

We also investigated another non-centrosymmetric compounds of Ce$_2$PdGe$_6$ and Ce$_2$CuGe$_6$ without inversion symmetry in the crystal structure.

5 Experimental

5.1 Single crystal growth

Single crystals of LaFeGe$_3$, LaRhGe$_3$, LaIrGe$_3$, CePtSi$_3$, CeFeGe$_3$, CeCoGe$_3$, CeRhGe$_3$, CeIrGe$_3$, PrCoGe$_3$, Ce$_2$PdGe$_6$ and Ce$_2$CuGe$_6$ were grown by the flux method. Moreover, the single crystals of LaRuSi$_3$ and CeRuSi$_3$ were grown by the Czochralski method. The single crystal growth will be introduced in this chapter.

5.1.1 Flux method

The flux method is a kind of the single crystal growth method, which corresponds to a slow cooling process of the premelted components, taken in non-stoichiometric amounts. The advantages of this technique are shown below: [127, 128]

(1) Single crystals can be grown often well below their melting points, and this often produces single crystals with fewer defects and much less thermal strain.

(2) Flux metals offer a clean environment for growth, since the flux getters impurities which do not subsequently appear in the crystal.

(3) There are no stoichiometric problems caused, for instance, by oxidation or evaporation of one of the components. Single crystal stoichiometry "control" itself.

(4) This technique can be applied to the compounds with high evaporation pressure, since the crucible is sealed in the ampule and the flux prevents evaporation.

(5) No special technique is required during the crystal growth and it can be done with the simple and inexpensive equipment. This is a reason why the flux method is sometimes called "poor man's" technique. [127]

There are, to be sure, a number of disadvantages to the technique. The first and foremost is that it is no always an applicable method: an appropriate metal flux from which the desired compound will crystallize may not be found. In addition, difficulties are encountered with some flux choices, when the flux enters the crystal as an impurity. The excessive nucleation causes small crystals, which takes place either due to a too fast cooling rate, or supercooling of the melt by subsequent multiple nucleation and fast growth of large but imperfect crystals usually containing inclusions. The contamination from the crucible cannot be ignored, when reactions with materials occur at high temperatures. Finally, the ability to separate crystals from the flux at the end of growth needs special considerations.
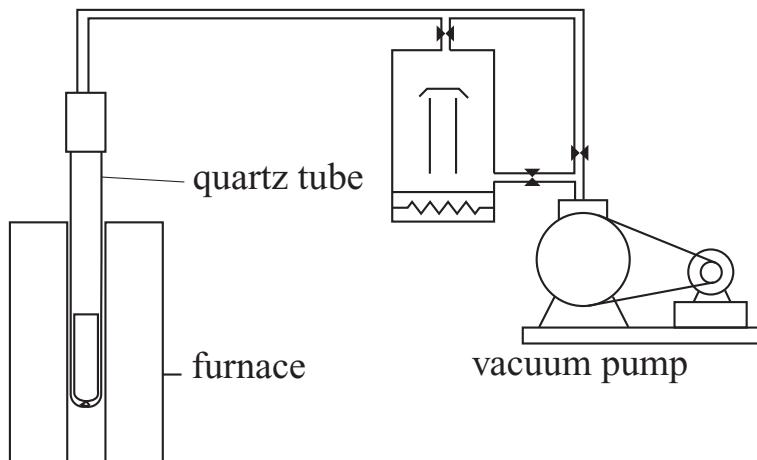
Fig. 5.1 Baking of an alumina crucible.

RTX$_3$(R: rare earth, T: transition metal, X: Si, Ge)

Single crystals of RTX$_3$ (R: rare earth, T: transition metal, X: Si or Ge) were grown by the flux method using Sn or Bi as a flux for RTSi$_3$ and RTGe$_3$, respectively. Here, we describe the growing process in CePtSi$_3$.

The high-quality alumina crucible (Al$_2$O$_3$: 99.9 %) was used as a container with outer diameter of 15.5 mm^3, inner diameter of 11.5 mm^3 and length of 60 mm^3. Since the crucible usually contains impurities, the crucible was cleaned in alcohol and baked it up to 1050 ℃ under high-vacuum (less than 1×10^{-6} torr), as shown in Fig. 5.1.

Polycrystalline ingots of CePtSi$_3$ was prepared by arc-melting stoichiometric quantities of high-pure metals of 4N(99.99 % pure)-Ce, 4N-Rh and 5N-Ge and smashed it into tiny pieces with a hammer. These polycrystalline samples, together with Sn-metal in the atomic ratio CePtSi$_3$: Bi = 1 : 20, were put into the alumina crucible and sealed in a quartz ampule with 160 mmHg pressure of Ar-gas, which is adjusted to reach at 1 atm at the highest temperature.

Next the sealed ampule was set in the electric furnace, as shown in Fig. 5.2. The furnace possesses the temperature gradient naturally. As we know from our own experience, the better results are obtained when we put the ampule where the temperature is more homogeneous. Therefore, we placed the ampule at the highest- and the flat-temperature gradient position. Nevertheless, the temperature gradient is useful for growing some compounds. There are some reports of growing crystals by temperature gradient method (ex. GdB$_6$). [127)]

The furnace is controlled by the PID temperature controller with Pt-PtRh13% (type-R) thermocouple. Figure 5.3 shows the block diagram of the furnace control system. In this system, we obtained the temperature stability less than 0.1 °C.

The growth process of CePtSi$_3$ is shown in Fig. 5.4. The crucible are heated up to 1050 °C which is the maximum temperature of the electric furnace. Then the temperature keeps for 24 hours. The temperature was decreased slowly. The cooling rate was gradually
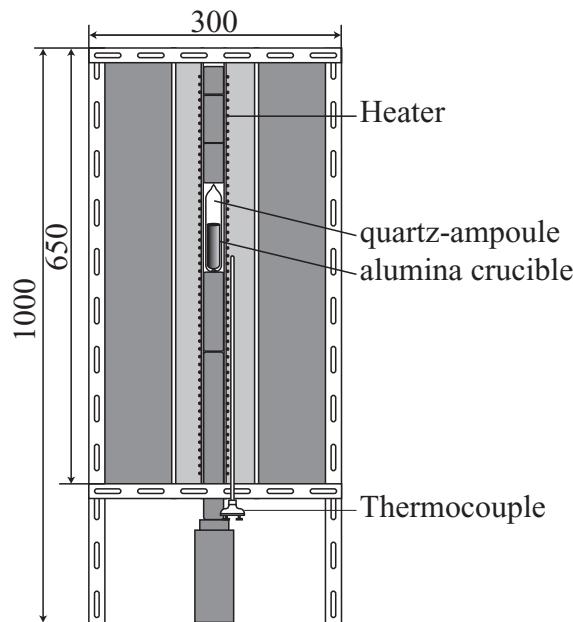
**Fig. 5.2** Illustration of the electric furnace.
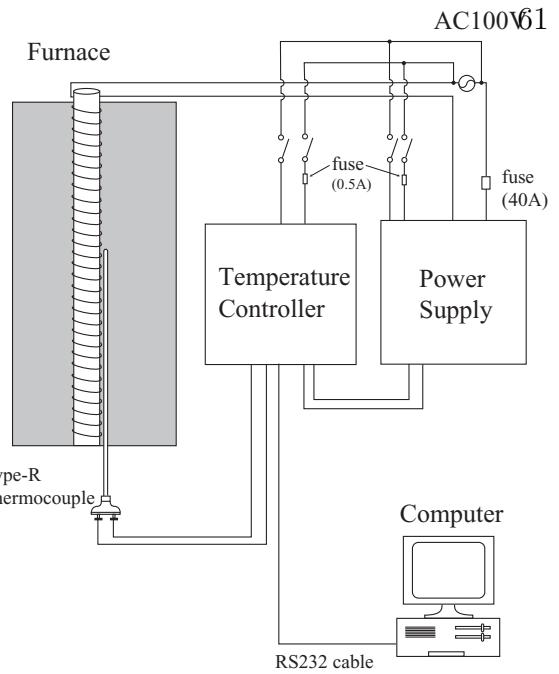
Fig. 5.3 Block diagram of the furnace control system.

increased with decreasing the temperature and the furnace was turned switch off at 650 °C.

After taking out the ampule from the furnace, the ampule was opened and sealed it again in a pyrex ampule under high vacuum, as shown in Fig. 5.5. The ampule was heated up to 320 ℃, which is sufficiently higher than the melting point of Sn-metal, in the muffle furnace. Next the ampule was taken out quickly from the furnace and was set into the centrifuge. Finally the flux was removed from the crystals by spinning the ampule in the centrifuge.

The photographs of these RTX_3(R: rare earth, T: transition metal, X: Si, Ge) single crystals are shown in Fig. 5.6(a) - 5.6(j). The orientation of the single crystal is denoted in Fig. 5.6(a), for example.

Here, we note that the single crystal for the dHvA experiment. As for the size of the single crystal sample, it is possible to detect the dHvA signal for $LaRhGe_3$ and $PrCoGe_3$, as shown in Figs. 5.6(g) and 5.6(j), respectively, but the filling factor of the dHvA pick-up coil system in the standard dHvA experiment becomes weak for small samples of $LaFeGe_3$ and $LaIrGe_3$, as shown in Figs. 5.6(f) and 5.6(i), respectively. We therefore carried out both the pick-up coil dHvA system and the cantilever type dHvA system for $LaIrGe_3$. For the cantilever type dHvA experiment, it is needed to prepare a very tiny sample with about $0.1 \times 0.1 \times 0.05 \, mm^3$, as shown in Fig. 5.6(i). In the case of $LaFeGe_3$, only the cantilever type dHvA experiment was carried out because an as-grown sample is extremely tiny.

Here, it was also noted how to avoid the Bi inclusion in the single crystal of $CeCoGe_3$. This is quite important to investigate the superconductivity in $CeCoGe_3$ because the superconductivity of Bi is also observed above $2 \, GPa$. In fact, the superconductivity
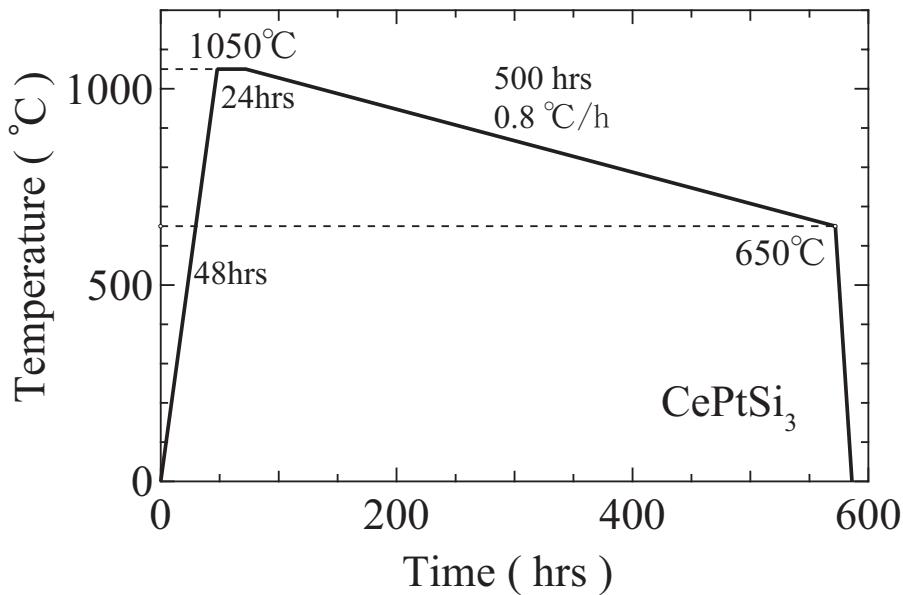
**Fig. 5.4** Time dependence of temperature during the growth process in CePtSi$_3$.
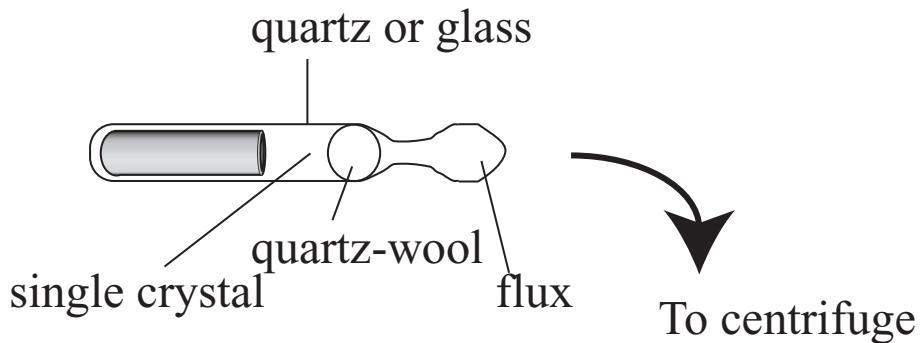
Fig. 5.5 Separation of flux and crystals by spinning the ampule in the centrifuge.

of Bi have been observed experimentally above $2\,\mathrm{GPa}$ in most of the samples grown by the Bi-flux method, including CeCoGe$_3$. In the present case, we polished first the single crystal sample of CeCeGe$_3$ carefully, with optical microscope. The color of Bi is different from that of the single crystal of CeCoGe$_3$. Then, we searched the Bi inclusion in a polished CeCoGe$_3$ sample by using a scanning electron microscope, as shown in Fig. 5.7. The electron beam was passed through the sample with thickness of $40\,\mu$m of CeCoGe$_3$, where the Bi inclusion in CeCoGe$_3$ was checked correctly within the resolution of the electron beam. The white color in Fig. 5.7 indicates the Bi inclusion in CeCoGe$_3$. Finally, a part of the CeCoGe$_3$ sample without Bi inclusion was used for the electrical resistivity measurement.

(a) CePtSi$_3$

(b) CeFeGe$_3$

(c) CeCoGe$_3$

(d) CeRhGe$_3$

(e) CeIrGe$_3$

(f) LaFeGe$_3$

(g) LaRhGe$_3$

(h) LaIrGe$_3$

(i) LaIrGe$_3$

(j) PrCoGe$_3$

(k) Ce$_2$PdGe$_6$

(l) Ce$_2$CuGe$_6$
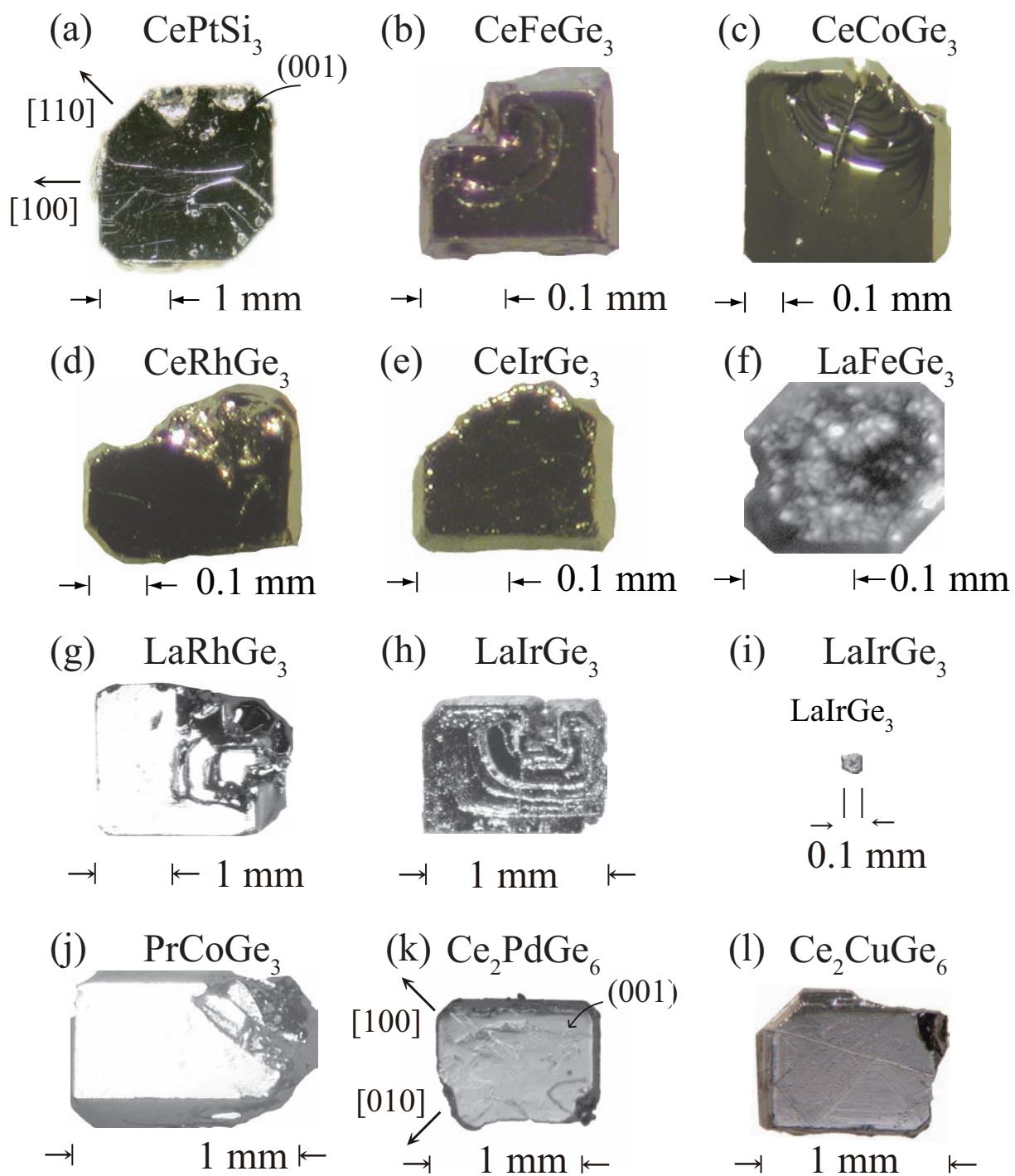
Fig. 5.6 Photographs of the single crystal of RTX$_3$.
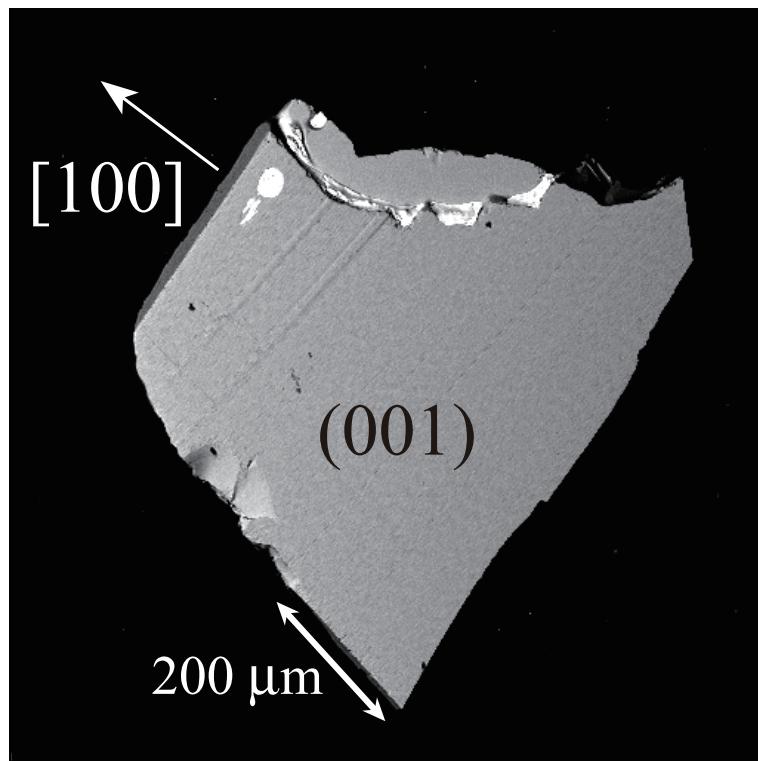
Fig. 5.7 Photograph of the single crystal sample of CeCoGe$_3$, obtained by using the scanning microscope.

Ce$_2$TGe$_6$(T: Pd, Cu)

Owing to the incongruent melting nature of Ce$_2$TGe$_6$(T: Pd, Cu), the growth from the direct melt was not possible. Therefore, we grew the single crystals of Ce$_2$PdGe$_6$ and Ce$_2$CuGe$_6$ by means of the flux method using Bi as flux. Here, we describe the growing process in Ce$_2$PdGe$_6$ At first an alloy button of Ce$_2$PdGe$_6$ was made by melting 3N-Ce, 4N-Pd and 5N-Ge metals in a tetra-arc furnace. The alloy button was remelted several times. The alloy button was then crushed into small pieces, and then these small pieces, together with 5N-Bi metal, were inserted in a high-quality alumina crucible, with the ratio 1:30 mol%. The alumina crucible was then sealed in a quartz ampule with a partial pressure of Ar gas. The temperature of the furnace was increased up to 1050 ℃ and kept at this temperature for 24 hours in order to achieve proper homogenization. Then the furnace was cooled down to 650 ℃ over a period of 4 weeks. The excess flux was separated by means of centrifuging. Relatively large single crystals with a typical size of $1.1 \times 0.9 \times 0.7$ mm^3 for Ce$_2$PdGe$_6$ and $0.9 \times 0.7 \times 0.2$mm^3 for Ce$_2$CuGe$_6$ were obtained, as shown in Fig. 5.6(k) and Fig. 5.6(l), respectively. The arrows in Fig. 5.6(k) indicate the sample orientation.

5.1.2 Czochralski method

The schematic view of the arc furnace is shown in Fig. 5.8. It has four tungsten torches to improve a stability of the temperature of the melted material and a Cu hearth, which corresponds to the crucible, is water-cooled one. Arc melting has been done under high-quality (6N) argon gas atmosphere. The melting procedure was repeated several times to ensure the sample homogeneity. This method is only applicable to the compounds with low-vapor pressure. When we pull up the crystal from a melt by using a seed, it is important to control the diameter of the crystal, a pulling speed and the power of torches. A typical necking diameter is about 1 mm, while a typical diameter of the ingot is 3-4 mm. The growth rate is 10-15 mm/h to avoid stacking faults in the sample. We usually keep this speed all over the time and do not rotate both the seed and hearth to avoid stacking faults in the sample.
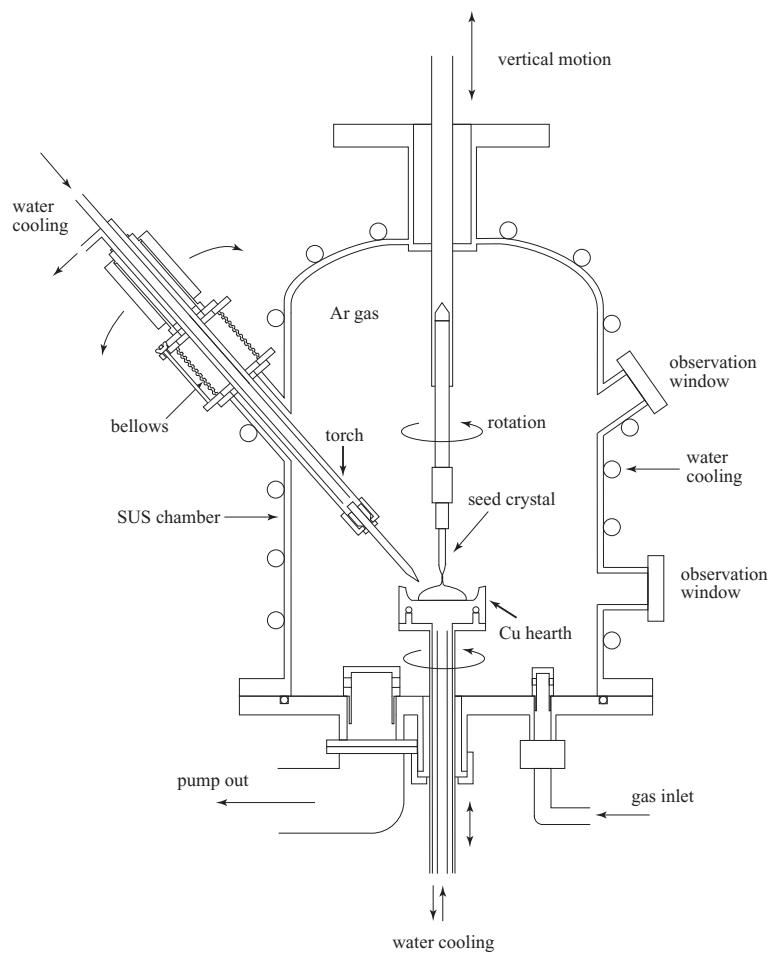
Fig. 5.8 Illustration of the tetra-arc furnace.

RRuSi$_3$(R: La, Ce)

Starting materials of RRuSi$_3$(R: La, Ce) were 3N-Ce, 4N-Ru and 5N-Si. Fortunately the isothermal cross-section of the ternary Ce-Ru-Si phase diagram at 600 ℃ was already studied by Yu. D. Seropegin *et al.*,[89] as shown in Fig. 5.9. According to this phase diagram, the atomic ratio between Ce(or La), Ru and Si was determined to be 1 : 1 : 3 - 3.5. First we used a polycrystal sample as a seed crystal in the Czochralski pulling method. Next we used the previous single crystal sample as the seed crystal. A pulling speed was 10-15mm/hour and the diameter is 2 - 3 mm. The photograph of a CeRuSi$_3$ ingot, together with a LaRuSi$_3$ ingot, is shown Fig. 5.10.

1. CeRuSi$_3$

2. CeRuSi$_2$

3. CeRu$_2$Si$_2$

4. CeRuSi

5. CeRu$_3$Si$_2$

6. Ce$_{25}$Ru$_{50}$Si$_{25}$

7. Ce$_{65}$Ru$_{10}$Si$_{25}$

8. Ce$_{33}$Ru$_{57}$Si$_{10}$
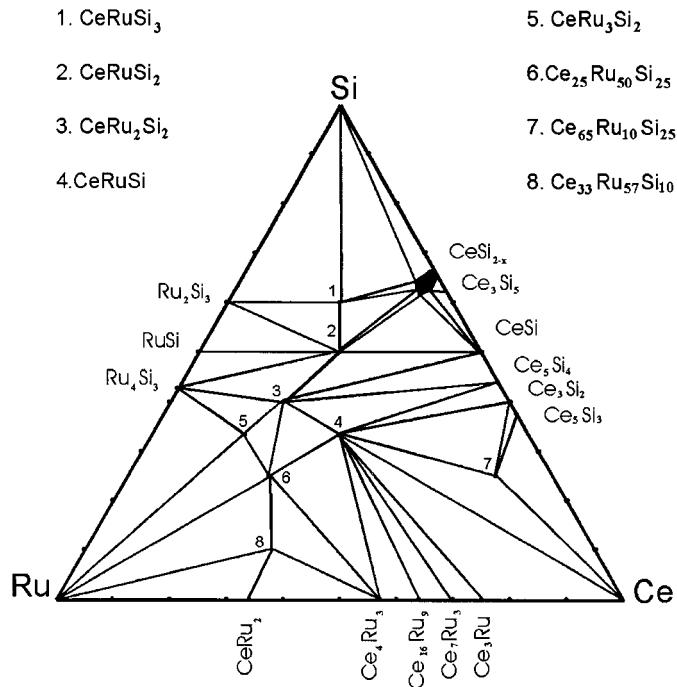
Fig. 5.9 Isothermal cross-section of the ternary Ce-Ru-Si phase diagram at 600 ℃.

(a) LaRuSi$_3$

(b) CeRuSi$_3$

10 mm
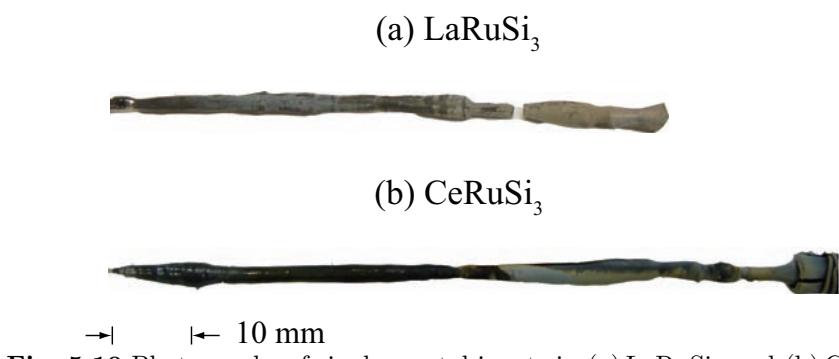
Fig. 5.10 Photographs of single crystal ingots in (a) LaRuSi$_3$ and (b) CeRuSi$_3$.

5.1.3 Crystal structural analyses

The single-crystal X-ray diffraction measurement was carried out by using a RIGAKU diffractometer with graphite monochromated Mo-Kα radiation(wave length, $\lambda = 0.71075$ Å) for LaRuSi$_3$, LaFeGe$_3$, LaRhGe$_3$, LaIrGe$_3$, CeRuSi$_3$, CePtSi$_3$, CeFeGe$_3$, CeRhGe$_3$, CeIrGe$_3$ and PrCoGe$_3$ because the single crystals of these compounds were grown for the first time. The lattice parameter, positional parameters and thermal parameters for these compounds were determined at room temperature, as shown in Table 5.I(a) - (j). The lattice parameters for RTX$_3$(R: rare earth, T: transition metal, X: Si, Ge) are approximately the same as the previous value,[82–91] although there is no information on the positional parameters of RTX$_3$(R: rare earth, T: transition metal, X: Si, Ge) except LaIrSi$_3$.[83]

Table 5.I Lattice parameters, atomic coordinates and thermal parameters of (a)LaRuSi$_3$, (b)LaFeGe$_3$, (c)LaRhGe$_3$, (d)LaIrGe$_3$, (e)CeRuSi$_3$, (f)CePtSi$_3$, (g)CeFeGe$_3$, (h)CeRhGe$_3$ (i)CeIrGe$_3$, (j)PrCoGe$_3$ where R and wR are the reliability factors, and B_{eq} is an isotropic atomic displacement parameter.

(a)LaRuSi$_3$

Space group	Lattice parameter	Atom(site)	Position			B_{eq}
T(K)	(Å)		x	y	z	
$I4mm$(#107)	$a = 4.2641(5)$	La(2a)	0.00000	0.00000	0.58120	0.590(14)
300 K	$c = 9.9526(10)$	Ru(2a)	0.00000	0.00000	0.23736	0.50(2)
		Si(2a)	0.00000	0.00000	0.00000	0.73(3)
		Si(4b)	0.00000	0.50000	0.34152	0.81(2)
			$R = 0.67\%$		$wR = 1.61\%$	

(b)LaFeGe$_3$

Space group	Lattice parameter	Atom(site)	Position			B_{eq}
$I4mm$(#107)	$a = 4.3684(4)$	La(2a)	0.00000	0.00000	0.56683	0.95(2)
300 K	$c = 9.9795(8)$	Fe(2a)	0.00000	0.00000	0.23040	0.87(5)
		Ge(2a)	0.00000	0.00000	0.00000	1.02(3)
		Ge(4b)	0.00000	0.50000	0.32327	1.05(2)
			$R = 3.46\%$		$wR = 3.80\%$	

(c)LaRhGe$_3$

Space group	Lattice parameter	Atom(site)	Position			B_{eq}
$I4mm$(#107)	$a = 4.42315(17)$	La(2a)	0.00000	0.00000	0.58057	0.51(5)
300 K	$c = 10.0541(4)$	Rh(2a)	0.00000	0.00000	0.23897	0.45(5)
		Ge(2a)	0.00000	0.00000	0.00000	0.60(7)
		Ge(4b)	0.00000	0.50000	0.34123	0.65(5)
			$R = 4.31\%$		$wR = 9.50\%$	

(d)LaIrGe$_3$

Space group	Lattice parameter	Atom(site)	Position			B_{eq}
$I4mm$(#107)	$a = 4.4343(3)$	La(2a)	0.00000	0.00000	0.58004	0.31(3)
300 K	$c = 10.0638(8)$	Ir(2a)	0.00000	0.00000	0.23840	0.14(2)
		Ge(2a)	0.00000	0.00000	0.00000	0.35(4)
		Ge(4b)	0.00000	0.50000	0.34230	0.33(3)
			$R = 2.29\%$		$wR = 5.45\%$	

(e)CeRuSi$_3$

Space group	Lattice parameter	Atom(site)	Position			B_{eq}
T(K)	(Å)		x	y	z	
$I4mm$(#107)	$a = 4.21577(16)$	Ce(2a)	0.00000	0.00000	0.57740	0.53(2)
300 K	$c = 9.9271(4)$	Ru(2a)	0.00000	0.00000	0.23526	0.46(3)
		Si(2a)	0.00000	0.00000	0.00000	0.63(6)
		Si(4b)	0.00000	0.50000	0.34120	0.73(4)
			$R = 2.55\%$		$wR = 5.85\%$	

(f)CePtSi$_3$

Space group	Lattice parameter	Atom(site)	Position			B_{eq}
$I4mm$(#107)	$a = 4.3215(3)$	Ce(2a)	0.00000	0.00000	0.60213	0.12
300 K	$c = 9.6075(8)$	Pt(2a)	0.00000	0.00000	0.25122	0.10(5)
		Si(2a)	0.00000	0.00000	0.00000	0.25(18)
		Si(4b)	0.00000	0.50000	0.36341	0.16(13)
			$R = 4.47\%$		$wR = 8.48\%$	

(g)CeFeGe$_3$

Space group	Lattice parameter	Atom(site)	Position			B_{eq}
$I4mm$(#107)	$a = 4.3371(3)$	Ce(2a)	0.00000	0.00000	0.56517	0.66(2)
300 K	$c = 9.9542(5)$	Fe(2a)	0.00000	0.00000	0.22940	0.11(3)
		Ge(2a)	0.00000	0.00000	0.00000	0.79(3)
		Ge(4b)	0.00000	0.50000	0.32302	0.83(2)
			$R = 2.18\%$		$wR = 5.01\%$	

(h)CeRhGe$_3$

Space group	Lattice parameter	Atom(site)	Position			B_{eq}
$I4mm$(#107)	$a = 4.3976(3)$	Ce(2a)	0.00000	0.00000	0.57960	0.75(6)
300 K	$c = 10.0322(7)$	Rh(2a)	0.00000	0.00000	0.23840	0.54(7)
		Ge(2a)	0.00000	0.00000	0.00000	0.80(8)
		Ge(4b)	0.00000	0.50000	0.34160	0.78(7)
			$R = 4.80\%$		$wR = 11.54\%$	

(i)CeIrGe$_3$

Space group	Lattice parameter	Atom(site)	Position			B_{eq}
$I4mm$(#107)	$a = 4.401(9)$	Ce(2a)	0.00000	0.00000	0.58008	0.44(5)
300 K	$c = 10.024(17)$	Ir(2a)	0.00000	0.00000	0.23919	0.32(3)
		Ge(2a)	0.00000	0.00000	0.00000	0.55(8)
		Ge(4b)	0.00000	0.50000	0.34320	0.51(6)
			$R = 2.99\%$		$wR = 6.36\%$	

(j)PrCoGe$_3$

Space group	Lattice parameter	Atom(site)	Position			B_{eq}
$I4mm$(#107)	$a = 4.3085(2)$	Pr(2a)	0.00000	0.00000	0.56826	0.614(19)
300 K	$c = 9.8290(6)$	Co(2a)	0.00000	0.00000	0.23252	0.45(3)
		Ge(2a)	0.00000	0.00000	0.00000	0.58(2)
		Ge(4b)	0.00000	0.50000	0.32729	0.64(2)
			$R = 2.02\%$		$wR = 2.81\%$	

5.2 Experimental methods

5.2.1 Electrical resistivity

Introduction to the electrical resistivity

An electrical resistivity consists of four contributions: the electron scattering due to impurities or defects ρ_0, the electron-phonon scattering ρ_{ph}, the electron-electron scattering $\rho_{\mathrm{e\text{-}e}}$ and the electron-magnon scattering ρ_{mag}:

$$\rho = \rho_0 + \rho_{\mathrm{ph}} + \rho_{\mathrm{e\text{-}e}} + \rho_{\mathrm{mag}}. \tag{5.1}$$

This relation is called a Matthiessen's rule.

The ρ_0-value, which originates from the electron scattering due to impurities and defects, is constant for a variation of the temperature. This value is important to know the quality of an obtained sample. If ρ_0 is large, the sample contains many impurities or defects. A quality of a sample can be estimated by determining a so-called residual resistivity ratio (RRR $= \rho_{\mathrm{RT}}/\rho_0$), where ρ_{RT} is the resistivity at room temperature. Of course, a large value of RRR indicates that the quality of the sample is good.

Let us introduce a scattering lifetime τ_0 and a mean free path l_0 from the resistivity. The residual resistivity ρ_0 can be written as

$$\rho_0 = \frac{m^*}{ne} \cdot \frac{1}{\tau_0}, \tag{5.2}$$

where n is a density of carrier and e is an electric charge. Then τ_0 and l_0 values are

$$\tau_0 = \frac{m^*}{ne\rho_0}, \tag{5.3}$$

$$l_0 = v_{\mathrm{F}}\tau_0 = \frac{\hbar k_{\mathrm{F}}}{ne\rho_0}. \tag{5.4}$$

The temperature dependence of ρ_{ph}, which originates from the electron scattering by phonon, changes monotonously. ρ_{ph} is proportional to T above the Debye temperature, while it is proportional to T^5 far below the Debye temperature, and ρ_{ph} will be zero at $T = 0$.

In the strongly correlated electron system, the contribution of $\rho_{\mathrm{e\text{-}e}}$, which can be expressed in terms of the reduction factor of the quasiparticle and the Umklapp process, is dominant at low temperatures. Therefore, we can regard the total resistivity in non-magnetic compounds at low temperatures as follows:

$$\rho(T) = \rho_0 + \rho_{\mathrm{e\text{-}e}}(T), \tag{5.5}$$

$$= \rho_0 + AT^2, \tag{5.6}$$

where the coefficient $\sqrt{A}$ is proportional to the effective mass. Yamada and Yosida obtained the rigorous expression of $\rho_{\mathrm{e\text{-}e}}$ in the strongly correlated electron system on the

basis of the Fermi liquid theory. [33)] According to their theory, $\rho_{\text{e-e}}$ is proportional to the imaginary part of the f electron self-energy $\Delta \boldsymbol{k}$, and $\Delta \boldsymbol{k}$ is written as

$$
\begin{aligned}
\rho_{\text{e-e}} \propto \Delta \boldsymbol{k} \;\simeq\; & \frac{4}{3}(\pi T)^2 \sum_{\boldsymbol{k}',\boldsymbol{q}} \pi D^f_{\boldsymbol{k}-\boldsymbol{q}}(0)\, D^f_{\boldsymbol{k}'}(0)\, D^f_{\boldsymbol{k}'+\boldsymbol{q}}(0) \\
& \times \left\{ \Gamma_{\uparrow\downarrow}{}^2(\boldsymbol{k},\boldsymbol{k}';\boldsymbol{k}'+\boldsymbol{q},\boldsymbol{k}-\boldsymbol{q}) + \frac{1}{2}\Gamma_{\uparrow\uparrow}{}^{A2}(\boldsymbol{k},\boldsymbol{k}';\boldsymbol{k}'+\boldsymbol{q},\boldsymbol{k}-\boldsymbol{q}) \right\},
\end{aligned} \tag{5.7}
$$

where $\Gamma_{\sigma\sigma}$ is the four-point vertex, which means the renormalized scattering interaction process of $\boldsymbol{k}(\sigma)\boldsymbol{k}'(\sigma) \rightarrow \boldsymbol{k}'+\boldsymbol{q}(\sigma)\boldsymbol{k}-\boldsymbol{q}(\sigma)$, $\Gamma^A_{\uparrow\uparrow}$ is denoted as $\Gamma_{\uparrow\uparrow}(\boldsymbol{k}_1,\boldsymbol{k}_2;\boldsymbol{k}_3,\boldsymbol{k}_4) - \Gamma_{\uparrow\uparrow}(\boldsymbol{k}_1,\boldsymbol{k}_2;\boldsymbol{k}_4,\boldsymbol{k}_3)$, and $D^f_{\boldsymbol{k}}(0)$ is the true (perturbed) density of states of f electrons with mutual interaction in the Fermi level. This $\Delta \boldsymbol{k}$ is proportional to the square of the enhancement factor and gives a large T^2-resistivity to the heavy Fermion system.

In a magnetic compound, an additional contribution to the resistivity must be taken into consideration, namely ρ_{mag}. This contribution describes scattering processes of conduction electrons due to disorder in the arrangement of the magnetic moments. In general, above the ordering temperature T_{ord}, ρ_{mag} is given by

$$
\rho_{\text{mag}} = \frac{3\pi N m^*}{2\hbar e^2 \varepsilon_{\text{F}}} |J_{\text{ex}}|^2 (g_{\text{J}}-1)^2 J(J+1), \tag{5.8}
$$

where J_{ex} is the exchange integral for the direct interaction between the local moments and conduction electrons. When $T = T_{\text{ord}}$, ρ_{mag} shows a pronounced kink, and when $T < T_{\text{ord}}$, ρ_{mag} strongly decreases with decreasing temperature. The magnetic resistivities in the actinides, however, are ascribed to strong scattering of the conduction electrons by the spin fluctuations of $5f$ electrons. This contribution to the resistivity at low temperatures is given by the square of the temperature, namely $\rho_{\text{mag}} = A'T^2$. In the heavy Fermion system, the coefficient A' is extremely large. Therefore, ρ_{mag} and $\rho_{\text{e-e}}$ are inseparable and ρ_{mag} can be considered to change to $\rho_{\text{e-e}}$. An analogous situation occurs to the specific heat. Namely, in the heavy Fermion system, the magnetic specific heat C_{mag} is changed into a large electronic specific heat C_{e}.

Experimental method of the resistivity measurement

We have done the resistivity measurement using a standard four-probe DC current method. The sample was fixed on a plastic plate by an instant glue. The gold wire with $0.025\,\text{mm}$ in diameter and silver paste were used to form contacts on the sample. The sample was mounted on a sample-holder and installed in a ^4He or ^3He cryostat. We measured the resistivity from 1.3 or $0.5\,\text{K}$ to the room temperature. The thermometers are a Cernox resistor for all temperature region or a combination between a RuO_2 resistor at lower temperatures (below $20\,\text{K}$) and a Diode resistor at higher temperatures.

5.2.2 Specific heat

Introduction to the specific heat

At low temperatures, the specific heat is written as the sum of electronic, lattice, magnetic and nuclear contributions:

$$C = C_{\mathrm{e}} + C_{\mathrm{ph}} + C_{\mathrm{mag}} + C_{\mathrm{nuc}} \tag{5.9}$$

$$= \gamma T + \beta T^3 + C_{\mathrm{mag}} + \frac{A}{T^2}, \tag{5.10}$$

where A, γ and β are constants with the characteristic of the material.

The electronic term is linear in T and is dominant at sufficiently low temperatures. If we can neglect the magnetic and nuclear contributions, it is convenient to exhibit the experimental values of C as a plot of C/T versus T^2:

$$\frac{C}{T} = \gamma + \beta T^2. \tag{5.11}$$

Then we can estimate the electronic specific heat coefficient γ. Using the density of states $D(\varepsilon_{\mathrm{F}})$, the coefficient γ can be expressed as

$$\gamma = \frac{\pi^2}{3} k_{\mathrm{B}}{}^2 D(\varepsilon_{\mathrm{F}}), \tag{5.12}$$

where k_B is the Boltzmann constant. Since the density of states based on the free electron model is proportional to the electron mass, the coefficient γ possesses an extremely large value in the heavy Fermion system.

According to the Debye T^3 law, for $T \ll \Theta_{\mathrm{D}}$:

$$C_{\mathrm{ph}} \simeq \frac{12\pi^4 N k_{\mathrm{B}}}{5} \left(\frac{T}{\Theta_{\mathrm{D}}} \right)^3 \equiv \beta T^3, \tag{5.13}$$

where Θ_{D} is the Debye temperature and N is the number of atoms. For the actual lattices the temperatures at which the T^3 approximation holds are quite low. It may be necessary to be below $T = \Theta_{\mathrm{D}}/50$ to get a reasonably pure T^3 law.

If the f energy level splits due to the crystalline electric field (CEF) in the paramagnetic state, the inner energy per one magnetic ion is given by

$$E_{\mathrm{CEF}} = \langle E_i \rangle = \frac{\sum\limits_i n_i E_i \exp(-E_i/k_{\mathrm{B}}T)}{\sum\limits_i \exp(-E_i/k_{\mathrm{B}}T)}. \tag{5.14}$$

where E_i and n_i are the energy and the degenerate degree on the level i. Thus the magnetic contribution to the specific heat is given by

$$C_{\mathrm{Sch}} = \frac{\partial E_{\mathrm{CEF}}}{\partial T}. \tag{5.15}$$

This contribution C_{Sch} is called a Schottky term. Here, the entropy of the f electron S is defined as

$$S = \int_0^T \frac{C_{\mathrm{Sch}}}{T} \, \mathrm{d}T. \tag{5.16}$$

The entropy is also described as

$$S = R \ln W, \tag{5.17}$$

where W is a state number at temperature T. Therefore we acquire information about the CEF level.

In the magnetic ordering state C_{mag} is:

$$C_{\mathrm{mag}} \propto T^{3/2} \qquad \text{(ferromagnetic ordering)} \tag{5.18}$$

$$\propto T^3 \qquad \text{(antiferromagnetic ordering)}. \tag{5.19}$$

When the antiferromagnetic magnon is accompanied with the energy gap Δ_{m}, eq. (5.19) is modified to $C_{\mathrm{mag}} \propto T^3 \exp(-\Delta_{\mathrm{m}}/k_{\mathrm{B}}T)$.

Experimental method of the specific heat

The specific heat was measured by the quasi-adiabatic heat pulse method using dilution refrigerator, ^{3}He and ^{4}He cryostat at temperatures down to 0.1, 0.6 and 1.7 K, respectively. The sample was put on the Cu-addenda. And the RuO_2 resister thermometer and two strain gage heaters were also put on the addenda. On of the strain gage heater generated constant heater to compensate heat leak via to the heat radiation and/or the thermal conduction by the wire which suspended the addenda.

We gave heat pulse to the sample and addenda due to the another heater. Then we measured the change of the temperature at addenda. The specific heat is deduced as follows:

$$C = \frac{\Delta Q}{\Delta T} = \frac{I \cdot V \cdot \Delta t}{\Delta T}. \tag{5.20}$$

Here, ΔQ is the amount of heat, I and V are the current and the voltage flowing to the heater, respectively, Δt is the duration of heating and ΔT is the change of temperature due to heating. Here, this C includes both of the specific heat of the sample and that of the addenda. The specific heat of the sample is thus derived by subtracting the specific heat of the addenda.

The heat capacity was also measured by the relaxation method on a commercial Physical Property Measurement System (PPMS), produced by Quantum Design. This was applicable to measure the specific heat in the temperature of 2-300 K and the magnetic field of 0-90 kOe.

5.2.3 Magnetic susceptibility

Introduction to the magnetic susceptibility

At high temperatures, the $4f$ electron in most of the Ce compounds is localized. The crystalline electric field (CEF) theory is thus well applicable to the magnetic property of the Ce compounds. By using the CEF theory, the $4f$ energy level in the Ce compounds with the non-cubic crystal structure splits into three doublets. Hamiltonian of this system is given by

$$H = H_{\mathrm{CEF}} + H_{\mathrm{Zeeman}}. \tag{5.21}$$

Here, H_{CEF} is expressed as

$$H_{\mathrm{CEF}} = B_2^0 O_2^0 + B_4^0 O_4^0 + B_4^4 O_4^4, \tag{5.22}$$

in the tetragonal symmetry and

$$H_{\mathrm{CEF}} = B_2^0 O_2^0 + B_2^2 O_2^2 + B_4^0 O_4^0 + B_4^2 O_4^2 + B_4^4 O_4^4, \tag{5.23}$$

in the orthorhombic symmetry, where B_l^m and O_l^m are the CEF parameters and the Stevens operators, respectively.[29,30] Due to the CEF effect, the sixfold degenerate $4f$-levels of the Ce ion are split into three doublets.

The CEF susceptibility is given by

$$\chi_{\mathrm{CEF}}^i = N(g_J \mu_{\mathrm{B}})^2 \frac{1}{Z} \left(\sum_{m \neq n} |\langle m | J_i | n \rangle|^2 \frac{1 - e^{-\frac{\Delta_{m,n}}{k_{\mathrm{B}} T}}}{\Delta_{m,n}} e^{-\frac{E_n}{k_{\mathrm{B}} T}} + \frac{1}{k_{\mathrm{B}} T} \sum_n |\langle n | J_i | n \rangle|^2 e^{-\frac{E_n}{k_{\mathrm{B}} T}} \right) \tag{5.24}$$

and

$$Z = \sum_n e^{-\frac{E_n}{k_{\mathrm{B}} T}}, \tag{5.25}$$

where g_J is the Landé g-factor (6/7 for Ce^{3+}), J_i is the component of the angular momentum and $\Delta_{m,n} = E_n - E_m$. The magnetization can be also calculated by

$$M_i = g_J \mu_{\mathrm{B}} \sum_n |\langle n | J_i | n \rangle| \frac{e^{-\frac{E_n}{k_{\mathrm{B}} T}}}{Z}. \tag{5.26}$$

Thus, the CEF susceptibility is also given by

$$\chi_{\mathrm{CEF}} = \lim_{H \to 0} \frac{dM}{dH}. \tag{5.27}$$

The magnetic susceptibility including the molecular field contribution λ_i is given as follows:

$$\chi_i^{-1} = (\chi_{\mathrm{CEF}}^i)^{-1} - \lambda_i. \tag{5.28}$$

The eigenvalue E_n and eigenfunction $|n\rangle$ are determined by diagonalizing the total Hamiltonian

$$H = H_{\mathrm{CEF}} - g_J\mu_{\mathrm{B}}J_i(H_i + \lambda_i M_i), \tag{5.29}$$

where the second term is the Zeeman term and the third one is a contribution from the molecular field. The magnetic susceptibility was measured by a commercial SQUID magnet meter, produced by Quantum Design.

5.2.4   de Haas-van Alphen effect

Introduction to the de Haas-van Alphen effect

Under a high magnetic field, the orbital motion of the conduction electron is quantized and forms Landau levels[7]. Therefore various physical qualities shows a periodic variation with H^{-1} since increasing the field strength H causes a sharp change in the free energy of the electron system when Landaus level crosses the Fermi energy. In a three-dimensional system this sharp structure is observed at extremal areas in $\boldsymbol{k}$-space, perpendicular to the field direction and enclosed by the Fermi energy because the density of state also becomes extremal. From the field and temperature dependence of various physical quantities, we can obtain the extremal area S, the cyclotron mass m_{c}^{*} and the scattering lifetime τ for this cyclotron orbit. The magnetization or the magnetic susceptibility is the most common one of these physical quantities, and its periodic character is called the de Haas-van Alphen (dHvA) effect. It provides one of the best tools for the investigation of Fermi surfaces of metals.

The theoretical expression for the oscillatory component of magnetization M_{osc} due to the conduction electrons was given by Lifshitz and Kosevich as follows:[129]

$$M_{\mathrm{osc}} = \sum_{r}\sum_{i}\frac{(-1)^{r}}{r^{3/2}}A_{i}\sin\left(\frac{2\pi r F_{i}}{H}+\beta_{i}\right), \tag{5.30a}$$

$$A_{i} \propto FH^{1/2}\left|\frac{\partial^{2}S_{i}}{\partial k_{\mathrm{H}}^{2}}\right|^{-1/2}R_{\mathrm{T}}R_{\mathrm{D}}R_{\mathrm{S}}, \tag{5.30b}$$

$$R_{\mathrm{T}} = \frac{\alpha r m_{\mathrm{c}i}^{*}T/H}{\sinh(\alpha r m_{\mathrm{c}i}^{*}T/H)}, \tag{5.30c}$$

$$R_{\mathrm{D}} = \exp(-\alpha r m_{\mathrm{c}i}^{*}T_{\mathrm{D}}/H), \tag{5.30d}$$

$$R_{\mathrm{S}} = \cos(\pi g_{i}r m_{\mathrm{c}i}^{*}/2m_{0}), \tag{5.30e}$$

$$\alpha = \frac{2\pi^{2}k_{\mathrm{B}}}{e\hbar}. \tag{5.30f}$$

Here the magnetization is periodic on $1/H$ and has a dHvA frequency F_{i}

$$\begin{aligned}F_{i} &= \frac{\hbar}{2\pi e}S_{i}\\ &= 1.05\times 10^{-12}\,[\mathrm{T}\cdot\mathrm{cm}^{2}]\cdot S_{i},\end{aligned} \tag{5.31}$$

which is directly proportional to the i-th extremal (maximum or minimum) cross-sectional area S_{i} $(i = 1,\ldots,n)$. The extremal area means a gray plane in Figure 5.11, where there is one extremal area in a spherical Fermi surface. The factor R_{T} in the amplitude A_{i} is related to the thermal damping at a finite temperature T. The factor R_{D} is also related to the Landau level broadening $k_{\mathrm{B}}T_{\mathrm{D}}$. Here T_{D} is due to both the lifetime broadening and inhomogeneous broadening caused by impurities, crystalline imperfections or strains.
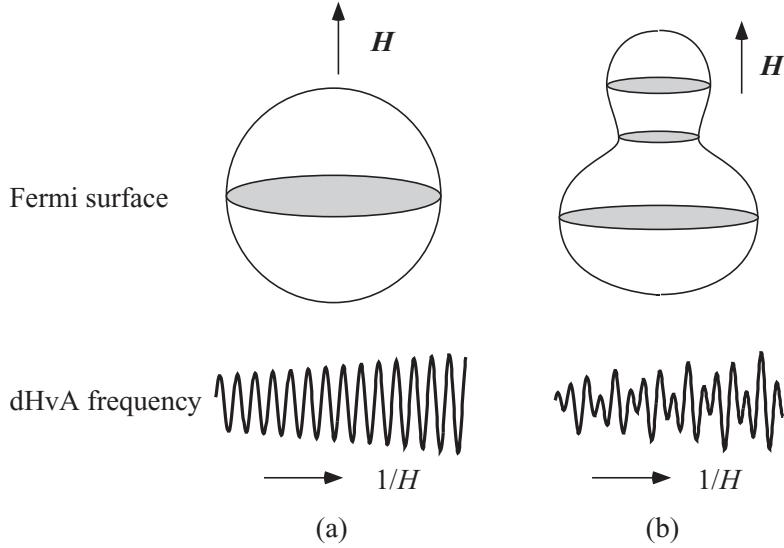
Fig. 5.11 Simulations of the cross-sectional area and its dHvA signal for a simple Fermi
surface. There is one dHvA frequency in (a), while there are three different
frequencies in (b).

The factor T_D is called the Dingle temperature and is given by

$$
\begin{aligned}
T_D &= \frac{\hbar}{2\pi k_B} \tau^{-1} \\
&= 1.22 \times 10^{-12} \, [\text{K} \cdot \text{sec}] \cdot \tau^{-1}.
\end{aligned}
\tag{5.32}
$$

The factor R_S is called the spin factor and related to the difference of phase between the
Landau levels due to the Zeeman split. When $g_i = 2$ (a free electron value) and $m_c^* = 0.5m_0$, this term becomes zero for $r = 1$. The fundamental oscillation vanishes for all
values of the field. This is called the zero spin splitting situation in which the up and down
spin contributions to the oscillation cancelled out, and this can be useful for determining
the value of g_i. Note that in this second harmonics for $r = 2$ the dHvA oscillation should
show full amplitude. The quantity $|\partial^2 S/\partial k_H{}^2|^{-1/2}$ is called the curvature factor. The
rapid change of cross-sectional area around the extremal area along the field direction
diminishes the dHvA amplitude for this extremal area.

The detectable conditions of dHvA effect are as follows:

1) The distance between the Landau levels $\hbar\omega_c$ must be larger than the thermal broad-
   ening width $k_B T$: $\hbar\omega_c \ll k_B T$ (high fields, low temperatures).

2) At least one cyclotron motion must be performed during the scattering, namely
   $\omega_c \tau/2\pi > 1$ (high quality samples). In reality, however, it can be observed even if
   a cyclotron motion is about ten percent of one cycle.

3) The fluctuation of the static magnetic field must be smaller than the field interval
   of one cycle of the dHvA oscillation (homogeneity of the magnetic field).

Shape of the Fermi surface

The angular dependence of dHvA frequencies gives very important information about a shape of the Fermi surface. As a value of Fermi surface corresponds to a carrier number, we can obtain the carrier number of a metal directly.
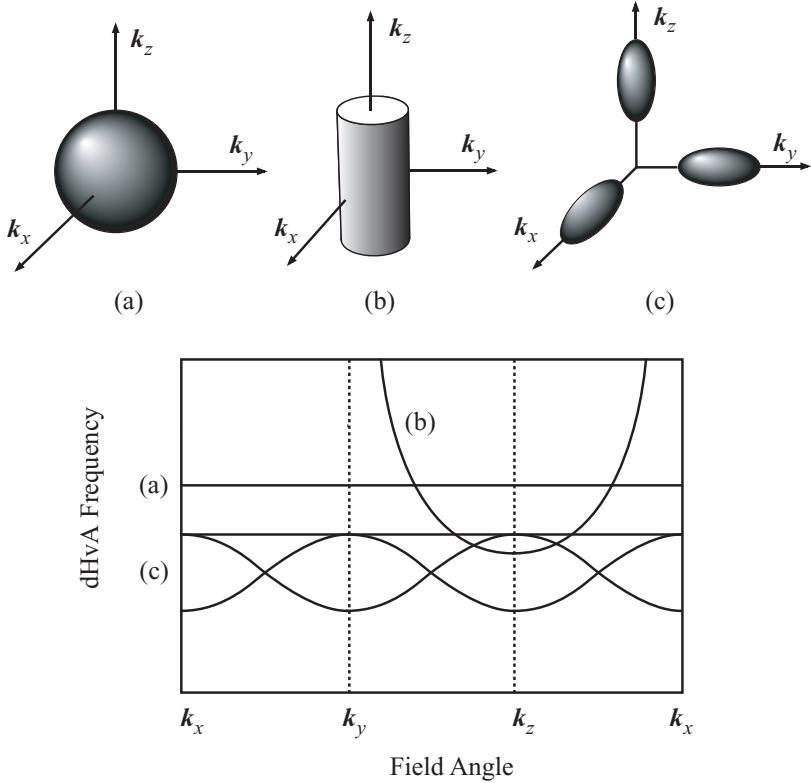
Fig. 5.12 Angular dependence of the dHvA frequency in three typical Fermi surfaces (a) sphere, (b) cylinder and (c) ellipsoid.

We show the typical Fermi surfaces and their angular dependences of dHvA frequencies in Figure 5.12. In a spherical Fermi surface, the dHvA frequency is constant for any field direction. On the other hand, in an ellipsoidal Fermi surface such as in Figure 5.12(b), it takes a minimum value for the field along the z-axis. These relatively simple shape Fermi surfaces can be determined only by the experiment. However, information from an energy band calculation is needed to determine a complicated one.

Cyclotron effective mass

We can determine the cyclotron effective mass m_{ci}^* from the measuring a temperature dependence of a dHvA amplitude. Equation (5.30c) is transformed into

$$\log\left\{A_i\left[1-\exp\left(\frac{-2\alpha m_{ci}^* T}{H}\right)\right]/T\right\} = \frac{-\alpha m_{ci}^*}{H}T + \text{const.} \qquad (5.33)$$

Therefore, from the slope of a plot of $\log\{A_i[1 - \exp(-2\lambda m_{ci}^* T/H)]/T\}$ versus T at constant field H, the effective mass can be obtained.

Let us consider the relation between the cyclotron mass and the electrical specific heat γ. Using a density of states $D(E_F)$, γ is written as

$$\gamma = \frac{\pi^2}{3} k_B{}^2 D(E_F). \tag{5.34}$$

In the spherical Fermi surface, using $E_F = \hbar^2 k_F{}^2/2m_c^*$ takes

$$\begin{aligned}
\gamma &= \frac{\pi^2}{3} k_B{}^2 \frac{V}{2\pi^2} \left(\frac{2m_c^*}{\hbar^2}\right)^{3/2} E_F{}^{1/2} \\
&= \frac{k_B{}^2 V}{3\hbar^2} m_c^* k_F,
\end{aligned} \tag{5.35}$$

where V is molar volume and $k_F = (S_F/\pi)^{1/2}$. We obtain from eq. (5.31)

$$\begin{aligned}
\gamma &= \frac{k_B{}^2 m_0}{3\hbar^2} \left(\frac{2e}{\hbar}\right)^{1/2} V \frac{m_c^*}{m_0} F^{1/2} \\
&= 2.87 \times 10^{-4} \, [(\text{mJ/K}^2 \cdot \text{mol})(\text{mol/cm}^3)\text{T}^{-1/2}] \cdot V \frac{m_c^*}{m_0} F^{1/2}.
\end{aligned} \tag{5.36}$$

In the case of the cylindrical Fermi surface,

$$\begin{aligned}
\gamma &= \frac{\pi^2}{3} k_B{}^2 \frac{V}{2\pi^2 \hbar^2} m_c^* k_z \\
&= \frac{k_B{}^2 V}{6\hbar^2} m_c^* k_z,
\end{aligned} \tag{5.37}$$

where the Fermi wave number k_z is parallel to an axial direction of the cylinder. If we regard simply the Fermi surfaces as sphere, ellipse or cylinder approximately and then we can calculate them.

Dingle temperature

We can determine the Dingle temperature T_D from measuring a field dependence of a dHvA amplitude. Equations (5.30b)-(5.30d) yield

$$\log\left\{ A_i H^{1/2} \left[1 - \exp\left(\frac{-2\lambda m_{ci}^* T}{H}\right)\right] \right\} = -\lambda m_{ci}^*(T + T_D)\frac{1}{H} + \text{const.} \tag{5.38}$$

From the slope of a plot of $\log\{A_i H^{1/2}[1 - \exp(-2\lambda m_{ci}^* T/H)]\}$ versus $1/H$ at constant T, the Dingle temperature can be obtained. Here, the cyclotron effective mass must have been already obtained.

We can estimate the mean free path l or the scattering life time τ from the Dingle temperature. The relation between an effective mass and lifetime takes the form

$$\hbar k_{\rm F} = m^* v_{\rm F}, \tag{5.39}$$

$$l = v_{\rm F}\tau. \tag{5.40}$$

Then eq. (5.32) is transformed into

$$l = \frac{\hbar^2 k_{\rm F}}{2\pi k_{\rm B} m_{\rm c}^* T_{\rm D}}. \tag{5.41}$$

When the extremal area can be regarded as a circle approximately, using the eq. (5.31), the mean free path is expressed as

$$\begin{aligned}
l &= \frac{\hbar^2}{2\pi k_{\rm B} m_0} \left(\frac{2e}{\hbar c}\right)^{1/2} F^{1/2} \left(\frac{m_{\rm c}^*}{m_0}\right)^{-1} T_{\rm D}^{-1} \\
&= 77.6 \, [\text{Å} \cdot \text{T}^{-1/2} \cdot \text{K}] \cdot F^{1/2} \left(\frac{m_{\rm c}^*}{m_0}\right)^{-1} T_{\rm D}^{-1}.
\end{aligned} \tag{5.42}$$

Field modulation method with the pick-up coil dHvA system

Experiments of the dHvA effect were constructed by using the usual ac-susceptibility field modulation method. Now we give an outline of the field modulation method with pick-up coil dHvA system.

A small ac-field $h_0 \cos \omega t$ is varied on an external field H_0 ($H_0 \gg h_0$) in order to obtain the periodic variation of the magnetic moment $M_{\rm osc}$. The sample is set up into a pair of balanced coils (pick up and compensation coils), as shown in Figure 5.13. An
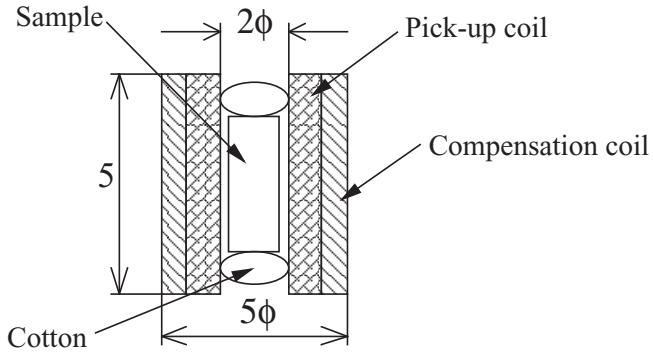
Fig. 5.13 Detecting coil and the sample location.

induced emf (electromotive force) V_{osc} will be proportional to $\mathrm{d}M_{\mathrm{osc}}/\mathrm{d}t$:

$$
\begin{aligned}
V_{\mathrm{osc}} &= c\frac{\mathrm{d}M_{\mathrm{osc}}}{\mathrm{d}t} \\
&= c\frac{\mathrm{d}M_{\mathrm{osc}}}{\mathrm{d}H}\frac{\mathrm{d}H}{\mathrm{d}t} \\
&= -ch_0\omega\sin\omega t\sum_{k=1}^{\infty}\frac{h_0^k}{2^{k-1}(k-1)!}\left(\frac{\mathrm{d}^k M_{\mathrm{osc}}}{\mathrm{d}H^k}\right)_{H_0}\sin k\omega t,
\end{aligned}
\tag{5.43}
$$

where c is constant which is fixed by the number of turns in the coil and so on, and the higher differential terms of the coefficient of $\sin k\omega t$ are neglected. Calculating the $\mathrm{d}^k M/\mathrm{d}H^k$ it becomes

$$
V_{\mathrm{osc}} = -c\omega A\sum_{k=1}^{\infty}\frac{1}{2^{k-1}(k-1)!}\left(\frac{2\pi h_0}{\Delta H}\right)^k\sin\left(\frac{2\pi F}{H}+\beta-\frac{k\pi}{2}\right)\sin k\omega t.
\tag{5.44}
$$

Here, $\Delta H = H^2/F$. Considering $h_0{}^2 \ll H_0{}^2$ the time dependence of magnetization $M(t)$ is given by

$$
M_{\mathrm{osc}}(t) = A\left[J_0(\lambda)\sin\left(\frac{2\pi F}{H_0}+\beta\right)+2\sum_{k=1}^{\infty}kJ_k(\lambda)\cos k\omega t\,\sin\left(\frac{2\pi F}{H_0}+\beta-\frac{k\pi}{2}\right)\right],
\tag{5.45}
$$

where

$$
\lambda = \frac{2\pi Fh_0}{H_0{}^2}.
\tag{5.46}
$$

Here, J_k is k-th Bessel function. Figure 5.14 shows the Bessel function of the first kind for the various order k. Finally we can obtain the output emf as follows:

$$
V_{\mathrm{osc}} = c\left(\frac{\mathrm{d}M}{\mathrm{d}t}\right) = -2c\omega A\sum_{k=1}^{\infty}kJ_k(\lambda)\sin\left(\frac{2\pi F}{H_0}+\beta-\frac{k\pi}{2}\right)\sin k\omega t.
\tag{5.47}
$$
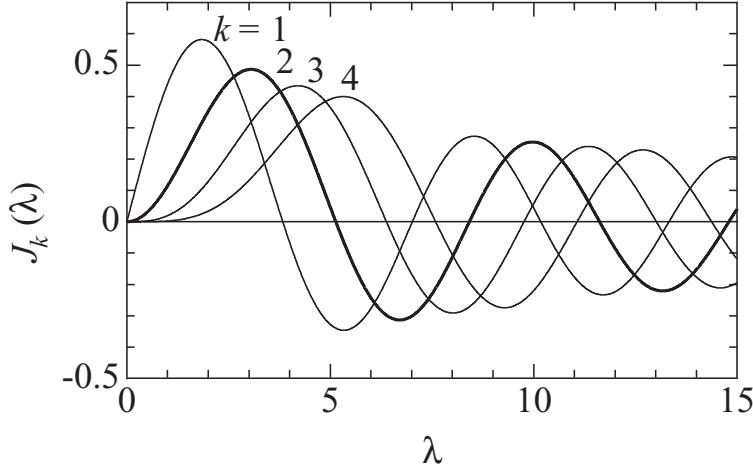
Fig. 5.14 Bessel function $J_k(\lambda)$ of the first kind.

The signal was detected at the second harmonic of the modulation frequency 2ω using a Lock-in Amplifier, since this condition may cut off the offset magnetization and then detect the component of the quantum oscillation only. Thus, the eq. (5.47) becomes

$$V_{\text{osc}} = -4c\omega A J_2(\lambda) \sin\left(\frac{2\pi F}{H_0} + \beta\right) \sin 2\omega t. \tag{5.48}$$

Here, we summarize eq. (5.48) as follow:

$$
\begin{aligned}
V_{\text{osc}} &= A \left|\frac{\partial^2 S_{\text{F}}(k_z)}{\partial k_z^2}\right|^{-1/2} R_{\text{T}} R_{\text{D}} R_{\text{S}} \sin\left(\frac{2\pi F}{H} + \beta\right), \tag{5.49} \\
A &\propto \omega J_2(x) H^{1/2},, \tag{5.50} \\
R_{\text{T}} &= \frac{2\alpha m_{\text{c}}^* T/H}{\sinh(2\alpha m_{\text{c}}^* T/H)}, \\
R_{\text{D}} &= \exp(-\alpha m_{\text{c}}^* T_{\text{D}}/H), \\
R_{\text{S}} &= \cos(\pi m_{\text{c}}^* g/2m_0), \\
\alpha &= 2\pi^2 c k_{\text{B}}/e\hbar. \\
x &= \frac{2\pi F h}{H^2}.
\end{aligned}
$$

A in eq. (5.50) is the factor depending on the detecting method. We usually choose the modulation field h_0 to make the value of $J_2(\lambda)$ maximum, namely $\lambda = 3.14$. A modulation frequency of $11\,\text{Hz}$ is also used in the dHvA experiment. Figure 5.15 shows a block diagram for the dHvA measurement in the present study.
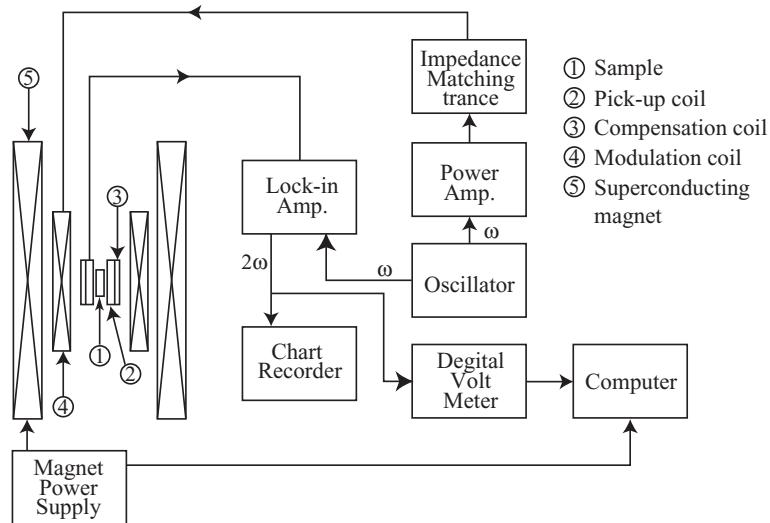
Fig. 5.15 Block diagram for the dHvA measurement.

Cantilever type dHvA experiment

The cantilever type dHvA experiment is a kind of the torque magnetization measurement.[129–132] We used the commercial micro-cantilever (MouldLessCantilever, SSI-SS-ML-PRC120, Seiko Instruments Inc.).[130] Schematic view and the photograph of cantilever are shown in Figs. 5.16(a) and 5.16(b), respectively.

The piezoresistive path detects the force as a voltage due to the torque $\boldsymbol{T} = \boldsymbol{M} \times \boldsymbol{H}$ between the magnetic moment of the sample $\boldsymbol{M}$ and the magnetic field $\boldsymbol{H} = \boldsymbol{H}_0 + h_0 \cos \omega t$, whereas the compensated pick-up coil detects the time derivative of a magnetic flux from the sample as a voltage. Therefore, the factor A in eq.(5.48) for the torque method using the cantilever without and with the modulation field h(and ω-detecting technique) is modified to be[129]

$$A \propto I_{\mathrm{AC}} \frac{dF}{d\theta} H^{\frac{3}{2}}. \tag{5.51}$$

and

$$A \propto I_{\mathrm{DC}} \omega J_1(x) \frac{dF}{d\theta} H^{\frac{3}{2}}, \tag{5.52}$$

respectively. Here, I_{AC} and I_{DC} are the AC and DC excitation current for the cantilever. $J_1(x)$ is the first Bessel function due to the modulation field.

Here we note the magnetic field term $H^{1/2}$ in eq. (5.50) and the term $H^{3/2}$ in eqs. (5.51) and (5.52). The torque T is given by $M_\perp HV$, where $M_\perp$ is the component of $\boldsymbol{M}$ perpendicular to H and V is the volume of the sample.[129] The component of this torque about any particular axis perpendicular to H is given by using $M_{//}$:

$$T = -\frac{1}{F} \frac{dF}{d\theta} M_{//} HV. \tag{5.53}$$

If we assume the Free energy

$$\Omega \sim H^{5/2} \cos \left(2\pi F/H + \phi\right), \tag{5.54}$$

$$M_{//} = -\partial\Omega/\partial H \sim H^{1/2} \sin \left(2\pi F/H + \phi\right) \tag{5.55}$$

and

$$T \sim H^{3/2} \sin \left(2\pi F/H + \phi\right), \tag{5.56}$$

are obtained. The terms of $H^{1/2}$ and $H^{3/2}$ are expressed in eq. (5.50) and eqs. 5.51 and 5.52, respectively. The Bessel functions $J_2(x)$ and $J_1(x)$ in eq. (5.50) and eq. (5.51), respectively, are derived from the modulation field detecting system. In the cantilever type dHvA system, we adopt the same modulation field as in the pick-up coil system

of $h \simeq 100\,\text{Oe}$ (a modulation frequency of $\omega/2\pi = 11\,\text{Hz}$) with the DC-current $I_{\text{DC}} \sim 0.05\,mA$ so as to reduce the temperature of cantilever lower than $100\,\text{mK}$.

In both the pick-up coil type and cantilever type dHvA experiments, we can determine the dHvA frequency and the cyclotron mass. By using the relations of $\varepsilon_F = \hbar^2 k_F{}^2/2m_c^*$, $S_F = \pi k_F{}^2$ and $S_F = (2\pi e/c\hbar)F$, the following formula is obtained from eq. (2.37),

$$|F_+ - F_-| = \frac{2c}{\hbar e}|\alpha p_\perp|m_c^*, \tag{5.57}$$

where F_+ and F_- correspond to two split dHvA frequencies.
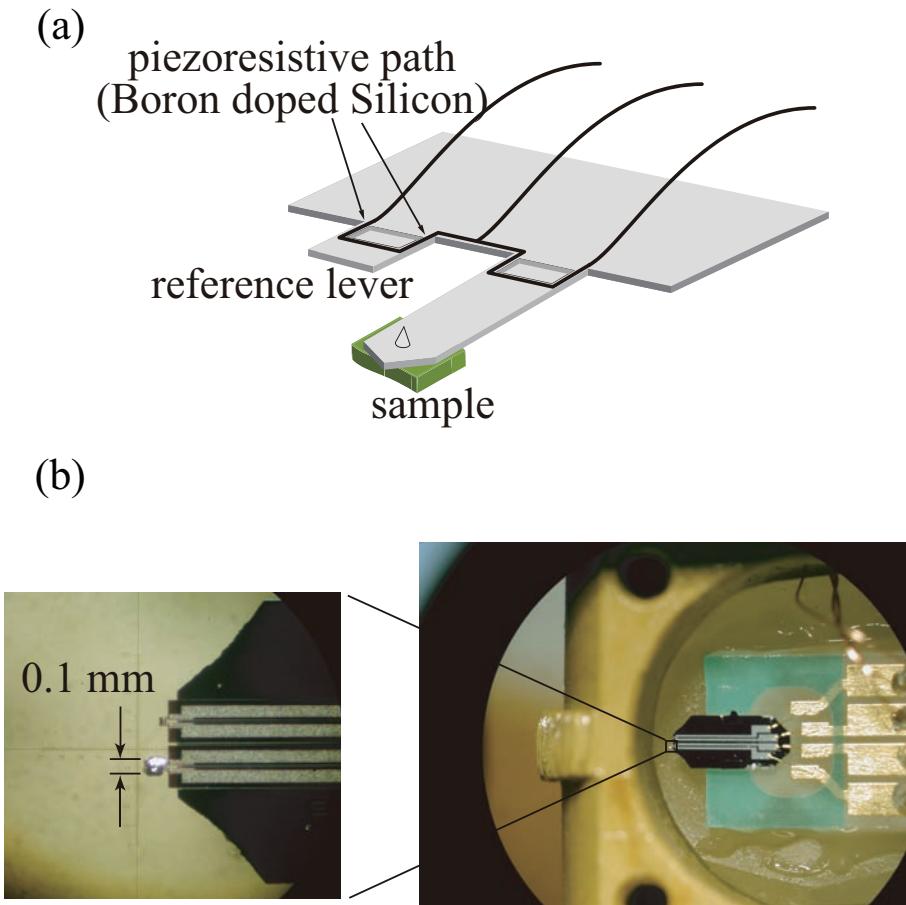
Fig. 5.16 (a) Schematic view and (b) the photograph of the cantilever

5.2.5   High-pressure techniques

Pressure is a useful tool to control the electronic states in the f-electron systems. We introduce two kinds of pressure cells.

Cubic anvil cell

To obtain higher pressures than those in a piston cylinder-type cell, we used a cubic-anvil device from 1.5 GPa to 8 GPa which has been developed by Môri *et al.*[133] for precise electrical measurements at low temperatures in Institute for Solid State Physics, University of Tokyo (ISSP). The cubic anvils made of sintered tungsten carbides having 4 mm on edge of square face press the sample from 6 directions as shown in Fig. 5.17. In Fig. 5.18 is shown the internal configuration of a gasket with a teflon cell in which the sample is immersed in fluid. The electrical resistivity of sample was measured by means of a four-terminal method. As electrical leads, gold wires of 20 micron in diameter. were used with silver paint contact on the surface of the specimen and connected to thin gold ribbons attached to back up blocks, as shown in Fig. 5.18. As a pressure transmitting fluid, we used a Daphne 7373 oil.

The cubic anvil dies were placed between the end of a pair of pressure transmitting columns consisting of fiber-reinforced plastic (FRP) disks as shown in Fig. 5.19. The whole specimen was cooled by liquid N_2 and liquid He down to 4.2 K. Furthermore, it was cooled down to 2.2 K by pumping out liquid He with the booster pump. During the cooling of the cell, the pressure changes due to the thermal contractions and stiffening of the various parts of the cell, compressing medium and sample. The pressure was kept constant for a temperature change. The pressure was determined from the measurements of the resistivity change of bismuth associated with the phase transitions, Bi I-II (2.55 GPa), II-III(2.7 GPa) and III-V(7.7 GPa) at room temperature. Pressure was also determined at low temperatures from the superconducting transition temperature T_c of lead with the pressure coefficient of $dT_c/dP = -3.81 \times 10^{-1}$ K/GPa up to 2.5 GPa. Above 2.5 GPa the pressure was estimated from a pressure-load calibration curve at room temperature.
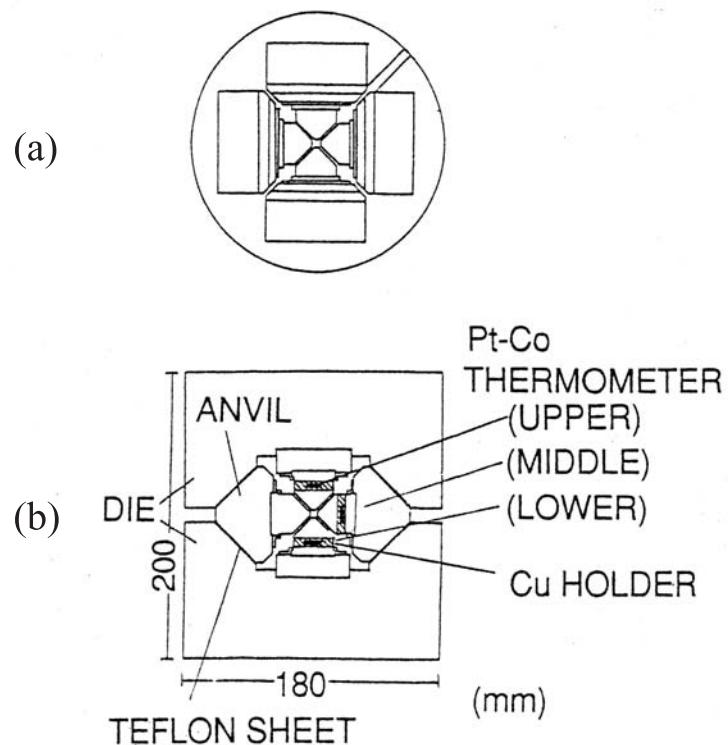
Fig. 5.17 Cubic anvil device: top(a) and side(b) views.
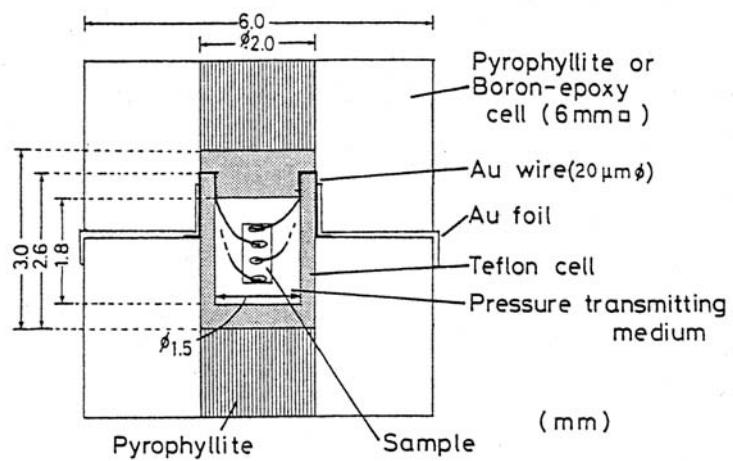
Fig. 5.18 Cross-sectional view of internal configuration of gasket with teflon capsule.
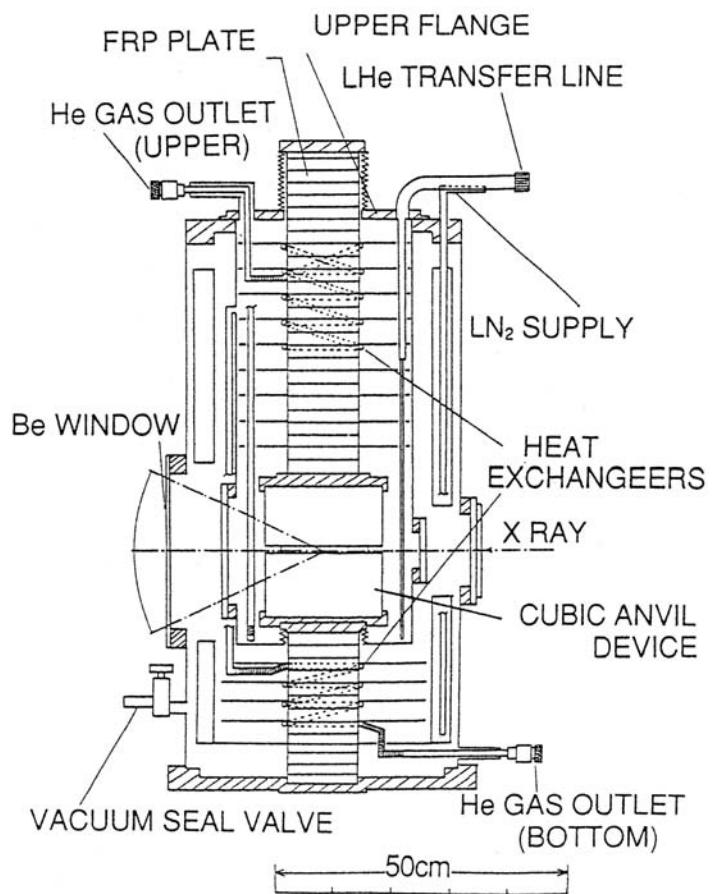
Fig. 5.19 Cross-sectional view of high pressure cryostat.

Diamond anvil cell

The electrical resistivity measurements under pressure were performed with a diamond anvil cell (DAC). Figure 5.20(a) shows the photograph of the DAC and its corresponding schematic view and the cross-sectional view of inside DAC are shown in Figs. 5.20(b) and 5.20(c), respectively. Most part of the pressure cell are made of Be-Cu alloy and two opposed anvils are made of diamond. We used the SUS material as a gasket and liquid Ar, which was obtained by liquefaction of 4N-pure Ar-gas, for a pressure transmitting medium, and the pressure was determined by the shift of the fluorescent line of ruby. Four Au-wires ($10\,\mu\mathrm{m}\phi$) were used to measure the voltage of the sample, which was spot-welded directly on the sample to ensure a good electrical contact. These four Au-wires were leaded out from the sample space through between the alumina insulator phase and the diamond, as shown in Fig. 5.20(c). The typical size of the samples for this diamond anvil cell is about $200 \times 100 \times 50\,\mu\mathrm{m}^3$. For more precise measurement, we used the single crystal of CeCoGe$_3$ with size of $250 \times 110 \times 30\,\mu\mathrm{m}^3$ for the electrical resistivity measurement.
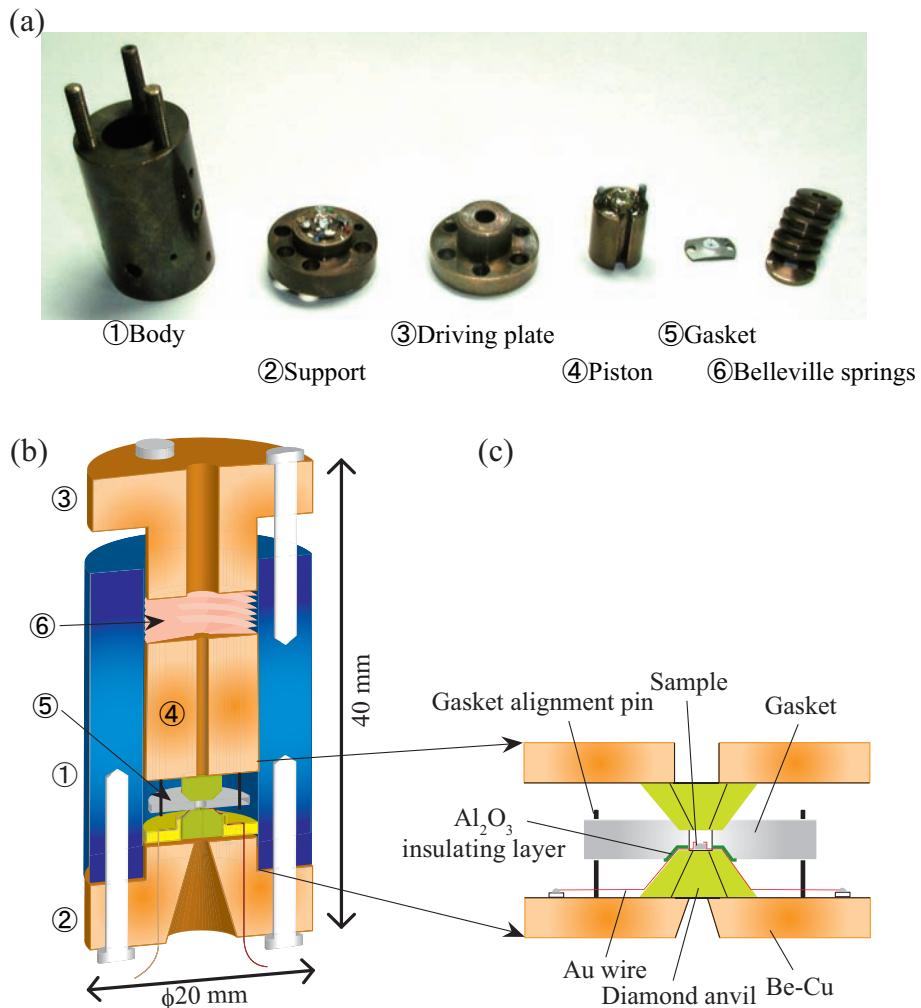
Fig. 5.20 (a) Photograph of the components of DAC, (b) schematic view of a diamond anvils cell and (b) the cross-sectional view of internal configuration of DAC.

Here, we mention about the hydrostatic homogeneity of argon. The melting curves of argon, helium 4 (^{4}He), ice (H_2O) and hydrogen (H_2) were studied by F. Datchi *et al.* from room temperature up to a maximum temperature of 750 K, as shown in Fig. 5.21.[134] Argon is chemically inert so that the reaction of argon with the sample and the materials around the sample space, gasket and Al_2O_3, for example, is unlikely. The melting point of argon is 83.78 K at ambient pressure. With increasing pressure, it increases continuously and reaches 300 K at pressure of 1.34 GPa, following a Simon-Glatzel equation: $P[\text{GPa}] = 2.172 \times 10^{-4} T^{1.556}[\text{K}]$ - 0.21. As for the hydrostatic homogeneity of argon, it is studied by Bell *et al.* that argon can be hydrostatic up to 9 GPa from the viewpoint of broadening of ruby fluorescent lines, and a pressure difference in the DAC becomes 1.7 GPa at pressure $P \simeq 75$ GPa.[135, 136] In fact, ruby pieces, which were put on three places around the sample in the diamond anvil cell, indicate the same pressure of 7.0 GPa at room temperature in the present electrical resistivity measurement for the single crystal of CeCoGe$_3$ at 6.5 GPa, indicating the excellent hydrostatic homogeneity in present experiment.
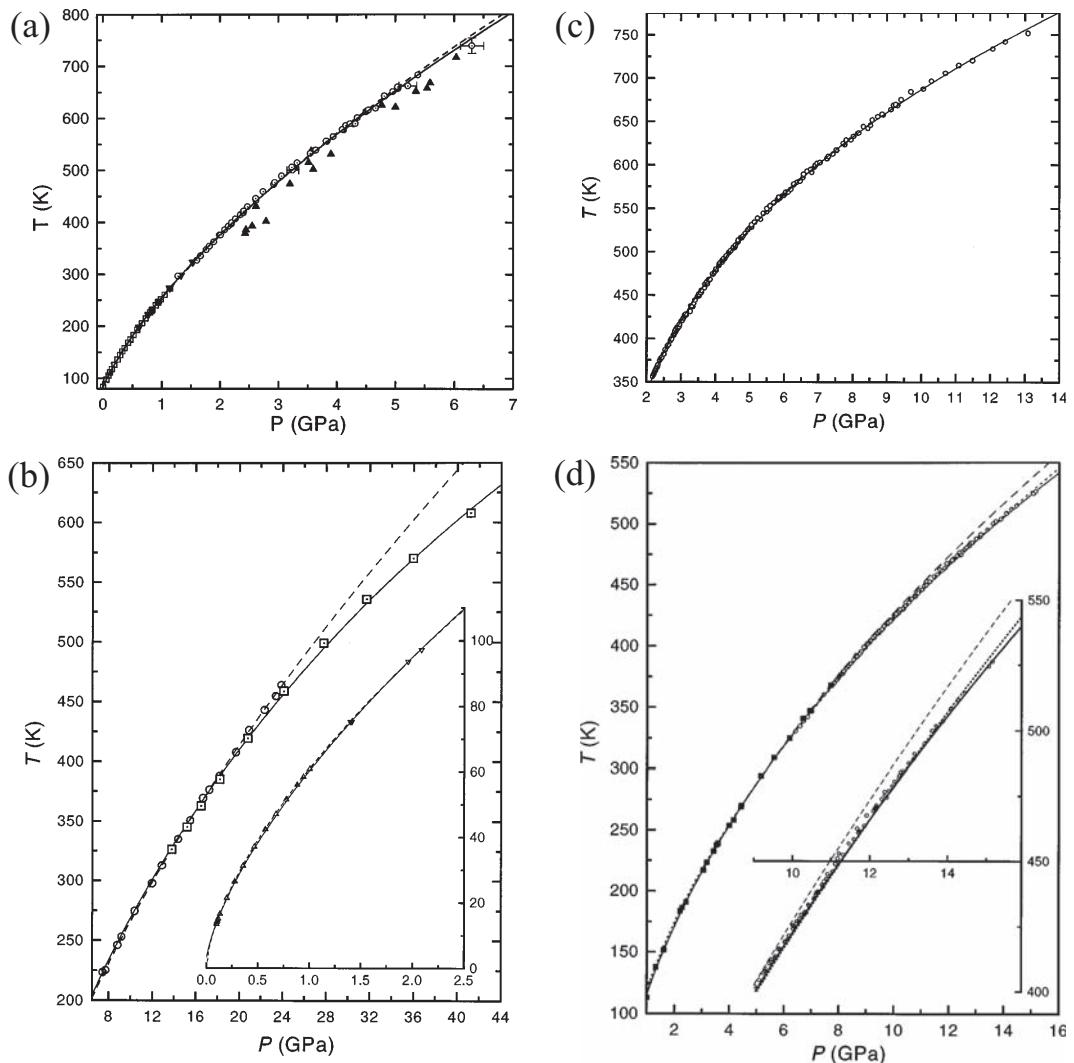
Fig. 5.21 Melting curves of (a) argon, (b) ^{4}He, (c) H_2O, (d) H_2.[134]

6 Experimental Results, Analyses and Discussion

6.1 Split Fermi Surface Properties

6.1.1 LaCoGe$_3$, LaRhGe$_3$ and LaIrGe$_3$

Figure 6.1 shows the temperature dependence of the electrical resistivity of LaCoGe$_3$, LaRhGe$_3$ and LaIrGe$_3$ for the current J along the [100] direction. The electrical resistivity decreases linearly with decreasing temperature. The residual resistivity ρ_0 and residual resistivity ratio RRR ($= \rho_{RT}/\rho_0$, ρ_{RT}: resistivity at room temperature) are $\rho_0 = 0.27\,\mu\Omega\cdot$cm and RRR $= 150$ in LaCoGe$_3$, $\rho_0 = 0.14\,\mu\Omega\cdot$cm and RRR $= 330$ in LaRhGe$_3$ and $\rho_0 = 0.87\,\mu\Omega\cdot$cm and RRR $= 35$ in LaIrGe$_3$. The present samples of LaCoGe$_3$ and LaRhGe$_3$ are in high-quality but LaIrGe$_3$ is not good in sample quality.
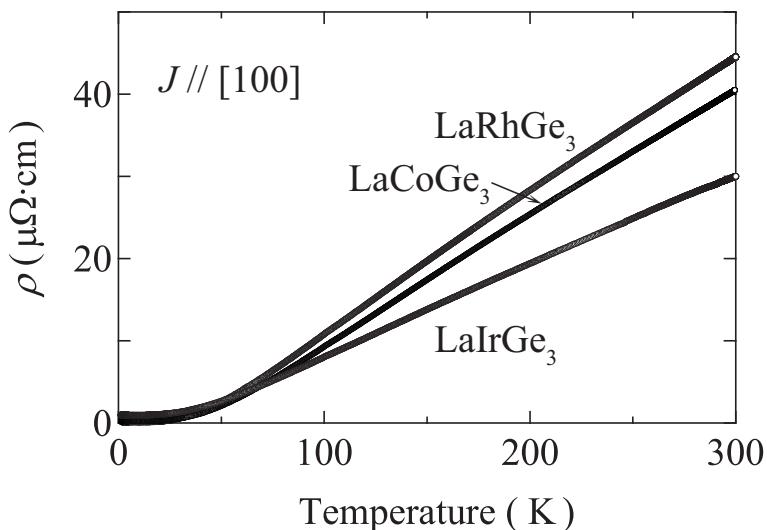
Fig. 6.1 Temperature dependence of the electrical resistivity for $J\,/\!/\,$[100] in LaTGe$_3$(T: Co, Rh, Ir).

The Fermi surface properties of LaCoGe$_3$ were previously clarified from the dHvA experiment and energy band calculation,[106)] which are shown later. First we show in Fig. 6.2(a) the typical dHvA oscillation of LaRhGe$_3$ for the magnetic field H along the [001] direction (c-axis) and its fast Fourier transformation (FFT) spectrum. The detected dHvA branches are named α, β, ε, θ and η, as shown in Fig. 6.2(b). The branch α with the largest dHvA frequency is clearly split into two branches, and each branch is furthermore split into two branches. The former splitting is due to the antisymmetric spin-orbit interaction, as mentioned above. The latter splitting is mainly due to the fact that each Fermi surface is slightly corrugated, possessing two extremal (maximum and minimum) cross-sections.
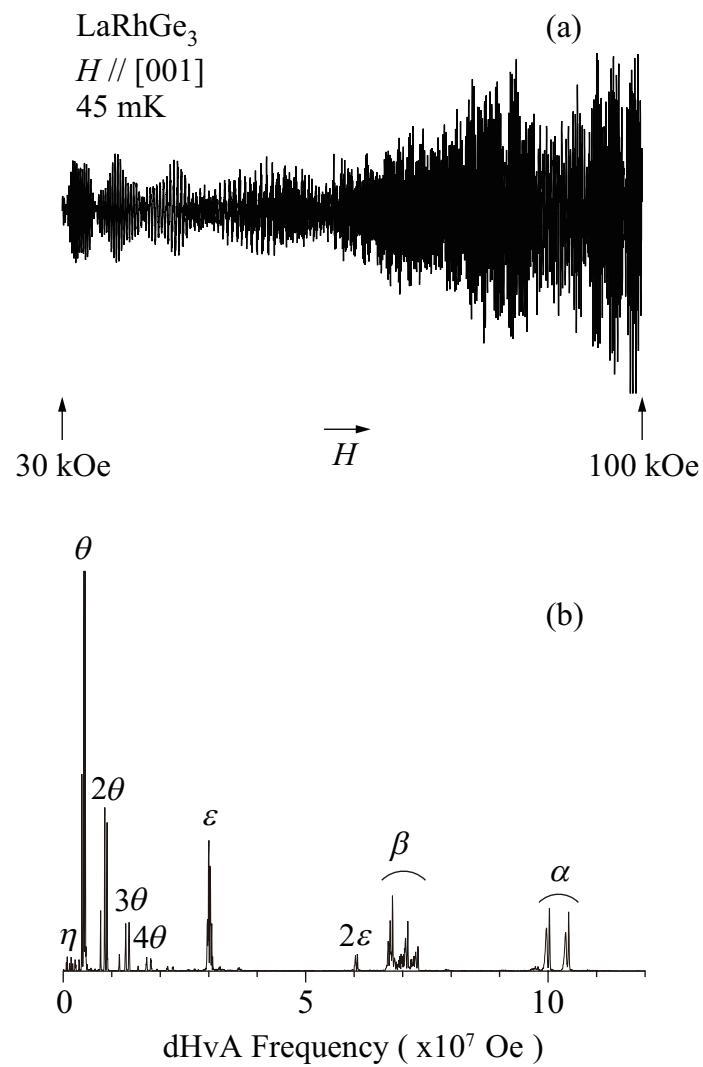
Fig. 6.2 (a) Typical dHvA oscillation for $H // [001]$ and (b) its FFT spectrum in LaRhGe$_3$.

Figures 6.3(a) and 6.3(b) show the angular dependence of the dHvA frequency in LaRhGe$_3$, together with the result of theoretical calculation based on the full potential APW (FLAPW) method as in LaCoGe$_3$[106] and LaIrSi$_3$.[22] The detected dHvA branches are well explained by the result of the present energy band calculation. The corresponding theoretical Fermi surfaces are shown in Fig. 6.4. The dHvA branches are identified as follows:

(1) branches α and η correspond to outer and inner orbits of the doughnut-like band 69 and 70-electron Fermi surfaces, respectively. Namely, the Fermi surfaces possess vacant space around the center of the Brillouin zone, Γ.

(2) branch β is due to the band 67 and 68-hole Fermi surfaces.

(3) branchs ε and θ also correspond to outer and inner orbits of the band 65 and 66-hole Fermi surfaces, respectively.

We determined the cyclotron effective mass m_c^* from the temperature dependence of the dHvA amplitude. The cyclotron mass is $1.04\,m_0$ (m_0: rest mass of an electron) for branch α in the magnetic field along the [001] direction, for example. The dHvA frequency F, cyclotron mass m_c^*, the corresponding theoretical frequency F_b and band mass m_b are summarized in Table 6.I. From the field dependence of the dHvA oscillation in Fig. 6.2(a), we can also determine the Dingle temperature $T_D = 1.88\,\mathrm{K}$ or the scattering lifetime $\tau = 6.53 \times 10^{-13}$ sec for branch α. The mean free path is thus determined to be 8060 Å for the orbit of branch α by using the relations in Chap. 5, namely eq. 5.40.
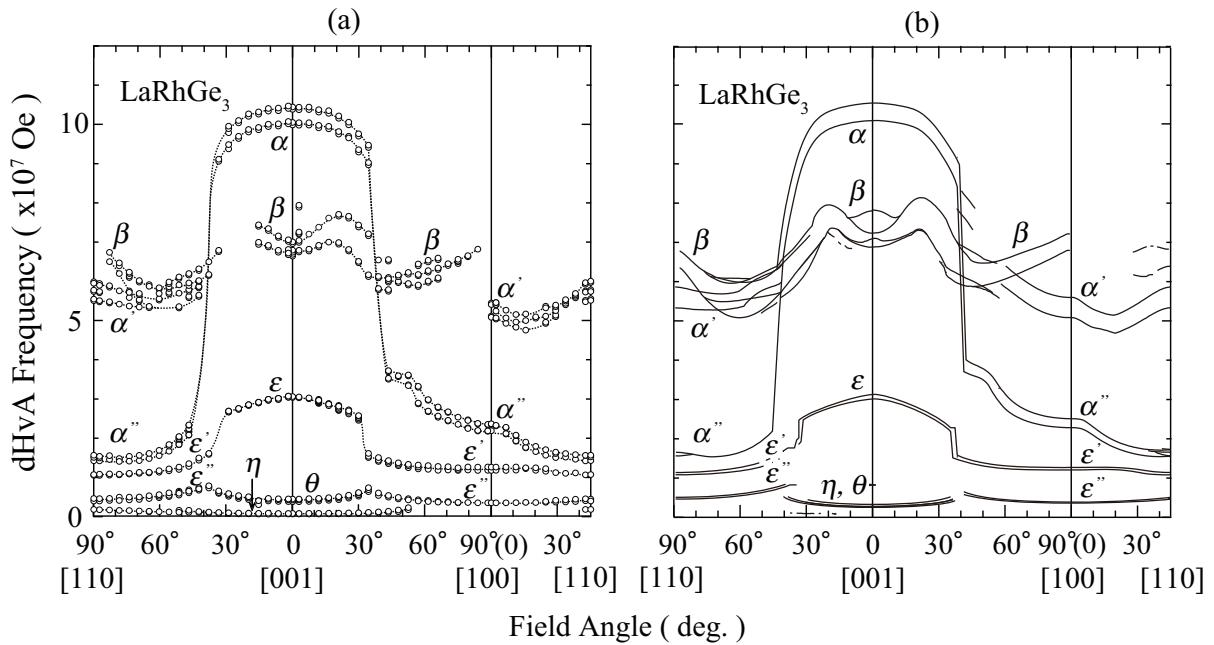
Fig. 6.3 (a) Angular dependence of dHvA frequency and (b) the theoretical one of LaRhGe$_3$.
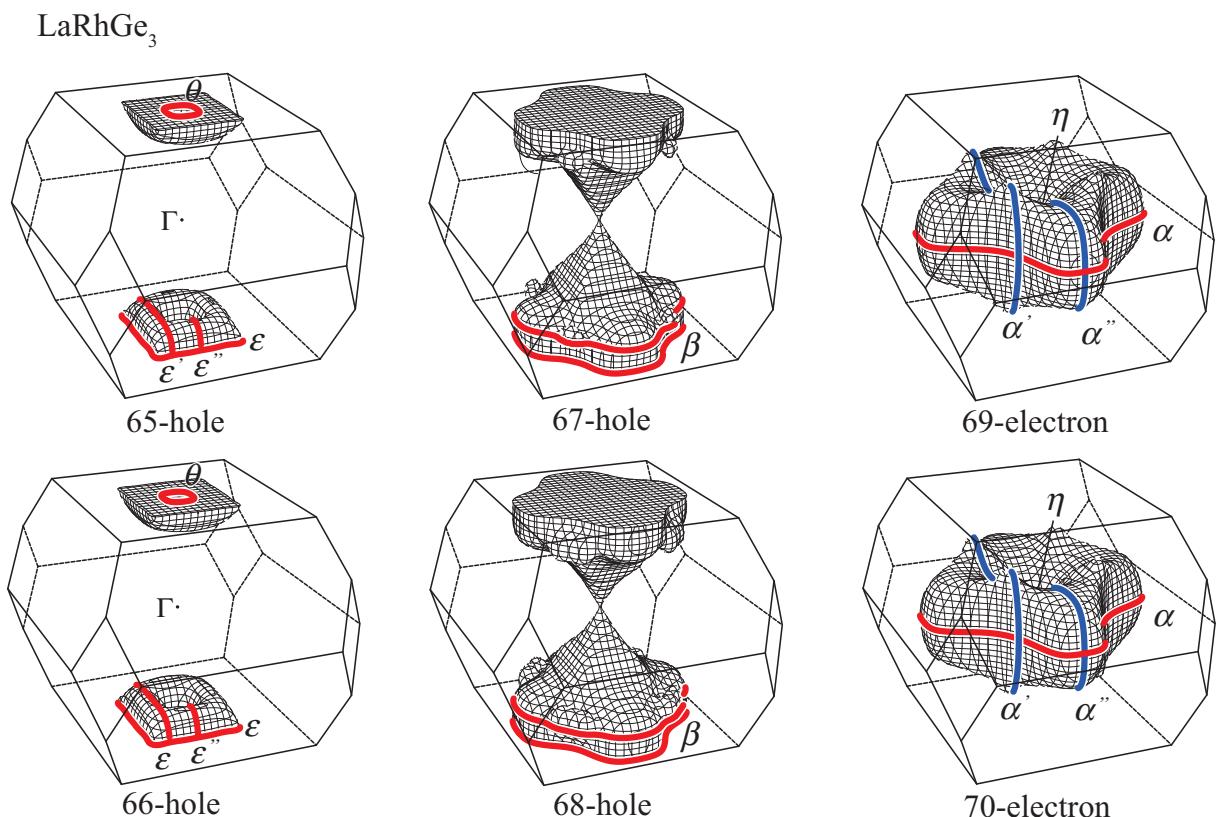
LaRhGe$_3$

Fig. 6.4 Theoretical Fermi surfaces of LaRhGe$_3$.

Table 6.I Detected dHvA Frequency F, cyclotron effective mass $m_{\rm c}^*$ and the theoretical frequency $F_{\rm b}$ and band mass $m_{\rm b}$ in LaRhGe$_3$.

Experiment			Theory		
Branch	$F(\times 10^7 \rm Oe)$	$m_{\rm c}^*(m_0)$	Branch	$F_{\rm b}(\times 10^7 \rm Oe)$	$m_{\rm b}(m_0)$
$H // [001]$					
α	10.4	1.04	α	band 69	10.5	1.11
	10.0	1.04		band 70	10.1	1.12
β	6.98	0.83	β	band 68	7.82	1.24
	6.77	1.89		band 68	7.24	0.91
	6.67	0.85		band 67	7.11	2.01
				band 67	6.89	0.88
ε	3.06	0.74	ε	band 66	3.13	0.68
	3.04	0.73		band 65	3.01	0.69
θ	0.44	0.44	θ	band 65	0.33	0.31
	0.38	0.51		band 66	0.28	0.24
η	0.08	0.22	η	band 70	0.03	0.27
	0.06	0.23		band 69	0.03	0.26
$H // [100]$					
α'	5.43	—	α'	band 69	5.60	1.47
	5.10	1.09		band 70	5.09	1.40
α''	2.36	0.60	α''	band 69	2.51	0.61
	2.19	0.69		band 70	2.28	0.60
ε'	1.22	0.46	ε'	band 66	1.27	0.40
	1.18	0.54		band 65	1.21	0.42
ε''	0.35	0.32	ε''	band 66	0.39	0.21
				band 65	0.36	0.20

Fig. 6.5 (a) Typical dHvA oscillation and (b) its FFT spectrum in the pick-up coil type dHvA system, and (c) typical dHvA oscillation and (d) its FFT spectrum in the cantilever type dHvA system for $H // [001]$ and close to [001], respectively, in LaIrGe$_3$.

The usual pick-up coil dHvA system was not powerful for LaIrGe$_3$, as shown in Figs. 6.5(a) and 6.5(b). Branches α, β and ε were detected, but branches θ and η were not detected. The reason is as follows. The present sample was not good in quality, with RRR = 35 and was small in size. An ample amplitude of the dHvA oscillation was, however, obtained in the cantilever type dHvA system, especially for branches ε, θ and η with small dHvA frequencies, as shown in Figs. 6.5(c) and 6.5(d). The cantilever type dHvA system is very effective for the small sample, although the dHvA signal becomes very weak in amplitude for the magnetic field along the symmetric directions of $H // [001]$ and [100], as shown in Fig. 6.6, reflecting the factor of $dF/d\theta$ in eq. (5.56). This is the reason why the dHvA oscillation in Fig. 6.5(c) is not for $H/[001]$ but for the field tilted by $\theta = 5\,^\circ$ from [001] to [100].
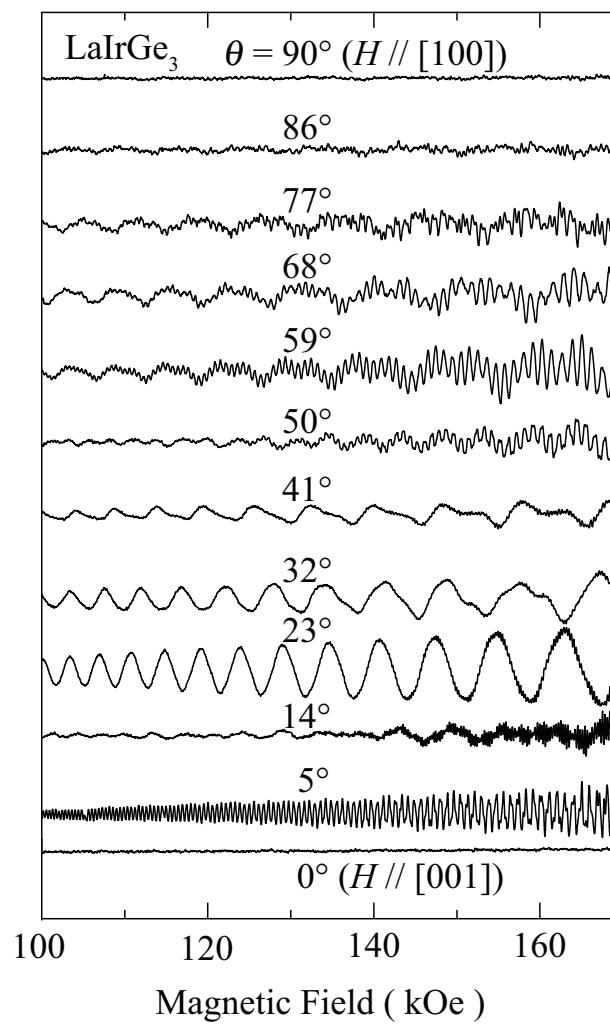
Fig. 6.6 Cantilever type dHvA oscillations in LaIrGe$_3$ as a function of the tilted angle θ.

The angular dependence of the dHvA frequency and the corresponding theoretical one are shown in Fig. 6.7. The dHvA data obtained from both the pick-up coil and the cantilever systems are combined in Fig. 6.7. The dHvA frequency and cyclotron mass, together with the theoretical ones, are summarized in Table 6.II.
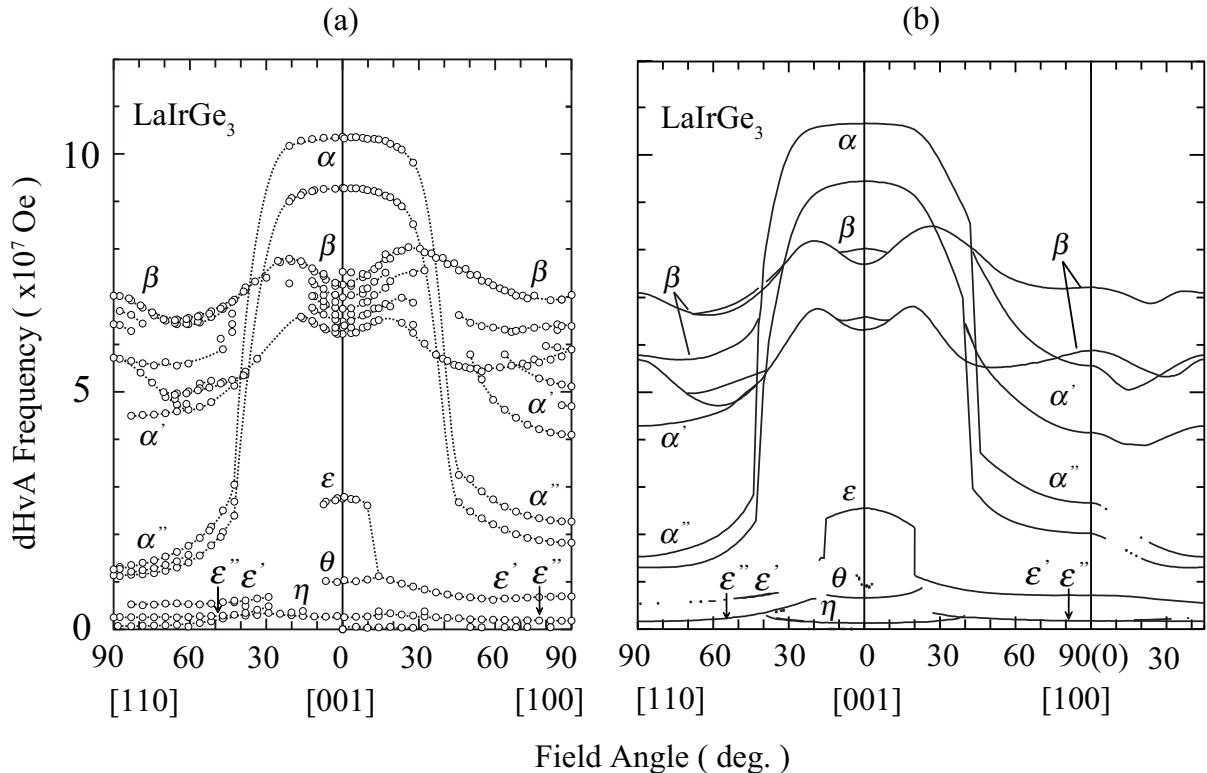
Fig. 6.7 (a) Angular dependence of dHvA frequency in LaIrGe₃, and (b) the theoretical one.

Table 6.II Detected dHvA Frequency F, cyclotron effective mass m_{c}^* and the theoretical frequency F_{b} and band mass m_{b} in LaIrGe$_3$.

Experiment			Theory		
Branch	$F(\times 10^7\mathrm{Oe})$	$m_{\mathrm{c}}^*(m_0)$	Branch	$F_{\mathrm{b}}(\times 10^7\mathrm{Oe})$	$m_{\mathrm{b}}(m_0)$
			$H\,/\!/\,[001]$		
α	10.4	1.13	α band 69	10.7	1.08
	9.29	1.51	band 70	9.46	1.09
β	7.53	1.37	band 68	8.04	1.20
	7.25	1.32		7.70	1.12
	6.99	1.58	β		
	6.75	1.84			
	6.48	1.27			
	6.36	1.55	band 67	6.59	1.18
	6.22	1.29		6.32	0.88
ε	2.75	0.98	ε band 66	2.56	0.65
θ	1.03	—	θ band 66	0.66	0.41
			η band70	0.15	0.24
			band69	0.14	0.23
			$H\,/\!/\,[100]$		
α'	5.11	1.57	α' band 69	5.57	1.46
	4.70	1.87			
	4.09	1.69	band 70	4.15	1.21
α"	2.27	1.08	α" band 69	2.66	0.64
	1.82	0.97	band 70	2.02	0.61
β	7.05	—	β band 68	7.22	1.04
	6.39	—			
	5.89	2.07	band 67	5.88	0.93
ε'	0.69	0.32	ε' band 66	0.72	0.46
ε"	0.18	—	ε" band 66	0.18	0.18

Fig. 6.8 Theoretical Fermi surfaces of LaIrGe$_3$.

The Fermi surfaces of LaIrGe$_3$ are very similar to those of LaRhGe$_3$, as shown in Fig. 6.8, although the band 65-hole Fermi surface does not exist theoretically. It is noticed that split branches are not observed experimentally for branch ε, as shown in Figs. 6.5(b) and 6.5(d), which is different from branch ε in LaRhGe$_3$.

6.1.2   LaFeGe$_3$, LaCoGe$_3$ and PrCoGe$_3$

We also investigated a change of the Fermi surface properties by changing the transition metal. Namely, LaFeGe$_3$ was studied from the dHvA experiment. The topology of the Fermi surface is expected to be drastically changed because the number of valence electrons in LaFeGe$_3$ is smaller than that in LaCoGe$_3$. We also succeeded in growing a single crystal of a paramagnet PrCoGe$_3$. It is expected that the topology of the Fermi surface is the same between LaCoGe$_3$ and PrCoGe$_3$, although the cyclotron effective mass in PrCoGe$_3$ is nearly twice as large as that of LaCoGe$_3$, as in the case of LaIn$_3$ and PrIn$_3$.[137] It is our experiment purpose to clarify the magnitude of $2|\alpha p_\perp|$ as a function of the cyclotron mass.

Figure 6.9 shows the temperature dependence of the electrical resistivity in LaFeGe$_3$, LaCoGe$_3$ and PrCoGe$_3$ for the current $J // [100]$. The resistivity decreases linearly with decreasing temperature in LaFeGe$_3$ and LaCoGe$_3$. The resistivity in PrCoGe$_3$ indicates
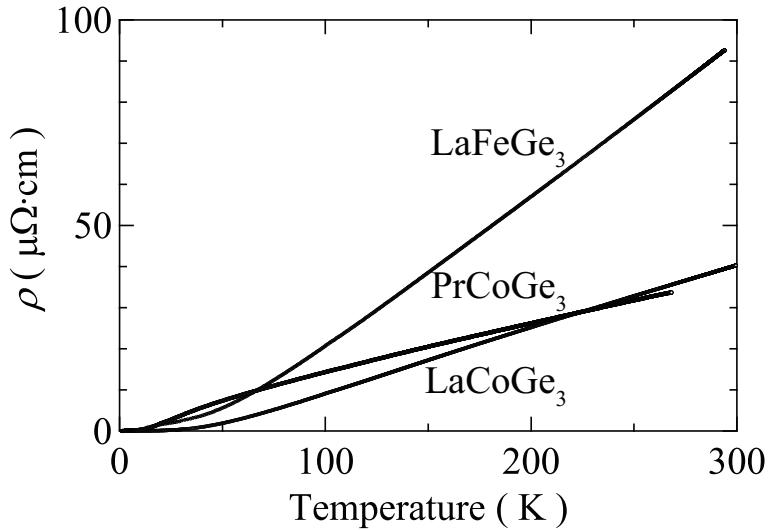
Fig. 6.9 Temperature dependence of the electrical resistivity in $LaFeGe_3$, $LaCoGe_3$ and $PrCoGe_3$.

a shoulder-like feature around $60\,K$, which is due to the crystalline electric field (CEF) effect. No magnetic ordering is observed at low temperatures down to $30\,mK$, indicating the singlet CEF-scheme. The ρ_0 and RRR values are $\rho_0 = 1.39\,\mu\Omega\cdot cm$ and RRR $= 67$ in $LaFeGe_3$, and $\rho_0 = 0.37\,\mu\Omega\cdot cm$ and RRR $= 120$ in $PrCoGe_3$, indicating the samples with relatively high-quality.

We show in Fig. 6.10 the typical dHvA oscillation in the usual pick-up coil system and the corresponding FFT spectrum in $PrCoGe_3$. The detected dHvA branches are the same as those of $LaCoGe_3$. The angular dependence of the dHvA frequency of $PrCoGe_3$ are shown in Fig. 6.11(a), together with that of $LaCoGe_3$ in Fig. 6.11(b) for comparison.

The cyclotron mass of $PrCoGe_3$ is approximately twice as large as that of $LaCoGe_3$. For example, the cyclotron masses of branches α and β are about $2\,m_0$, which are larger than $1.2\,m_0$ in $LaCoGe_3$. We summarize in Table 6.III the dHvA frequency and cyclotron mass in $PrCoGe_3$ and $LaCoGe_3$, together with those in $LaCoGe_3$.
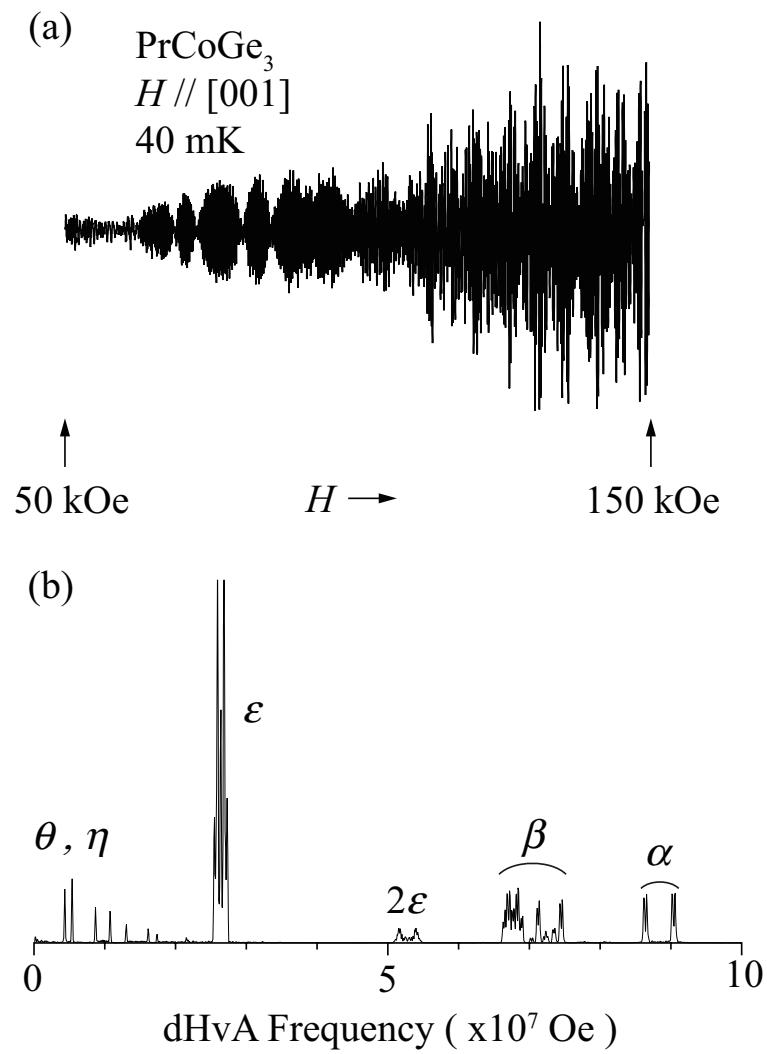
Fig. 6.10 (a) Typical dHvA oscillation for $H //$ [001] and (b) its FFT spectrum in PrCoGe$_3$.
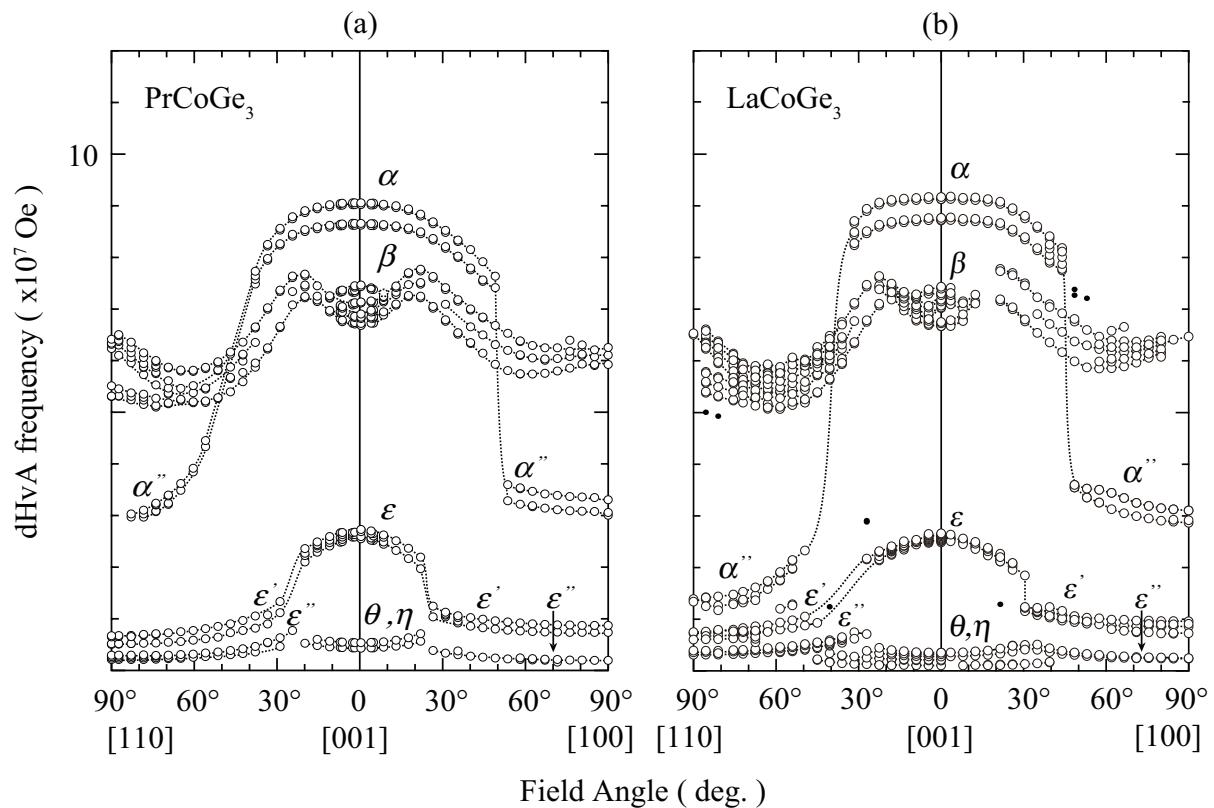
Fig. 6.11 Angular dependence of dHvA frequency in (a) PrCoGe$_3$ and (b) LaCoGe$_3$.

Table 6.III Detected dHvA frequency F, cyclotron effective mass m_{c}^* in $PrCoGe_3$ and $LaCoGe_3$.

	$PrCoGe_3$			$LaCoGe_3$	
Branch	$F(\times 10^7 \mathrm{Oe})$	$m_{\mathrm{c}}^*(m_0)$	Branch	$F(\times 10^7 \mathrm{Oe})$	$m_{\mathrm{c}}^*(m_0)$
		$H // [001]$			
α	9.04	1.80	α	9.15	1.19
	8.64	1.97		8.74	1.20
β	7.45	2.23	β	7.42	1.36
	7.13	2.04		7.27	1.26
	6.90	1.67		7.12	1.41
	6.83	1.63		7.06	1.15
	6.70	1.70		6.72	1.11
ε	2.71	1.16	ε	2.62	0.89
	2.57	1.18		2.55	0.80
θ	0.54	0.95	θ	0.35	0.58
				0.28	—
η	0.43	0.76	η	0.21	—
				0.10	—
		$H // [100]$			
α"	3.48	2.03	α"	3.10	2.04
	3.12	—		2.87	1.25
β	6.25	2.22			
	6.11	2.42	β	6.47	2.71
	5.93	2.29			
ε'	0.87	0.86	ε'	0.96	1.00
	0.74	0.86		0.86	1.04
ε"	0.20	0.87	ε"	0.23	0.59

Figure 6.12(a) shows the typical cantilever type dHvA oscillation for the magnetic field tilted by $\theta = 2°$ from [001] to [100] in LaFeGe$_3$. Several dHvA branches are observed in the FFT spectrum, as shown in Fig. 6.12(b). Branches α and β are clearly split due to the antisymmetric spin-orbit interaction. We also show in Fig. 6.13 the dHvA oscillations as a function of the tilted angle θ from [001] to [100]. The dHvA oscillation is very small in amplitude for $H \,//\, [001]$ and [100], as in LaIrGe$_3$. We show in Figs. 6.14(a) and 6.14(b) the angular dependence of the dHvA frequency, together with the theoretical one, respectively. Almost all the detected branches are identified by the theoretical ones. The corresponding orbits and Fermi surfaces are shown in Fig. 6.15.

We will compare the Fermi surface of LaFeGe$_3$ with that of LaTGe$_3$ (T: Co, Rh, Ir). When one conduction electron is added to the Fermi surface of LaFeGe$_3$, bands 65 and 66-hole Fermi surfaces in LaFeGe$_3$ slightly shrink in volume, with vacant space in center, and are changed into doughnut-like bands 65 and 66-hole Fermi surfaces in LaTGe$_3$ (T: Co, Rh, Ir). Connected parts of bands 67 and 68-hole Fermi surfaces in LaFeGe$_3$ disappear

(a)

LaFeGe$_3$
$H \,//\, 2°$ tilted from
　　　　[001] to [100]
53 mK

100 kOe　　　　　　$H \longrightarrow$　　　　169 kOe

(b)

ε

β

γ

2ε

α

0　　　　5　　　　10　　　　15
dHvA Frequency ($\times 10^7$ Oe)
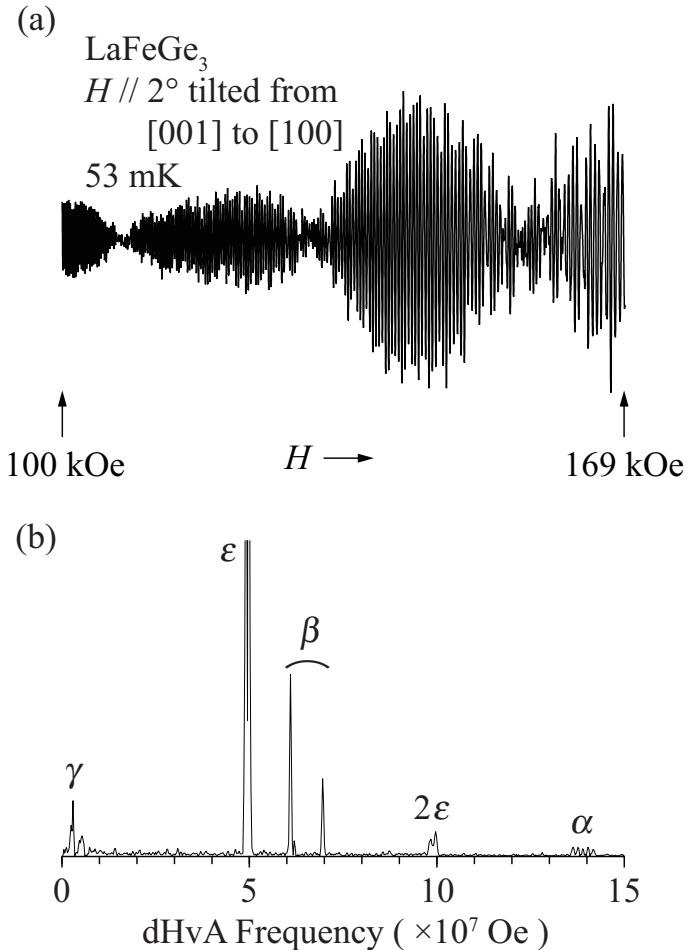
Fig. 6.12 (a) Typical dHvA oscillation for the magnetic field close to the [001] direction and (b) its FFT spectrum of LaFeGe$_3$ in the cantilever type dHvA system.

and are changed into pyramid-like bands 67 and 68-hole Fermi surfaces in LaTGe$_3$ (T: Co, Rh, Ir). Furthermore, four small nearly spherical bands 69 and 70-electron Fermi surfaces in LaFeGe$_3$ expand in volume and are connected, forming square doughnut-like bands 69 and 70-electron Fermi surfaces in LaTGe$_3$ (T: Co, Rh, Ir).

We determined the cyclotron mass from the temperature dependence of the dHvA amplitude in LaFeGe$_3$. The cyclotron mass of branches α and β is about $4-5$ m_0, revealing the relatively large masses. This is mainly due to the contribution of $3d$ electrons in the Fe atom, which will be discussed later. We summarize in Table 6.IV the dHvA frequency and the cyclotron mass, together with the theoretical ones.
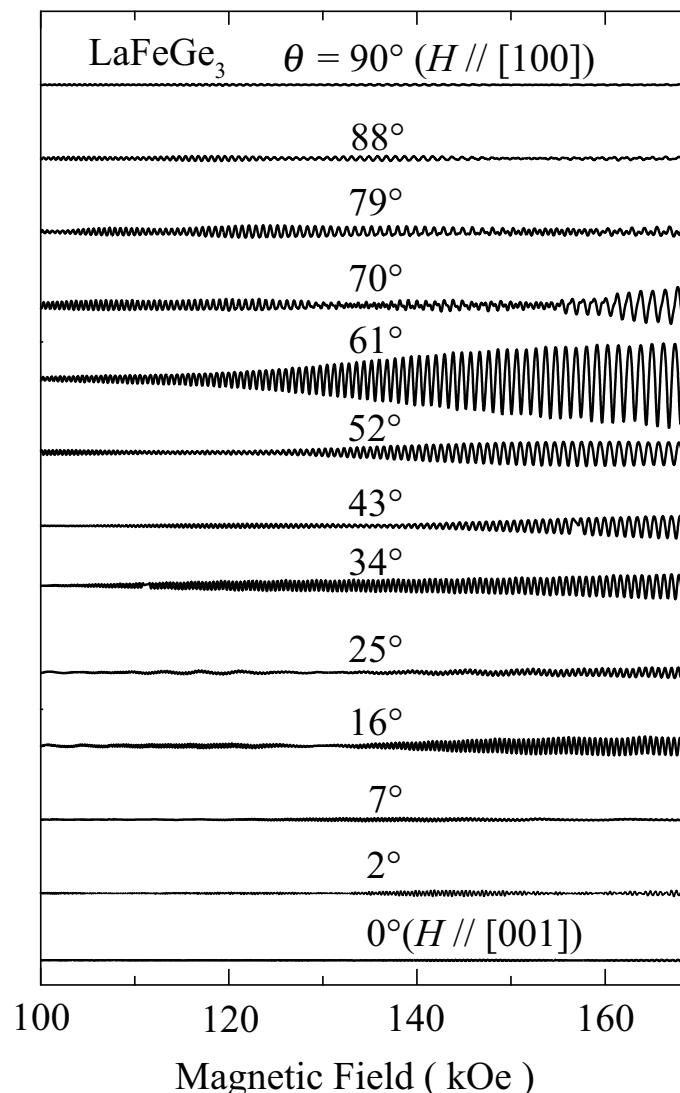
Fig. 6.13 Cantilever type dHvA oscillations in LaFeGe$_3$ as a function of the tilted angle θ.
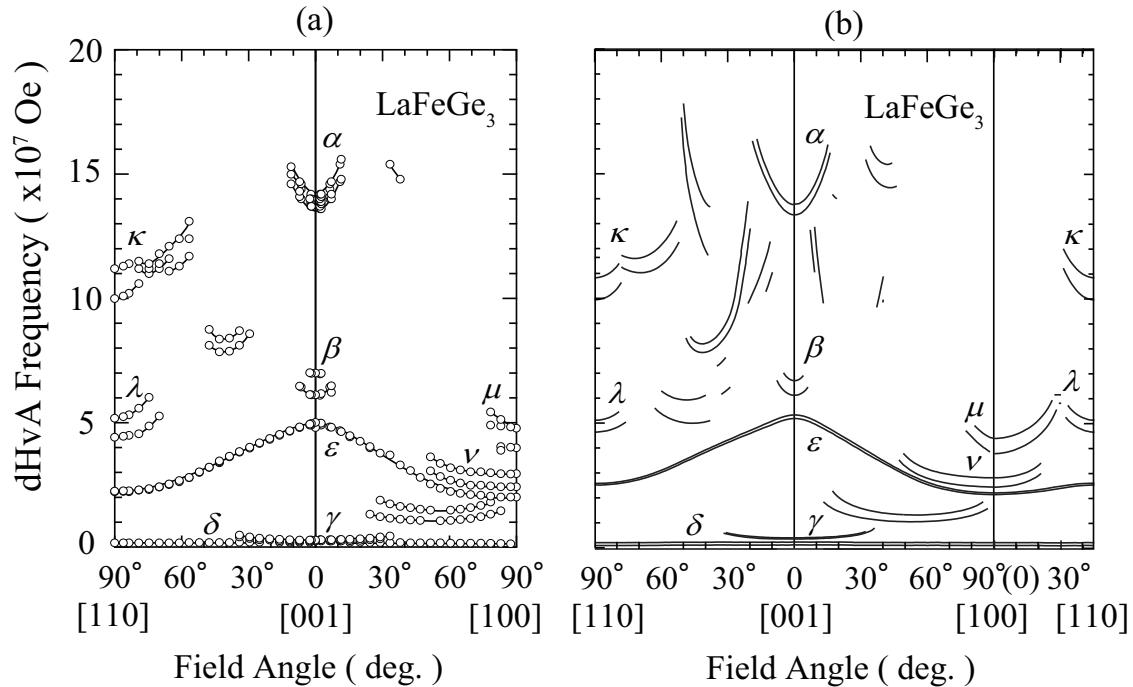
Fig. 6.14 (a) Angular dependence of dHvA frequency in LaFeGe$_3$ and (b) the theoretical one, where the dHvA frequency was theoretically calculated by shifting the $4f$ level of La upward by 0.2 Ry.
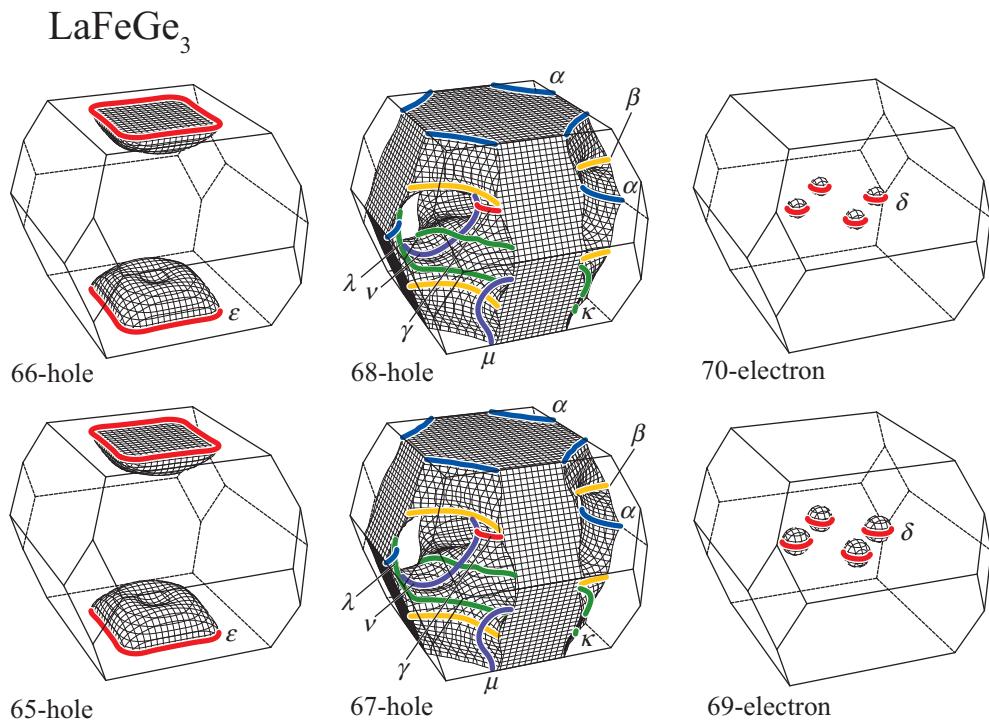
Fig. 6.15 Theoretical Fermi surfaces of LaFeGe$_3$, where the Fermi surface was constructed by shifting the $4f$ level of La upward by 0.2 Ry.

Table 6.IV Detected dHvA frequency F, cyclotron effective mass m_c^* and the theoretical frequency F_b and band mass m_b in LaFeGe$_3$.

	Experiment			Theory		
Branch	$F(\times 10^7 \text{Oe})$	$m_c^*(m_0)$		Branch	$F_b(\times 10^7 \text{Oe})$	$m_b(m_0)$
			$H \mathbin{/\mkern-5mu/} [001]$			
α	14.2	4.32	α	band 68	13.8	2.31
	14.1	3.41				
	13.9	3.83				
	13.8	3.87				
	13.7	4.93		band 67	13.4	2.20
β	7.01	4.93	β	band 67	6.73	2.44
	6.13	3.91		band 68	6.15	2.17
ε	4.99	1.50	ε	band 66	5.37	0.98
	4.93	1.38		band 65	5.21	0.95
			γ	band 68	0.45	0.22
				band 67	0.42	0.23
δ	0.28	0.64	δ	band 69	0.28	0.44
				band 70	0.15	0.44
			$H \mathbin{/\mkern-5mu/} [100]$			
μ	4.78	—	μ	band 68	4.43	2.52
	3.99	2.03		band 67	3.82	3.33
ν	2.91	2.52	ν	band 67	2.85	0.95
	2.39	2.06		band 68	2.48	0.93
ε	2.01	0.76	ε	band 66	2.31	0.58
	1.99	0.77		band 65	2.25	0.57
	1.92	0.89				
δ			δ	band 69	0.26	0.42
				band 70	0.13	0.40
			$H \mathbin{/\mkern-5mu/} [110]$			
κ	11.2	3.69	κ	band 68	10.9	2.54
	10.0	4.83		band 67	9.97	2.45
λ	5.17	3.55	λ	band 67	5.15	1.77
	4.42	3.03		band 68	4.68	1.71
ε	2.22	1.34	ε	band 66	2.63	0.64
				band 65	2.57	0.65
			δ	band 69	0.25	0.40
				band 70	0.13	0.39

6.1.3 Discussion

We will discuss the Fermi surface properties and the magnitude of the antisymmetric spin-orbit interaction in LaTX$_3$. First we will compare the present dHvA data of LaRhGe$_3$ and LaIrGe$_3$ with those of LaCoGe$_3$, as shown in Fig. 6.16. The topology of the Fermi surface is approximately the same in LaTGe$_3$ (T = Co, Rh, Ir). This is simply understood from the fact that the valence electrons are approximately the same in LaTGe$_3$: $3d^7 4s^2$ in Co, $4d^8 5s^1$ in Rh and $5d^9$ in Ir. It is, however, noticed that the dHvA frequency of branch α in LaCoGe$_3$ is smaller than those in LaRhGe$_3$ and LaIrGe$_3$, and the width of the split dHvA frequencies, $|F_+ - F_-|$, for branch α in LaIrGe$_3$ is larger than those in LaCoGe$_3$ and LaRhGe$_3$. The former indicates that the Fermi surface in LaCoGe$_3$ is slightly smaller in volume than those in LaRhGe$_3$ and LaIrGe$_3$. The latter indicates that the antisymmetric spin-orbit interaction of $2|\alpha p_\perp|$ in LaIrGe$_3$ is larger than those in LaCoGe$_3$ and LaRhGe$_3$: $2|\alpha p_\perp| = 460\,\mathrm{K}$ in LaCoGe$_3$, $510\,\mathrm{K}$ in LaRhGe$_3$ and $1090\,\mathrm{K}$ in LaIrGe$_3$ for branch α. Precise values for the other branches are also summarized in Table 6.V.

The present dHvA result of LaIrGe$_3$ is also compared with that of LaIrSi$_3$, as shown in Fig. 6.17. Here, the valence electrons are $3s^2 3p^2$ in Si and $4s^2 4p^2$ in Ge. The dHvA frequency of LaIrGe$_3$ is slightly smaller than that of LaIrSi$_3$ because the lattice constants of $a = 4.4343\,\text{Å}$ and $c = 10.0638\,\text{Å}$ in LaIrGe$_3$ are larger than $a = 4.2820\,\text{Å}$ and $c = 9.8391\,\text{Å}$ in LaIrSi$_3$ and the corresponding Brillouin zone in LaIrGe$_3$ is smaller than that in LaIrSi$_3$ in volume. The $2|\alpha p_\perp|$ value is almost the same between two compounds. The $2|\alpha p_\perp|$ values are summarized in Table 6.V.
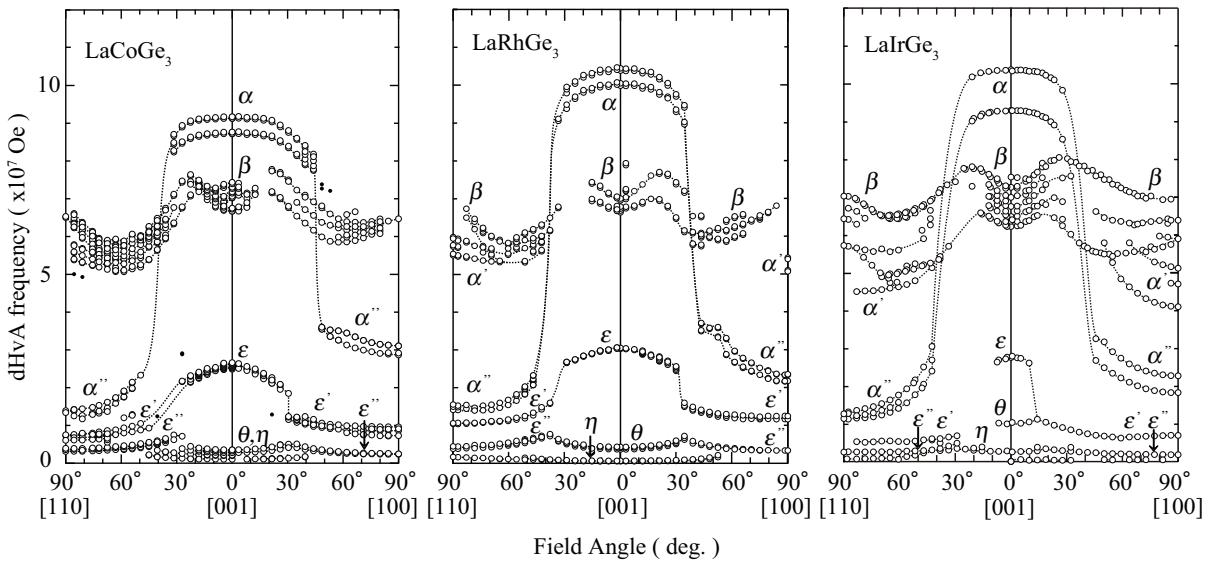
Fig. 6.16 Angular dependence of dHvA frequency in LaCoGe$_3$, LaRhGe$_3$ and LaIrGe$_3$.

Table 6.V Magnitude of the antisymmetric spin-orbit interaction for $H // [001]$ in LaTX$_3$ (T = Co, Rh, Ir and X = Si, Ge) and PrCoGe$_3$.

	branch α			branch β		
	$F(\times 10^7 \text{Oe})$	$m_c^*(m_0)$	$2|\alpha p_\perp|(\text{K})$	$F(\times 10^7 \text{Oe})$	$m_c^*(m_0)$	$2|\alpha p_\perp|(\text{K})$
LaCoGe$_3$	9.15	1.19	461	7.09	1.28	416
	8.74	1.20		6.72	1.11	
LaRhGe$_3$	10.4	1.04	511	6.98	0.83	505
	10.0	1.04		6.67	0.85	
LaIrGe$_3$	10.4	1.13	1090	7.25	1.32	1066
	9.29	1.51		6.22	1.29	
LaIrSi$_3$	10.9	0.97	1100	7.64	0.97	1250
	10.0	1.03		6.76	0.92	
PrCoGe$_3$	9.04	1.80	284	7.13	2.04	302
	8.64	1.97		6.71	1.70	
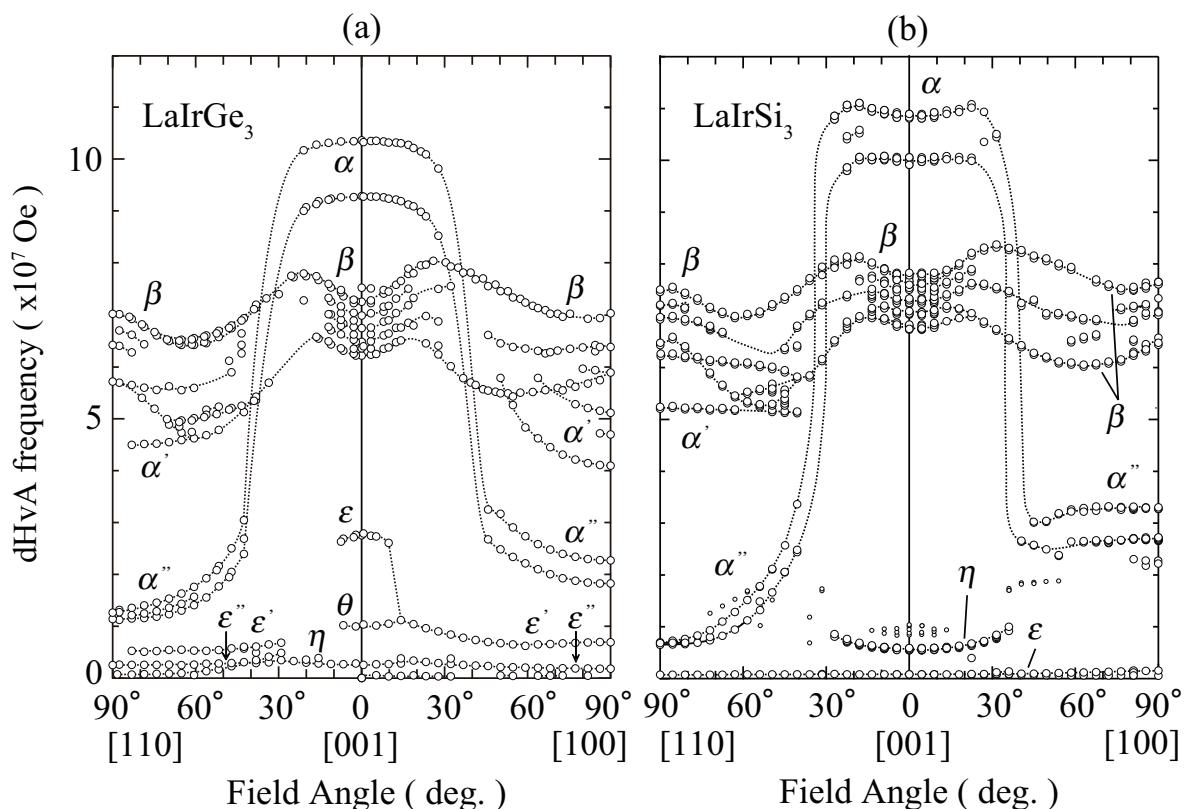
Fig. 6.17 Angular dependence of dHvA frequency in LaIrGe$_3$ and LaIrSi$_3$.

In the present dHvA experiment, we changed the potentials by changing the transition metal T = Co, Rh and Ir in LaTGe$_3$. We will explain the reason why the antisymmetric spin-orbit interaction in LaIrGe$_3$ is relatively large compared with those in LaCoGe$_3$ and LaRhGe$_3$. This is related to both the characteristic radial wave function $\phi(r)$ of Ir-5d electrons and the relatively large effective atomic number Z_{eff} in Ir close to the nuclear center. Here we simply calculate the spin-orbit interaction for the d electrons, not in the lattice but in the isolated atom, following the method presented by Koelling and Harmon.[138]

Figure 6.18 shows the radial wave function $r\phi(r)$ as a function of the distance r for Ir-5d, Rh-4d and Co-3d electrons. Here, we assumed the valence electrons to be $3d^74s^2$ in Co, $4d^75s^2$ in Rh and $5d^76s^2$ in Ir. The $r\phi(r)$ function of Ir-5d electrons possesses a maximum at $r = 0.11$ a. u., very close to the atomic center, while the corresponding distance r is 0.23 a. u. in Rh-4d and 0.66 a. u. in Co-3d, far from the atomic center.

Next we will consider the potential $V(r)$, which corresponds to the sum of the nuclear potential, and the classical Coulomb and exchange-correlation potential derived from electrons. Figure 6.19(a) shows the coupling constant of the spin-orbit interaction, $r^2 dV(r)/dr$. Simply thinking, this value corresponds to the effective atomic number Z_{eff} in the potential $V(r) = -Z_{\text{eff}}/r$. Z_{eff} at $r = 0$ is very close to the atomic number Z in the nuclear potential $V(r) = -Z/r$, where Z is 77, 45 and 27 for Ir, Rh and Co, respectively. As shown in Fig. 6.19(a), the coupling constant of the spin-orbit interaction is reduced steeply as a function of the distance r because of a screening of the nuclear charge by the electron charge, reaching $Z_{\text{eff}} \to 1$ for $r \to \infty$.

Finally we calculate the spin-orbit interaction, I_{so}:

$$I_{\text{so}} = \frac{\hbar^2}{2m^2c^2} \int_0^r \frac{1}{r} \frac{dV(r)}{dr} |r\phi(r)|^2 \, dr, \tag{6.1}$$

which is shown in Fig. 6.19(b) as a function of the distance r. The spin-orbit interaction becomes constant at about 1.0 a. u., but approximately reaches this constant value at $r = 0.11$ a. u. for Ir-5d, 0.23 a. u. for Rh-4d and 0.66 a. u. for Co-3d, where the corresponding radial wave functions possess the extremal values, respectively, as mentioned above. The spin-orbit interaction is thus obtained to be 38.0 mRy (6000 K) in Ir-5d, 12.8 mRy (2020 K) in Rh-4d and 5.72 mRy (900 K) in Co-3d. The present calculations indicate that the radial wave function of Ir-5d electrons possesses a large distribution at the distance close to the center, compared with those of Rh-4d and Co-3d electrons, which produces the relatively large value of the spin-orbit interaction in Ir, closely connected to the relatively large effective atomic number Z_{eff} in Ir at the distance r close to the atomic center.

The present result of the spin-orbit interaction for the isolated atom is applied to the lattice or the non-centrosymmetric crystal. In the case of the non-centrosymmetric crystal, the degenerate Fermi surface is split into two Fermi surfaces of which the magnitude of the antisymmetric spin-orbit interaction is approximately proportional to the spin-orbit interaction based on eq. (6.1) because the same potential is in principle used in the band structure calculation. The d electrons in the T atom as well as the 5d electrons in the La atom and the other electrons contribute to the conduction electrons in LaTGe$_3$.
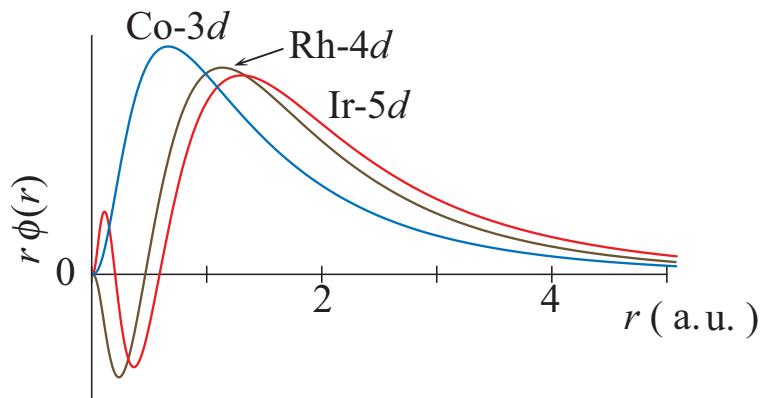
Fig. 6.18 Radial wave function $r\phi(r)$ as a function of the distance r for Ir-5d, Rh-4d and Co-3d electrons in the isolated atoms.
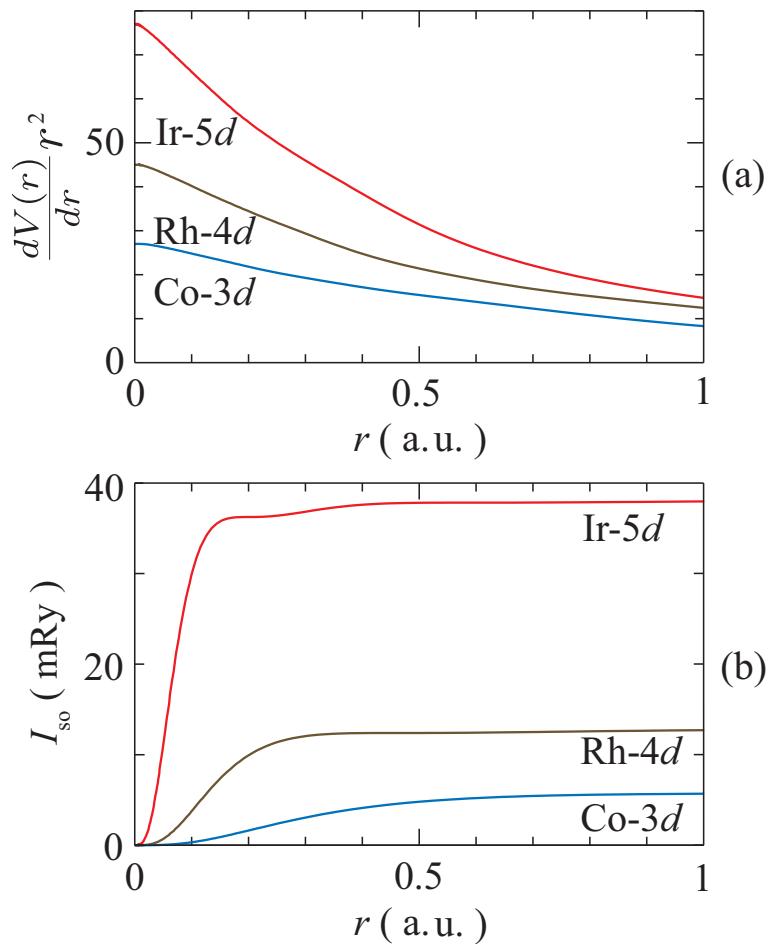

Fig. 6.19 (a) Coupling constant of the spin-orbit interaction $(\mathrm{d}^2 V(r)\mathrm{d}r^2)r^2$ and (b) the spin-orbit interaction I_{so} as a function of the distance r for Ir-5d, Rh-4d and Co-3d electrons in the isolated atoms.

This is the main reason why the antisymmetric spin-orbit interaction $2|\alpha p_\perp|$ in LaIrGe$_3$ and LaIrSi$_3$ is larger than those of LaCoGe$_3$ and LaRhGe$_3$. The present result is also applied to the antisymmetric spin-orbit interaction of non-centrosymmetric paramagnetic compounds Li$_2$Pt$_3$B and Li$_2$Pd$_3$B,[139)] where the antisymmetric spin-orbit interaction in Li$_2$Pt$_3$B, which is mainly due to the contribution of Pt-5d electrons, is expected to be larger than that in Li$_2$Pd$_3$B.

Next we will discuss the antisymmetric spin-orbit interaction in PrCoGe$_3$. As shown in Table 6.V, the $2|\alpha p_\perp|$ value in PrCoGe$_3$ is nearly half or smaller than the corresponding one in LaCoGe$_3$ because the cyclotron mass of PrCoGe$_3$ is nearly twice as large as that of LaCoGe$_3$. It is also noticed that the width of the split dHvA frequencies, $|F_+ - F_-|$, is unchanged between PrCoGe$_3$ and LaCoGe$_3$. This can be simply understood when we compare the angular dependence of the dHvA frequency of PrCoGe$_3$ in Fig. 6.11(a) with that of LaCoGe$_3$ shown in Fig. 6.11(b). The contribution of localized $4f$ electrons to the topology of Fermi surface is thus very small in PrCoGe$_3$, but enhances the cyclotron mass.

Finally we will discuss the reason why the cyclotron mass of LaFeGe$_3$ is relatively large. The electronic specific heat coefficient γ is $\gamma = 9.4\,\mathrm{mJ/K^2 \cdot mol}$ in LaFeGe$_3$, $4.4\,\mathrm{mJ/K^2 \cdot mol}$ in LaCoGe$_3$, $5.0\,\mathrm{mJ/K^2 \cdot mol}$ in LaRhGe$_3$ and $4.5\,\mathrm{mJ/K^2 \cdot mol}$ in LaIrGe$_3$.[95, 99, 103)] The corresponding theoretical one γ_b is calculated to be $5.74\,\mathrm{mJ/K^2 \cdot mol}$ in LaFeGe$_3$, $4.48\,\mathrm{mJ/K^2 \cdot mol}$ in LaCoGe$_3$, $4.28\,\mathrm{mJ/K^2 \cdot mol}$ in LaRhGe$_3$ and $3.58\,\mathrm{mJ/K^2 \cdot mol}$ in LaIrGe$_3$. The relatively large γ value of LaFeGe$_3$ is due to the contribution of $3d$ electrons in the Fe atom. Figure 6.20 shows the density of states in LaFeGe$_3$, together with the partial density of states such as the Fe-$3d$ electrons. The large γ value corresponds to
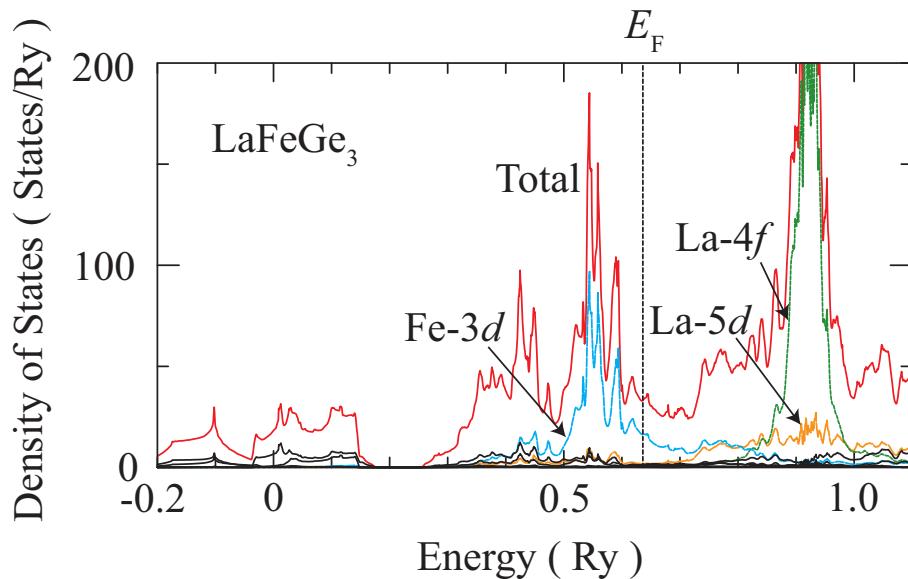
Fig. 6.20 Electronic density of states in LaFeGe$_3$, where the $4f$ level of La was shifted upward by $0.2\,\mathrm{Ry}$.

the large cyclotron mass in LaFeGe$_3$, ranging from $m_c^* = 0.76\, m_0$ to $4.9\, m_0$. It is noticed that the mass enhancement produces a small magnitude of the antisymmetric spin-orbit interaction: $2|\alpha p_\perp| = 134$ K in branch α and 267 K in branch β, as shown in Table 6.VI.

Recently, the γ value of CeIrSi$_3$ is found to be unchanged as a function of pressure even at the critical pressure $P_c = 2.25$ GPa,[107] where the Néel temperature $T_N = 5.0$ K at ambient pressure becomes zero. The magnitude of the antisymmetric spin-orbit interaction of CeIrSi$_3$ can be simply estimated from the γ value: $2|\alpha p_\perp| \simeq 40$ K is obtained in CeIrSi$_3$ from $2|\alpha p_\perp| \simeq 1000$ K and $\gamma = 4.5$ mJ/K^2·mol in LaIrSi$_3$, and $\gamma = 110$ mJ/K^2·mol in CeIrSi$_3$.[22] This value is extremely larger than the superconducting transition temperature $T_{sc} = 1.6$ K at 2.65 GPa in CeIrSi$_3$. The dHvA experiment for CeIrSi$_3$ under pressure is now in progress to clarify the $2|\alpha p_\perp|$ value in CeIrSi$_3$.

Table 6.VI Magnitude of the antisymmetric spin-orbit interaction for $H\,//\,[001]$ in LaFeGe$_3$.

	LaFeGe$_3$		
	Experiment		
Branch	$F(\times 10^7 \mathrm{Oe})$	$m_c^*(m_0)$	$2|\alpha p_\perp|$(K)
α	$\left\{\begin{array}{l} 14.2 \\ 13.7 \end{array}\right.$	3.86 4.40	134
β	$\left\{\begin{array}{l} 7.01 \\ 6.13 \end{array}\right.$	4.93 3.91	267
ε	$\left\{\begin{array}{l} 4.99 \\ 4.93 \end{array}\right.$	1.50 1.38	57

6.2 Magnetic and superconducting properties of CeTX$_3$

6.2.1 Overview of magnetic properties of CeTX$_3$

We measured the magnetic susceptibility χ in CeTSi$_3$ and CeTGe$_3$ single crystals, as shown in Fig. 6.21. The susceptibility data of CeRhSi$_3$, CeIrSi$_3$ were cited from refs. 22, 100, respectively. The anisotropy of the magnetic susceptibility is almost the same in CeTSi$_3$ and CeTGe$_3$, meaning that the susceptibility in the paramagnetic state for $H /\!/ [100]$, χ_a, is larger than that for $H /\!/ [001]$, χ_c, except for CeCoGe$_3$. The Néel temperature is in the range from $T_N = 1.8\,\mathrm{K}$ in CeRhSi$_3$ to $T_N = 21\,\mathrm{K}$ in CeCoGe$_3$.

The magnetic susceptibility was analyzed on the basis of the CEF model for CePtSi$_3$, CeIrSi$_3$,[22] and CeCoGe$_3$[103], as mentioned Chap. 6.2.2. The CEF Hamiltonian for tetragonal point symmetry is given as follows:

$$\mathcal{H}_{\mathrm{CEF}} = B_2^0 \boldsymbol{O}_2^0 + B_4^0 \boldsymbol{O}_4^0 + B_4^4 \boldsymbol{O}_4^4, \tag{6.2}$$

where B_l^m are the CEF parameters and $\boldsymbol{O}_l^m$ are the Stevens operators. [29,30] It is clear from the previous CEF analyses that the present anisotropy of the magnetic susceptibil-
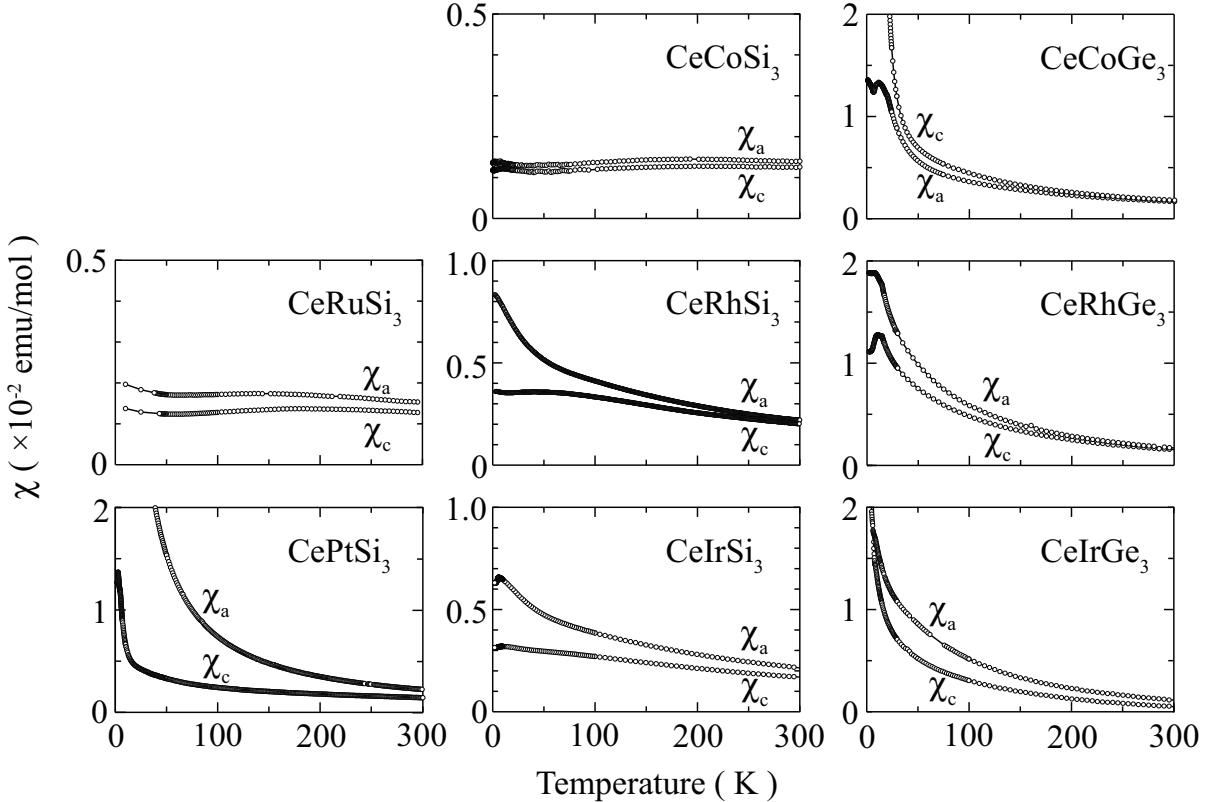
Fig. 6.21 Temperature dependence of the magnetic susceptibility in CeTSi$_3$ and CeTGe$_3$. The data of CeRhSi$_3$ and CeIrSi$_3$ are cited from refs. 100 and 22, respectively.

ity mentioned above is mainly due to the positive and large value of B_2^0: $B_2^0 = 14\,\mathrm{K}$ in CePtSi$_3$, $9\,\mathrm{K}$ in CeIrSi$_3$ and $3\,\mathrm{K}$ in CeCoGe$_3$. Namely, the magnetic easy-axis in magnetization is determined from the contribution of the value of B_2^0 in the present tetragonal structure.

Here we briefly describe the magnetic properties of CeTSi$_3$. Among CeTSi$_3$, CeRuSi$_3$, CeOsSi$_3$ and CeCoSi$_3$ are paramagnets. We could not, however, succeed in growing single crystals of CeOsSi$_3$, where some magnetic impurities are included even in the polycrystal samples. As shown in Fig. 6.21, the magnetic susceptibility possesses a maximum around $150\,\mathrm{K}$ in CeRuSi$_3$ and $200\,\mathrm{K}$ in CeCoSi$_3$. Next, antiferromagnets CeRhSi$_3$ and CeIrSi$_3$ are very similar each other in the electrical and magnetic properties, which order antiferromagnetically at $T_\mathrm{N} = 1.8\,\mathrm{K}$ and $5.0\,\mathrm{K}$, respectively. CePdSi$_3$ and CePtSi$_3$ also order antiferromagnetically at $T_\mathrm{N} = 5.2\,\mathrm{K}$ and $4.8\,\mathrm{K}$, respectively, although single crystals were not obtained in CePdSi$_3$. In order to reduce space, the susceptibility data in CePtSi$_3$ are shown in the left hand side of Fig. 6.21, namely below the CeRuSi$_3$ data. In the next section, we precisely studied the electrical and magnetic properties of a single crystal CePtSi$_3$. The CEF analyses are also carried out.

6.2.2   CePtSi$_3$

First we show in Fig. 6.22(a) the temperature dependence of the electrical resistivity ρ for a single crystal sample in the current J along the [100] direction. The resistivity decreases monotonically with decreasing the temperature and decreases steeply below the Néel temperature $T_\mathrm{N1} = 4.8\,\mathrm{K}$, as shown in Fig. 6.22(b). The present ordering temperature of $T_\mathrm{N1} = 4.8\,\mathrm{K}$ is smaller than the ordering temperature of $11\,\mathrm{K}$ with a spin glass character in the previous report. [102] The spin glass property is not observed in the present single crystal sample, as shown later. The electrical resistivity is found to show a step-like decrease at $T_\mathrm{N2} = 2.4\,\mathrm{K}$, suggesting a first-order like change of the magnetic structure. Below $1\,\mathrm{K}$, the resistivity follows the Fermi liquid relation of $\rho = \rho_0 + AT^2$ ($\rho_0 = 16.4\,\mu\Omega\cdot\mathrm{cm}$ and $A = 0.78\,\mu\Omega\cdot\mathrm{cm/K}^2$).
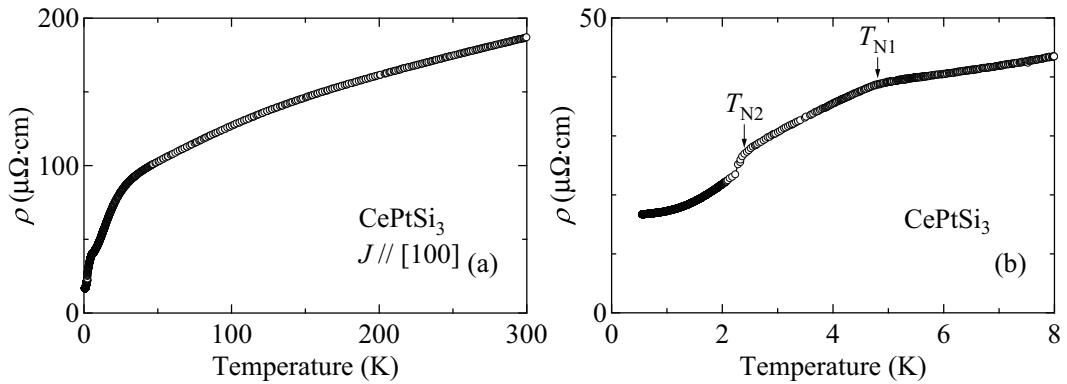
Fig. 6.22 Temperature dependence of the electrical resistivity (a) below room temperature and (b) at low temperatures in CePtSi$_3$.

Next we measured the temperature dependence of the specific heat C in the form of C/T in the temperature range from 0.5 to 8 K. The specific heat indicates clear peaks at $T_{N1} = 4.8$ K and at $T_{N2} = 2.4$ K, as shown by arrows in Fig. 6.23(a). We note that the specific heat anomaly at T_{N1} is of the usual λ-shape, while the anomaly at T_{N2} is sharp, suggesting the first-order like phase transition. In Fig. 6.23(b) we show the T^2-dependence of C/T. The low-temperature specific heat consists of the electronic specific heat γT and the specific heat βT^3 of phonon and antiferromagnetic contributions. The γ value is obtained as $\gamma = 29$ mJ/K^2·mol from the data in Fig. 6.23(b). We also estimated the magnetic entropy S_{mag} by simply integrating C/T over temperature up to T_{N1}: S_{mag} $= 0.8R\ln 2$, indicating a doublet ground state of the $4f$-crystalline electric field (CEF) scheme.
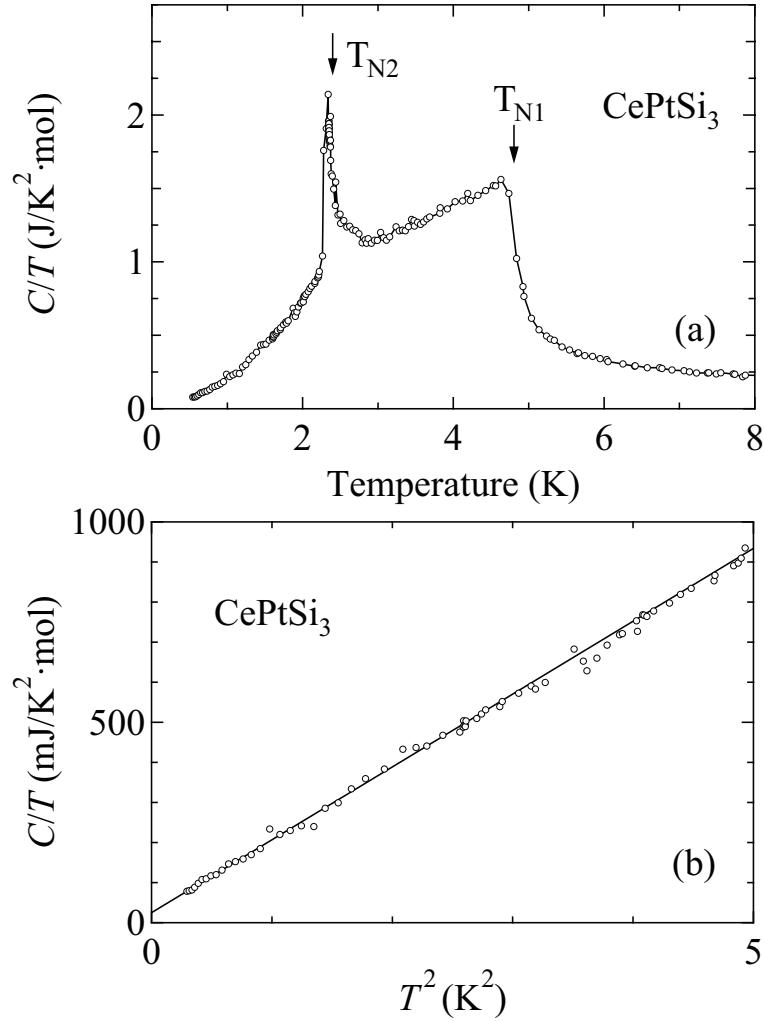
Fig. 6.23 (a) Temperature dependence of the specific heat C in the form of C/T and (b) the T^2-dependence of C/T in CePtSi$_3$.

Next we measured the temperature dependence of the magnetic susceptibility. Figure 6.24 shows the logarithmic scale of temperature dependence of the magnetic susceptibility χ. The susceptibility is highly anisotropic between $H \,//\, [100]$ and $H \,//\, [001]$, which is mainly due to the CEF effect, as discussed below. The low-temperature susceptibility indicates characteristic features at T_{N1} and T_{N2}, shown by arrows. Note that the susceptibility shows a step-like decrease at T_{N2} for $H \,//\, [100]$.
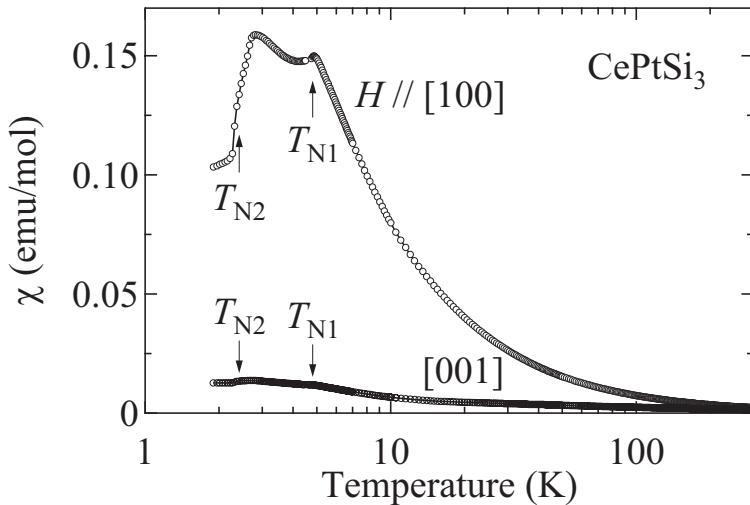
Fig. 6.24 Logarithmic scale of temperature dependence of the magnetic susceptibility in CePtSi$_3$.

The susceptibility follows the Curie-Weiss law above about 200 K, as shown in Fig. 6.27(a), and the effective magnetic moment μ_{eff} is obtained as $2.27\,\mu_{\text{B}}/\text{Ce}$ and $2.42\,\mu_{\text{B}}/\text{Ce}$ for $H \,//\, [100]$ and $[001]$, respectively. These values are slightly smaller than the free ion value of $2.54\,\mu_{\text{B}}/\text{Ce}$ for Ce^{3+} ion, suggesting that the total energy of CEF splitting is large in CePtSi$_3$, which will be discussed later. The Weiss constant was determined as $\theta_{\text{p}} = 12.2\,\text{K}$ and $-211\,\text{K}$ for $H \,//\, [100]$ and $[001]$, respectively. The present anisotropy of the susceptibility is similar to that in CeRhSi$_3$ and CeIrSi$_3$.[21, 100]

We measured the magnetization at 2 K, as shown in Fig. 6.25. The magnetization for $H \,//\, [100]$ indicates metamagnetic transitions at $H_{c1} = 1.8\,\text{kOe}$ and $H_{c2} = 15\,\text{kOe}$ and saturates above $H_s = 45\,\text{kOe}$, with an ordered moment of $1.15\,\mu_B/\text{Ce}$. The magnetization for $H \,//\, [001]$ also indicates a small metamagnetic transition at $H_c = 52\,\text{kOe}$. From these magnetization curves, the magnetic structure is complicated, but the $[100]$ direction is the easy-axis in magnetization, while the $[001]$ direction corresponds to the hard-axis.

We also measured the temperature dependence of magnetization under several magnetic fields. Figure 6.26(a) and 6.26(b) show the magnetic phase diagrams for $H \,//\, [100]$ and $[001]$, respectively. The metamagnetic transition fields H_{c1} and H_{c2} for $H \,//\, [100]$ are found to be connected to $T_{N2} = 2.4\,\text{K}$ at zero field, while the saturation field H_s is connected to the Néel temperature $T_{N1} = 4.8\,\text{K}$ at zero field. The magnetic phase diagram
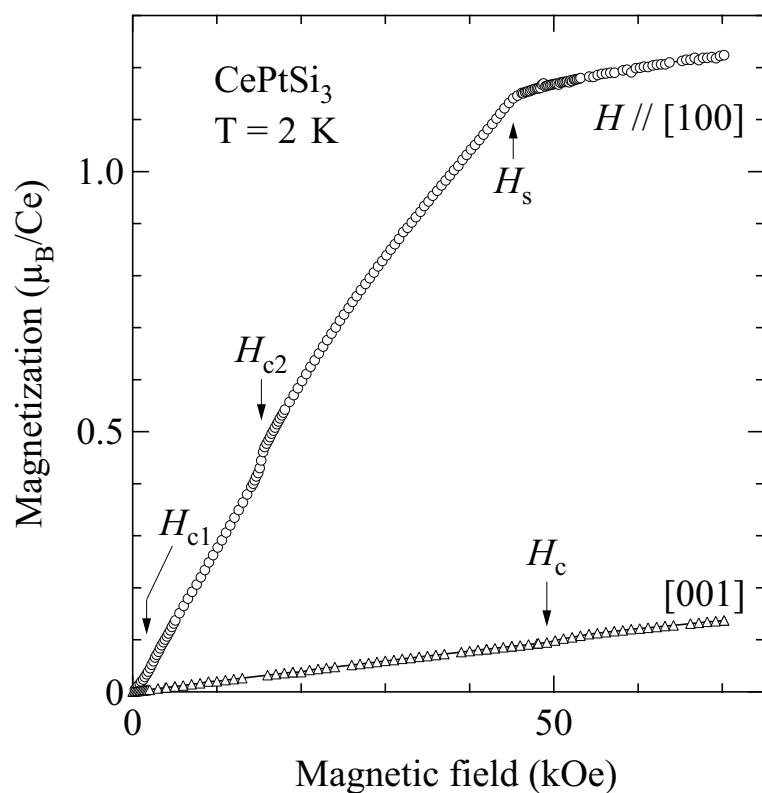
Fig. 6.25 Magnetization curves in CePtSi$_3$.
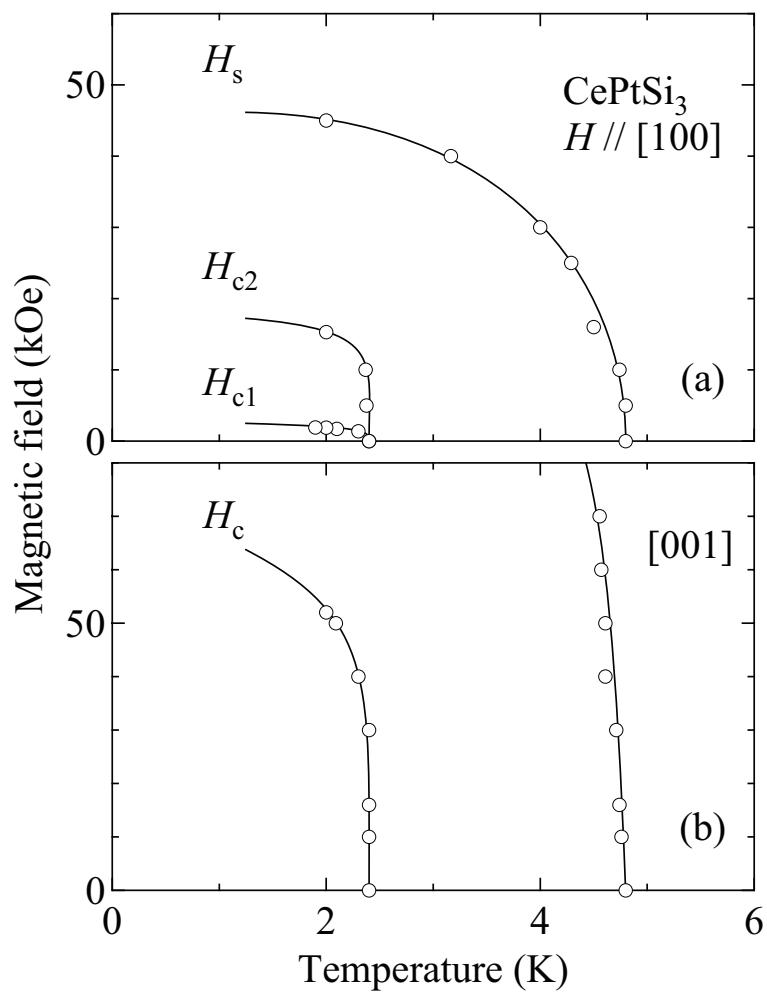
Fig. 6.26 Magnetic phase diagrams in CePtSi$_3$. Solid lines connecting the data are guidelines.

is approximately similar between $H // [100]$ and $[001]$, although the saturation field for $H // [001]$ is expected to be extremely large.

The present anisotropy of the magnetic susceptibility and magnetization between $H // [100]$ and $[001]$ is very similar to that of pressure-induced superconductors of CeRhSi₃ and CeIrSi₃.[21,100] This is commonly ascribed to the CEF effect in these compounds. The magnetic structure and magnetic moment in CePtSi₃ are highly different from those of CeRhSi₃ and CeIrSi₃, although these compounds are antiferromagnets with an easy-axis along [100]. For example, our pulse-field magnetization experiment for CeIrSi₃ indicated that the magnetization for $H // [100]$ at 1.3 K increases linearly as a function of magnetic field, $0.5\,\mu_B$/Ce at 500 kOe. A phase boundary between an antiferromagnetic state and the paramagnetic state is not attained in fields up to 500 kOe.

On the other hand, the magnetization for $H // [100]$ in CePtSi₃ with $T_{N1} = 4.8$ K saturates at a small field of 45 kOe at 2 K. The ordered moment is determined as $1.15\,\mu_B$/Ce in CePtSi₃. CePtSi₃ is thus classified as a usual f-localized compound, whereas CeRhSi₃ and CeIrSi₃ are Kondo compounds with antiferromagnetic ordering.[97] In fact, the γ value of 29 mJ/K²· mol is small in CePtSi₃, which is compared with 110 and 120 mJ/K²· mol in CeRhSi₃ and CeIrSi₃, respectively.

Here we discuss the CEF effect in CePtSi₃. The $J = 5/2$ multiplet of the Ce³⁺ ion splits into three doublets in the $4f$-CEF scheme with tetragonal symmetry. In order to understand the present anisotropy in the susceptibility and the magnetization, we have performed the CEF analysis on these data. The CEF Hamiltonian for the tetragonal site symmetry is given by eq. 6.2 The magnetic susceptibility based on the CEF model, χ^i_{CEF} ($i = x, y, z$), is given by

$$\chi^i_{\text{CEF}} = N(g_J\mu_B)^2 \frac{1}{Z}\left(\sum_{m \neq n} |\langle m | J_i | n \rangle|^2 \frac{1 - e^{-\frac{\Delta_{m,n}}{k_B T}}}{\Delta_{m,n}} e^{-\frac{E_n}{k_B T}}\right.$$
$$\left. + \frac{1}{k_B T} \sum_n |\langle n | J_i | n \rangle|^2 e^{-\frac{E_n}{k_B T}}\right), \qquad (6.3)$$

and

$$Z = \sum_n e^{-\frac{E_n}{k_B T}}, \qquad (6.4)$$

where g_J is the Landé g-factor ($= 6/7$ for Ce³⁺), J_i is the component of the angular momentum and $\Delta_{m,n} = E_n - E_m$. The magnetic susceptibility χ_i including a small temperature-independent susceptibility χ_0 and the molecular field contribution λ_i is given as follows:

$$\chi_i^{-1} = (\chi^i_{\text{CEF}} + \chi_0)^{-1} - \lambda_i. \qquad (6.5)$$

We have also calculated the magnetization by using the following formula:

$$M_i = g_J\mu_B \sum_n |\langle n | J_i | n \rangle| \frac{e^{-\beta E_n}}{Z}, \qquad (6.6)$$

where the eigenvalue E_n and the eigenfunction $|n\rangle$ are determined by diagonalizing the total Hamiltonian:

$$\mathcal{H} = \mathcal{H}_{\text{CEF}} - g_J\mu_{\text{B}}J_i(H + \lambda_i M_i), \tag{6.7}$$

where $\mathcal{H}_{\text{CEF}}$ is given by eq. (6.2), the second term is the Zeeman term and the third one is the molecular field. Solid lines in Fig. 6.27 are the results of CEF calculations.

The CEF parameters of B_l^m, energy level scheme and the corresponding wave functions are summarized in Table 6.VII. It is noted that the obtained splitting energy Δ_2 between the ground state and the second excited state is large: $\Delta_2 = 1002\,\text{K}$. This is quite contrastive to the case of CeIrSi$_3$, $\Delta_1 = 160\,\text{K}$ and $\Delta_2 = 501\,\text{K}$. [21)] Furthermore, the ground
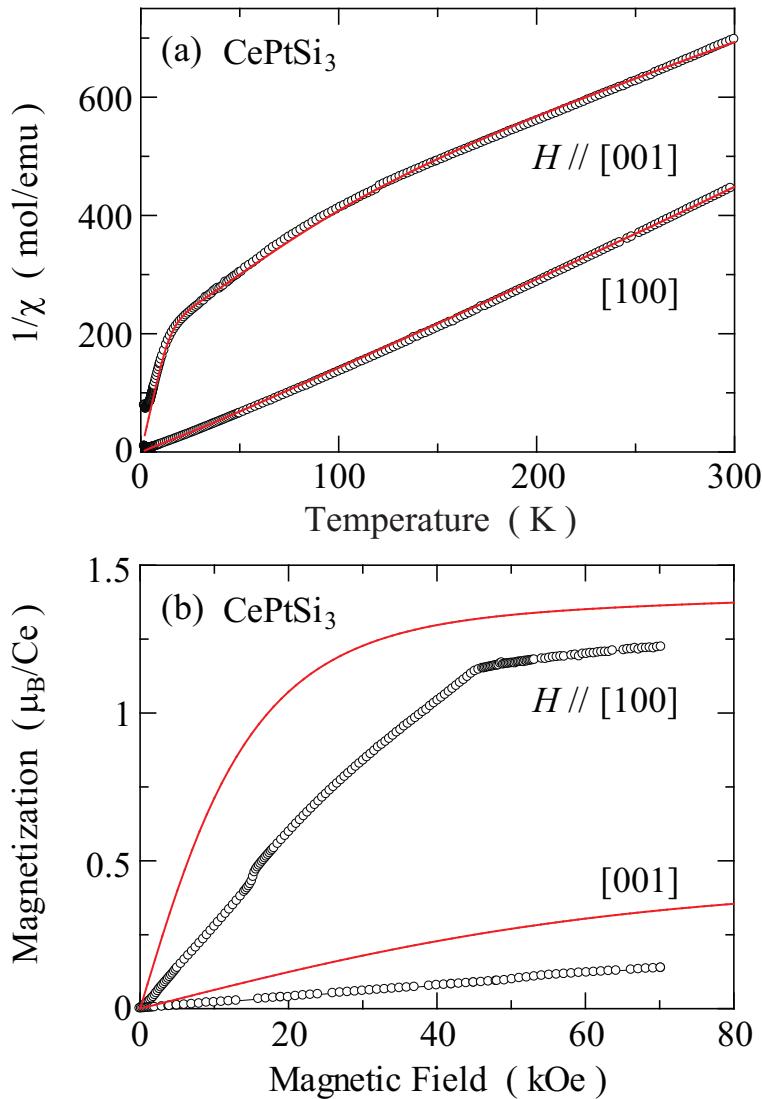
Fig. 6.27 (a) Inverse susceptibility and (b) magnetization curves of CePtSi$_3$. Solid lines are the results of CEF calculations.

state $|\pm 1/2\rangle$ in CePtSi$_3$ is also different from that in CeIrSi$_3$, $0.607|\pm 5/2\rangle - 0.795\,|\mp 3/2\rangle$. It is also noted that the B_2^0 value is positive, and is relatively large, which determines the easy-axis in magnetization or magnetic susceptibility in the paramagnetic state.

Table 6.VII CEF parameters, energy level schemes and the corresponding wave functions for CePtSi$_3$.

CEF parameters					
B_2^0 (K)	B_4^0 (K)	B_4^4 (K)	λ (emu/mol)$^{-1}$	χ_0 (emu/mol)	
14	-2	16.7	$\lambda^{x,y} = 1$	$\chi_0^{x,y} = -3.7 \times 10^{-4}$	
			$\lambda^z = 1$	$\chi_0^z = -1.2 \times 10^{-4}$	
energy levels and wave functions					
E (K)	$|-5/2\rangle$	$|-3/2\rangle$	$|-1/2\rangle$	$|+1/2\rangle$	$|+3/2\rangle$	$|+5/2\rangle$
1002	-0.579	0	0	0	-0.815	0
1002	0	-0.815	0	0	0	-0.579
53.5	0.815	0	0	0	-0.579	0
53.5	0	-0.579	0	0	0	0.815
0	0	0	1	0	0	0
0	0	0	0	1	0	0

6.2.3   CeTGe$_3$

Next, we describe the magnetic properties of CeTGe$_3$. CeCoGe$_3$, CeRhGe$_3$ and CeIrGe$_3$ order antiferromagnetically. The Néel temperature and the successive magnetic transitions are reported to be $T_{N1} = 21$ K, $T_{N2} = 12$ K and $T_{N3} = 8$ K in CeCoGe$_3$,[103] T_{N1} $= 14.6$ K, $T_{N2} = 10$ K and $T_{N3} = 0.55$ K in CeRhGe$_3$, and $T_{N1} = 8.7$ K, $T_{N2} = 4.7$ K and T_{N3} $= 0.7$ K in CeIrGe$_3$.[97] There exists another compound of CeFeGe$_3$ in CeTGe$_3$. CeFeGe$_3$ is a paramagnet with a broad maximum around 50 K in the magnetic susceptibility.[95] We succeeded in growing single crystals of CeFeGe$_3$ by the Bi-flux method, but reliable susceptibility data were not obtained because single crystals are extremely small in size.

The magnetic structures in CeTX$_3$ are not simple, most likely reflecting the incommensurate magnetic structure. For example, the incommensurate magnetic reflections with the wave vector $\boldsymbol{q} = (\pm 0.215, 0, 0.5)$ were observed in CeRhSi$_3$.[140] We previously investigated the magnetic properties of CeCoGe$_3$, CeIrSi$_3$ and CePtSi$_3$ by measuring the magnetic susceptibility, magnetization and specific heat, and clarified the CEF schemes for these compounds, although the magnetic structure was not simply speculated from the magnetization curves.[22, 103] Here we present the characteristic magnetization curves for CeRhGe$_3$ and CeIrGe$_3$.

Figure 6.28 shows the magnetization curves in CeRhGe$_3$. From the magnetization curves and the magnetic susceptibility in Fig. 6.21, the magnetic easy-axis in the antiferromagnetic state is close to the [001] direction. Note that the magnetic easy-axis
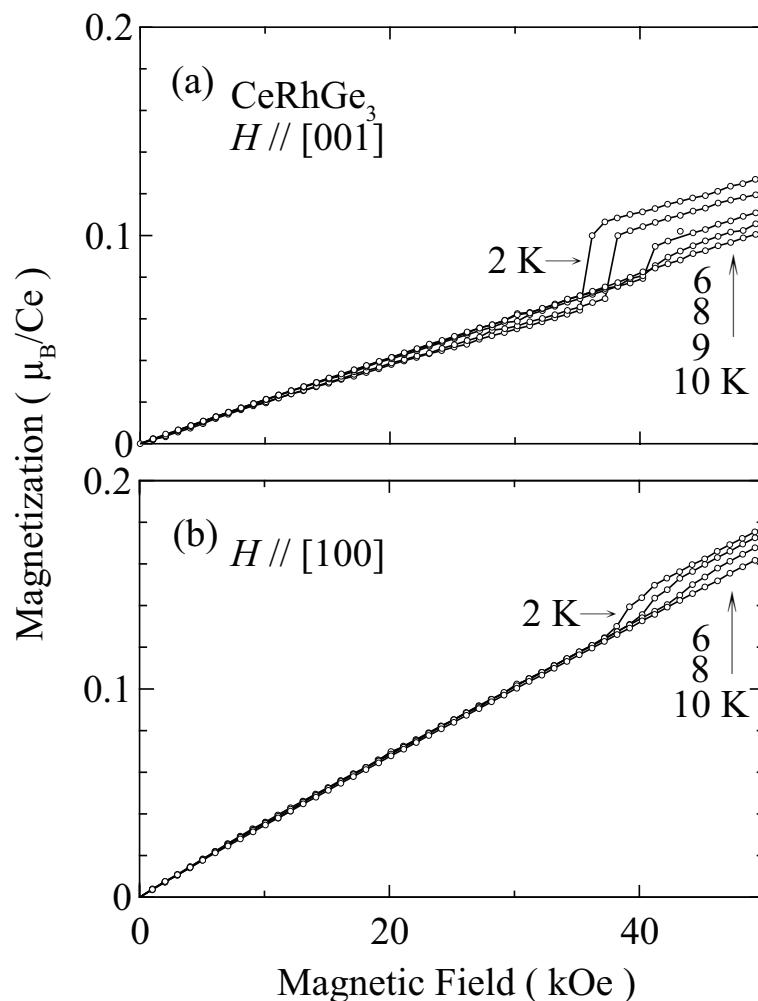
Fig. 6.28 Magnetization curves in CeRhGe$_3$.

in the paramagnetic state is directed along the [100] direction. Both magnetizations for $H // [100]$ and [001] show the metamagnetic transition at low temperatures. As for $H // [001]$ and below $T_{N1} = 14.9\,\text{K}$, the magnetization increases linearly with increasing the magnetic field, as shown in the magnetization curve at $10\,\text{K}$, but indicates a metamagnetic transition below $T_{N2} = 8.2\,\text{K}$, which is smaller than $T_{N2} = 10\,\text{K}$ in the previous report.[97] The critical field H_c decreases from $42\,\text{kOe}$ at $9\,\text{K}$ to $36\,\text{kOe}$ at $2\,\text{K}$. The magnetization above H_c is about $0.10\,\mu_B/\text{Ce}$ in magnitude at $2\,\text{K}$, indicating a very small value. The similar magnetization curves are obtained for $H // [100]$. The corresponding magnetic phase diagram for $H // [100]$ and [001] is shown in Fig. 6.29. The magnetic phase diagram is, however, incomplete, and it is needed to measure the magnetization at much higher fields.
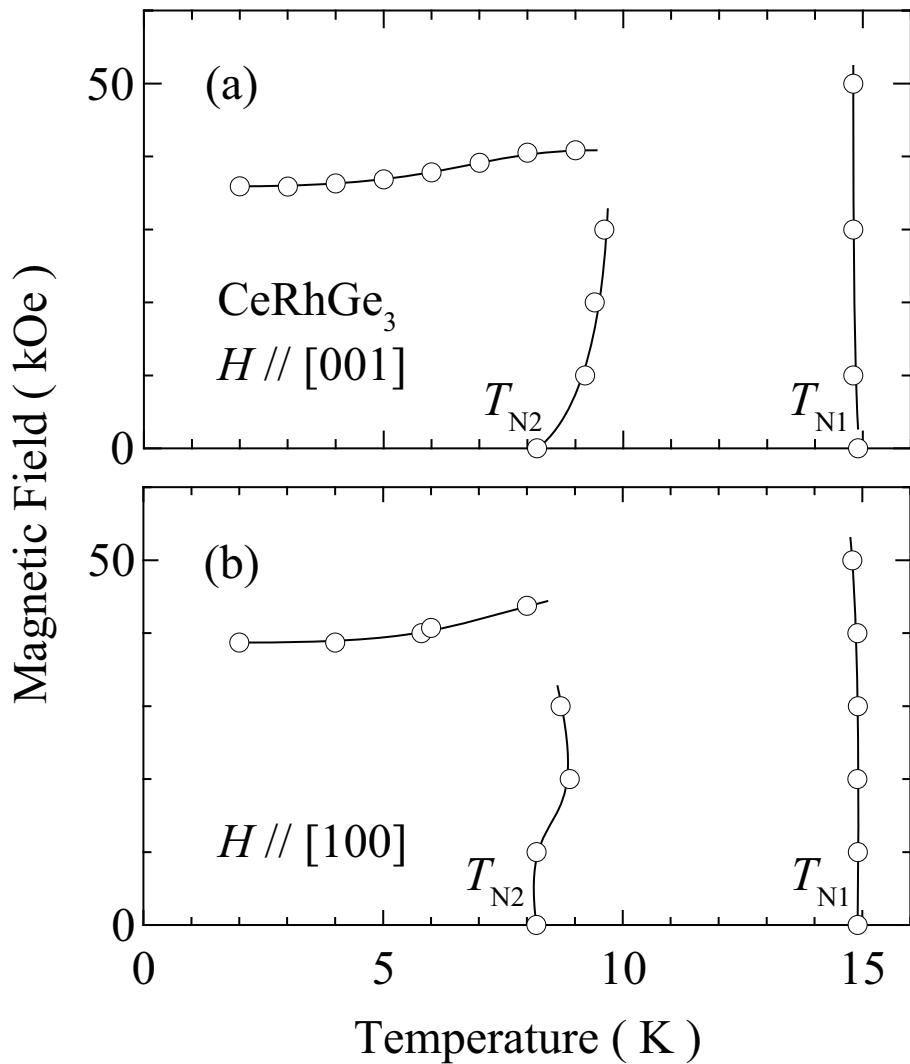
Fig. 6.29 Magnetic phase diagram in CeRhGe$_3$.

Figures 6.30 and 6.31 show the magnetization curves and the corresponding magnetic phase diagram for $H // [001]$ in CeIrGe$_3$, respectively. Below the Néel temperature $T_{N1} = 8.7 \, \mathrm{K}$, the easy-axis magnetization for $H // [001]$ indicates a metamagnetic transition, for example, at $H_c = 12.7 \, \mathrm{kOe}$ under $7 \, \mathrm{K}$, as shown in Fig. 6.30(a). This is a characteristic feature in an antiferromagnet. The critical field H_c is, however, shifted to lower fields with decreasing temperatures, and becomes zero below $T_{N2} = 4.8 \, \mathrm{K}$. Namely, the magnetization below T_{N2} indicates a so-called ferromagnetic curve with a small magnetic moment of $0.14 \, \mu_B/\mathrm{Ce}$ at $2 \, \mathrm{K}$. It is not clear at present whether this magnetic moment corresponds to an ordered moment or not because the magnetic moment of $0.14 \, \mu_B/\mathrm{Ce}$ is very small in magnitude. It is, however, noted that the electronic specific heat γ is relatively large, $80 \, \mathrm{mJ/K^2 \cdot mol}$, which is twice as large as $\gamma = 40 \, \mathrm{mJ/K^2 \cdot mol}$ in CeRhGe$_3$.[97]

The present characteristic magnetization curves are closely related to the first-order magnetic transition at $T_{N2} = 4.8 \, \mathrm{K}$ in CeIrGe$_3$, obtained in the specific heat
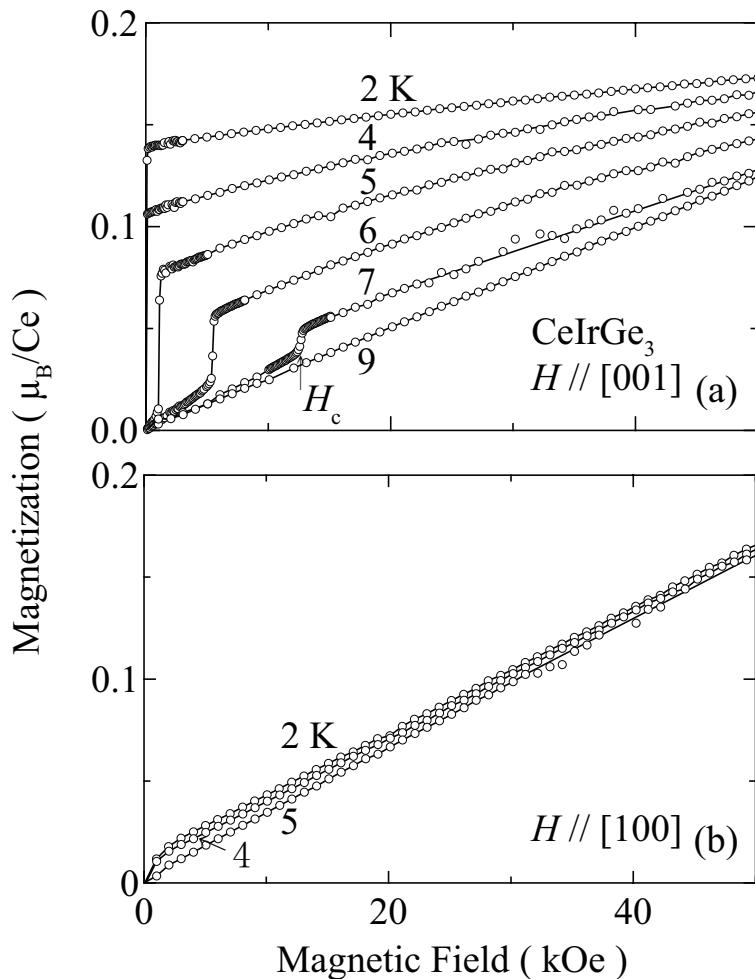
Fig. 6.30 Magnetization curves for (a)$H // [001]$ and (b)[100] in CeIrGe$_3$.

measurement[97)] and also seen in the electrical resistivity discussed below. Similar magnetization curves are observed in UCu$_2$Si$_2$ with the incommensurate longitudinal and nearly sinusoidal spin density modulation. In this compound, the antiferromagnetic state is changed into the ferromagnetic state, and the corresponding magnetic moment corresponds to an order moment of $1.6\,\mu_B$/U.[141, 142)] Another example is the case in CeRu$_2$Ge$_2$, which orders antiferromagnetically below $T_N = 8.5$ K and ferromagnetically below $T_C = 7.5$ K. An ordered moment is, however, large, $1.98\,\mu_B$/Ce.[143)]

On the other hand, the hard-axis magnetization curve for $H // [100]$ increases approximately linearly as a function of magnetic field, reaching $0.16\,\mu_B$/Ce at 50 kOe, as shown in Fig. 6.31(b). The magnitude of magnetization for $H // [100]$ is the same as the saturation value of $0.14\,\mu_B$/Ce for H $//$ [001]. The simple ferromagnetic state is most likely not realized below T_{N2} in this compounds. It is thus needed to measure the magnetization at much higher fields, especially for $H // [001]$.
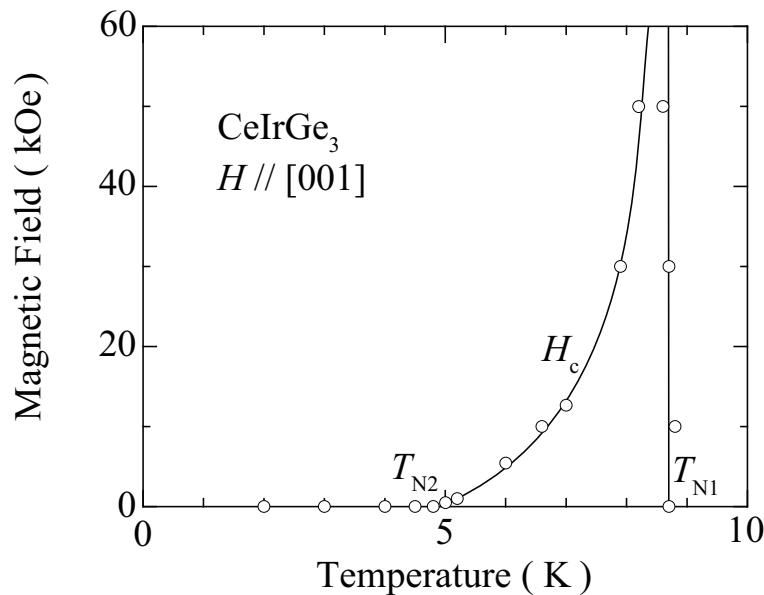
Fig. 6.31 Magnetic phase diagram for $H // [001]$ in CeIrGe$_3$.

6.2.4   Pressure effect and superconductivity in CePtSi$_3$ and CeTGe$_3$(T: Co, Rh, Ir)

The localization of $4f$ electrons is enhanced in CeTGe$_3$(T: Co, Rh, Ir) compared with that in CeTSi$_3$. The corresponding Néel temperature in CeTGe$_3$ is larger than that in CeTSi$_3$. This is because the lattice constants of CeTGe$_3$ are larger than those of CeTSi$_3$: $a = 4.398$ Å and $c = 10.032$ Å in CeRhGe$_3$ and $a = 4.237$ Å and $c = 9.785$ Å in CeRhSi$_3$, for example. Namely, Ge in CeTGe$_3$ increases the molar volume and enhances the antiferromagnetic ordering, as discussed in CeT$_2$X$_2$ (T: transition metal, X: Ge, Si).[55]

We plotted the Néel temperature and the electronic specific heat coefficient γ as a function of the molar volume $V(= a^2c)$, as shown in Figs. 6.32(a) and 6.32(b), respec-
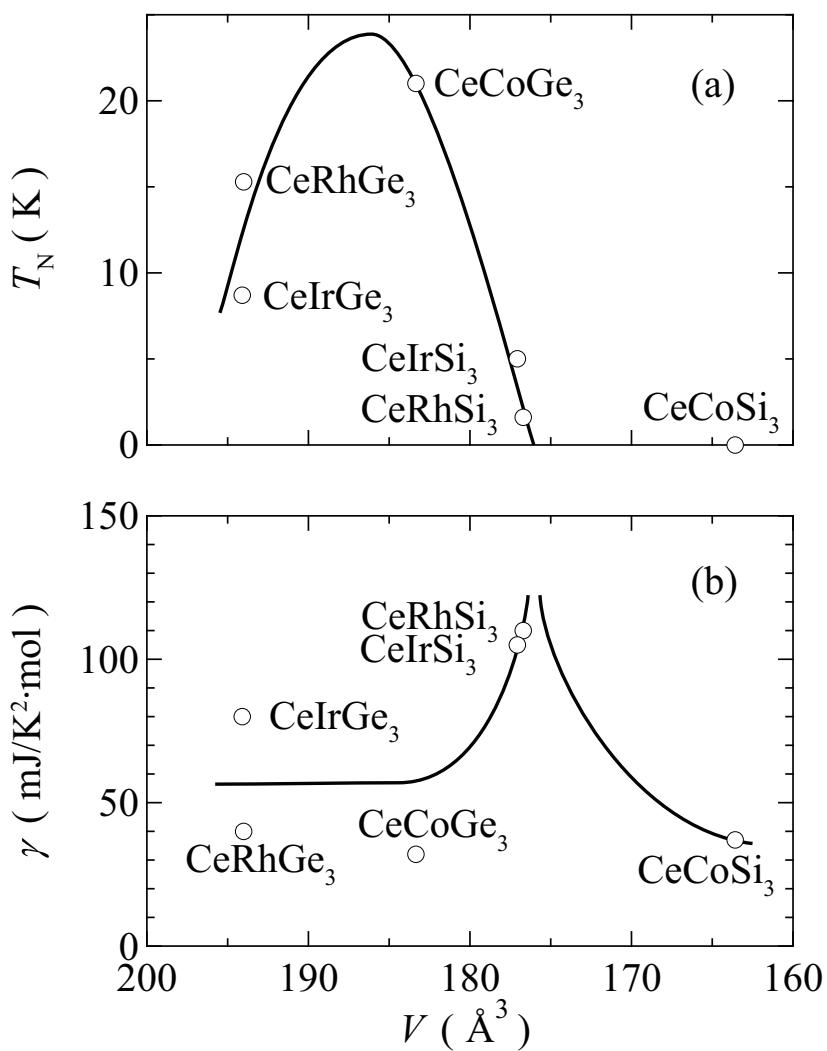
Fig. 6.32 Molar volume dependence of (a)the Néel temperature and (b)the γ value in CeTSi$_3$ and CeTGe$_3$(T: Co, Rh, Ir).

tively. It is noted that the volume in the left side is larger than that in the right side. These data are cited from refs. 22, 96, 97 and 103. The present relation of T_N vs V in Fig. 6.32 roughly corresponds to the Doniach phase diagram, which indicates competition between the RKKY interaction and the Kondo effect. Namely, the magnetic ordering temperature is shown as a function of $|J_{cf}|\,D(\varepsilon_F)$ in the Doniach phase diagram,[5] where J_{cf} is the magnetic exchange interaction and $D(\varepsilon_F)$ is the electronic density of states at Fermi energy ε_F. Experimentally, $|J_{cf}|\,D(\varepsilon_F)$ corresponds to pressure. In fact, the Néel temperature in CeRhSi$_3$ and CeIrSi$_3$ becomes zero at a relatively small value of pressure, $P_c \simeq 2\,$GPa, which corresponds to the magnetic quantum critical point.

We investigated the effect of pressure on the electronic states in CePtSi$_3$ and CeTGe$_3$(T: Co, Rh, Ir) by measuring the electrical resistivity under pressure.[23, 144, 145]

CePtSi$_3$ was studied by measuring the electrical resistivity under pressure for a polycrystal sample,[145] as shown in Fig. 6.33. The Néel temperature is $T_N = 6.4\,$K, which is higher than $T_{N1} = 4.8\,$K in the single crystal sample. The Néel temperature T_N is appreciably unchanged as a function of pressure. The critical pressure is much larger than $8\,$GPa.
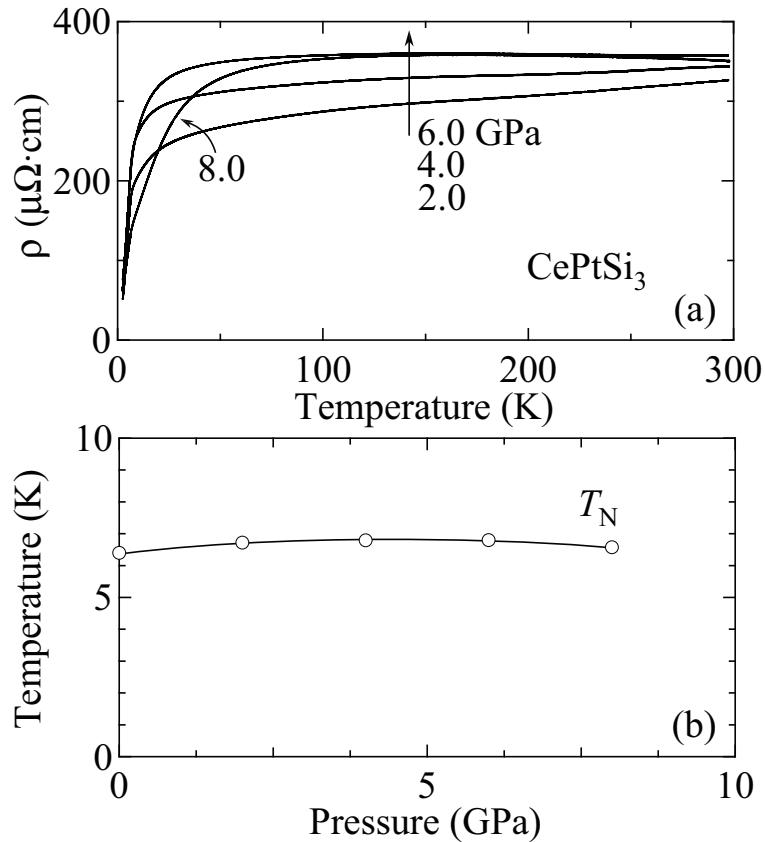

Fig. 6.33 (a)Temperature dependence of the electrical resistivity under several pressures and (b)corresponding pressure phase diagram in CePtSi$_3$.

Next, we will switch from the pressure effect in CePtSi$_3$ to the electrical resistivity in CeTGe$_3$ at ambient pressure. The temperature dependence of the electrical resistivity at ambient pressure is approximately the same in CeTGe$_3$, as shown in Fig. 6.34. A shoulder-like peak around 100 K is a characteristic feature, which is a combined phenomenon of the Kondo and CEF effects. The antiferromagnetic ordering and the change of the magnetic structure occur at lower temperatures, as mentioned above, as shown in Fig. 6.34(b). As for CeCoGe$_3$, the resistivity change is seen only at $T_{N1} = 21$ K for the current J along the [100] direction, although the successive transitions at $T_{N2} = 12$ K and $T_{N3} = 8$ K are observed for J // [001].[103] It is noticed that a step-like decrease of the resistivity occurs at $T_{N2} = 4.8$ K in CeIrGe$_3$, consistent with the first-order magnetic transition, as mentioned above. It is noted that the magnetic transitions $T_{N3} = 0.55$ K in CeRhGe$_3$ and $T_{N3} = 0.7$ K in CeIrGe$_3$ were not observed in the present measurement, as shown in Fig. 6.34(b).

From the low-temperature resistivity, we obtained the A value in the Fermi-liquid relation of $\rho = \rho_0 + AT^2$: $A = 0.011\,\mu\Omega\cdot$cm/K^2 in CeCoGe$_3$, $A = 0.022\,\mu\Omega\cdot$cm/K^2 in CeRhGe$_3$ and $A = 0.149\,\mu\Omega\cdot$cm/K^2 in CeIrGe$_3$. Following the Kadowaki-Woods relation,[41] these values correspond to the electronic specific coefficient $\gamma = 34$ mJ/K$^2\cdot$mol in CeCoGe$_3$, 47 mJ/K$^2\cdot$mol in CeRhGe$_3$ and 122 mJ/K$^2\cdot$mol in CeIrGe$_3$, which are close to $\gamma = 32$ mJ/K$^2\cdot$mol in CeCoGe$_3$, 40 mJ/K$^2\cdot$mol in CeRhGe$_3$ and 80 mJ/K$^2\cdot$mol in CeIrGe$_3$ obtained from the specific heat measurement.
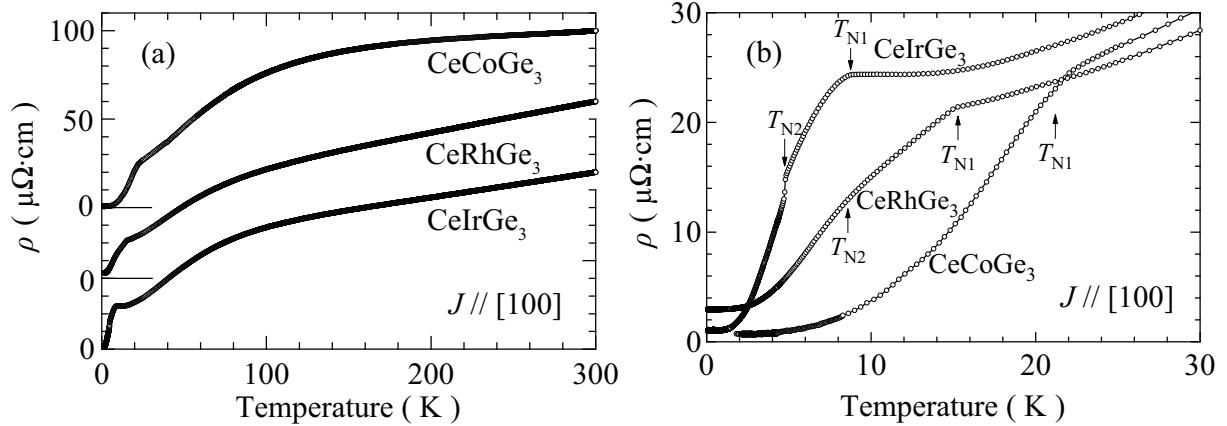
Fig. 6.34 Electrical resistivity (a)in the temperature range from room temperature to low temperatures and (b)below 30 K in CeTGe$_3$(T: Co, Rh, Ir).

The effect of pressure on the electronic states in CeTGe$_3$ compounds are highly different from that in CeRhSi$_3$ and CeIrSi$_3$. The Néel temperature does not change appreciably against pressure in CeRhGe$_3$ and CeIrGe$_3$. Figures 6.35 and 6.36 show the temperature dependence of the electrical resistivity under several pressures and corresponding pressure phase diagram in CeRhGe$_3$ and CeIrGe$_3$, respectively. The Néel temperature for the polycrystal sample increases with increasing pressure from $T_{N1} = 14.6$ K at ambient pressure to $T_{N1} = 21.3$ K at 8.0 GPa in CeRhGe$_3$. The similar result is obtained in CeIrGe$_3$, where the antiferromagnetic ordering temperature T_{N1} and the magnetic transition temperature T_{N2} merge at 4 GPa, but the antiferromagnetic ordering temperature is appreciably unchanged as a function of pressure up to 8 GPa. High pressures of 10-15 GPa are needed for $T_{N1} \rightarrow 0$ in CeRhGe$_3$ and CeIrGe$_3$, revealing that both compounds are sited far from the magnetic quantum critical point, which can be understood from the molar volume dependence of the Néel temperature and γ value in Fig. 6.32.
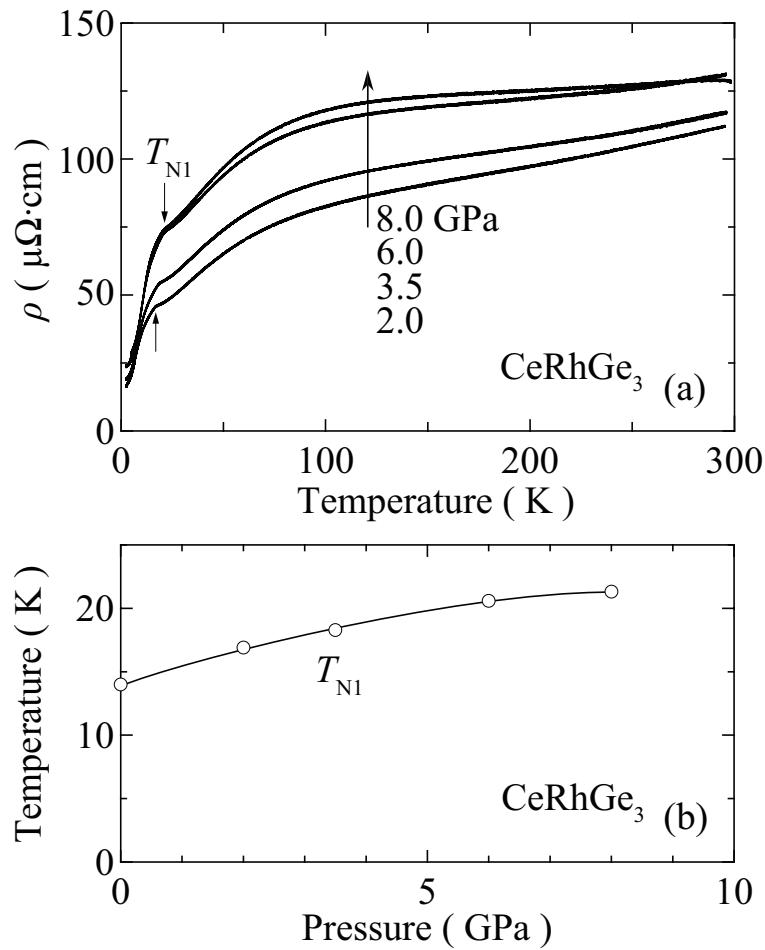
Fig. 6.35 (a) Temperature dependence of the electrical resistivity under several pressures and (b) corresponding pressure phase diagram in CeRhGe$_3$.[145]
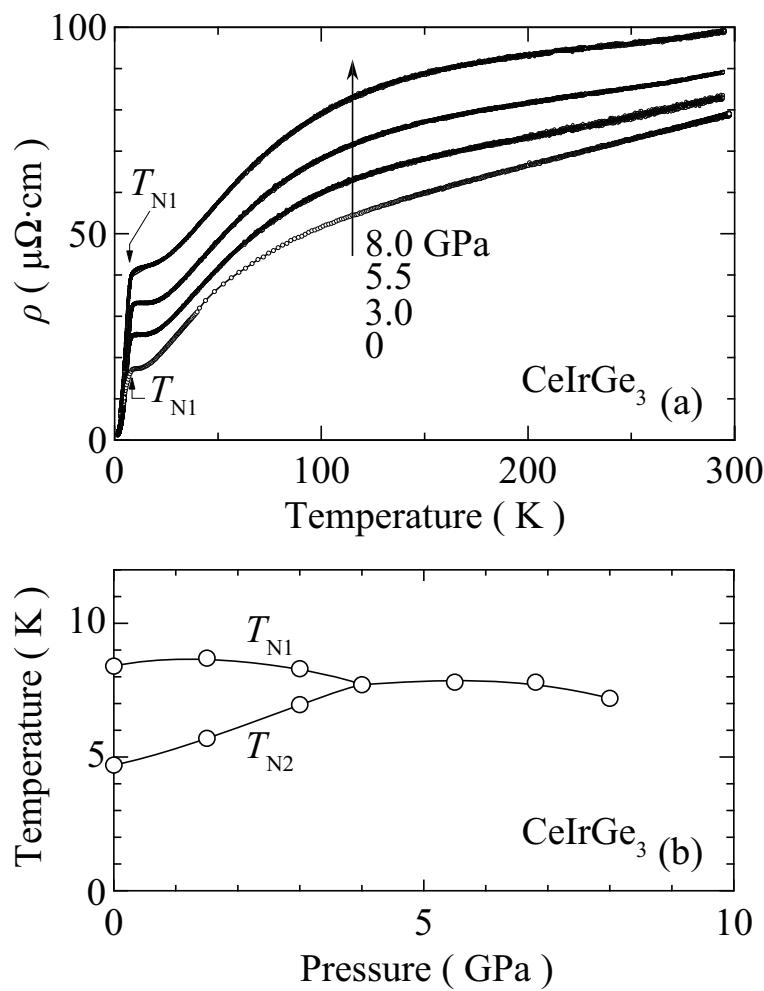
Fig. 6.36 (a) Temperature dependence of the electrical resistivity under several pressures and (b) corresponding pressure phase diagram in CeIrGe$_3$.[144]

On the other hand, the critical pressure, where the Néel temperature becomes zero, was roughly estimated at $P_c \simeq 5.5$ GPa in the previous resistivity measurement under pressure in CeCoGe$_3$, and superconductivity was observed at 5.6 GPa, with the superconducting transition temperature $T_{sc} = 0.42$ K.[23] The previous experiment was carried out by using a polycrystal sample. We measured the electrical resistivity under pressure up to 7 GPa by using a high-quality single crystal sample with the residual resistivity ratio RRR = 130, as shown in Fig. 6.34.

Figure 6.37(a) shows a typical temperature dependence of the electrical resistivity at 6.5 GPa, together with the resistivity at ambient pressure. The overall feature of the resistivity is approximately the same between at 6.5 GPa and ambient pressure, although the Néel temperature $T_{N1} = 21$ K at ambient pressure becomes zero and superconductivity appears below $T_{sc} = 0.69$ K at 6.5 GPa.

Figure 6.37(b) shows the low-temperature resistivity at 5.4, 6.5 and 6.9 GPa. At 5.4 GPa, the electrical resistivity decreases steeply below the Néel temperature $T_{N1} = 2.9$ K, and drops below 0.43 K, indicating onset of superconductivity and reaches zero at $T_{sc} = 0.13$ K. We define the superconducting transition temperature T_{sc} as the temperature showing the zero-resistivity. At 6.5 and 6.9 GPa, the clear antiferromagnetic ordering is not seen, and the electrical resistivity, which shows a T^2-dependence of the resistivity, $\rho = \rho_0 + AT^2$, below about 2.5 K at 5.4 GPa, is changed into a T-linear temperature dependence below about 4 K at 6.9 GPa, indicating the non-Fermi liquid character. Here, the A value of $A = 0.357\,\mu\Omega$·cm/K^2 at 5.4 GPa corresponds to the electronic specific heat coefficient $\gamma = 190$ mJ/K^2·mol, following the Kadowaki-Woods relation,[41] which is compared with $A = 0.011\,\mu\Omega$·cm/K^2 and $\gamma = 34$ mJ/K^2·mol at ambient pressure. Superconductivity in CeCoGe$_3$ is realized in a moderate heavy fermion state. It is noted that the γ value of about 120 mJ/K^2·mol at ambient pressure in CeIrSi$_3$ is unchanged as a function of pressure, even at about 2.6 GPa where the characteristic superconducting state is realized.[107]

Superconductivity in CeCoGe$_3$ is observed at $T_{sc} = 0.69$ K at 6.5 GPa and $T_{sc} = 0.65$ K at 6.9 GPa. The maximum superconducting transition temperature might be realized at 6.5 GPa. We show in Fig. 6.38 the pressure phase diagram. The Néel temperature $T_{N1} = 21$ K at ambient pressure decreases with increasing pressure and superconductivity appears in the pressure region from 5.4 GPa to about 7.5 GPa. The critical pressure is estimated to be $P_c \simeq 6.5$ GPa

We precisely investigated superconductivity in magnetic fields. Figure 6.39 shows the magnetic phase diagram at 5.4 GPa for the magnetic field along the [001] direction. The antiferromagnetic ordering is quite stable against magnetic fields. Superconductivity is realized below $T_{sc} = 0.13$ K at zero field. The upper critical field at H_{c2} at 0 K is roughly estimated to be $H_{c2}(0) = 1.5$ kOe for the magnetic field along the [001] direction. It is noted that onset of superconductivity is not destroyed by magnetic field, which is 0.43 K at zero field and 0.2 K at 50 kOe.

Next we shown in Fig. 6.40 the temperature dependence of the electrical resistivity under the magnetic field of 0, 30 and 80 kOe at 6.5 GPa, where the magnetic field is directed along the [001] direction. The electrical resistivity drops very steeply due to
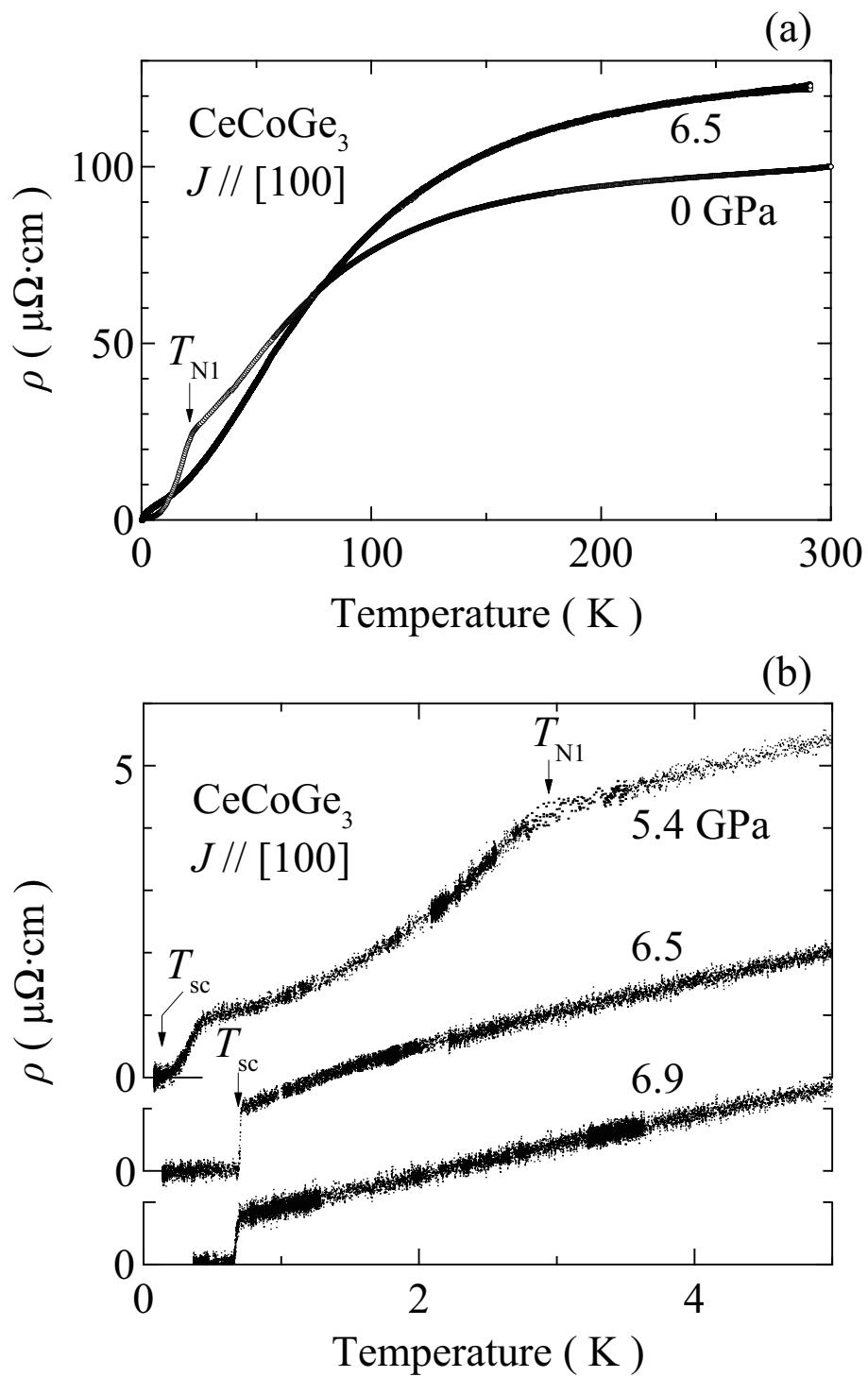
Fig. 6.37 Temperature dependence of the electrical resistivity under pressure in CeCoGe$_3$.
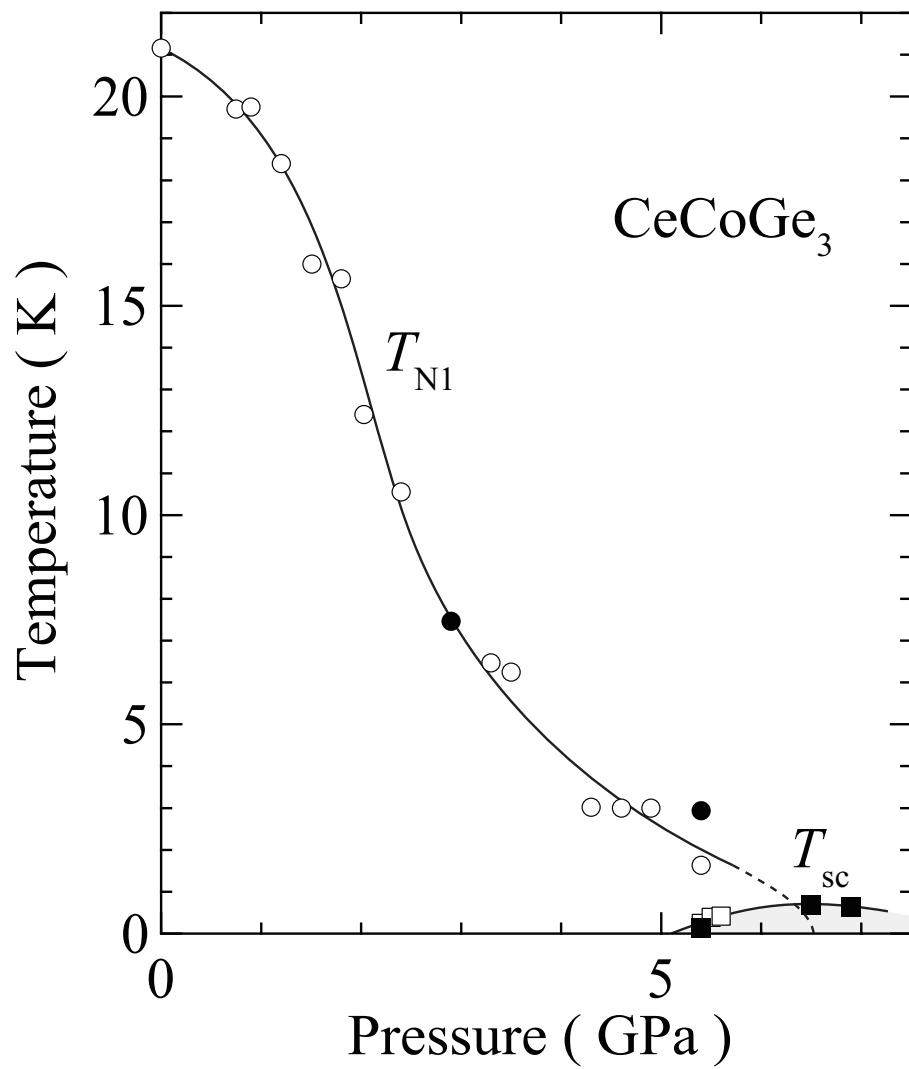
Fig. 6.38 Pressure phase diagram in CeCoGe₃. The data shown by open circles and open squares are cited from ref. 23.
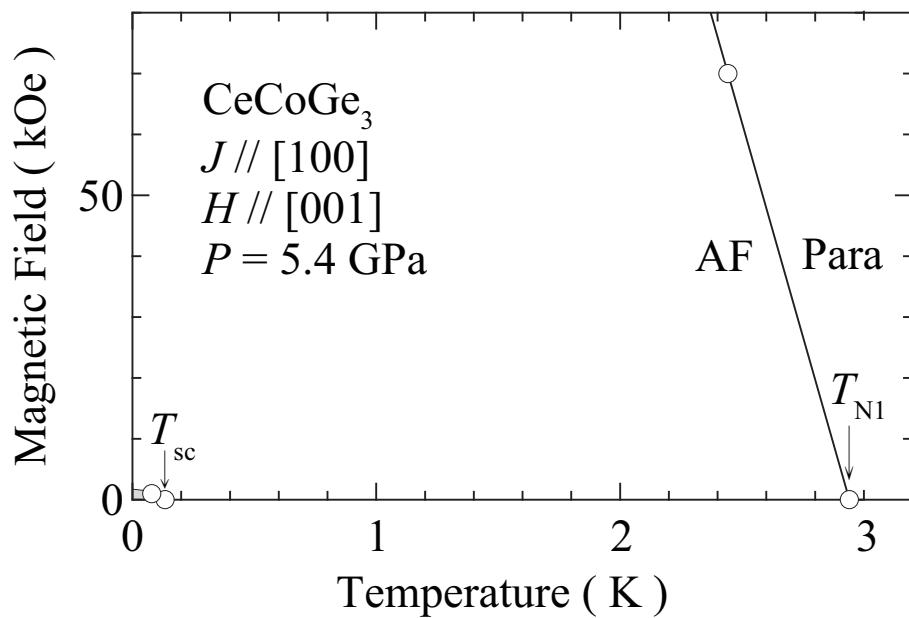
Fig. 6.39 Magnetic phase diagram at $5.4\,\mathrm{GPa}$ in CeCoGe$_3$.
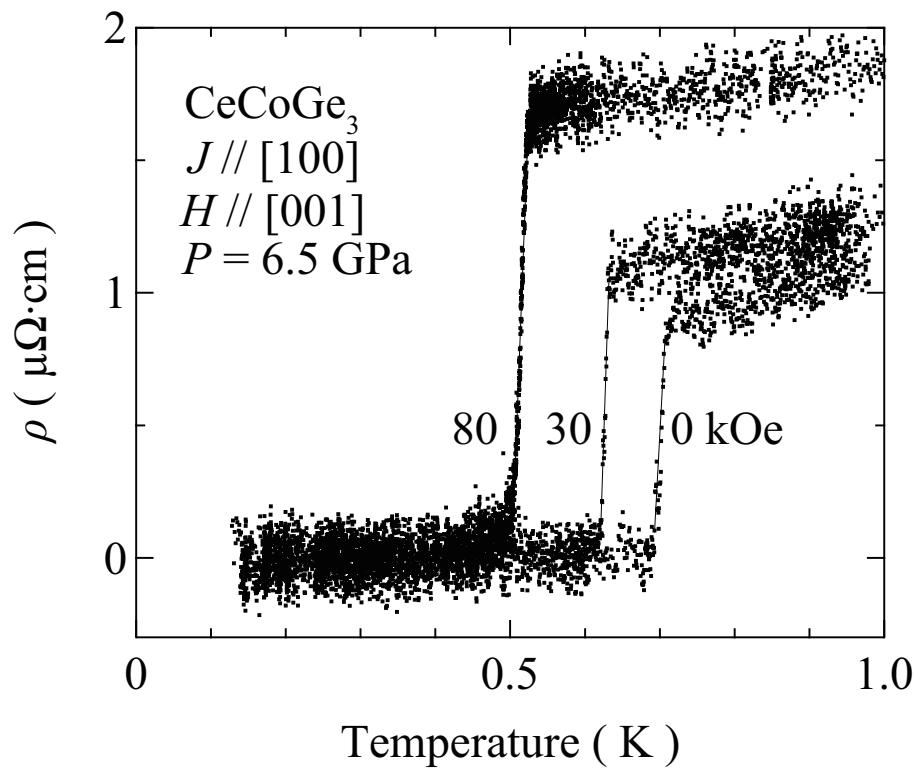
Fig. 6.40 Temperature dependence of the electrical resistivity under the magnetic field of 0, 30 and $80\,\mathrm{kOe}$ at $6.5\,\mathrm{GPa}$ in CeCoGe$_3$.

onset of superconductivity. The present superconductivity is not destroyed by magnetic fields: $T_{sc} = 0.47$ K at 80 kOe. The corresponding slope of H_{c2} as a function of temperature is extremely large: $-dH_{c2}/dT = 200$ kOe/K at $T_{sc} = 0.69$ K, which is larger than $-dH_{c2}/dT = 154$ kOe/K at $T_{sc} = 1.56$ K at 2.65 GPa in CeIrSi$_3$. The upper critical field indicates an upturn curvature with decreasing temperature, as shown in Fig. 6.41, and unconventional superconductivity is achieved with a huge slope of the upper critical field. In Fig. 6.41, the upper critical field at 6.9 GPa is also shown: $-dH_{c2}/dT = 190$ kOe/K at $T_{sc} = 0.65$ K, together with the upper critical field in CeIrSi$_3$.[8, 21, 22]

CeCoGe$_3$ is thus another candidate which might be a spin-triplet superconductor in the non-centrosymmetric crystal structure as in CeRhSi$_3$ and CeIrSi$_3$. It is, however, needed to determine experimentally the upper critical field $H_{c2}(0)$ for $H // [001]$ and the temperature dependence of H_{c2} for $H // [100]$, which are left to the future study.
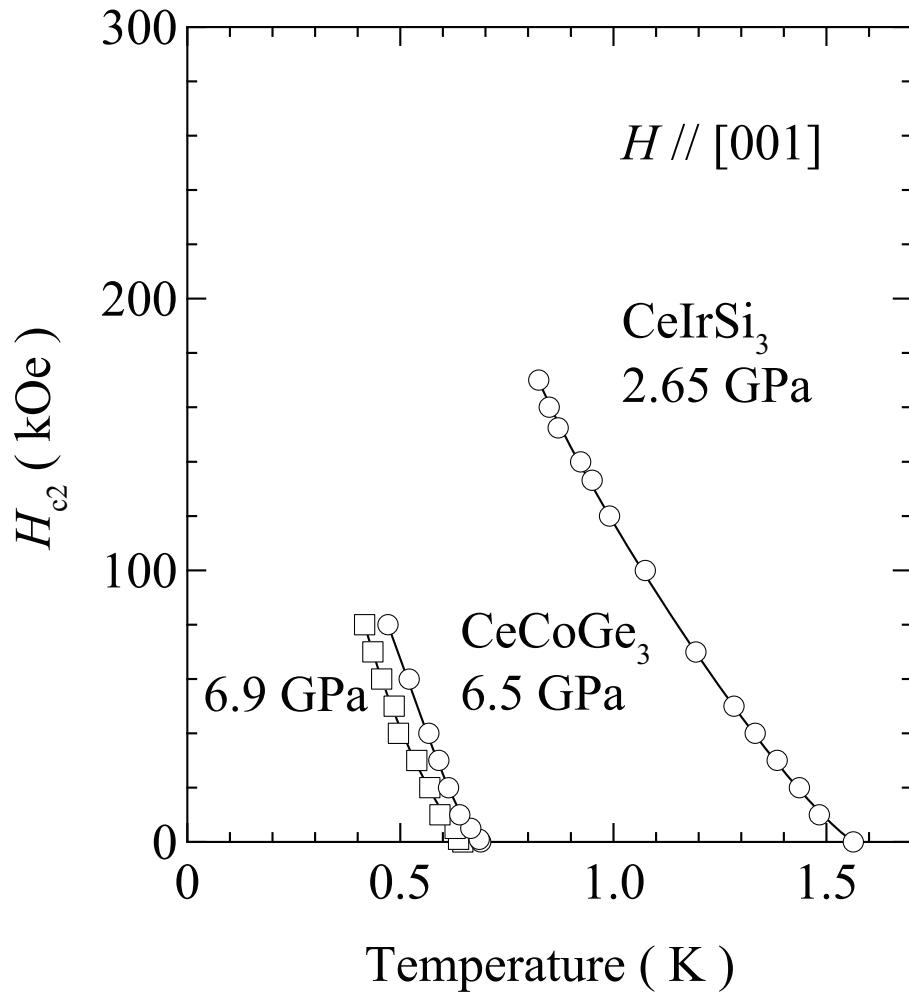
Fig. 6.41 Upper critical field for $H // [001]$ in CeCoGe$_3$ and CeIrSi$_3$. The data of CeIrSi$_3$ are cited from ref. 22.

6.3   Magnetic properties and the pressure effect in Ce$_2$TGe$_6$

6.3.1   Ce$_2$PdGe$_6$

Figure 6.42 shows the temperature dependence of magnetic susceptibility in the temperature range 2 - 20 K measured in a field of 5 kOe. The susceptibility for all the three principal directions clearly indicated the antiferromagnetic ordering of the Ce moments at $T_N = 11.3$ K, thereby corroborating the previous results on the polycrystalline samples. The magnetic susceptibility is very large for the field parallel to the [010] direction, while the anisotropy along the [100] and [001] directions is very small. The huge drop in the susceptibility for $H // [010]$ just below the Néel temperature $T_N = 11.3$ K indicates an easy-axis of magnetization.
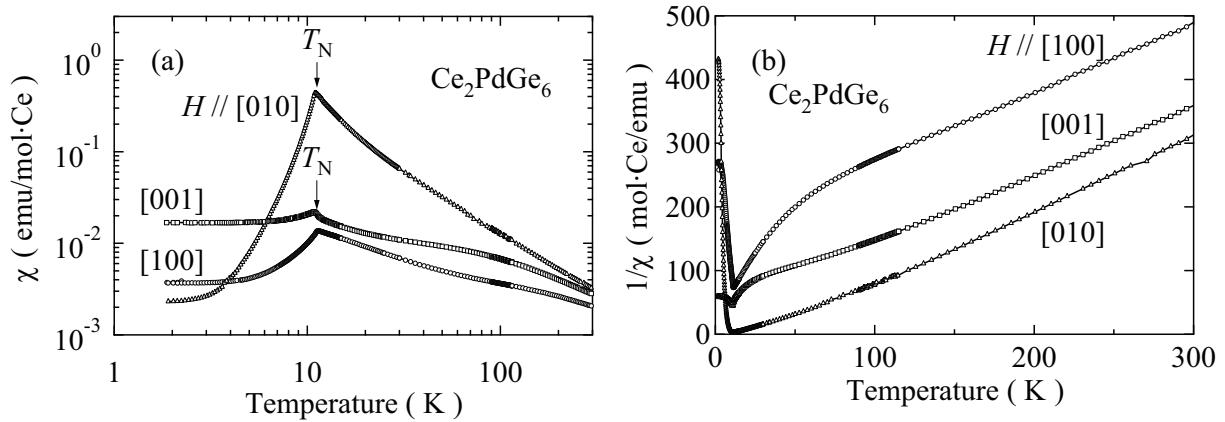
Fig. 6.42 Temperature dependence of (a) the magnetic susceptibility and (b) the inverse magnetic susceptibility along the three principal directions in Ce$_2$PdGe$_6$.

Figure 6.43 shows the isothermal magnetization of Ce$_2$PdGe$_6$ along the three principal directions at $T = 2$ K. As can be seen from the figure, the magnetic anisotropy is very large for the field directions parallel to [010]. The magnetization along the [100] and [001] directions is very small and remains linear up to a field of about 7 T, indicating the hard-axes of magnetization. The magnetization along [010] is very small for fields up to 10.5 kOe at which point a metamagnetic transition is observed. At 12.7 kOe, a sharp metamagnetic transition, which is like a spin flop type, is observed, thereby entering into a field-induced ferromagnetic state. The magnetization saturates at this field to a value of 1.94 μ_B/Ce. This large value of saturation moment at substantially low fields indicates that Ce atoms are trivalent and possess magnetic moments.

The small metamagnetic transition at 10 kOe vanishes for temperatures above 9 K. Furthermore the sharp metamagnetic transition also vanishes for temperatures above the ordering temperature and it becomes linear at 20 K. Based on the isothermal magnetization measurement, we have constructed the magnetic phase diagram, as shown in
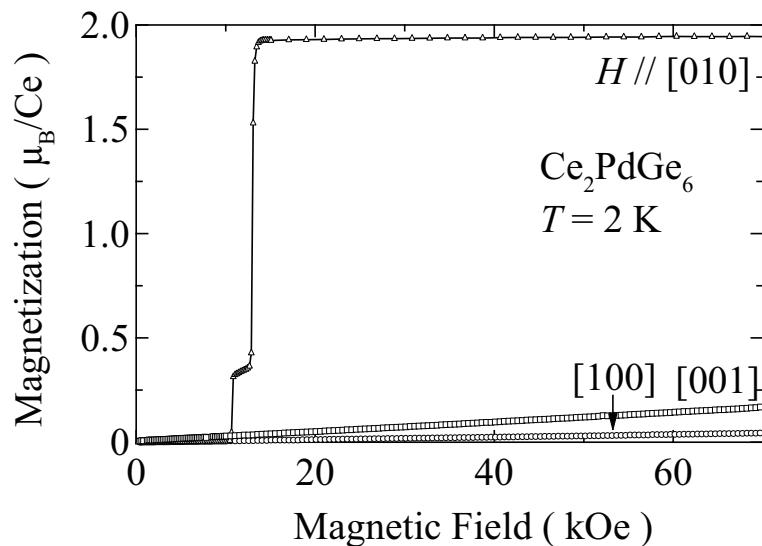
Fig. 6.43 Magnetic field dependence of magnetization along the three principal directions in Ce$_2$PdGe$_6$ at $T = 2$ K.
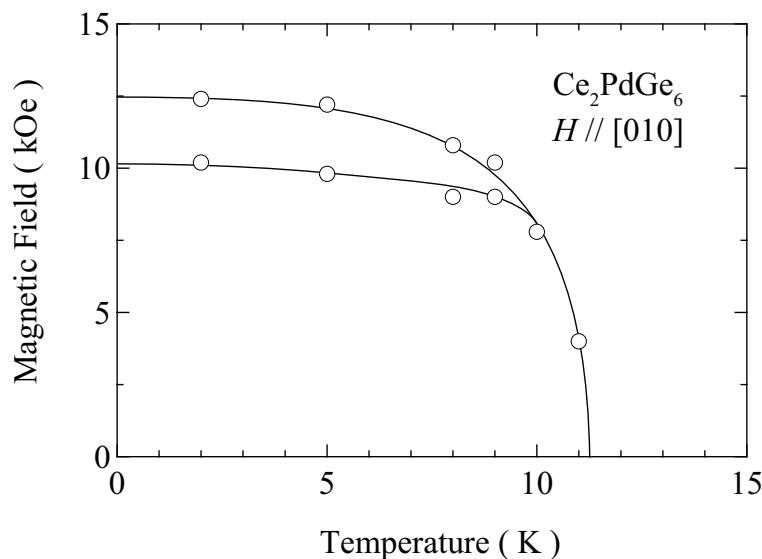
Fig. 6.44 Magnetic phase diagram of Ce$_2$PdGe$_6$.

Fig. 6.44. The transition points can be traced by smooth lines to the magnetic ordering temperature $T_N = 11.3$ K at zero field.

The temperature dependence of the specific heat C in the temperature region from 2 to 20 K is shown in Fig. 6.45. A jump in the heat capacity data clearly shows the bulk antiferromagnetic ordering of Ce^{3+} moments at $T_N = 11.3$ K. Just below the magnetic
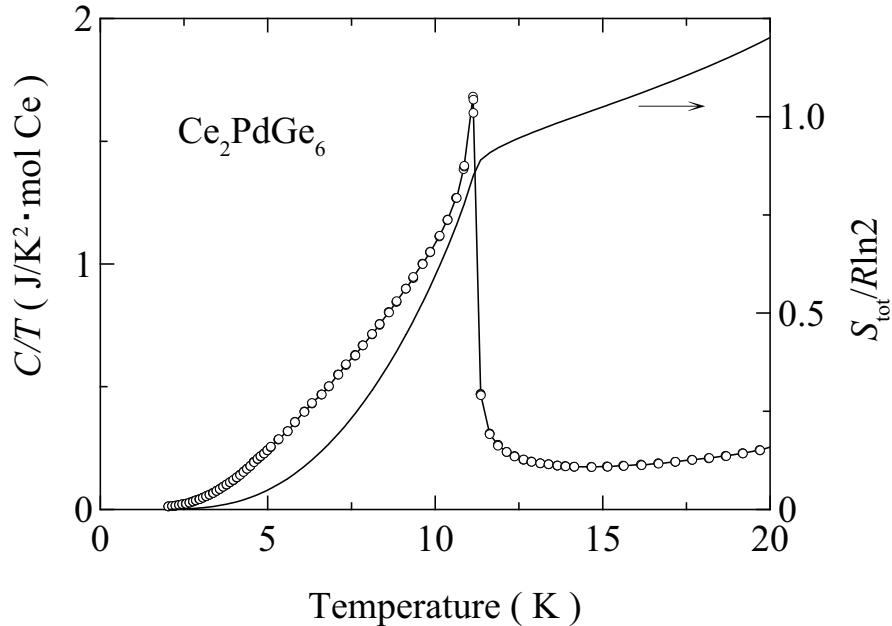
Fig. 6.45 Temperature dependence of specific heat in the form of C/T versus T and the total entropy S_{tot} of Ce_2PdGe_6.

ordering, the specific heat data can be fitted to the antiferromagnetic magnon spectrum with an energy gap as given by the relation $C(T) = \gamma T + \beta T^3 \exp(-\Delta/k_B T)$. The γ value thus obtained is $9\,mJ/K^2 \cdot Ce$ mol. The spin wave gap is found to be $\Delta = 2.3$ K, which is much less than that observed from the low-temperature resistivity data, shown later. We have estimated the total entropy S_{Tot} and is shown in Fig. 6.45. The total entropy is almost equal to $R\ln 2$ at the magnetic ordering temperature, indicating a doublet ground state. From the specific heat data down to 2 K and the magnetization data, it can be understood that the two Ce atoms occupying two different sites order magnetically at the same temperature. It is to be mentioned here that some of the Ce compounds with multi-cerium sites indicate a complex magnetism due to the different electronic nature of the various kinds of cerium atoms [146].

The temperature dependence of electrical resistivity in the temperature range from 1.3 to 300 K is shown in Fig. 6.46. The resistivity shows a broad hump around 150 K and decreases with decreasing temperature. A rapid drop in the electrical resistivity is observed below $T_N = 11.3$ K, indicating the the antiferromagnetic ordering. This type of huge drop in the electrical resistivity below the Néel temperature suggests the appearance of a spin density wave. The resistivity data of Ce_2PdGe_6 can be fitted to the following
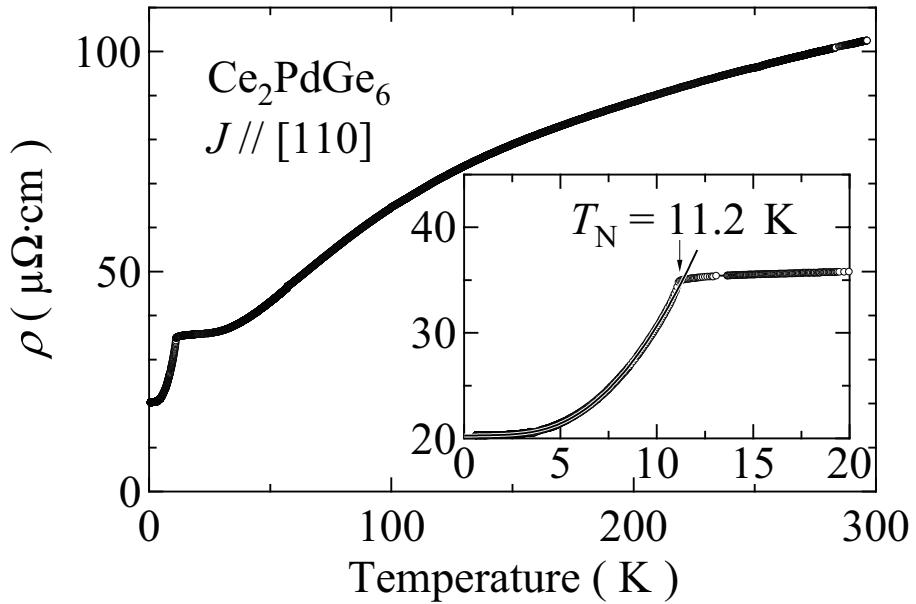
Fig. 6.46 Temperature dependence of electrical resistivity of Ce$_2$PdGe$_6$ in a single crystal sample for current $J // [110]$. The solid line indicates the fitting to spin density wave relation as mentioned in the text.

spin density wave relation:

$$\rho(T) = \rho_0 + AT^2 + BT(1 + 2T/\Delta)\exp(-\Delta/T), \tag{6.8}$$

where ρ_0 is the residual resistivity, AT^2 is the Fermi liquid contribution and Δ is the gap in the spin density wave spectrum. The solid line in Fig. 6.46 indicates the least square fitting to the above equation. As can be seen from the figure, the fitting is good for temperatures up to the Néel temperature. The parameters obtained from the fitting are $\rho_0 = 20.3\,\mu\Omega\cdot$cm, $A = 0.0147\,\mu\Omega\cdot$cm/K^2, $B = 1.48$ $\mu\Omega\cdot$cm/K and $\Delta = 14.0$ K. The residual resistivity ρ_0 is almost three times smaller than those reported by Fan *et al*[117] but is comparable to that reported by Strydom *et al* [116].

We measured the electrical resistivity under pressures up to 8 GPa by using the a cubic anvil pressure cell in the temperature range from 2 K to 300 K, as shown in Fig. 6.47(a). The Néel temperature $T_N = 11.3$ K at ambient pressure is shifted to slightly higher temperatures at low pressures, $T_N = 12.2$ K at 2 GPa, for example, but is shifted to lower temperatures with further increasing pressure: $T_N = 7$ K at 5.5 GPa, which was determined as the temperature showing a maximum of $-\mathrm{d}^2\rho/\mathrm{d}T^2$, as shown by arrows in Fig. 6.47(b). The Néel temperature is not defined at 7.0 and 8.0 GPa, most likely $T_N = 0$ at these pressures. Figures. 6.48(a) and 6.48(b) show the pressure phase diagram, and the corresponding A and ρ_0 values of the Fermi liquid relation $\rho = \rho_0 + AT^2$. These A and ρ_0 values increase with increasing pressure. Unfortunately, we could not determine the A and ρ_0 values at 7.0 and 8.0 GPa because the resistivity data at much lower temperature are needed to determine these values.
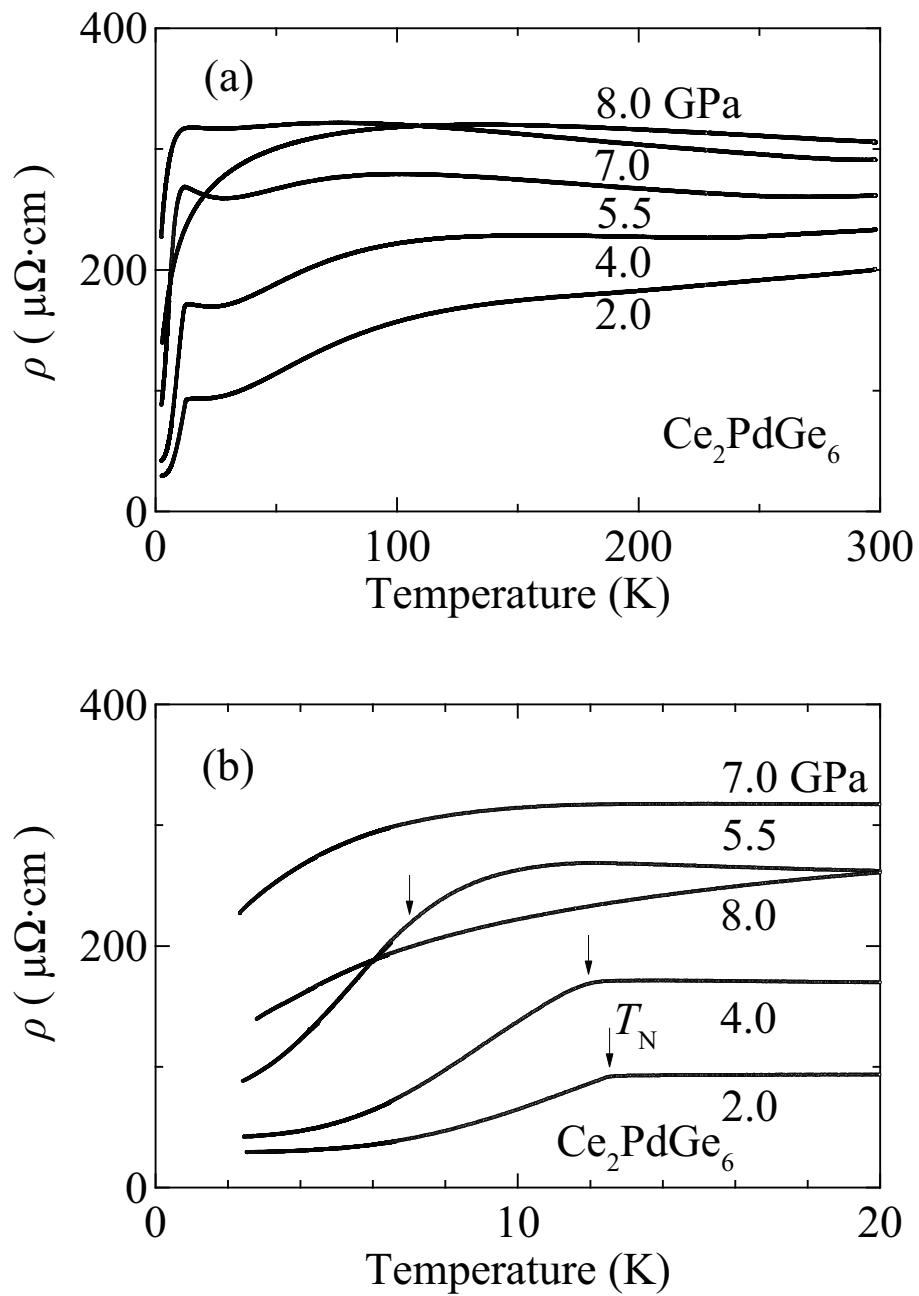
Fig. 6.47 Temperature dependence of the electrical resistivity under several pressures in Ce$_2$PdGe$_6$.
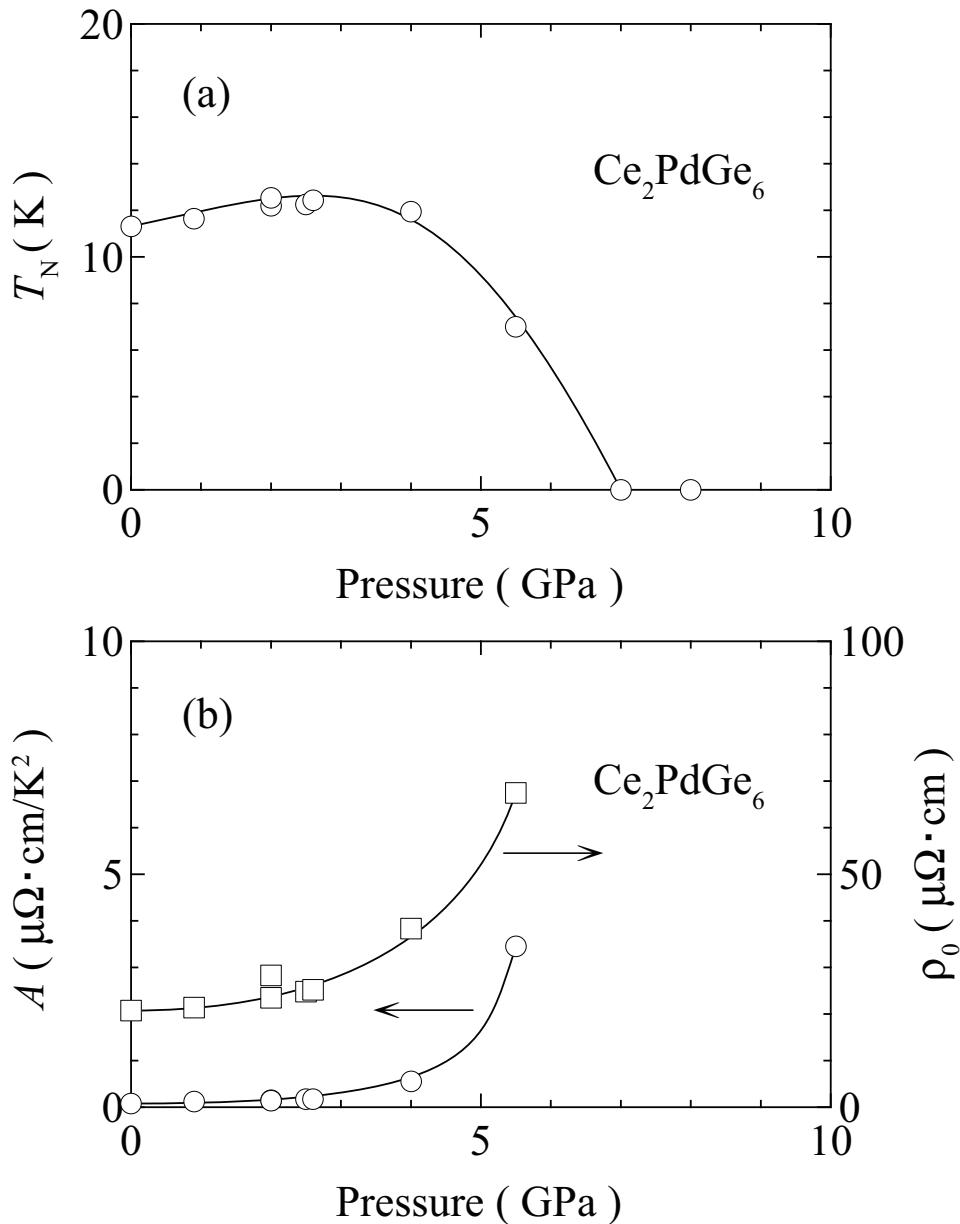
Fig. 6.48 (a)Pressure phase diagram and the pressure dependence of ρ_0 and A values in Ce$_2$PdGe$_6$.

6.3.2   Ce$_2$CuGe$_6$

Figures 6.49(a) and 6.49(b) show the temperature dependence of the magnetic susceptibility and the inverse magnetic susceptibility in the magnetic field along three principal directions, respectively. The magnetic susceptibility in the magnetic field along [010] is very large compared with those of $H \,/\!/\, [100]$ and [010] and, a steep decrease of the susceptibility is found for $H \,/\!/\, [010]$ below $T_N = 15.0\,\mathrm{K}$, which indicates an easy-axis of magnetization for $H \,/\!/\, [010]$. This is almost the same as that in Ce$_2$PdGe$_6$.
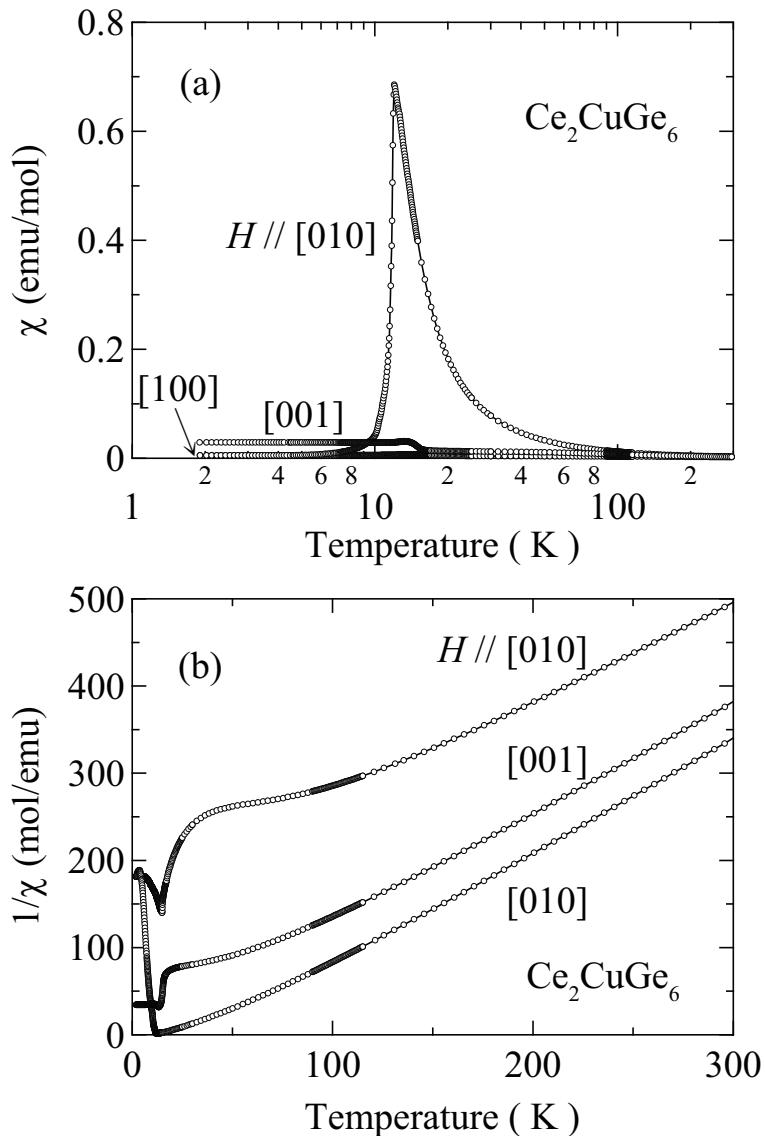
Fig. 6.49 Temperature dependence of (a) the magnetic susceptibility and (b) the inverse magnetic susceptibility along the three directions in Ce$_2$CuGe$_6$.

The temperature dependence of specific heat is shown in Fig. 6.50. A clear peak at 14.8 K is due to the bulk antiferromagnetic ordering. We have estimated the total entropy S_{tot}, as shown in Fig. 6.50, which is almost equal to $R\ln2$ at T_N, indicating a doublet ground state of $4f$ electrons in the CEF scheme.
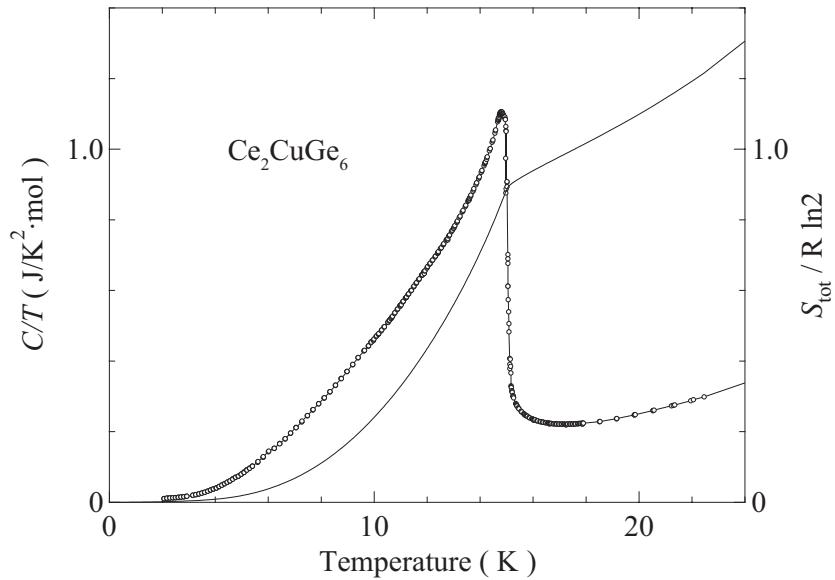
Fig. 6.50 Temperature dependence of the specific heat in the form of C/T and the total entropy S_{tot} in Ce$_2$CuGe$_6$.

The temperature dependence of the electrical resistivity is shown in Fig. 6.51. The electrical resistivity decreases steeply below $T_N = 15$ K. Pressure experiments were carried out mainly by using a cubic anvil cell[133] at high pressures up to 8 GPa in the temperature range from 2 to 300 K. Figure 6.52 shows the temperature dependence of the electrical resistivity under pressures up to 8 GPa. The resistivity at 0 GPa shows the broad hump around 100 K and a steep decrease below $T_N = 15.4$ K. T_N increases gradually up to 4 GPa, and then decreases rather steeply above 5 GPa. Since there is no signature of T_N at 8 GPa, T_N is found to become zero around $P_c = 7.2$ GPa, as shown in Fig. 6.53(a). We obtained the A and ρ_0 values from the T^2-dependence of the electrical resistivity at low temperatures, following a Fermi liquid relation $\rho(T) = \rho_0 + AT^2$. The A value shows a maximum around P_c, as shown in Fig. 6.53(b). The enhanced A-value around P_c indicates that the heavy fermion state is formed around P_c.[147,148] The residual resistivity ρ_0 also becomes maximum around P_c, as shown in Fig. 6.53(c). Much lower temperature experiments are required to clarify the heavy-fermion state around P_c and also to find superconductivity in Ce$_2$CuGe$_6$ as well as Ce$_2$PdGe$_6$.
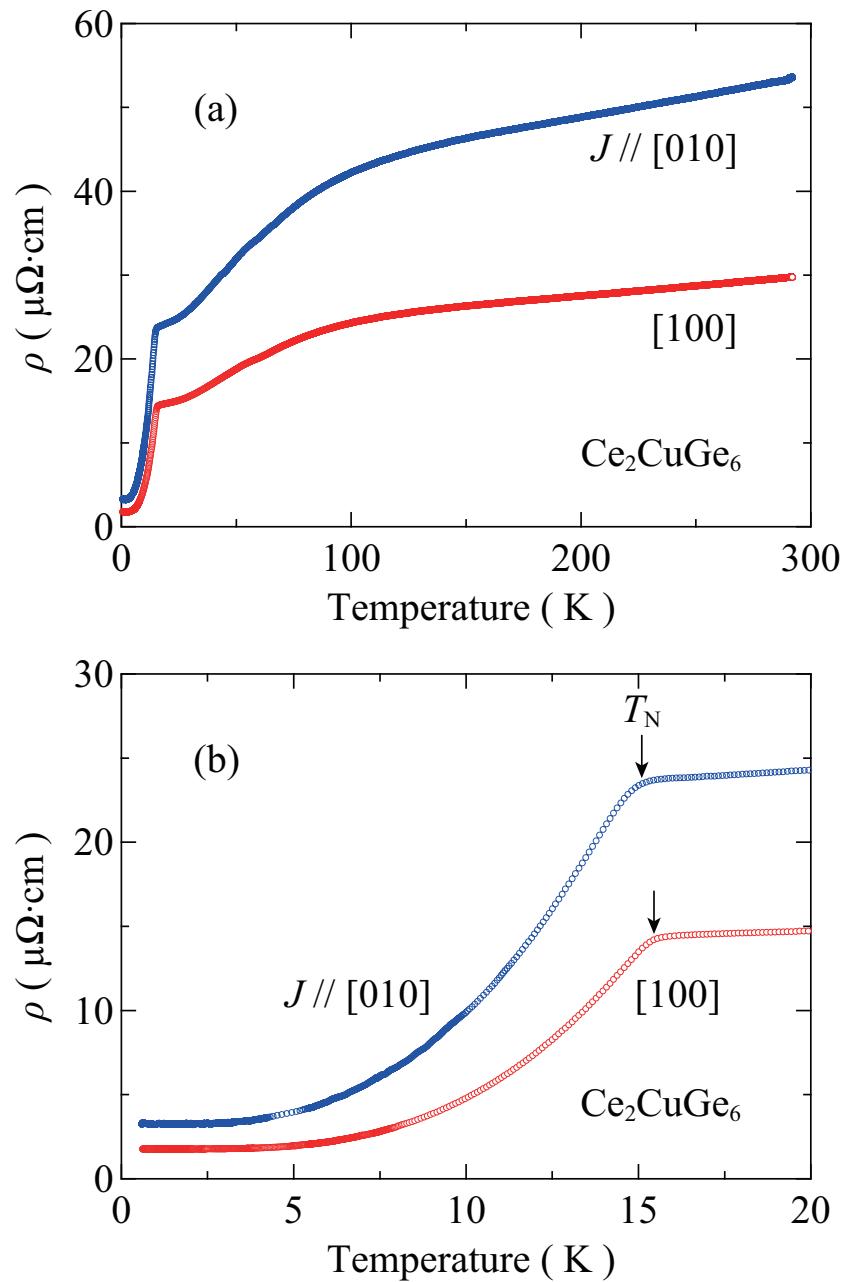
Fig. 6.51 Temperature dependence of the electrical resistivity in Ce_2CuGe_6 for the current along [100] and [010] directions.
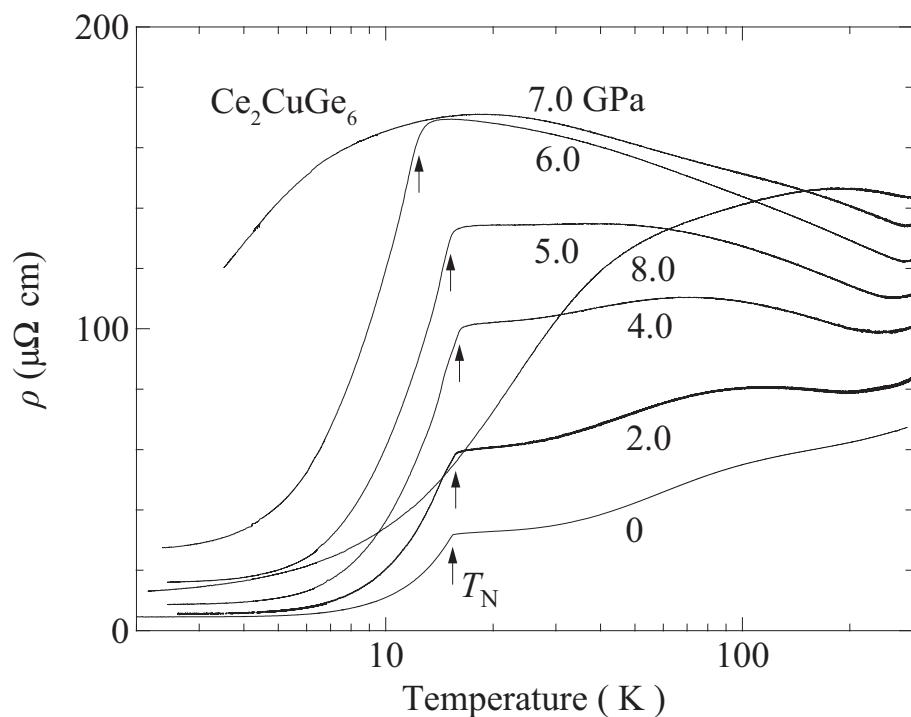
Fig. 6.52 Temperature dependence of the electrical resistivity under several pressures in Ce$_2$CuGe$_6$.
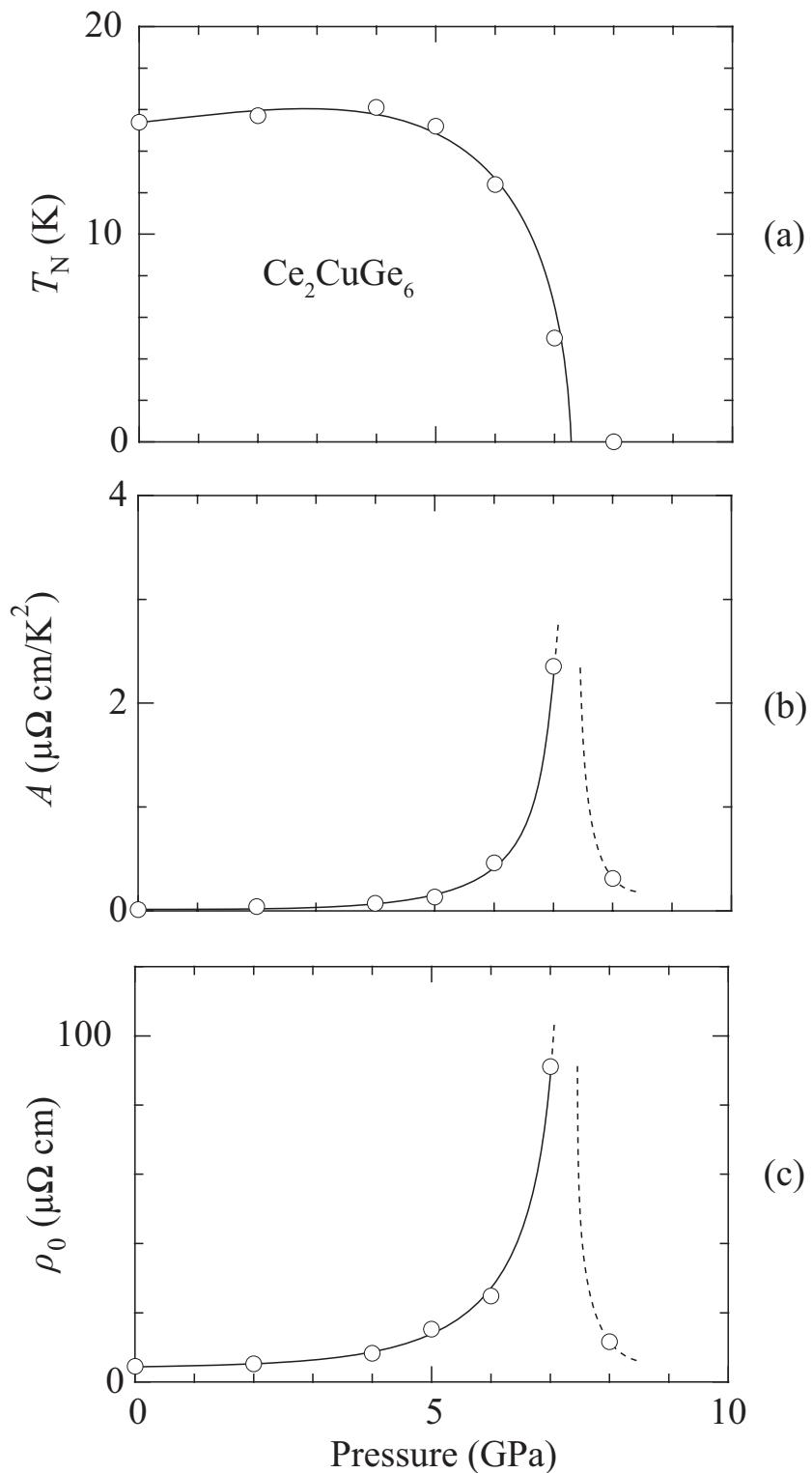
Fig. 6.53 Pressure phase diagram of (a) T_N, (b) A and (c) ρ_0 in Ce_2CuGe_6. Solid and dotted lines connecting the data are guidelines.

7 Conclusion

The electrical and magnetic properties of the non-centrosymmetric rare earth compounds of RTX_3 (R: rare earth, T: transition metal and X: Si and Ge) and Ce_2TGe_6 were studied by measuring the electrical resistivity, specific heat, magnetic susceptibility, magnetization and de Haas-van Alphen (dHvA) effect, together with the resistivity measurement under pressure. Two significant experimental results were obtained in RTX_3: the antisymmetric spin-orbit interaction and the unique superconducting property, which are based on the non-uniform lattice potential along the non-centrosymmetric tetragonal [001] direction.

I) We grew single crystals of $LaTGe_3$(T: Fe, Co, Rh, Ir) and a paramagnet $PrCoGe_3$ by the Bi-flux method, and measured the dHvA effect to clarify the split Fermi surface properties and the antisymmetric spin-orbit interaction based on the non-centrosymmetric crystal structure. The dHvA data are compared with the result of energy band calculations. The experimental results are summarized as follows:

(1) The detected dHvA branches are clearly identified by the theoretical Fermi surfaces. The Fermi surfaces are found to be split into two different Fermi surfaces due to the antisymmetric spin-orbit interaction in $LaTGe_3$ (T: Fe, Co, Rh, Ir) and $PrCoGe_3$.

(2) The magnitude of the antisymmetric spin-orbit interaction $2|\alpha p_\perp|$ is found to be changed when the transition metal T is changed from T = Co, Rh to Ir in $LaTGe_3$, but unchanged in X is changed from X = Si to Ge in $LaIrX_3$. It is noticed that the value of $2|\alpha p_\perp| \simeq 1100$ K for the outer orbits named α of the main bands 69 and 70 electron Fermi surface in $LaIrSi_3$ and $LaIrGe_3$ is larger than $2|\alpha p_\perp| = 460$ K in $LaCoGe_3$ and 510 K in $LaRhGe_3$. This is due to the large effective atomic number of Ir and a large distribution of the radial wave function of Ir-$5d$ electrons close to the nuclear center, compared with those of Co and Rh.

(3) The topology of the Fermi surface in a paramagnet $PrCoGe_3$ is the same as that of $LaCoGe_3$, although the cyclotron mass of $PrCoGe_3$ is approximately twice as large as that of $LaCoGe_3$, which produces a smaller value of $2|\alpha p_\perp| = 284$ K for branch α compared with 461 K in $LaCoGe_3$. It is experimentally confirmed that the antisymmetric spin-orbit interaction becomes small in magnitude with increasing the cyclotron mass, being inversely proportional to the cyclotron mass.

(4) On the other hand, the topology of the Fermi surface in $LaFeGe_3$ is different from that of $LaTGe_3$(T: Co, Rh, Ir), and furthermore the cyclotron mass of $LaFeGe_3$ is three to four times larger than that of $LaTGe_3$, which produces a much smaller value of $2|\alpha p_\perp|$ $= 134$ K for a main bands 67 and 68-Fermi surface, named α.

(5) We carried out the cantilever type dHvA experiment. An ample dHvA amplitude was obtained in the whole field direction except a few degree of the symmetrical direction. This method is found to be extremely useful for a very tiny single crystal with $0.1 \times 0.1 \times 0.05$ mm^3.

II) We grew single crystals of antiferromagnetic $CeTX_3$ compounds and clarified the electrical and magnetic properties. We succeeded in growing a single crystal of $CeRuSi_3$ from the Czochralski method, and single crystals of $CePtSi_3$ by the Sn-flux method and

CeRhGe$_3$ and CeIrGe$_3$ by the Bi-flux method. The unique superconducting property on the upper critical field was obtained in CeCoGe$_3$. Experimental results are summarized as follows:

(1) The magnetic susceptibility for $H // [100]$ (a-axis), χ_a, is larger than that for $H // [001]$, χ_c, in the paramagnetic state of CeTSi$_3$ and CeTGe$_3$, except for CeCoGe$_3$. This is due to the contribution of the positive and large value of B_2^0 in the CEF scheme for the present tetragonal structure.

(2) The characteristic magnetization curves are obtained in antiferromagnets CeRhGe$_3$ and CeIrGe$_3$, including the metamagnetic transition. In CeIrGe$_3$, the critical field at the metamagnetic transition, $H_c = 12.6$ kOe at 7 K, decreases with decreasing temperature from the Néel temperature $T_{N1} = 8.7$ K, and becomes zero at the first-order magnetic transition temperature $T_{N2} = 4.8$ K, indicating a ferromagnetic curve with a small magnetic moment of $0.14\,\mu_B$/Ce at 2 K.

(3) The Néel temperature and the electronic specific heat coefficient are plotted as a function of molar volume in the crystal structure for CeTSi$_3$ and CeTGe$_3$ (T: Co, Rh, Ir). This relation roughly corresponds to the Doniach phase diagram indicating the competition between the RKKY interaction and the Kondo effect. Following this relation, we investigated the effect of pressure on the electronic states in antiferromagnets CeCoGe$_3$, CeRhGe$_3$ and CeIrGe$_3$. CeRhGe$_3$ and CeIrGe$_3$ are sited far from the magnetic quantum critical point. On the other hand, we observed clear pressure-induced superconductivity in the pressure region from 5.4 GPa to about 7.5 GPa in CeCoGe$_3$. The slope of the upper critical field at 6.5 GPa is found to be extremely large, with an upturn curvature with decreasing temperature: $-dH_{c2}/dT = 200$ kOe/K at $T_{sc} = 0.69$ K for the magnetic field along the [001] direction. The upper critical field at 0 K, $H_{c2}(0)$, is roughly estimated to be about 200 kOe. This is a common feature of superconductivity in CeCoGe$_3$, CeIrSi$_3$ and CeRhSi$_3$, and might be an experimental evidence of the spin-triplet superconductivity in the non-centrosymmetric crystal structure.

In addition to these experimental results on the electrical and magnetic properties of RTX$_3$, we grew another non-centrosymmetric compounds of antiferromagnets Ce$_2$PdGe$_6$ and Ce$_2$CuGe$_6$ by the Bi-flux method and studied the electrical and magnetic properties. Both compounds are found to indicate the similar electronic states. Pressure experiments were also performed in the temperature range from 2 K to room temperature. The antiferromagnetic state was found to be changed into the paramagnetic state above 7 GPa. The measurements at much lower temperatures are needed to find superconductivity, which are left to the future study.

Acknowledgments

References

1) M. A. Ruderman, and C. Kittel, Phys. Rev. **96**, 99 (1954).

2) T. Kasuya, Prog. Theor. **16**, 45 (1956).

3) K. Yosida, Phys. Rev. **106**, 893 (1957).

4) J. Kondo, Prog. Theor. **32**, 37 (1964).

5) S. Doniach, Physica B **91**, 231 (1977).

6) S. Doniach, in Valnece Instabilities and Related Narrow-Band Phenomena, ed. by R. D. Parks, p. 169 (Plenum, New York, 1977).

7) Y. Ōnuki, T. Goto, and T. Kasuya, Materials Science and Technology, Vol.3A, ed. K. H. J. Buschow, Part I, Ch. 7, p. 545 (VCM, Weinheim 1991).

8) R. Settai, T. Takeuchi, and Y. Ōnuki, J. Phys. Soc. Jpn. **76**, 051003 (2007).

9) F. Steglich, J. Aarts, C. D. Bredl, W. Lieke, D. Meschede, W. Franz, and H. Schäfer, Phys. Rev. Lett. **43**, 1892 (1979).

10) M. Kyogaku, Y. Kitaoka, K. Asayama, C. Geibel, C. Schank, and F. Steglich, J. Phys. Soc. Jpn. **62**, 4016 (1993).

11) H. Tou, Y. Kitaoka, K. Ishida, K. Asayama, N. Kimura, Y. Ōnuki, E. Yamamoto, Y. Haga, and K. Maezawa, Phys. Rev. Lett. **80**, 3129 (1998).

12) J. Bardeen, L. N. Cooper, and J. R. Schrieffer, Phys. Rev. **108**, 1175 (1957).

13) E. Bauer, G. Hilscher, H. Michor, C. Paul, E. W. Scheidt, A. Gribanov, Y. Seropegin, H. Noël, M. Sigrist, and P. Rogl, Phys. Rev. Lett. **92**, 027003 (2004).

14) E. Bauer, H. Kaldarar, A. Prokofiev, E. Royanian, A. Amato, J. Sereni, W. Brämer-Escamilla, and I. Bonalde, J. Phys. Soc. Jpn. **76**, 051009 (2007).

15) T. Akazawa, H. Hidaka, T. Fujiwara, T. C. Kobayashi, E. Yamamoto, Y. Haga, R. Settai, and Y. Ōnuki, J. Phys. Condens. Matter **16**, L29 (2004).

16) T. Akazawa, H. Hidaka, H. Kotegawa, T. C. Kobayashi, T. Fujiwara, E. Yamamoto, Y. Haga, R. Settai, and Y. Ōnuki, J. Phys. Soc. Jpn. **73**, 3129 (2004).

17) T. C. Kobayashi, A. Hori, S. Fukushima, H. Hidaka, H. Kotegawa, T. Akazawa, K. Takeda, Y. Ohishi, and E. Yamamoto, J. Phys. Soc. Jpn. **76**, 051007 (2007).

18) N. Kimura, K. Ito, K. Saitoh, Y. Umeda, H. Aoki, and T. Terashima, Phys. Rev. Lett. **95**, 247004 (2005).

19) N. Kimura, K. Ito, H. Aoki, S. Uji, and T. Terashima, Phys. Rev. Lett. **98**, 197001 (2007).

20) N. Kimura, Y. Muro, and H. Aoki, J. Phys. Soc. Jpn. **76**, 051010 (2007).

21) I. Sugitani, Y. Okuda, H. Shishido, T. Yamada, A. Thamizhavel, E. Yamamoto, T. D. Matsuda, Y. Haga, T. Takeuchi, R. Settai, and Y. Ōnuki, J. Phys. Soc. Jpn. **75**, 043703 (2006).

22) Y. Okuda, Y. Miyauchi, Y. Ida, Y. Takeda, C. Tonohiro, Y. Oduchi, T. Yamada, N. D. Dung, T. D. Matsuda, Y. Haga, T. Takeuchi, M. Hagiwara, K. Kindo, H. Harima, K. Sugiyama, R. Settai, and Y. Ōnuki, J. Phys. Soc. Jpn. **76**, 044708 (2007).

23) R. Settai, Y. Okuda, I. Sugitani, Y. Ōnuki, T. D. Matsuda, Y. Haga, and H. Harima, International Journal of Modern Physics B **21**, 3238 (2007).

24) P. Badica, T. Kondo, and K. Togano, J. Phys. Soc. Jpn. **74**, 1014 (2005).

25) K. Togano, P. Badica, Y. Nakamori, S. Orimo, H. Takeya, and K. Hirata, Phys. Rev. Lett. **93**, 247004 (2004).

26) P. Badica, T. Kondo, T. Kubo, Y. Nakamori, S. Orimo, and K. Togano, Appl. Phys. Lett. **85**, 4433 (2004).

27) Y. Ōnuki, and A. Hasegawa, in Handbook on the Physics and Chemistry of Rare Earths, ed. J. K. A. Gschneidner and L. Eyring, Vol. 20, p. 1 (North-Holland, Amsterdam, 1995).

28) K. Ueda, and Y. Ōnuki, Physics of Heavy Fermions, p. 163 (Shokabo, 1988)(in Japanese).

29) K. W. H. Stevens, Proc. Phys. Soc., London, Sect. A **65**, 209 (1952).

30) M. T. Hutchings, *Solid State Physics, Advances in Research and Applications* edited by F. Seitz, and B. Turnbull, Vol.16, p.227 (Academic, New York, 1965).

31) K. H. J. Buschow, H. J. van Daal, F. E. Maranzana, and P. B. van Aken, Phys. Rev. B **3**, 1662 (1971).

32) A. Sumiyama, Y. Oda, H. Nagano, Y. Ōnuki, K. Shibutani, and T. Komatsubara, J. Phys. Soc. Jpn. **55**, 1294 (1986).

33) K. Yamada, and K. Yosida, Prog. Theor. Phys. **76**, 621 (1986).

34) K. Satoh, T. Fujita, Y. Maeno, Y. Ōnuki, and T. Komatsubara, J. Phys. Soc. Jpn. **58**, 1012 (1989).

35) H. Aoki, S. Uji, A. K. Albessard, and Y. Ōnuki, J. Phys. Soc. Jpn. **61**, 3457 (1992).

36) H. Aoki, S. Uji, A. K. Albessard, and Y. Ōnuki, Phys. Rev. Lett. **71**, 2110 (1993).

37) C. D. Bredl, J. Magn. Magn. Mater. **63-64**, 355 (1987).

38) J. Etourneau, J.-P. Mercurio, R. Naslain, and P. Hagenmuller, J. Solid State Chem. **2**, 332 (1970).

39) G. R. Stewart, Rev. Mod. Phys. **56**, 755 (1984).

40) K. Miyake, T. Matsuura, and C. M. Varma, Solid State Commun. **71**, 1149 (1989).

41) K. Kadowaki, and S. B. Woods, Solid State Commun. **58**, 507 (1986).

42) P. A. Lee, T. M. Rice, J. W. Serene, L. J. Sham, and J. W. Wilkins, Comments Condens. Matter Phys. **12**, 99 (1986).

43) N. B. Brandt, and V. V. Moshchalkov, Adv. Phys. **33**, 373 (1984).

44) J. Rossat-Mignod, L. P. Regnault, J. L. Jacoud, C. Vettier, R. Lejay, J. Flouquet, E. Walker, D. Jaccard, and A. Amato, J. Magn. Magn. Mater. **76-77**, 376 (1988).

45) A. Schröder, H. G. Schlager, and H. v. Löhneysen, J. Magn. Magn. Mater. **108**, 47 (1992).

46) P. Haen, J. Flouquet, F. Lapierre, P. Lejay, and G. Remenyi, J. Low. Temp. Phys. **67**, 391 (1987).

47) G. G. Lonzarich, J. Magn. Magn. Mater. **76-77**, 1 (1988).

48) Y. Ōnuki, I. Umehara, A. K. Albessard, T. Ebihara, and K. Satoh, J. Phys. Soc. Jpn. **61**, 960 (1992).

49) H. Yamagami, and A. Hasegawa, J. Phys. Soc. Jpn. **62**, 592 (1993).

50) I. Umehara, Y. Kurosawa, N. Nagai, M. Kikuchi, K. Satoh, and Y. Ōnuki, J. Phys. Soc. Jpn. **59**, 2848 (1990).

51) A. Hasegawa, H. Yamagami, and H. Johbettoh, J. Phys. Soc. Jpn. **59**, 2457 (1990).

52) D. Jaccard, P. Link, E. Vargoz, and K. Alami-Yadri, Physica B **230-232**, 297 (1997).

53) Y. Ōnuki, R. Settai, K. Sugiyama, T. Takeuchi, T. C. Kobayashi, Y. Haga, and E. Yamamoto, J. Phys. Soc. Jpn. **73**, 769 (2004).

54) N. D. Mathur, F. M. Grosche, S. R. Julian, I. R. Walker, D. M. Freye, R. K. W. Haselwimmer, and G. G. Lonzarich, Nature **394**, 39 (1998).

55) D. Jaccard, K. Behnia, and J. Sierro, Phys. Lett. A **163**, 475 (1992).

56) R. Movshovich, T. Graf, D. Mandrus, M. F. Hundley, J. D. Thompson, R. A. Fisher, N. E. Phillips, and J. L. Smith, Physica B **223-224**, 126 (1996).

57) R. Movshovich, T. Graf, D. Mandrus, J. D. Thompson, J. L. Smith, and Z. Fisk, Phys. Rev. B **53**, 8241 (1996).

58) B. Bellarbi, A. Benoit, D. Jaccard, J. M. Mignot, and H. F. Braun, Phys. Rev. B **30**, 1182 (1984).

59) A. T. Holmes, D. Jaccard, and K. Miyake, Phys. Rev. B **69**, 024508 (2004).

60) M. Yogi, Y. kitaoka, S. Hashimoto, T. Yasuda, R. Settai, T. D. Matsuda, Y. Haga, Y. Ōnuki, P. Rogl, and E. Bauer, Phys. Rev. Lett. **93**, 027003 (2004).

61) S. K. Yip, Phys. Rev. B **65**, 144508 (2002).

62) E. I. Rashba, Sov. Phys. Solid State. **2**, 1109 (1960).

63) S. Fujimoto, Phys. Rev. B **72**, 024515 (2005).

64) V. M. Edelstein, Sov. Phys. JETP **68**, 1244 (1989).

65) L. P. Gor'kov, and E. Rashba, Phys. Rev. Lett. **87**, 037004 (2001).

66) I. A. Sergienko, and S. H. Curnoe, Phys. Rev. B **70**, 214510 (2004).

67) V. M. Edelstein, Phys. Rev. Lett. **75**, 2004 (1995).

68) S. K. Yip, J. Low Temp. Phys. **140**, 67 (2005).

69) K. V Samokhin, Phys. Rev. B **70**, 104521 (2004).

70) R. P. Kaur, D. F. Agterberg, and M. Sigrist, Phys. Rev. Lett. **94**, 137002 (2005).

71) N. Hayashi, K. Wakabayashi, P. A. Frigeri, and M. Sigrist, Phys. Rev. B **73**, 092508 (2006); ibid **73**, 024504 (2006).

72) T. Yokoyama, Y. Tanaka, and J. Inoue, Phys. Rev. B **72**, 220504(R) (2006).

73) M. Oka, M. Ichioka, and K. Machida, Phys. Rev. B **73**, 214509 (2006).

74) P. A. Frigeri, D. F. Agterberg, A. Koga, and M. Sigrist, Phys. Rev. Lett. **92**, 097001 (2004) [Errata; **93**, 099903 (2004)].

75) T. Takeuchi, T. Yasuda, M. Tsujino, H. Shishido, R. Settai, H. Harima, and Y. Ōnuki, J. Phys. Soc. Jpn. **76**, 014702 (2007).

76) A. M. Clogston, Phys. Rev. Lett. **9**, 266 (1962).

77) B. S. Chandrasekhar, Appl. Phys. Lett. **1**, 7 (1962).

78) K. Scharnberg, and R. A. Klemm, Phys. Rev. B **22**, 5233 (1980).

79) P. A. Frigeri, D. F. Agterberg, and M. Sigrist, New J. Phys. **6**, 115 (2004).

80) W. Dörrscheidt, and H. Schäfer, J. Less-Common Met. **58**, 209 (1978).

81) E. Parthé, B. Chabot, H. F. Braun, and N. Engel, Acta Cryst. B **39**, 588 (1983).

82) N. Engel, H. F. Braun, and E. Parthé, J. Less-Common Met. **95**, 309 (1983).

83) P. Lejay, I. Higashi, B. Chevalier, J. Etourneau, and P. Hagenmuller, Mat. Res. Bull. **19**, 115 (1984).

84) G. Venturini, M. Méot-Meyer, B. Malaman, and B. Roques, J. Less-Common Met. **113**, 197 (1985).

85) H. Yamamoto, H. Sawa, and M. Ishikawa, Phys. Lett. A **196**, 83 (1994).

86) P. Salamakha, M. Konyk, O. Sologub, and O. Bodak, J. Alloys Comps. **234**, 151 (1996).

87) A. V. Morozkin, and Yu. D. Seropegin, J. Alloys Comps. **237**, 124 (1996).

88) J. Kitagawa, Y. Muro, N. Takeda, and M. Ishikawa, J. Phys. Soc. Jpn. **66**, 2163 (1997).

89) Yu. D. Seropegin, B. I. Shapiev, A. V. Gribanov, and O I. Bodak, J. Alloys Comps. **288**, 147 (1999).

90) A. V. Gribanov, Y. D. Seropegin, A. I. Tursina, O. I. Bodak, P. Rogl, and H. Noël, J. Alloys Comps. **383**, 286 (2004).

91) A. V. Tkachuk, and A. Mar, Acta Cryst. E **61**, i1 (2005).

92) P. Salamakha, M. Konyk, O. Sologub, and O. Bodak, J. Alloys Comps. **236**, 206 (1996).

93) Yu. D. Seropegin, B. I. Shapiev, A. V. Gribanov, and O. I. Bodak, J. Alloys Comps. **288**, 155 (1999).

94) P. Haen, P. Lejay, B. Chevalier, B. Lloret, J. Etourneau, and M. Sera, J. Less-Common Met. **110**, 321 (1985).

95) H. Yamamoto, M. Ishikawa, K. Hasegawa, and J. Sakurai, Phys. Rev. B **52**, 10136 (1995).

96) D. H. Eom, M. Ishikawa, J. Kitagawa, and N. Takeda, J. Phys. Soc. Jpn. **67**, 2495 (1998).

97) Y. Muro, D. H. Eom, N. Takeda, and M. Ishikawa, J. Phys. Soc. Jpn. **67**, 3601 (1998).

98) Y. Muro, D. H. Eom, N. Takeda, M. Ishikawa, K. Kanai, M. Watanabe, and S. Shin, Physica B **259-261**, 1114 (1999).

99) Y. Muro, Dr. Thesis, Faculty of Science, University of Tokyo, Tokyo(2000) [in Japanese].

100) N. Kimura, Y. Umeda, T. Asai, T. Terashima, and H. Aoki, Physica B **294-295**, 280 (2001).

101) Y. Muro, M. Ishikawa, K. Hirota, Z. Hiroi, N. Takeda, N. Kimura, and H. Aoki, J. Phys. Soc. Jpn. **76**, 033706 (2007).

102) C. Geibel, C. Kämmerer, E. Göring, R. Moog, G. Sparn, R. Henseleit, G. Cordier, S. Horn, and F. Steglich, J. Magn. Magn. Mater. **90-91**, 435 (1990).

103) A. Thamizhavel, T. Takeuchi, T. D. Matsuda, Y. Haga, K. Sugiyama, R. Settai, and Y. Ōnuki, J. Phys. Soc. Jpn. **74**, 1858 (2005).

104) H. R. Ott, H. Rudigier, Z. Fisk, and J. L. Smith, Phys. Rev. Lett. **50**, 1595 (1983).

105) L. N. Bulaevskii, O. V. Dolgov, and M. O. Ptitsyn, Phys. Rev. B **38**, 11290 (1988).

106) A. Thamizhavel, H. Shishido, Y. Okuda, H. Harima, T. D. Matsuda, Y. Haga, R. Settai, and Y. Ōnuki, J. Phys. Soc. Jpn. **75**, 044711 (2006).

107) N. Tateiwa, Y. Haga, T. D. Matsuda, S. Ikeda, E. Yamamoto, Y. Okuda, Y. Miyauchi, R. Settai, and Y. Ōnuki, J. Phys. Soc. Jpn. **76**, 083706 (2007).

108) M. B. Konyk, P. S. Salamakha, O. I. Bodak, and V. K. Pecharskii, Kristallografiya **33**, 838 (1988).

109) O. Sologub, K. Hiebl, P. Rogl, and O. I. Bodak, J. Alloys. Comps **227**, 37 (1995).

110) A. V. Gribanov, Y. D. Seropegin, O. I. Bodak, V. N. Nikiforov, A. A. Velikhovskii, and J. Mirkovic, J. Phase Equilibria **17**, 196 (1996).

111) Yu. D. Seropegin, A. V. Gribanov, and O. I. Bodak, J. Alloys. Comps **269**, 157 (1998).

112) H. Yamamoto, I. Oguro, and M. Ishikawa, J. Phys. Soc. Jpn **65**, 3464 (1996).

113) B. Chevalier, and J. Etourneau, J. Magn. Magn. Mater. **196-197**, 880 (1999).

114) M. Konyk, L. Romaka, D. Gignoux, D. Fruchart, O. I. Bodak, and Yu. Gorelenko, J. Alloys Comps **398**, 8 (2005).

115) M. B. Konyk, L. P. Romaka, Yu. K. Gorelenko, and O. I. Bodak, J. Alloys Comps. **311**, 120 (2000).

116) A. M. Strydom, A. V. Gribanov, Yu. D. Seropegin, R. Wawryk, and R. Troć, J. Magn. Magn. Mater. **283**, 181 (2004).

117) Y. T. Fan, W. H. Lee, and Y. Y. Chen, Phys. Rev. B **69**, 132401 (2004).

118) T. -W. Tseng, W. -H. Lee, and Y. -Y. Chen, Jpn. J. Appl. Phys. **43**, L66 (2004).

119) M. Ohashi, G. Oomi, K. Ishida, I. Satoh, T. Komatsubara, T. Kawae, and K. Takeda, J. Alloys Comps. **408-412**, 84 (2006).

120) Y. Haga, H. Sakai, and S. Kambe, J. Phys. Soc. Jpn. **76**, 051012 (2007).

121) V. P. Mineev, and K. V. Samokhin, Phys. Rev. B **72**, 212504 (2005).

122) M. Shirakawa, M. Ona, H. Aoki, A. Ochiai, and H. Harima, Acta Physica Polonica B **34**, 1157 (2003).

123) Y. Inada, P. Wiśniewski, M. Murakawa, D. Aoki, K. Miyake, N. Watanabe, Y. Haga, E. Yamamoto, and Y. Ōnuki, J. Phys. Soc. Jpn. **70**, 558 (2001).

124) E. Yamamoto, Y. Haga, T. D. Matsuda, A. Nakamura, R. Settai, Y. Inada, H. Sugawara, H. Sato, and Y. Ōnuki, J. Nucl. Sci. Technol. Suppl. **3**, 187 (2002).

125) R. Settai, Y. Yoshida, A. Yamaguchi, Y. Ōnuki, S. Yoshii, M. Kasaya, H. Harima, and K. Takegahara, J. Phys. Soc. Jpn. **68**, 3615 (1999).

126) S. Hashimoto, T. Yasuda, T. Kubo, H. Shishido, T. Ueda, R. Settai, T. D. Matsuda, Y. Haga, H. Harima, and Y. Ōnuki, J. Phys. Condens. Matter **16**, L287 (2004).

127) Z. Fisk, and J. P. Remeika, *in Handbook on the Physics ans Chemistry of Rare Earths*, edited by K. A. Gschneidner Jr. and L. Eyring, Vol.12, Chap. 81, p. 53 (North-Holland, Amsterdam, 1995).

128) Z. Kletowski, N. Iliev, Z. Henkie, and B. Staliński, J. Less-Common Met. **110**, 235 (1985).

129) D. Shoenberg, Magnetic Oscillations in Metals (Cambridge University Press, Cambridge, 1984).

130) E. Ohmichi, and T. Osada, Rev. Sci. Inst. **73**, 3022 (2002).

131) J. R. Cooper, A. Carrington, P. J. Meeson, E. A. Yelland, N. E. Hussey, L. Balicas, S. Tajima, S. Lee, S. M. Kazakov, and J. Karpinski, Physica C **385**, 75 (2003).

132) R. Settai, T. Kawai, T. Endo, H. Muranaka, Y. Doi Y. Ōnuki, and H. Harima, printed in J. Phys. Soc. Jpn. suppl.

133) N. Mori, H. Takahashi, and N. Takeshita, High Pressure Res. **24**, 225 (2004).

134) F. Datchi, P. Loubeyre, and R. LeToullec, Phys. Rev. B **61**, 6535 (2000).

135) P. M. Bell, and H. K. Mao, *Carnegie Institute Washington Yearbook* **80**, 404 (1981).

136) M. Eremets, *High Pressure Experimental Methods*, p.186 (Published by Oxford University Press Inc., New York, 1996).

137) H. Kitazawa, Q. Z. Gao, H. Shida, T. Suzuki, A. Hasegawa, and T. Kasuya, J. Magn. Magn. Mater. **52**, 286 (1985).

138) D. D. Koelling, and B. N. Harmon, J. Phys. C: Solid State Phys. **10**, 3107 (1977).

139) M. Nishiyama, Y. Inada, and G.- Q. Zheng, Phys. Rev. Lett. **98**, 047002 (2007).

140) N. Aso, H. Miyano, H. Yoshizawa, N. Kimura, T. Komatsubara, and H. Aoki, J. Magn. Magn. Mater. **310**, 602 (2007).

141) T. D. Matsuda, Y. Haga, S. Ikeda, A. Galatanu, E. Yamamoto, H. Shishido, M. Yamada, J. -I. Yamaura, M. Hedo, Y. Uwatoko, T. Matsumoto, T. Tada, S. Noguchi, T. Sugimoto, K. Kuwahara, K. Iwasa, M. Kohgi, R. Settai, and Y. Ōnuki, J. Phys. Soc. Jpn. **74**, 1552 (2005).

142) F. Honda, N. Metoki, T. D. Matsuda, Y. Haga, and Y. Ōnuki, J. Phys. Condens. Matter **18**, 479 (2006).

143) A. Loidl, K. Knorr, G. Knopp, A. Krimmel, R. Caspary, A. Böhm, G. Sparn, C. Geibel, F. Steglish, and A. P. Murani, Phys. Rev. B **46**, 9341 (1992).

144) Y. Okuda, I. Sugitani, H. Shishido, T. Yamada, A. Thamizhavel, E. Yamamoto, T. D. Matsuda, Y. Haga, T. Takeuchi, R. Settai, and Y. Ōnuki, J. Magn. Magn. Mater. **310**, 563 (2007).

145) T. Kawai, M. Nakashima, Y. Okuda, H. Shishido, T. Shimoda, T. D. Matsuda, Y. Haga, T. Takeuchi, M. Hedo, Y. Uwatoko, R. Settai, and Y. Ōnuki, J. Phys. Soc. Jpn. **76**, Suppl. A, 166 (2007).

146) K. A. Gschneidner Jr., and V. K. Pecharsky, Physica B **223&224**, 131 (1996).

147) W. Assmus, M. Herrmann, U. Rauchschwalbe, S. Riegel, W. Lieke, H. Spille, S. Horn, G. Weber, F. Steglich, and G. Cordier, Phys. Rev. Lett. **52**, 469 (1984).

148) M. Nakashima, K. Tabata, A. Thamizhavel, T. C. Kobayashi, M. Hedo, Y. Uwatoko, K. Shimizu, R. Settai, and Y. Ōnuki, J. Phys., Condens. Matter **16**, L255 (2004).

Publication List

1) **T. Kawai**, Y. Okuda, H. Shishido, A. Thamizhavel, T. D. Matsuda, Y. Haga, M. Nakashima, T. Takeuchi, M. Hedo, Y. Uwatoko, R. Settai, and Y. Ōnuki, Magnetic and Electrical Properties in CePtSi$_3$ without Inversion Symmetry in the Crystal Structure, *J. Phys. Soc. Jpn.* **76**, 014710 (2007).

2) **T. Kawai**, M. Nakashima, Y. Okuda, H. Shishido, T. Shimoda, T. D. Matsuda, Y. Haga, T. Takeuchi, M. Hedo, Y. Uwatoko, R. Settai, and Y. Ōnuki, Pressure Effect of Electronic States in Antiferromagnets CeTX$_3$ (T: Transition metal, X: Si and Ge), *J. Phys. Soc. Jpn.* **76** *Suppl. A*, 166 (2007).

3) T. Shimoda, Y. Okuda, Y. Takeda, Y. Ida, Y. Miyauchi, **T. Kawai**, T. Fujie, I. Sugitani, A. Thamizhavel, T. D. Matsuda, Y. Haga, T. Takeuchi, M. Nakashima, R. Settai, and Y. Ōnuki, Magnetic and electronic properties in CeTSi$_3$ and CeTGe$_3$ (T: transition metal), *J. Magn. Magn. Mat.* **310**, 308 (2007).

4) T. Ueda, H. Harima, T. Yasuda, **T. Kawai**, R. Settai, and Y. Ōnuki, de Haas-van Alphen effect and the electronic state in CePtAl, *J. Magn. Magn. Mat.* **310**, 391 (2007).

5) H. Shishido, R. Settai, **T. Kawai**, H. Harima, and Y. Ōnuki, de Haas-van Alphen effect of CeIr$_{1-x}$Rh$_x$In$_5$, *J. Magn. Magn. Mat.* **310**, 303 (2007).

6) **T. Kawai**, R. Settai, H. Shishido, T. Shiromoto, K. Maezawa, and Y. Ōnuki, de Haas-van Alphen Effect and the Electrical Resistivity Measurements in α-Ce Under Pressure, *Frontiers of Basic Science Towards New Physics Earth and Space Science Mathematics*, Osaka University Press, 251 (2005).

7) R. Settai, **T. Kawai**, T. Endo, H. Muranaka, Y. Doi, Y. Ōnuki, and H. Harima, De Haas-van Alphen Effects Using a Micro-cantilever: Application to LaFeGe$_3$, *printed in J. Phys. Soc. Jpn. Suppl.*

8) M. Nakashima, **T. Kawai**, T. Shimoda, T. Takeuchi, T. Yoneyama, T. D. Matsuda, Y. Haga, K. Shimizu, M. Hedo, Y. Uwatoko, R. Settai, and Y. Ōnuki, Single crystal growth and pressure effect of an antiferromagnet Ce$_2$CuGe$_6$, *Physica B* **403**, 789 (2008).

9) **T. Kawai**, H. Muranaka, T. Endo, N. D. Dung, Y. Doi, S. Ikeda, T. D. Matsuda, Y. Haga, H. Harima, R. Settai, and Y. Ōnuki,
Split Fermi Surface Properties of $LaTGe_3$ (T: Transition Metal) and $PrCoGe_3$ with the Non-centrosymmetric Crystal Structure,
submitted in J. Phys. Soc. Jpn..

10) **T. Kawai**, H. Muranaka, M.-A. Measson, T. Shimoda, Y. Doi, T. D. Matsuda, Y. Haga, G. Knebel, G. Lapertot, D. Aoki, J. Flouquet, T. Takeuchi, R. Settai, and Y. Ōnuki,
Magnetic and Superconducting Properties of $CeTX_3$ (T: Transition Metal and X: Si and Ge) With Non-centrosymmetric Crystal Structure,
submitted in J. Phys. Soc. Jpn..